UNIVERSITY OF SOUTHAMPTON

FACULTY OF ENGINEERING AND APPLIED SCIENCES

INSTITUTE OF SOUND AND VIBRATION RESEARCH

VIBRATION CONTROL WITH ELECTRODYNAMIC ACTUATORS

by

Christoph Paulitsch

A thesis submitted for the award of

Doctor of Philosophy

September 2005

To my parents and grandparents

UNIVERSITY OF SOUTHAMPTON

ABSTRACT

FACULTY OF ENGINEERING AND APPLIED SCIENCE

INSTITUTE OF SOUND AND VIBRATION RESEARCH

<u>Doctor of Philosophy</u>
VIBRATION CONTROL WITH AN ELECTRODYNAMIC ACTUATOR
by Christoph Paulitsch

This thesis deals with different configurations of an electrodynamic actuator that is used to control vibrations of mechanical structures. Stability and vibration reduction performance are investigated both with theoretical and experimental studies on the model problem of an aircraft panel.

At first a conventional, electrodynamic, reactive actuator acting on the aircraft panel and reacting against a fixed base is studied. Direct velocity feedback with ideal velocity sensor and force actuator, with an accelerometer sensor and with different self-sensing control schemes such as a shunted resistor, positive current feedback, induced voltage feedback and induced voltage feedback with inductance compensation are compared.

Then the design of a more practical, lightweight, electrodynamic, inertial actuator is studied. Important design considerations for the mechanical and the electrical parts are highlighted and some designed characteristics are validated at a prototype actuator.

Finally the lightweight, electrodynamic, inertial actuator is applied on the aircraft panel and vibration reduction is compared to passive means of vibration reduction. First internal relative velocity and external absolute velocity feedback are investigated considering ideal sensors. In practice, the external velocity feedback loop is implemented using a commercial accelerometer while the internal velocity feedback loop is implemented with self-sensing control schemes or, as an alternative, with a secondary coil sensor. Then internal and external direct velocity feedback loops are implemented simultaneously using either the accelerometer – self-sensing or accelerometer – secondary coil sensor combination. The best combination of external and internal direct velocity feedback for maximum vibration reduction and robust stability of the inertial actuator is identified. Alternative ways to stabilise the inertial actuator are also studied. The result is a competitive, lightweight system for broadband vibroacoustic control.

EUROPEAN DOCTORATE IN SOUND AND VIBRATION STUDIES

Vibration Control with Electrodynamic Actuators

by Christoph Paulitsch

6th September 2005

This doctorate was carried out as part of the EDSVS program with Home Institute

University of Southampton, Institute of Sound and Vibration Research (ISVR)

and Hosting Institute(s):

Katholieke Universiteit Leuven, Department of Mechanical Engineering (KUL)

The doctoral degree has been awarded by the Home Institute, ISVR, following the local rules and procedures for the thesis dissertation and degree award.

Also the thesis was examined and defended in accordance with the criteria laid down by the "*Confederation of European Union Rectors' Conferences*"

Criteria laid down by the *"Confederation of European Union Rectors' Conferences"* for the award of European Doctorate certificates:

1) the PhD thesis defence will be accorded if at least two professors from two higher education institutions of two European countries, other than the one where the PhD thesis will be defended, have given their judgement concerning the manuscript;

2) at least one member of the jury should come from a higher education institution in European Countries, other than the one, where the PhD thesis will be defended;

3) part of the defence must take place in one of the official languages, other than the one(s) of the country, where the PhD thesis will be defended;

4) the PhD thesis must partly have been prepared as a result of a period of research of at least one trimester spent in another European Country.

LIST OF CONTENTS

LIST OF TABLES

LIST OF SYMBOLS

Phasors

Y_o	measured output	
Y_i	control input	
V_s	plate velocity at the secondary actuator position	[m s^{-1}]
F_p	primary excitation force	[N]
F_s	secondary control force	[N]
I	actuator driving current	[A]
U_{ind}	induced voltage in the primary coil	[V]
U_{AB}	voltage difference between voltage at connections A and B	[V]
U_{AC}	voltage difference between voltage at connections A and C	[V]
U_{BC}	voltage difference between voltage at connections B and C	[V]
U_{AD}	voltage difference between voltage at connections A and D	[V]
I_1	current in half-bridge	[A]
F_{s2}	force between inertial actuator and plate	[N]
V_a	velocity of the moving mass of the inertial actuator	[m s^{-1}]
F_{s1}	force between the moving mass and the suspension of the inertial actuator	[N]
$\mathbf{f}_s$	transmitted force vector with components F_{s1} and F_{s2}	[N, N]
$\mathbf{f}_a$	actuation force vector with actuation force components F_a and $-F_a$	[N, N]
$\mathbf{v}_s$	velocity vector comprising plate velocity V_s and moving mass velocity	[m s^{-1}, m s^{-1}]
I_c	control current in the primary coil of the inertial actuator	[A]
I_s	current in the secondary coil of the inertial actuator	[A]
B_v	vertical component of the magnetic field generated by the primary and the secondary coil	[T]
U_s	secondary coil voltage	[V]
U_{inds}	induced voltage in the secondary coil	[V]
F_t	transmitted force by the actuator on the structure	[N]
I_{ec}	eddy current induced in the coil former	[A]
U_{ec}	voltage due to eddy current in the coil former	[V]
I_p	current in the primary disturbance shaker	[A]

Abbreviations

j	imaginary unit ($=\sqrt{-1}$)
N	number of considered mode shapes
n	index of mode shape

$\mathbf{I}$	identity matrix in $R^{2\times 2}$	
μ_0	$4\pi 10^{-7} Hm^{-1}$	
π	~3.1415926535, ratio of circumference to diameter of a circle	
g	$9.81 ms^{-2}$, gravity constant	

Impedances and mobilities

G_{sp}	general FRF between the disturbance input and the controlled output	
G_{si}	general FRF between the control input and the controlled output	
G_{op}	general FRF between the disturbance input and the measured output	
G_{oi}	general FRF between the control input and the measured output	
Y_{sp}	transfer mobility of the plate between primary and secondary Actuator	$[m\,s^{-1}/N]$
Y_{ss}	point mobility of the plate at the position of the secondary actuator	$[m\,s^{-1}/N]$
Y'_{sp}	transfer mobility of the plate with primary force transducer	$[m\,s^{-1}/N]$
Y'_{ss}	point mobility of the plate with attached secondary actuator mass	$[m\,s^{-1}/N]$
Y''_{sp}	transfer mobility of the plate with attached secondary actuator	$[m\,s^{-1}/N]$
Y''_{ss}	point mobility of the plate with attached secondary actuator	$[m\,s^{-1}/N]$
Z	transfer impedance of the secondary actuator suspension	$[N/(m\,s^{-1})]$
Z_e	electrical impedance of the secondary actuator driving coil	$[V/A]$
Z'_e	modified electrical impedance of the secondary actuator driving coil	$[V/A]$
Z_1	electrical bridge impedance 1	$[V/A]$
Z_2	electrical bridge impedance 2	$[V/A]$
Y_m	mobility of the moving mass of the inertial actuator	$[m\,s^{-1}/N \ldots m\,s^{-1}/N \ldots m\,s^{-1}/N]$
$\mathbf{y}_{sp}$	transfer mobility vector of plate including force transducer and housing mass	$[m\,s^{-1}/N \ldots m\,s^{-1}/N \ldots m\,s^{-1}/N]$
$\mathbf{Y}_{ss}$	point mobility matrix of plate including force transducer and housing mass	$[m\,s^{-1}/N \ldots m\,s^{-1}/N \ldots m\,s^{-1}/N]$
$\mathbf{y}'_{sp}$	transfer mobility vector of plate with attached inertial actuator and force transducer and housing mass	$[m\,s^{-1}/N \ldots m\,s^{-1}/N \ldots m\,s^{-1}/N]$
$\mathbf{Y}'_{ss}$	point mobility matrix of plate with attached inertial actuator and force transducer and housing mass	$[m\,s^{-1}/N \ldots m\,s^{-1}/N \ldots m\,s^{-1}/N]$
$\mathbf{y}''_{sp}$	transfer mobility vector of plate with attached inertial actuator	$[m\,s^{-1}/N \ldots m\,s^{-1}/N \ldots m\,s^{-1}/N]$
$\mathbf{Y}''_{ss}$	point mobility matrix of plate with attached inertial actuator	$[m\,s^{-1}/N \ldots m\,s^{-1}/N \ldots m\,s^{-1}/N]$
$\mathbf{y}'''_{sp}$	transfer mobility vector of plate	$[m\,s^{-1}/N \ldots m\,s^{-1}/N \ldots m\,s^{-1}/N]$
$\mathbf{Y}'''_{ss}$	point mobility matrix of plate	$[m\,s^{-1}/N \ldots m\,s^{-1}/N \ldots m\,s^{-1}/N]$

Z_s	input impedance of the electrical circuit connected to the secondary coil	[V / A]
Z_m	blocked mechanical impedance of plate and actuator	[N / (ms^{-1})]
Z_p	electrical impedance shunted to the electrodynamic control Actuator	[V / A]

Parameters

ω_0	fundamental resonance of the inertial actuator	[rad s^{-1} or Hz]
ω	circular frequency	[rad s^{-1} or Hz]
ω_n	nth natural frequency of the plate	[rad s^{-1} or Hz]
$\Phi_n(x,y)$	nth mode shape of the plate evaluated at position x, y	[-]
ρ	mass density of the plate	[kg m^{-3}]
η	loss factor of the plate	[-]
l_x	plate length	[m]
l_y	plate width	[m]
h	plate thickness	[m]
x_p	x coordinate of primary force position	[m]
y_p	y coordinate of primary force position	[m]
x_s	x coordinate of secondary force position	[m]
y_s	y coordinate of secondary force position	[m]
E	Young's modulus of plate material	[N m^{-2}]
v	Poisson's ratio	[-]
K_1	coefficient to adjust for non-ideal boundary conditions	[-]
K_2	coefficient to adjust for non-ideal boundary conditions	[-]
Mp	mass of force transducer at the primary actuator position	[kg]
M	mass of the secondary actuator attached to the plate	[kg]
ψ	electrodynamic transducer coefficient (Bl product) of the secondary actuator	[N A^{-1}]
K	stiffness of the secondary actuator suspension	[N m^{-1}]
D	viscous damping coefficient of the secondary actuator suspension	[N s m^{-1}]
R_e	electrical resistance of the driving coil	[Ω]
L_e	electrical self-inductance of the driving coil	[H]
R_l	shunted, measurement, Wheatstone or Owens bridge resistor	[Ω]
R_1	upper resistor for Wheatstone bridge	[Ω]
R_2	lower resistor for Wheatstone bridge	[Ω]
R_3	lower resistor for Owens bridge	[Ω]
C	capacitor for Owens bridge	[F]
G	feedback gain	[various]
g	internal velocity feedback gain	[various]

ξ_n	non-dimensional viscous damping coefficient of the nth plate mode	[-]
m	moving / inertial mass of the inertial actuator	[kg]
Ψ_p	electrodynamic transducer coefficient (*Bl* product) of primary coil	[N A^{-1}]
$\boldsymbol{\psi}_p$	vector of electrodynamic transducer coefficients of primary coil	[N A^{-1} N A^{-1}]
Ψ_s	electrodynamic transducer coefficient (*Bl* product) of secondary coil	[N A^{-1}]
$\boldsymbol{\psi}_s$	vector of electrodynamic transducer coefficients of secondary coil	[N A^{-1} N A^{-1}]
N_p	number of windings of the primary coil	[-]
h_p	height of the primary coil	[m]
A_p	cross section of the primary coil	[m^2]
N_s	number of windings of the secondary coil	[-]
h_s	height of the secondary coil	[m]
A_s	cross section of the secondary coil	[m^2]
L_s	self-inductance of the secondarycoil	[H]
L_{sp}	mutual or coupling inductance between the primary and the secondary coil	[H]
μ	equivalent permeability of the magnetic circuit	[H m^{-1}]
G_1	proportional feedback gain in compensator for inertial actuator dynamics	[V V^{-1}]
C_1	capacitor for integrated displacement cut-on frequency	[F]
R_4	resistor for integrated displacement cut-on frequency	[Ω]
C_2	capacitor for damping adjustment in compensator for inertial actuator dynamics	[F]
R_5	resistor for damping adjustment in compensator for inertial actuator dynamics	[Ω]
ω_{co}	cut-on frequency of high-pass filter and compensator for inertial actuator dynamics	[rad s^{-1} or Hz]
ω_{hp}	cut-on frequency of high-pass filter	[rad s^{-1} or Hz]
ω_b	saturation break frequency	[rad s^{-1} or Hz]
d	actuator stroke	[m]
B_{go}	magnetic flux density at the outer diameter of the air gap	[Wb m^{-2}]
B_{gi}	magnetic flux density at the inner diameter of the air gap	[Wb m^{-2}]
B_w	magnetic flux density in the outer wall of the yoke	[Wb m^{-2}]
B_m	magnetic flux density in the permanent magnet	[Wb m^{-2}]
A_i	diameter of the hole in the permanent magnet	[m]
A	diameter of the permanent magnet	[m]
b	height of the permanent magnet	[m]
t	yoke thickness	[m]
s	air gap width	[m]
h_g	air gap height	[m]

h_{gl}	height of the lower yoke	[m]
B_r	remanence of the permanent magnet	[Wb m^{-2}]
H_l	coerciviy of the permanent magnet	[A m^{-1}]
p	configuration factor of magnetic circuit	[-]
q	shape factor of magnetic circuit	[-]
ρ_{wi}	electric resistivity of coil wire	[V / (Am)]
P	electrical power dissipated in electrodynamic actuator	[W]
ρ_{fe}	mass density of the yoke material	[kg m^{-3}]
ρ_{mag}	mass density of the permanent magnet material	[kg m^{-3}]
R	length of dominant dimension of suspension	[m]
I_d	moment of inertia of ring shaped spring	[m^4]
I_b	moment of inertia of clamped-guided leaf spring	[m^4]
I_c	moment of inertia of hinged-hinged leaf spring	[m^4]
I_a	moment of inertia of clamped-free leaf spring	[m^4]
E_s	Young's modulus of suspension material	[N m^{-2}]
σ_d	maximum internal stress in ring shaped spring	[N m^{-2}]
σ_b	maximum internal stress in clamped-guided leaf spring	[N m^{-2}]
σ_c	maximum internal stress in hinged-hinged leaf spring	[N m^{-2}]
σ_a	maximum internal stress in clamped free leaf spring	[N m^{-2}]
B_g	magnetic flux density in the air gap	[Wb m^{-2}]
ΔR_e	change in primary coil resistance due to temperature change	[Ω]
ΔT	temperature change	[K]
α_{20}	temperature coefficient of copper	[m K^{-1}]
ϕ_p	vector of modal contributions at (x_p, y_p)	[-]
ϕ_s	vector of modal contributions at (x_s, y_s)	[-]
a_n	second order resonance term of the nth mode	[s^2 kg^{-1}]
$\mathbf{A}$	matrix of second order resonance terms	[s^2 kg^{-1} ... s^2 kg^{-1} ... s^2 kg^{-1}]
E_{kin}	kinetic energy of the plate	[Nm]
l	characteristic dimension	[m]
R_0	primary coil resistance at 20ºC	[Ω]
δ	static sag of inertial actuator	[m]
F_{sp}	spring force	[N]
Ψ_{ec}	equivalent transducer coefficient for eddy current	[N / A]
R_{ec}	electrical resistance of the coil former	[Ω]
ξ_0	non-dimensional viscous damping factor of the inertial actuator	[-]
l_c	length of the coil in the air gap	[m]
r	radius of ring spring	[m]
M_{st}	static moment in the ring spring	[N m]

S_s	safety factor for static bending of the ring spring	[-]
R_m	yield strength of the ring spring material	[N m^{-2}]
h_{rs}	thickness of the ring spring	[m]
b_{sp}	width of the ring spring	[m]
M_d	amplitude of the dynamic moment in the ring spring	[N m]
S_d	safety factor for dynamic bending of the ring spring	[-]
σ_H	maximum allowable stress in a material	[N m^{-2}]
σ_u	lower stress	[N m^{-2}]
σ_o	upper stress	[N m^{-2}]
σ_{dy}	dynamic stress	[N m^{-2}]
σ_{st}	static stress	[N m^{-2}]
L	characteristic dimension in direction of the actuator stroke	[m]

ACKNOWLEDGEMENTS

1. INTRODUCTION

In many practical cases it is important to control mechanical vibrations since they may result in excessive radiated noise which may harm operators, machines, the environment or may compromise the functionality of attached devices [1-3]. In some cases active vibration or active structural acoustic control systems may be more effective than passive treatments of the same weight [4-6]. Passive treatments are especially bulky for control of high wavelength and low frequency noise [2]. When a signal correlated to the primary disturbance is not available or cannot be obtained far enough in advance feedforward control cannot be implemented [7]. In this case feedback control schemes should be used [4]. Direct velocity feedback adds active damping and is robust to changes in the vibrating structure if closely located and dual actuator sensor pairs are used [24]. In order to ensure stability of direct velocity feedback the sensor and actuator transducers have to be carefully chosen and designed. Also, an appropriate reaction structure has to be used [8]. For direct velocity feedback electrodynamic sensor-actuator transducers are interesting because they directly measure velocity and generate a force. When actuators are simultaneously used as sensors potentially collocation and duality properties are improved [29, 30]. This thesis summarizes a study of single input single output (SISO) and multiple input multiple output (MIMO) active feedback control schemes with an electrodynamic actuator and the appropriate sensor.

1.1 Active vibroacoustic control

Normally, active control systems are used in parallel to, or as a substitute of, passive means to improve low frequency structure-borne sound generation, transmission or radiation. For instance, active vibration systems can be used to influence vibration generation mechanisms or to reduce vibration of a receiving structure [8]. Active isolators might also be added in parallel to passive mounting elements in order to enhance isolation effects [9]. Finally smart beams or smart panels with integrated actuators and sensors can be used to reduce structure-borne sound transmission of truss structures or noise radiation of enclosures or partitions [10]. Especially in this last application active systems should be lightweight, cost-effective, robust and simple in order to be able to compete with passive vibration reduction treatments.

In general active control architectures can be divided into two families: feedforward and feedback control systems [4]. Feedforward control schemes are particularly suited for the control of tonal disturbances that are usually identified by a reference sensor. Feedback control architectures do not use reference sensors and are especially advantageous for control of broadband random excitation.

Previous applications

Up to present SISO feedback control systems have been developed in practice for the solution of particular acoustic problems [11] as for example the control of low frequency noise propagation in ventilation ducts [12] or low frequency noise insulation in headsets and headrests [13]. Currently, commercially available active headsets use an analogue feedback control system with a collocated error microphone and loudspeaker actuator for the low frequency noise reduction that could not be controlled by the headset shells only. Also, Active Noise Control (ANC) systems for the reduction of cabin noise in propeller aircrafts have been developed [14]. In this case a MIMO feedforward control system is used where a tonal reference signal is taken from the rotor of the propeller and a relatively large number of control loudspeakers and error microphones are used. Alternatively vibration actuators on the fuselage replace loudspeakers in order to implement so called Active Noise and Vibration Control (ANVC) [11, 15]. These systems are not suited for controlling wide band excitations and moreover they are affected by a number of drawbacks. First they require a relatively expensive and delicate multi-channel controller. Second they require a lot of wiring, actuators and sensors, which implies weight, reliability and installation problems. Third MIMO feedforward control systems are sensitive to failures of any single sensor or actuator component so that the controller is constantly updated based on all sensor signals in order to avoid instabilities. Finally due to their complexity multi-channel controllers are usually implemented using digital signal processors (DSPs), which limits a) the control bandwidth because of an anti-alising filter [7] and the time needed for calculation and b) the dynamic range and resolution because of the limited number of bits.

Active structural acoustic control (ASAC)

As a result during the past ten years scientists have begun to develop active structural acoustic control (ASAC) systems where structural sensors and actuators are closely attached or even embedded on partitions in order to control sound transmission. Most of

2

this research is motivated by the reduction of radiation or structure-borne noise transmission of the fuselage walls or marine hulls in aerospace and naval applications respectively [16]. These structures generally consist of thin and lightly damped panels with well separated resonances at lower frequencies so that the sound radiation is governed by the self-radiation of each resonant structural mode [4, 17]. Initially feedforward control systems measuring a reference signal at the noise source were used to drive the structural actuator to minimize sound radiation into the interior of the enclosure [18]. Therefore systems were still limited to the control of tonal disturbances. In parallel researchers have also developed feedback control systems where the signals from structural sensors are fed back to the structural actuators in such a way as to minimize the vibration component that contributes to the sound radiation. This has led to the design of relatively complicated multichannel feedback controllers using state space design [19].

Distributed sensors and actuators

Two interesting alternative approaches have been proposed recently [20]. The first one uses distributed sensors and actuators that enable control of the principal low frequency radiation components of the panel vibration [21]. In this case it is possible to implement a SISO feedback control system using the classic feedback control design theory (Nyquist criterion, root locus criterion and frequency domain design). The main problem encountered with this type of system is the design of suitable sensor-actuator pairs for the implementation of active structural acoustic control (ASAC) and also a stable feedback control system with a sufficient bandwidth as highlighted in [22-24].

Decentralised sensor-actuator pairs

The second type uses a large number of collocated sensor-actuator systems acting independently from each other with localized feedback control loops [25]. As schematically illustrated in Figure 1.1 each control unit implements direct velocity feedback control in such a way as to provide active damping on the panel. Active damping is especially interesting when vibration and sound radiation at resonance is to be reduced as in the case of low frequency noise radiation and transmission of thin, lightly damped panels. This arrangement has given very interesting initial simulation results especially for ideal out of plane point force actuators that could result in sound reduction of several decibels (dBs) if the individual control unit is stable.
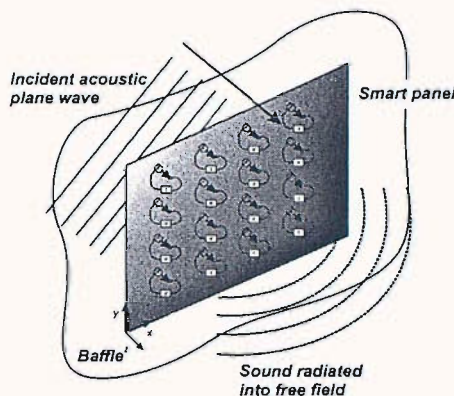
Figure 1.1: *Active structural acoustic control (ASAC) with a large number of collocated sensor-actuator pairs.*

Collocation and duality

In order for the individual SISO direct velocity feedback control unit to be unconditionally stable and robust, the real part of the sensor actuator transfer function must be positive real at all frequencies [26]. Unconditional stability is theoretically guaranteed by collocated and dual sensor-actuator pairs [27]. A sensor-actuator pair is often referred to as being dual when each transducer is of the same type i.e. the sensing / actuation direction, spatial distribution and reaction characteristics are the same [28]. Additionally when a collocated sensor-actuator pair is described by two power-conjugated dual variables, for example a force and a velocity, direct feedback becomes robust to changes in the plant response [29]. In the case of the control of flexible structures a physically dual sensor-actuator pair has the same function form for the sensing and actuation modal coupling coefficients [27]. For example a force actuator is dual to a linear displacement, velocity or acceleration sensor. Moment actuators are instead dual **to rotational** displacement, velocity or acceleration sensors. In reality there is not something like a pure moment or force actuator. For example piezoelectric patch actuators bonded on plates generate both out of plane moments and forces and in plane forces [22]. A possibility to obtain better collocation of piezoelectric patch actuators and point sensors is appropriate shaping of the patch actuator [30]. Also, in reality even a closely placed shaker force actuator and accelerometer sensor does not act as a collocated and dual pair since sensor and actuator dynamics interfere at higher and lower frequencies [31].

Self-sensing actuator

A possibility to obtain better collocation and duality properties are self-sensing actuators [32]. For example a shaker force actuator can be simultaneously used as a velocity sensor

[33]. In this case a velocity output signal could be directly measured by the actuation transducer itself instead of using the sophisticated electronics necessary to obtain such a signal from an accelerometer. Then although the measured signal Y_o is slightly different from the structural velocity V_s to be controlled it still might be used for active feedback control. This concept could be readily explained with the block diagram in Figure 1.2 [34] where G_{sp} is the frequency response function (FRF) from F_p to V_s, G_{op} is the FRF from F_p to Y_o, G_{si} is the FRF from Y_i to V_s and G_{oi} is the FRF from Y_i to Y_o.
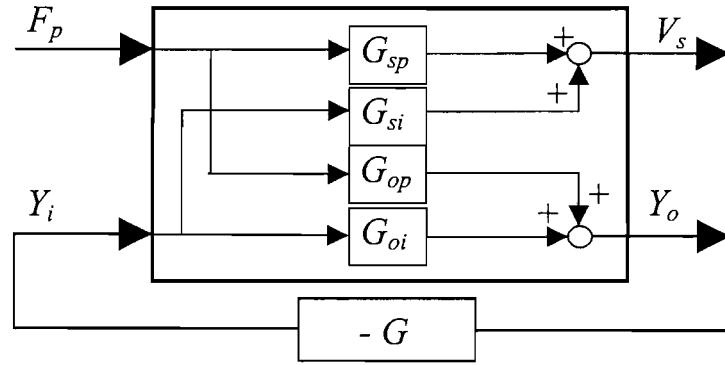
Figure 1.2: *General feedback control framework for self-sensing active vibration control.*

In order to implement simple feedback control, the measured output signal Y_o should be fed back with a real feedback gain G to the control input Y_i such that the influence of the disturbance force F_p on the controlled velocity V_s is reduced. The general frequency response functions (FRFs) G_{sp}, G_{si}, G_{op} and G_{oi} as well as the control input Y_i and the measured output Y_o are different for different self-sensing (SS) active control schemes. One aim of this thesis is to investigate different self-sensing active control schemes for an electrodynamic reactive actuator (RA) reacting against a fixed base and an electrodynamic inertial actuator (IA) reacting against an internal inertial mass. Based on Figure 1.2 the FRF for the investigation of stability is $Y_o/Y_i = G_{oi}$ and the closed loop performance is given by $V_s/F_p = (G_{sp} + G(G_{oi}G_{sp} - G_{si}G_{op}))/(1 + GG_{oi})$ in comparison to the open loop FRF $V_s/F_p = G_{sp}$.

Inertial actuators

According to Newton's laws [35], mechanical actuators or sensors react or sense relative to a reference structure. These reaction characteristics also determine duality of the actuator-sensor pair [28]. Only in rare occasions a fixed environment can be used as a reaction base. Often such a reference structure is relatively flexible and interferes with the active control. An interesting example is the case of piezoelectric patch actuators bonded to a mechanical structure where forces and moments in one direction on one side of the patch are globally

5

cancelled by reacting forces and moments in the opposite direction on the opposite side of the patch [36, 37, 26]. As a result actuation and reaction forces and moments are against the same flexible structure at slightly different locations. At smaller wavelengths the slightly different location of action and reaction moments leads to non-collocation with point sensors. Point sensors such as accelerometers usually use an inertial mass as reference system that does not have resonances in the measurement range. A force actuator reacting against an inertial mass as reference system (inertial actuator) is the simplest implementation of an actuator with a combined reaction system. Inertial actuators have been used in machine tool [38], automotive [39], aircraft [40] or especially space [41-43] applications. Because of the required forces for large structures to be controlled rather heavy actuators have been used. In some cases inertial actuators can be simultaneously used as passive vibration absorbers [44, 45], alone or with several actuators together [46]. It has also been observed that sensor [47] or actuator dynamics [8, 48, 49] influence stability of active control. Especially the inertial mass introduces a well-known rigid body mode that may lead to stability problems when direct velocity feedback is implemented [50]. The fundamental resonance of the inertial actuator due to this rigid body mode leads to a high-pass filter behaviour shown in Figure 1.3 [26]. Thus in contrast to reactive actuators, the actuation force F_a of inertial actuators is different from the actual force transmitted on the structure F_t.
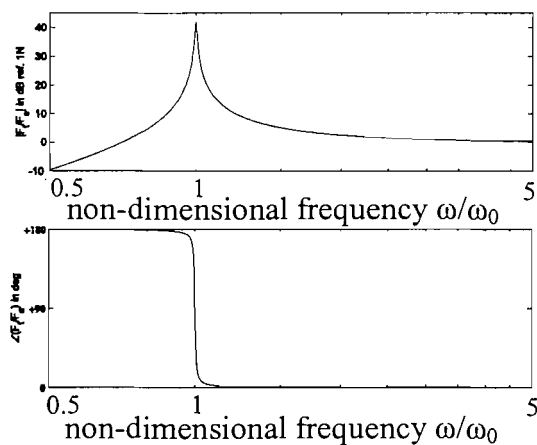
Figure 1.3: *Bode plot of the frequency response function (FRF) between the actuation force F_a and the transmitted force F_t.*

For frequencies much higher than the fundamental resonance frequency ω_0 of the inertial actuator the transmitted force converges to the actuation force, but for frequencies smaller than ω_0 the transmitted force is much smaller. Most importantly in correspondence to the fundamental resonance frequency there is an additional phase shift that influences the stability behaviour of the inertial actuator in a direct velocity feedback loop. One way to tackle this stability issue would be to reduce the fundamental resonance frequency by

decreasing the stiffness of the actuator suspension or by increasing the inertial mass of the actuator during its design. There are geometrical and mechanical limits on stiffness reduction and mass increase for small, lightweight actuators [51]. An aim of this thesis is to investigate practical solutions for reduction in suspension stiffness and increase in inertial mass for the design of a lightweight inertial actuator (IA). Adjusting internal actuator damping has also been proposed [49]. An active control scheme might use an internal relative displacement sensor with a low-order controller [52]. Another aim of this thesis is to investigate self-sensing (SS) control and an internal velocity sensor (IVS) to add optimum internal damping. The use of an inertial actuator for active control is further limited by the maximum transmitted force that is directly related to the inertial mass and its maximum displacement i.e. the stroke of the actuator [53]. Therefore stroke saturation may influence actuator performance [54-56]. In general the described behaviour is independent from the generation mechanism of the actuation force, although the transduction mechanism should be compatible with the required stroke and inertial mass.

1.2 Transduction mechanisms for inertial actuators

The generation mechanism of the actuation force F_a should not add much additional weight or should be integrated into the inertial mass of the actuator. In particular the contrasting requirements compiled in Table 1.1 demand a transducer mechanism with low added mass, high stroke, high internal damping and as small as possible suspension stiffness.

Table 1.1: *List of contrasting requirements and proposed solution (underlined)* [57].

Contrasting requirements
A **lightweight design** implies <u>**low mass**</u> and **small dimensions** that lead to a <u>**lower limit on vertical suspension stiffness**</u>.
A **high transmitted actuator force** can be realized by a **high inertial mass** and <u>**a high stroke**</u> that <u>**limits possible transduction mechanisms**</u>.
A **low lower limit on the control bandwidth** implies a **low, well-damped resonance frequency** of the actuator that can be realized by a **high inertial mass, low suspension stiffness** and <u>**high internal damping**</u>.
A **high actuation force** tends to <u>**increase the actuator mass**</u> and **limits possible transduction mechanisms**.

Actuator technologies

Following [58] actuator technologies with mechanical output include electromagnetic, fluid, bimetallic, electrochemical, electrorheological, piezoelectric, magnetostrictive, shape memory and micro actuators. In addition braided pneumatic actuators [59] can also be used as actuators for mechanical systems. Only small forces F_a and small displacements can be generated by microactuators [60], chemomechanical actuators have a large time constant, electrochemical actuators are still in development, magnetorheological, electrorheological and hydraulic actuators have a response time in the milliseconds range and shape memory, bimetallic and braided pneumatic actuators are even slower. A subclass of actuators are electromechanical transducers that can be either classified in inductive, capacitive or resistive actuators or following the used materials [61]. Magnetostrictive and piezoelectric actuators allow large forces and small displacements [62], whereas electromagnetic actuators can be designed for a large force range and large displacements. In contrast to magnetostrictive actuators piezoelectric actuators do not need an external magnetic field generator. The two commonly used transduction mechanisms for active vibration control at acoustic frequencies are electrodynamic and piezoelectric [4, 26].

Piezoelectric actuators

The piezoelectric effect results from a material property where molecules or atoms are placed within a material in such a way that their positive and negative charges locally do not compensate [61]. When a tensile or compressive stress is applied to the material a net charge can be sensed at the surface. Inversely when a voltage is applied across the material the charged parts are repulsed or attracted leading to an overall extension or contraction of the material. This property is strongest in ceramic materials. Ceramics have a high mechanical stiffness and the maximum stroke is proportional to the length of the actuator. The maximum stroke can be amplified for example by lever mechanisms, but then the resulting force also is reduced [63]. Hence the maximum stroke and force are to be balanced in a specific application as is also indicated in the diagram of Figure 1.4. This figure shows the maximum stroke versus the maximum actuation force for a number of commercially available piezoelectric actuators with different stroke amplification mechanisms [64, 65]. The maximum stroke is achieved when the actuator is not blocked and the maximum force is obtained when the actuator is connected to a very high impedance structure [62]. The number in each box shows the weight in grams for the actuator.

Free displacement in μm

[Figure graph showing Free displacement in μm vs Blocked force in N with labeled boxes]

Linear piezo motors

5000

350

Amplified piezo actuators

1000

200

19

Parallel pre-
stressed actuators

275

15.7

160

2   17.4

164   142

100

4.2   19.5

117

4.5   20

25   92

18

12

2

6

110

100   1000   5000
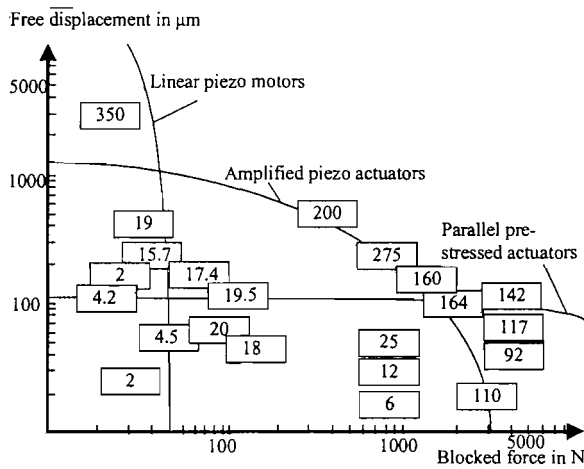
Blocked force in N

Figure 1.4: *Free displacement in μm and blocked force in N for various piezoelectric actuator technologies, boxes indicate actuator weight in grams, graph modified from* [64, 65].

The data collected in this graph indicates that strokes up to 1mm and forces up to 5kN can be generated. Actuators with higher strokes seem to increase in weight and have a smaller force generation capacity.

Electrodynamic actuators

Electrodynamic actuators are based on the Lorentz force principle where an electrically conductive wire is immersed in a constant magnetic field [61, 66]. They belong to the group of electromagnetic actuators [67, 68]. Alternative names for electrodynamic actuators are voice coil motor (VCM) [69] or moving coil type actuator [70]. When there is an electrical current in the wire a force on the wire is generated perpendicular to the direction of the current flow and the magnetic field. Inversely when the wire moves in the magnetic field there is a voltage induced in the wire in a direction perpendicular to the magnetic field and the direction of wire displacement. For electrodynamic actuators the stiffness of the suspension for the moving coil can be designed independently from the force generation mechanism and should be small for vibroacoustic control. The stroke and force also can be designed over a large range with major constraints given by the available space and possible weight [71]. At a given weight the maximum force depends on the material used for the coil wire and for the generation of the magnetic field. The wire material gives a limit on the temperature increase that results from the current flow. The material of the permanent magnet limits the realizable magnetic field densities. Figure 1.5 shows the maximum stroke versus the maximum actuation force for a number of commercially available electrodynamic actuators whose main characteristics are compiled in Appendix A.

9
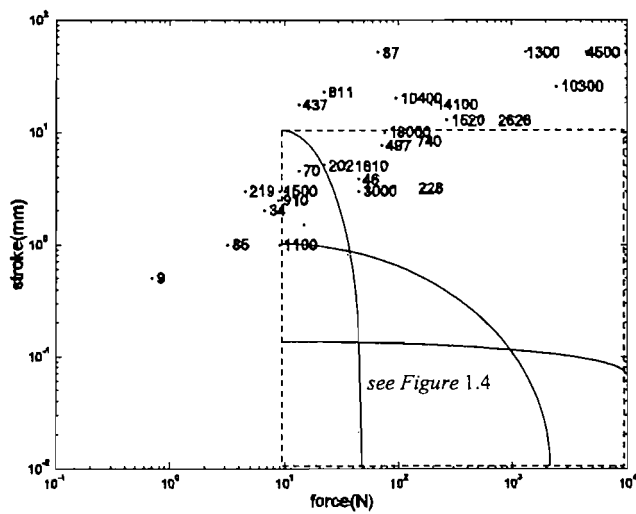
Figure 1.5: *Stroke in mm and actuation force in N for various commercially available electrodynamic actuators indicated by a dot '.' and the actuator weight in grams, values from* [72-85].

Electrodynamic actuators are designed for high strokes and a large range of forces. The actuator weight in grams indicated by the numbers tends to increase significantly for high forces. There is no clear relation between weight and force since for example an actuator with a maximum force of about 10N and a maximum stroke of about 2.5mm can be obtained with an actuator of 71 grams or 910grams. Also, the choice between maximum stroke and maximum force is not as clear for electrodynamic actuators as for piezoelectric ones where it is mostly influenced by the used mechanical amplification mechanism. This weak correlation could be the result of different scaling laws considered for the design of electrodynamic actuators [86]. For example if the magnetic energy is considered to stay constant when the actuator is scaled up or down the actuator force scales with l^2, where l is a characteristic dimension of the actuator. If the current density is kept constant the actuator force scales like l^4, whereas assuming increased current density for decreasing dimensions the actuator force scales like l^2. Scaling effects hence strongly depend on design considerations of a specific application.

In conclusion, the challenge for piezoelectric inertial actuators is the high stroke required for a low inertial mass whereas the challenge for electrodynamic inertial actuators is the actuation force. The stroke – blocked force characteristic is well known for piezoelectric actuators to be related to the deformation energy and Figure 1.4 clearly shows that strokes higher than 1mm can only be achieved with substantial addition of weight. But this characteristic is not very well known for electrodynamic actuators because of the uncertainty in the design [87]. Additionally, as discussed in Section 1.1, for inertial actuators higher strokes potentially lead to a lower actuator mass. Therefore another aim of this study is to investigate the force – mass relationship for electrodynamic actuators and to

illustrate the design choices listed in Table 1.1 in order to realize a high stroke inertial actuator.

1.3 Self-sensing control

In Section 1.1 it has been mentioned that using a self-sensing actuator might be a potential means of guaranteeing better collocation and duality properties for the implementation of direct velocity feedback loops. Additionally, weight and complexity could be reduced.

In principle self-sensing actuators, also called sensoriactuators, sense and act on the same mechanical degree of freedom (DOF). Depending on reciprocity many transducers may be used both as sensor or actuator [88], whereas usually they are designed to be efficient for one function only, the other being a disturbance usually minimized. Several types of transducers based on the magnetostrictive or piezoelectric phenomena have been investigated for their use as sensoriactuators [89, 90, 32]. Magnetic bearings have also been investigated to become self-sensing, thus eliminating a special sensor for the rotor position [91]. Also sensorless electric motors can be seen as electromagnetic sensoriactuators where the current is used to obtain information about the motor rotational speed [92]. Loudspeakers are a common example for linear, electrodynamic actuators where self-sensing usually is used to increase damping. In general additional potential advantages of self-sensing actuators for practical applications are the reduced number of transducers, amplifiers and cables, reduced size and reduced risk of failure.

There are passive, active, hybrid active-passive and semi-active ways to influence the structural vibration by sensoriactuators. In the passive case no additional power source is used so that for a real feedback gain the real part of the open loop FRF is positive at all frequencies. Active control uses an additional power source so that the real part of the open loop actuator – sensor FRF may also be negative. Hybrid active-passive control involves a system where passive treatments and active control are used in parallel, for instance to improve the stability margin of active control or improve performance of passive control. The real part of the passive open loop FRF always is positive at all frequencies whereas for the active open loop FRF it may also be negative. Semi-active control is defined by a number of authors [4, 26]. Semi-active actuators are described "as essentially passive elements in that they can only store or dissipate energy. Their use in active control stems from the fact that their passive mechanical properties can be adjusted by the application of a control signal and such systems are thus sometimes called 'adaptive'" [4, p.59].

"Relatively steady-state or slowly time-varying control inputs" are applied "which tend to change the system response by altering the system characteristics itself. As these types of inputs are not vibratory in nature and do not add energy to the dynamic system we call these systems 'semi-active' or 'adaptive'" [4, p.147]. Since active feedback systems can also change the system characteristics, the main difference between purely active and semi-active devices would then be the 'relatively steady-state or slowly time-varying' nature of the control action. By definition semi-active control is then restricted to control at lower frequencies. A second difference would be the fact that control devices do not add energy to the system. This is achieved by restricting the control action to "control forces [f] opposing the ... velocity [v] which are exclusively dissipative ($fv \leq 0$)" [26, p.267]. Semi-active devices are used in feedback loops with control circuits switching between two states. First higher frequency dynamics might be excited because of the periodic step excitation of the switching that has a wide-band frequency spectrum. Second the switching frequency limits the control range. Hence, feedback with switched devices "works well for narrow-band disturbances, but tends to be less effective when subjected to wide-band disturbances" [26 p.273]. In conclusion, semi-active feedback control is a subclass of active feedback control where low frequencies are targeted and the real part of the open loop FRF is positive in the control bandwidth emulating a passive system. Less energy is necessary than for active control because first the switching frequency determines a bandwidth limit and second the switching states could be implemented solely in a passive way.

Piezoelectric sensoriactuators

A first widely studied example of sensoriactuators are piezoelectric patches that are used to apply and sense stress and strain components on a structure [4]. Passive vibration control with piezoelectric actuators has been implemented by using a resistor shunted across the connections of the piezoelectric patch in which case the stiffness of the structure is changed [93]. An adaptive device can be obtained by electronically varying the resistance [94]. Additionally, an electrical inductance in series to the resistance can be used to optimally tune the resonance frequency of the shunted circuit to a resonance frequency of the structure so that the electrical current in the shunt and hence the dissipated electrical energy is increased [95]. When damping of multiple structural resonance frequencies is targeted a digital implementation of multiple resonant inductors is more convenient [96]. For optimum vibration reduction these devices require tuning to the targeted resonance frequency of the structure and hence are sensitive to changes in structural resonance

frequencies. Additionally the control at low structural resonance frequencies requires high inductance values and hence increases weight or effort [97].

Broadband vibration control can be achieved when purely active methods are used. A bridge circuit can then be applied to measure the structural strain and electronically generate the control action i.e. the control stress [32, 98]. Then by feeding back the strain rate damping is added to the mechanical structure. Because of the balancing problems and in order to reduce power requirements the bridge parameters can be adapted electronically [99-102]. Obviously the adjustment of the bridge can be avoided by using separate closely located sensor and actuator patches used as actuator and sensor. This arrangement normally does not guarantee perfect collocation [103]. An active solution for the balancing problem is to use robust design techniques that require knowledge about parameter changes to be incorporated in the controller design [104]. In such systems a trade-off between robustness and performance must be found [105]. Finally instead of using positive electrical parameters a negative capacitance can be used to cancel the internal capacitance of the piezoelectric patch [106-108] so that only the induced signal remains that can be fed back or dissipated over an additional resistance. Since piezoelectric actuators show hysteresis at large displacements and not an ideal capacitive behaviour this linear compensation has limits [109]. Once the inherent, piezoelectric capacitance has been compensated no electric parameters need to be tuned to a structural resonance so that broadband control is realised. Technically the negative capacitance circuits are not much different from a bridge circuit with high-gain feedback that is interpreted as a negative impedance amplifier [108]. For example digital impedance synthesis [96] or analogue electronics of the Riordan-type [108, 110] are used.

As a combination between active and passive devices active constraint layer damping can also use piezoelectric sensoriactuators in order to actively influence the properties of viscoelastic damping treatments usually attached between the patch and the structure [111-113]. Since broadband control is targeted and there is no restriction on the energy applied to the structure this is a purely active technique [114]. Hybrid control improves stability of the sensoriactuator active control loop by using passive treatments [115]. In this case it is important to properly design the passive and active component so that they complement each other to enable control of both high and low frequency modes of vibration.

Semi-active shunt-switching has been introduced that allows switching between at least two different shunted circuits [97]. State-switching implements switching between a small

shunted resistance, where significant electrical energy is dissipated and a very high, open circuit, shunted resistance, where nearly no electrical energy is dissipated. The circuit is closed when the displacement reaches a maximum and it is opened when the displacement is zero again at the static equilibrium position. State-switching is reported to suit well applications where the stiffness of the piezoelectric patch dominates the stiffness of the structure [97]. Pulse switching allows switching between a shunted resistance and inductance in series and a very high (open circuit) resistance [116]. The circuit is closed when the displacement is maximum and it is reopened when the applied charge reaches a peak that is out of phase with the velocity [97]. In the same reference it is stated that pulse switching has a lower sensitivity to environmental changes than the resonant shunt technique and it is easier to tune [97]. Since shunt-switching is a semi-active method it is limited to a certain frequency range.

Electrodynamic, self-sensing actuators

A second example of self-sensing actuators are linear, electrodynamic actuators that apply a point force on the structure and sense a linear velocity. It has been found that force actuators give relatively good results for ASAC at low frequencies when arrays of sensor-actuator pairs are used to implement direct velocity feedback control loops [25]. Additionally electrodynamic actuators are more suitable for the control of low frequency vibration as piezo actuators tend to excite high frequency structural modes more efficiently [20]. Self-sensing, electrodynamic force actuators are particularly advantageous when the induced voltage is proportional to the velocity of the mechanical system. Then feeding back their output should be similar to direct velocity feedback resulting in active damping. Thus, other sources of instability such as non-ideal time integrators for acceleration or time differentiators for displacement sensors are avoided. Electrodynamic self-sensing has been studied for active vibration damping at disk drives [117], high-speed lifts [69], for shunt damping [118], viscosity measurements [119] and extensively at electrodynamic loudspeakers. At this last application usually a signal proportional to the coil velocity has been used to add damping to the first rigid mode. Thus, mainly low frequency loudspeaker behaviour is influenced only.

A purely passive control circuit uses a shunted resistance in order to feedback a current proportional to the induced voltage in the coil. Since the induced voltage is proportional to the coil velocity and the applied force is proportional to the coil current, damping is added to the structure in a broad frequency range. When an appropriate capacitor is shunted to the

coil the electrical circuit resonates with the mechanical resonance so that the current in the shunt, and hence the energy dissipation, is increased in the electrical circuit in a narrow frequency band [118].

The induced voltage can also be determined using a Wheatstone bridge [120]. When induced voltage feedback is implemented without an additional amplifier that potentially inserts energy into the system passive vibration control results as in the shunted resistor case. With an additional feedback amplifier a negative resistance component can be implemented that cancels the internal coil resistance and actively adds damping in a broad frequency range [121]. When induced voltage feedback is used to influence the mechanical low frequency behaviour of a loudspeaker, the coil inductance is usually neglected [122-124]. Therefore the necessary balance of the Wheatstone bridge is simple in theory [122], but restricted to the low frequency region. The upper frequency loudspeaker behaviour can be controlled using inductors and capacitors in the bridge circuit usually targeting the pressure response directly rather than the intermediate coil velocity [125, 126]. Care has to be taken to also consider the output impedance of the amplifier that "comes in parallel with the bridge, thus spoiling the correction" [122] and making tuning more cumbersome.

The tuning problem can be avoided by feeding back the voltage induced in a secondary sensing coil mechanically linked to the primary driving coil as proposed by [127, 128] and in a number of loudspeaker patents [129-135]. If the sensing and the driving coil are collocated and oriented perpendicular to each other the mutual coil inductance between the coils is minimum and maximum sensing bandwidth is achieved, but vibrations can only be sensed in different directions. When the coils are placed side-by-side driving and sensing are closely located, but there is an increased mutual coupling inductance. Examples for double-coil applications are pickup actuators in optical disk drives [136], vibrating pressure transducers [137] and force-feedback joysticks [138]. In order to build a more compact system and potentially allow collocated sensing, the primary and secondary coil can be aligned. This configuration results in an important mutual coupling inductance between both coils that leads to a steady increase and phase shift in the open loop FRF at increasing frequencies [139]. A proposed cut-off filter may compensate for the rise, but it also limits the sensing bandwidth [140]. Therefore another aim of this thesis is to introduce a compensator that allows a relatively larger sensing bandwidth.

Another solution that benefits from the apparent amplifier resistance is proposed by [141, 142] where a negative output impedance amplifier is used [143-145]. This amplifier partly

cancels the internal loudspeaker impedance so that the induced voltage, proportional to velocity, can be used to generate the wanted control force. A negative output impedance amplifier has been considered as an additional bass compensating stage [146], as a bridge circuit [147, 121] with high feedback gains or as positive current proportional feedback [148]. At first, studies concentrated on reducing the effective loudspeaker resistance by direct positive current feedback [147-152] or using combined sensor self-sensing schemes [153-155]. Hence, the real part of the internal loudspeaker impedance was targeted only. When the self-inductance of the coil is not compensated large vibration amplification at higher frequencies results because of positive feedback [146]. Since at those frequencies the loudspeaker enclosure plays an important part [146], further developments that aimed at the compensation for the acoustical surrounding rather compensated only for the coil resistance than also for the coil inductance [156-158]. Nowadays in order to compensate for the reduction of the high-frequency response [159] or to minimize dissipation in the amplifier output stage [160], inductance compensators are commonly used in the power amplifier. This necessitates either a combined amplifier-loudspeaker design [161] or an amplifier-loudspeaker interface which may be added including a so-called Zobel compensation [162]. Recently a rather complicated estimator based on positive current and negative voltage feedback compensating for an ideal coil inductance has been presented for active vibration control [33]. It has been applied at loudspeakers using operational amplifiers and digital compensation [163]. Also in [164] an ideal inductive behaviour is assumed for the implementation of a current fluxion amplifier that is used to either synthesise an impedance or admittance shunted to the actuator depending on whether the voltage or the current is to be controlled. In conclusion, for loudspeakers the vibration response has usually not been investigated at higher frequencies since the sound pressure response has been targeted only [164]. For active vibration control applications the inductance has been compensated to allow control at relatively low frequencies and a small number of mechanical modes. In this thesis vibration control that targets mechanical modes at high frequencies is investigated. Therefore a further aim is to demonstrate the feasibility of a simple inductance compensator presented in [165] for vibration control of a large number of mechanical modes.

Passive treatments could be used in combination with self-sensing active control. A loudspeaker application may consist of a copper ring placed close to the air gap. In this ring eddy currents [166] are induced and electrical energy is dissipated into heat in order to reduce distortion and power consumption. In this thesis it is also shown that passive treatments may increase the stability margin of active control.

Recently low frequency semi-active shunt-switching as for piezoelectric actuators has also been applied to electrodynamic actuators [210]. Also, high-frequency pulse width modulation (PWM) amplifiers are commonly used to drive electrodynamic actuators in an energy efficient way.

1.4   Scope and objective

This PhD dissertation presents a theoretical and experimental study of active vibration control with an electrodynamic actuator. The test rig used to study the actuator consists of a clamped, thin aluminium panel of dimensions $l_x \times l_y = 0.414\text{m} \times 0.314\text{m}$ which is excited by a primary electrodynamic shaker. Two control actuation configurations have been considered. First a reactive configuration where the electrodynamic actuator reacts against a rigid base (RA) and second an inertial configuration where the electrodynamic actuator reacts against the mass of the magnet (IA) are used.

The three main objectives of this thesis are
1. to investigate self-sensing (SS) active vibration control of the low frequency modes of the panel;
2. to design, build and implement a prototype lightweight, electrodynamic, inertial actuator;
3. to assess stability and performance of external absolute velocity feedback and internal relative velocity feedback implemented with either self-sensing control, passive means (eddy currents) or an internal velocity sensor (IVS).

A numerical, fully coupled model of the panel and an electrodynamic reactive actuator (RA) and the electrical circuit used for self-sensing active vibration control has been formulated and compared to measurements. The self-sensing control schemes

- shunted resistor,
- positive current feedback,
- induced voltage feedback and
- induced voltage feedback with inductance compensation

are compared to direct velocity feedback using a separate sensor. Moreover, important considerations for the design of an inertial actuator regarding

- the stroke and inertial mass
- the electromagnetic circuit and
- the suspension

have been studied and aspects for miniaturisation highlighted. Eddy current damping and the self-sensing control schemes

- shunted resistance ,
- proportional current feedback,
- induced voltage feedback and
- induced voltage feedback with inductance compensation

are applied to an inertial actuator (IA). Also, an internal velocity sensor (IVS) with inductance compensation is proposed. The benefit of self-sensing vibration control for increased performance and stabilisation of inertial actuators used for direct velocity feedback is shown in comparison to

- an internal velocity feedback sensor
- a compensator for the fundamental actuator resonance and
- a high-pass filter.

Finally the active control effects are compared to the passive effects generated by a) a passive inertial actuator with high internal Eddy current damping and b) a passive damping treatment of a similar weight as the actuator.

The effectiveness of active vibration control of a plate with a lightweight, self-sensing, inertial actuator is demonstrated experimentally and theoretically for these control schemes in terms of the reduction of plate vibrations at the secondary actuator position relative to a primary force disturbance. Stability limits are also investigated.

1.5   Structure and organisation

The thesis is organised in three parts. In the first part, Chapter 2, self-sensing (SS) active vibration control with electrodynamic reactive actuators (RA) is investigated with reference to the model problem. A numerical model based on the exact solution of a clamped plate is developed. Experiments and simulations are presented for different self-

sensing control schemes. In particular it is investigated whether self-sensing active vibration control leads to improved collocation and duality and how the effectiveness of self-sensing active vibration control at higher modes can be improved.

Since the reactive actuator (RA) considered in the first part of the thesis is relatively bulky a more practical lightweight, inertial actuator has been developed and tested for the study of vibration control with inertial actuators. An inertial actuator (IA) also does not need to be connected to a fixed base. In the second part, Chapters 3 and 4, important design considerations are discussed and self-sensing control schemes are applied to the lightweight, inertial actuator. Chapter 3 highlights the constraints due to the mechanical system and the used geometry that lead to a functional relation between maximum actuator force and size respectively mass. The characterisation of the constructed prototype is also presented. As alternative to self-sensing, an internal velocity sensor is proposed and studied in simulations and experiments. Chapter 4 investigates the previously studied self-sensing control schemes for the inertial actuator with simulations and measurements. Also, it compares these control schemes with control using the internal velocity sensor.

The third part, Chapter 5, is focused on combined internal and external velocity feedback. Simulations and experimental results are presented which show the benefits of hybrid control when passive Eddy current damping is used to improve stability of active vibration control. The notion of a best combination of internal and external velocity feedback gains is introduced and validated in experiments and simulations.

1.6   Contributions

The main original contributions of this thesis are:

1. An investigation of limits of electrodynamic, self-sensing vibration control for higher frequencies and possible means to overcome these limits.
2. The description of the design and validation procedure of an innovative, lightweight, electrodynamic, inertial actuator.
3. The analysis of stability of active vibration control with inertial actuators and the role of internal and external velocity feedback.
4. The description and validation of a competitive system for broadband vibroacoustic control.

2. VIBRATION CONTROL OF A PLATE WITH A REACTIVE ACTUATOR

This chapter is focused on how a self-sensing actuator can be used for active damping. It is investigated how an electrodynamic actuator can be simultaneously used as an actuator and sensor in a direct velocity feedback loop. Special focus is on whether a self-sensing actuator helps to guarantee improved sensor-actuator collocation and duality and how it can be used to add damping to more than only the first few structural vibration modes.

In addition to the reference cases ideal direct velocity feedback and direct velocity feedback with an accelerometer sensor, self-sensing vibration control using a conventional electrodynamic shaker actuator as in [165] is investigated. The following four circuits have been added to the actuator:

a) a shunted resistor,

b) a positive current feedback loop,

c) a Wheatstone bridge for induced voltage feedback and

d) an Owens bridge for induced voltage feedback with inductance compensation.

Whenever possible both simulation and experimental results are shown for the model problem where the electrodynamic control actuator is connected to a clamped plate and reacts against a fixed base as a reactive actuator (RA). As schematically shown in Figure 2.1 a primary force is generated on the panel by a shaker in such a way as to excite most of the low frequency resonant modes of the panel. A force transducer measures the primary force whereas a monitor velocity sensor measures the plate velocity at the control position to be reduced.

Section 2.1 considers an ideal secondary out of plane force actuator and an ideal out of plane velocity sensor. The change in the kinetic energy of the whole plate is shown for different direct velocity feedback gains and the integrated kinetic energy of the plate between 10Hz and 1kHz is also shown. As a reference case in Section 2.2 direct velocity feedback with an electrodynamic, reactive actuator (RA) and an accelerometer
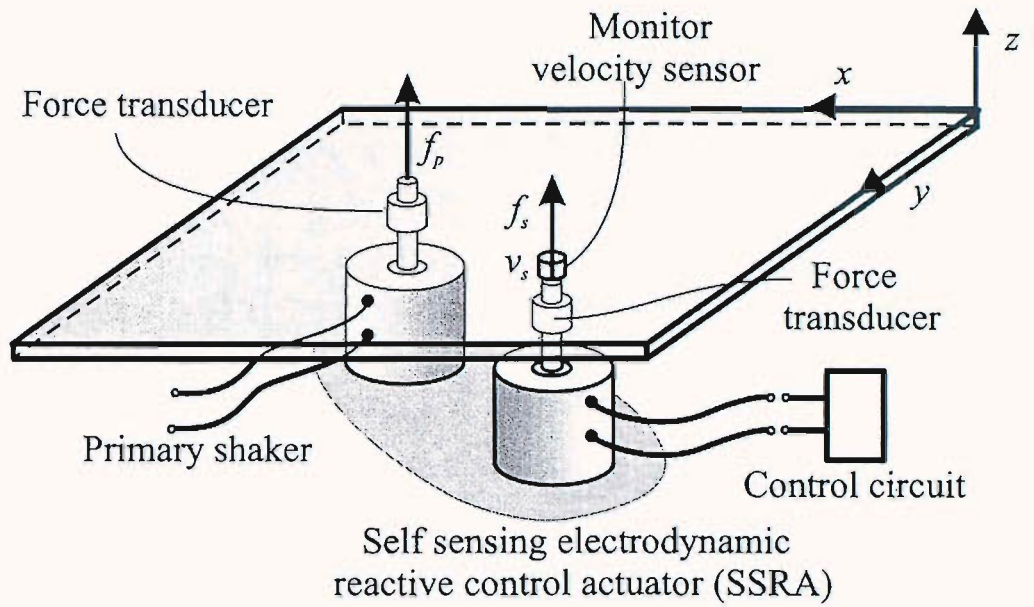
Figure 2.1: *Sketch of the model problem where a test panel is connected to a self sensing electrodynamic actuator which is set to control the vibrations generated by a primary force disturbance.*

is investigated. Both current command and voltage command of the actuator are considered in simulations and measurements. Sections 2.3 to 2.6 contrast simulated and experimental results with a shunted resistor, positive current feedback and induced voltage feedback with and without inductance compensation. In each section the model is first presented and the FRFs for the general control framework shown in Figure 1.1 are given. Then the stability of the feedback control schemes is investigated with reference to the open loop sensor–actuator response function. Finally the active damping performance is evaluated considering the reduction of the vibration of the panel at the control position with reference to the primary disturbance excitation. Whenever simulations and measurements are different, measured results are compared. As also described in Appendix F for Nyquist plot measurements amplification due to measurement and feedback amplifiers are included in the open loop FRF i.e. sensors are not calibrated. For measurements of the closed loop FRF, however, additional amplification due to the measurement amplifiers is removed from the measured signal i.e. the sensor signal is calibrated.

2.1   Direct velocity feedback

This section presents the model and simulation results regarding stability and performance in the ideal case when there are neither actuator nor sensor nor feedback amplifier dynamics, but ideal primary and secondary out of plane forces are applied on the panel, the out of plane plate velocity is ideally measured and direct velocity feedback is realised by a

real gain. Under these conditions direct velocity feedback with a number of decentralised, collocated out-of-plane force actuator velocity sensor pairs gives more vibration reduction than in the case with strain actuator out of plane velocity sensor pairs [25].

2.1.1 Model

For a single out of plane force actuator velocity sensor pair the model problem shown in Figure 2.1 is much reduced to a plate to which two ideal forces are applied. A cross-section view of the plate is schematically shown in Figure 2.2.
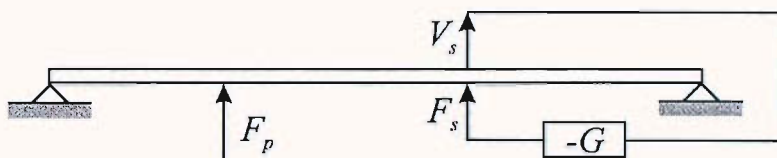
Figure 2.2: *Schematic plate model with disturbance force F_p, secondary force F_s and secondary velocity V_s sensor.*

The plate is assumed to be clamped along the four edges and to be made of aluminium with dimensions $l_x \times l_y = 0.414 \text{ m} \times 0.314 \text{ m}$ and thickness $h = 0.001 \text{ m}$. The material and geometrical properties of the panel test rig and self-sensing actuator valid for the whole Chapter 2 are summarised in Table 2.1.

Table 2.1: *Parameter values used for simulations in Chapter 2.*

Parameter	Value	Description
l_x	0.414m	Plate length
l_y	0.314m	Plate width
h	0.001m	Plate thickness
x_p	0.345m	X coordinate of primary force position
y_p	0.254m	Y coordinate of primary force position
x_s	0.225m	X coordinate of secondary force position
y_s	0.12m	Y coordinate of secondary force position
ρ	2700kg/m^3	Mass density of plate
K_1	1.2037	Coefficient to adjust for boundary conditions
H	0.04	Damping coefficient
E	71 10^{9}N/m^2	Young's modulus of plate
K_2	0.7042	Coefficient to adjust for boundary conditions
v	0.33	Poisson's ratio
M_p	0.03kg	Added mass of primary shaker
M	0.0177kg	Added mass of secondary shaker
Ψ	3N/A	Transducer coefficient (*Bl* product) of secondary shaker
K	989N/m	Suspension stiffness of secondary shaker
D	1Ns/m	Suspension damping of secondary shaker
R_e	3.05Ω	Electrical resistance of shaker
L_e	0.0002H	Electrical inductance of shaker
R_l	0.5/1/3.0347 Ω	Shunted / measurement / Owens bridge resistor
R_1	4 Ω	Upper resistance in Wheatstone bridge
R_2	1 Ω	Lower resistance in Wheatstone bridge
R_3	6293.8 Ω	Lower resistance of Owens bridge
C	10 nF	Capacitance of Owens bridge

The steady state flexural response of the panel has been derived assuming the primary force disturbance to be harmonic, with time dependence of the form $\mathrm{Re}\{\exp(j\omega t)\}$ where ω is the circular frequency and $j = \sqrt{-1}$. The mechanical and electrical functions in the model have therefore been taken to be the real part of anticlockwise rotating complex vectors, i.e. phasors, given in the form $X(\omega)e^{j\omega t}$ where $X(\omega)$ is the phasor at $t = 0$.

The phasor of the complex velocity at the error sensor, $V_s(\omega)$, can be expressed in terms of the phasors of the primary, $F_p(\omega)$, and secondary, $F_s(\omega)$, force excitations with the following mobility relation

$$V_s = Y_{sp}F_p + Y_{ss}F_s \tag{2.1}$$

where the two mobility functions, $Y_{sp}(\omega)$ and $Y_{ss}(\omega)$, have been derived with the following modal expansions

$$Y_{sp} = j\omega \sum_{n=1}^{N} \frac{\phi_n(x_s,y_s)\phi_n(x_p,y_p)}{\rho l_x l_y h \left[\omega_n^2(1+j\eta) - \omega^2\right]} = \phi_s^T A \phi_p$$

$$Y_{ss} = j\omega \sum_{n=1}^{N} \frac{\phi_n(x_s,y_s)\phi_n(x_s,y_s)}{\rho l_x l_y h \left[\omega_n^2(1+j\eta) - \omega^2\right]} = \phi_s^T A \phi_s \tag{2.2a,b}$$

where

$$\phi_p^T = \left\{\phi_1\left(x_p,y_p\right) \quad \cdots \quad \phi_n\left(x_p,y_p\right) \quad \cdots \quad \phi_N\left(x_p,y_p\right)\right\},$$

$$\phi_s^T = \left\{\phi_1\left(x_s,y_s\right) \quad \cdots \quad \phi_n\left(x_s,y_s\right) \quad \cdots \quad \phi_N\left(x_s,y_s\right)\right\},$$

$$\mathbf{A} = \begin{bmatrix} a_1 & 0 & \cdots & 0 & 0 \\ 0 & \ddots & & & 0 \\ \vdots & & a_n & & \vdots \\ 0 & & & \ddots & 0 \\ 0 & 0 & \cdots & 0 & a_N \end{bmatrix} \quad \text{and } a_n = \frac{j\omega}{\rho l_x l_y h \left[\omega_n^2(1+j\eta) - \omega^2\right]}.$$

In the two equations above (x_p, y_p) and (x_s, y_s) are the coordinates of the primary and control positions, ρ is the density of the material, η is the loss factor. Finally ω_n and $\phi_n(x,y)$ are respectively the n-th natural frequency and natural mode which have been taken from reference [167] for a clamped panel. ω_n is adjusted by a factor $\sqrt{K_1/K_2}$ to

23

improve the agreement with measurements since neither ideally clamped nor simply supported boundary conditions could be implemented on the set-up. Modes having natural frequencies up to 2000Hz are considered and the effect of residual modes [26] is taken into account by adjusting the measured FRF with a constant factor to fit simulations.

When ideal feedback components are assumed and actuator and sensor dynamics are neglected direct velocity feedback is implemented by a secondary feedback force

$$F_s = -GV_s. \tag{2.3}$$

Closed loop stability is verified by investigating the locus of the open loop FRF

$$V_s/F_s = Y_{ss} \tag{2.4}$$

in the real imaginary plane. In order to guarantee closed loop stability the locus of the open loop FRF should not encircle the critical point (-1, $0j$) [168]. Vibrations are amplified in the closed loop case for those frequencies where the open loop locus lies within a circle of radius 1 about the critical point. This effect is called spillover. If the locus lies completely in the real half-plane unconditional stability and no spillover effects result since there is no real positive feedback gain G for which the open loop encircles the critical point [4].

Then the closed loop plate velocity at the sensor per unit primary disturbance force is given by

$$V_s/F_p = (1+GY_{ss})^{-1}Y_{sp}F_p. \tag{2.5}$$

Using a similar result from [25] the kinetic energy of the plate at each frequency is

$$E_{kin}(\omega) = (\mathbf{A}\boldsymbol{\phi}_p - \mathbf{A}\boldsymbol{\phi}_s G (1+\boldsymbol{\phi}^\mathbf{T}_s \mathbf{A}G\boldsymbol{\phi}_s)^{-1}\boldsymbol{\phi}^\mathbf{T}_s \mathbf{A}\boldsymbol{\phi}_p)^\mathbf{H}(\mathbf{A}\boldsymbol{\phi}_p - \mathbf{A}\boldsymbol{\phi}_s G (1+\boldsymbol{\phi}^\mathbf{T}_s \mathbf{A}G\boldsymbol{\phi}_s)^{-1}\boldsymbol{\phi}^\mathbf{T}_s \mathbf{A}\boldsymbol{\phi}_p)(\rho l_x l_y h)/2 \tag{2.6}$$

that can be summed up over the required frequency range. For this control scheme the FRFs of the general control scheme in Figure 1.2 are given by $G_{oi} = G_{si} = Y_{ss}$ and $G_{sp} = G_{op} = Y_{sp}$ when the control output $Y_o = V_s$ and control input $Y_i = F_s$.

2.1.2 Stability

Figure 2.3 shows the simulated open loop FRF between the secondary control force and the measured plate velocity following Eq. (2.4). This FRF cannot be measured since it would be distorted by the dynamics of measurement devices. It lies in the positive real half-plane indicating unconditional stability of the closed loop. When reaching the resonance frequencies of the plate the locus has intersected with the real axis an odd number of times. At anti-resonances it has intersected an even number of times. Additionally at the resonance frequencies the locus lies far away from the critical point so that more vibration reduction is predicted than at the anti-resonances that lie closer to the critical point. Also, vibration reduction is different for each mode so that the relative importance of resonance peaks is predicted to change in the closed loop case.
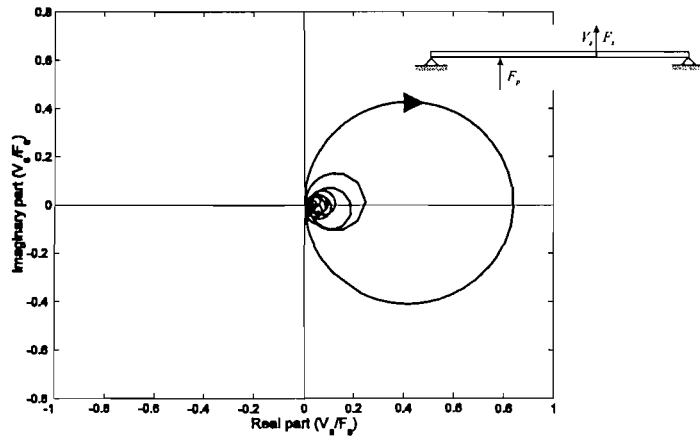
Figure 2.3: *Simulated Nyquist plot of the FRF between the secondary force F_s and the plate velocity V_s at the secondary force position.*

2.1.3 Performance

Figure 2.4 shows the simulated FRF between the primary disturbance force and the plate velocity at the secondary force position in the open loop case (thick solid line) and for direct velocity feedback gains of 10 (thin dashed line), 30 (dotted line) and 100 (thick dash-dotted line). In this case measurements also are not possible for the same reasons as mentioned before. Large vibration reduction is visible in the whole frequency range and vibration reduction increases for increasing feedback gains. Additionally in the closed loop case the relative importance of the resonance peaks changes. In the model given by Eq. (2.2a,b) the relative importance or weighting of the resonances is given by the vector of modal contributions Φ_s that is determined by the mode shapes. Hence, Figure 2.4 indicates that the observable modal contributions and mode shapes are changed by velocity feedback which adds an additional constraint on the plate. Since the modal contributions also

25

influence the kinetic energy as illustrated by Eq. (2.6) the kinetic energy of the plate should also be changed by direct velocity feedback. From Figure 2.4 it is not clear whether the kinetic energy will be reduced or increased since the relative vibration amplitude of some modes relative to other modes is decreased or increased although the absolute vibration amplitude at the control actuator point is decreased.
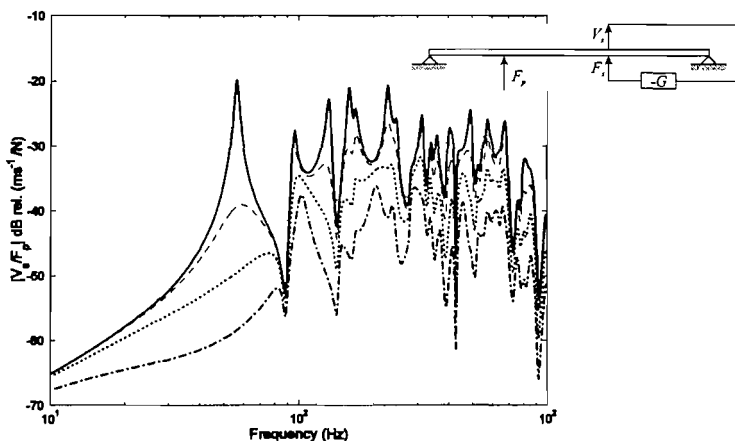
Figure 2.4: *Amplitude of the simulated FRF between the primary disturbance force and the plate velocity at the secondary force position in the open loop case (thick solid line), for a feedback gain of* 10 *(thin dashed line),* 35 *(dotted line) and* 100 *(thick dash-dotted line).*

Figure 2.5 shows the kinetic energy of the plate in the open loop case (thick solid line) and for direct velocity feedback gains 10 (thin dashed line), 35 (dotted line) and 100 (thick dash-dotted line). For a feedback gain of 10 and 35 the kinetic energy of the plate is reduced at resonance and there is a slight increase at anti-resonance. For a gain of 100 there clearly are new resonance peaks whereas some open loop peaks do no longer appear. Hence, there seems to be an optimum feedback gain for which the sum of the kinetic energy over this frequency range is minimum. The reduction in kinetic energy is small using one actuator and it is more important at low frequencies.
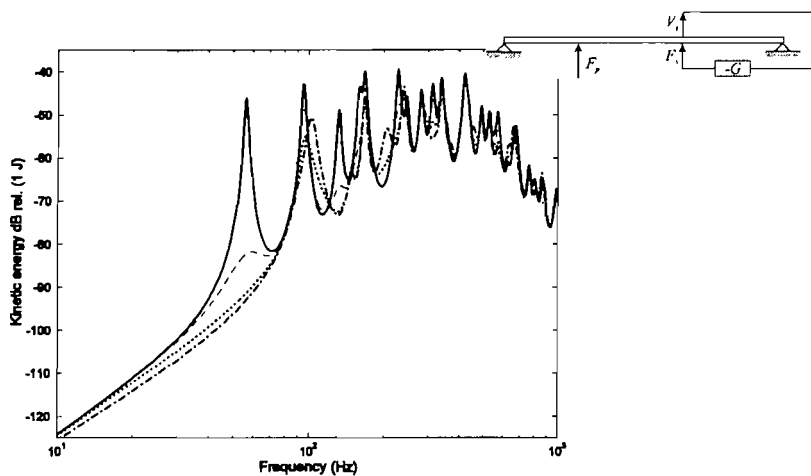
Figure 2.5: *Kinetic energy of the panel excited by a primary force in the open loop case (thick solid line), for a feedback gain of* 10 *(thin dashed line),* 35 *(dotted line) and* 100 *(thick dash-dotted line).*

Figure 2.6 shows the integral of the kinetic energy between 10Hz and 1kHz for different direct velocity feedback gains. There is a minimum at a feedback gain of about 35. At this minimum the vibration energy is not reduced at every frequency since Figure 2.5 clearly shows that there is reduction at resonances and amplification at anti-resonances. Also, the position of the minimum depends on which frequency range is used for the integration.
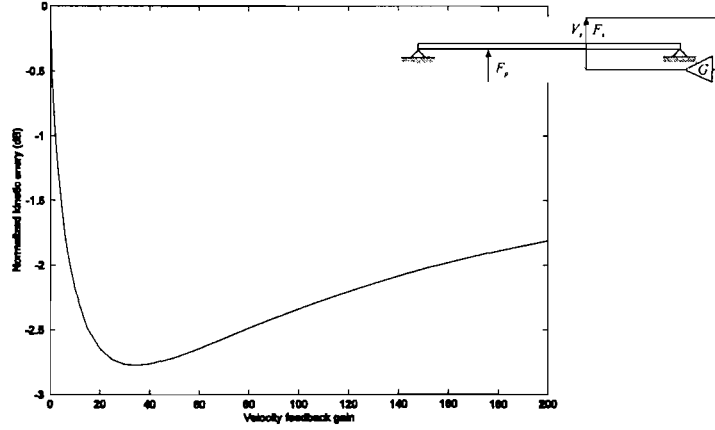
Figure 2.6: *Normalized kinetic energy level of the panel, integrated from 10Hz to 1kHz, plotted against the gain of the direct velocity feedback controller.*

2.2   Direct velocity feedback with accelerometer sensor

In the previous section it has been illustrated that changes in mode shapes are already visible in the FRF between the primary disturbance force and the plate velocity at the secondary force position. In the remaining part of the thesis only this FRF to a single point on the plate is considered from which the kinetic energy is not, in general, precisely known. Also, in a real system collocation and duality properties of an actuator sensor pair should allow at least those feedback gains for which changes in observable mode shapes are clearly visible in the FRF or even those gains for which minimum kinetic energy of the plate can be achieved in the targeted frequency range between about 20Hz and about 1kHz.

The practical implementation of the direct velocity feedback system considered in this section is shown in Figure 2.7. The primary force generated by a primary shaker is measured with an Endevco 2313 force transducer that adds a mass M_p to the plate at position (x_p, y_p) so that the transfer mobility Y_{sp} is modified to be $Y'_{sp} = \dfrac{Y_{sp}}{1 + j\omega M_p Y_{pp}}$.

The secondary force at position (x_s, y_s) is generated by an electrodynamic reactive actuator (RA) that also reacts against a fixed base. Due to the mass of an intermediate B&K 8230 force transducer and the moving coil the point mobility of the plate at the

27

control position (x_s, y_s) is modified to be $Y'_{ss} = \dfrac{Y_{ss}}{1 + j\omega M Y_{ss}}$. In some cases the force

transducer at the control actuator position is not used in order to reduce distortion due to its mass effect. On the opposite side of the control actuator a B&K 4375 accelerometer is added. Integration of its output signal with a B&K 2635 charge amplifier gives a signal proportional to the plate velocity.
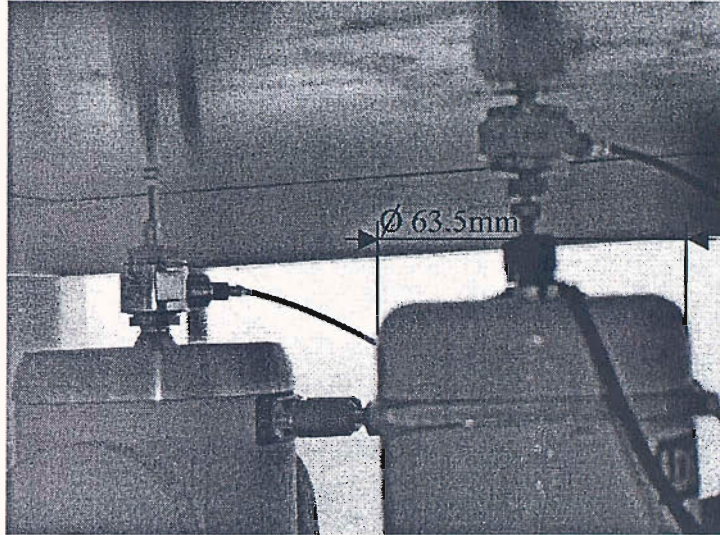
Figure 2.7: *Photography of the experimental set-up with the primary shaker on the left hand side in the background and the secondary control actuator in the foreground.*

In the following subsection direct velocity feedback with the described set-up and a current command amplifier is investigated, whereas Subsection 2.2.2 focuses on direct velocity feedback with a voltage command amplifier.

2.2.1 current command

Considering the lumped parameter model of the control actuator shown in Figure 2.8, the secondary force exerted on the plate is given by

$$F_s = -ZV_s + \psi I \tag{2.7}$$

where $Z = \dfrac{K}{j\omega} + D$ is the impedance of the coil suspension system here modelled as a stiffness K and viscous damper D in parallel; ψ is the electrodynamic transducer coefficient (*Bl* product) of the actuation mechanism in the RA and I is the driving current of the RA.

28
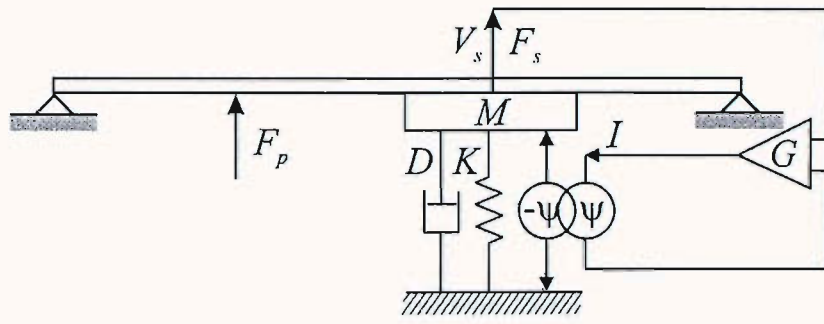
Figure 2.8: *Model of the electrodynamic current driven actuator connected to the plate and reacting against a fixed base.*

Taking into account the mass, damping and stiffness of the control actuator, the modified transfer and point mobility of the plate based on Eqs. (2.1) and (2.7) become $Y''_{ss} = \dfrac{Y'_{ss}}{1 + Y_{ss}Z}$

and $Y''_{sp} = \dfrac{Y'_{sp}}{1 + Y_{ss}Z}$. The secondary force depends on the actuation force that is proportional to the current in the shaker coil which is driven by a current command amplifier. Direct velocity feedback with a current command amplifier leads to

$$I = -GV_s . \tag{2.8}$$

The open loop FRF to be investigated for the stability of this feedback scheme is

$$\frac{V_s}{I} = Y''_{ss}\psi \tag{2.9}$$

when amplifier dynamics are neglected. The closed loop FRF to check performance then becomes

$$\frac{V_s}{F_p} = \left(1 + GY''_{ss}\psi\right)^{-1} Y''_{sp} . \tag{2.10}$$

When considering $Y_o = V_s$ and $Y_i = I$ for the general control scheme the FRFs $G_{op} = G_{sp} = Y''_{sp}$ and $G_{si} = G_{oi} = Y''_{ss}\psi$ result.

Stability

Figure 2.9 shows the simulated (left) and measured (right) Nyquist plot of the FRF between the input voltage to the current command amplifier and the time integrated accelerometer output signal. Simulations with Eq. (2.9) and measurements show a number of loops in the positive real half-plane due to the resonances of the plate. Measurements

29

additionally show relatively smaller loops in the negative real half-plane because of internal actuator resonances beyond about 10kHz so that unconditional stability is not guaranteed. Because of these loops spillover into internal actuator resonances is predicted in the closed loop case in addition to large vibration reduction at other structural resonances.
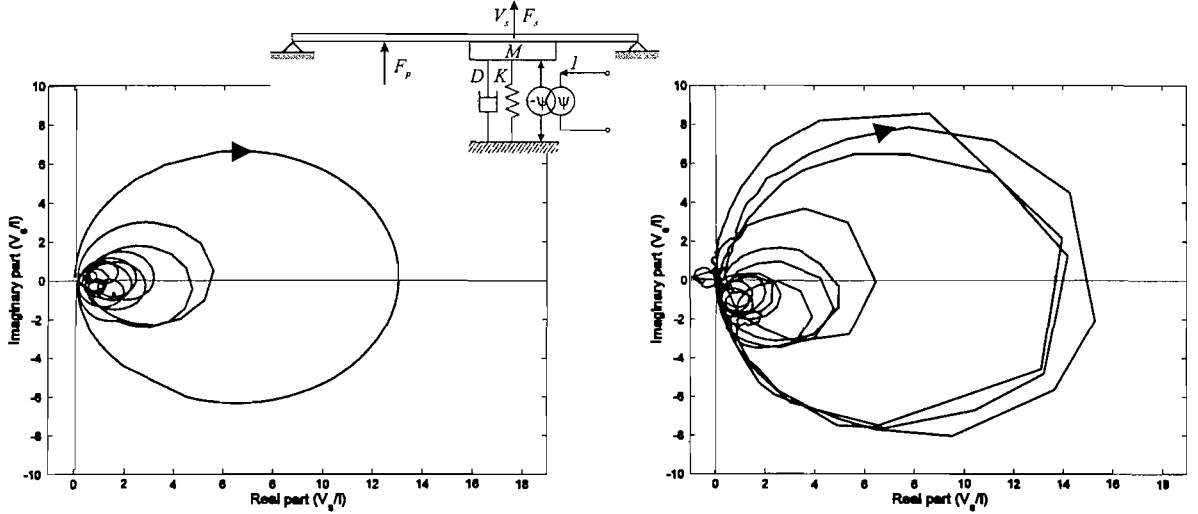
Figure 2.9: *Simulated (left) and measured (right) Nyquist plot of the FRF between the driving current I and the time-integrated accelerometer output signal V_s.*

Performance

Figure 2.10 shows the simulated (left) and measured (right) FRF between the primary disturbance force and the plate velocity at the secondary actuator position in the open loop case (thick solid line) and for velocity feedback with the same feedback gain as in Figure 2.9 (thin solid line). Contrasting the open loop response function in Figures 2.4 and 2.10 the passive mass effect of the primary and secondary force transducers are clearly visible in simulations and measurements by a shift of resonance frequencies of the panel to lower values. Furthermore the amplitude of the panel response decreases at higher frequencies. The stiffening effect generated by the suspension system in the control shaker is also visible in simulations and measurements by an upwards shift of the first resonance frequency of the panel. Large vibration reductions similar to those simulated in Section 2.1 for the ideal control case are visible indicating that this active feedback scheme could be used in practice to implement optimum direct velocity feedback. Similar to Figure 2.4 the relative importance of the resonance peaks at the sensor position also changes.

30
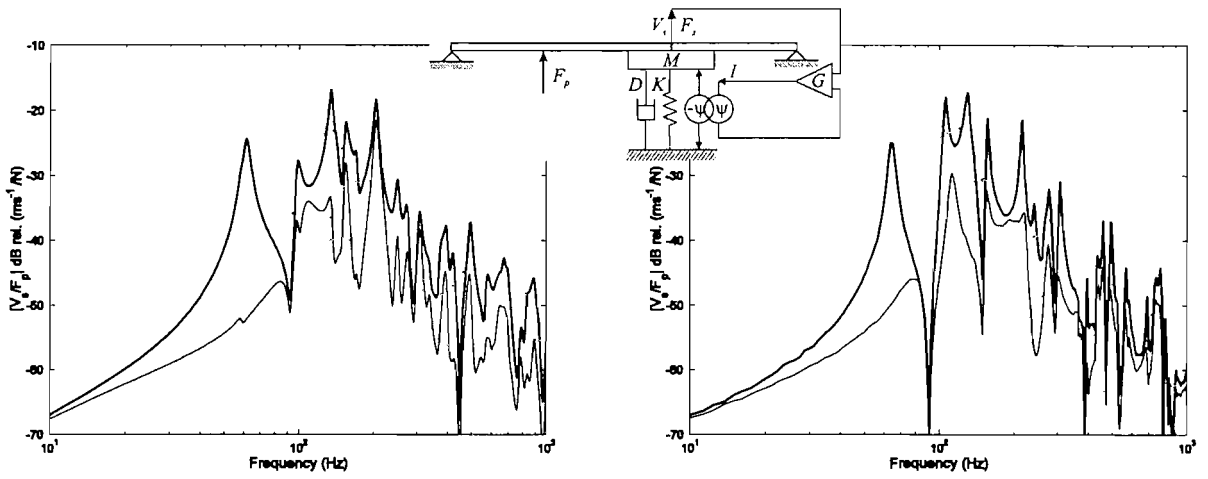
Figure 2.10: *Simulated (left) and measured (right) amplitude of the FRF between the primary disturbance force F_p and the plate velocity V_s at the control actuator position in the open loop case (thick solid line) and for plate velocity feedback (thin solid line).*

2.2.2 voltage command

A current command amplifier demands the design of an extra current control loop internal to the amplifier. Such a control loop could become unstable if a different combination of actuator and amplifier was used [160]. An appropriate current command amplifier is not always available. Therefore direct velocity feedback with a voltage command amplifier is studied. As represented by the electrical circuit in Figure 2.11, in contrast to a current command amplifier, for a voltage command amplifier the current in the actuator coil is given by

$$I = \frac{1}{Z_e}\left(U_{AB} - U_{ind}\right) \tag{2.11}$$

where $Z_e = R_e + j\omega L_e$ is the electrical impedance of the control actuator and R_e, L_e are the resistance and self-inductance of the coil. U_{AB} is the driving voltage applied to the RA and U_{ind} is the induced voltage in the driving circuit generated by the back electro motive force (back-emf).
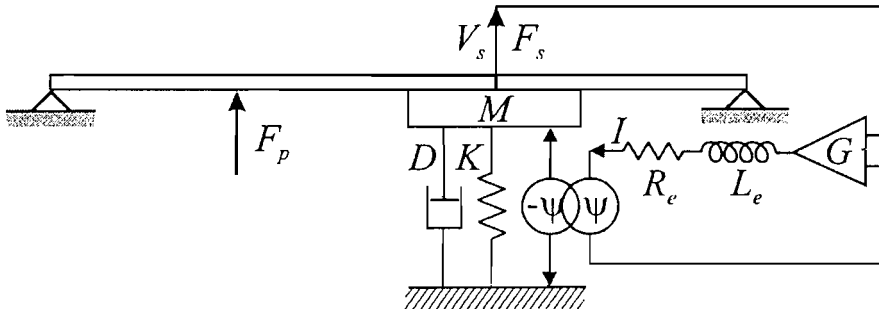
Figure 2.11: *Model of the electrodynamic voltage driven actuator connected to the plate and reacting against a fixed base.*

31

The back-emf, or induced voltage, is due to the vibration of the coil that is excited by the plate vibrations at the control point [33]:

$$U_{ind} = \psi V_s.$$ (2.12)

The open loop FRF investigated for stability is then

$$V_s/U_{AB} = (1 + Y''_{ss}\psi^2/Z_e)^{-1} Y''_{ss}\psi/Z_e$$ (2.13)

and if direct velocity feedback is implemented by

$$U_{AB} = -GV_s$$ (2.14)

the FRF to assess vibration is given by

$$V_s/F_p = (1 + Y''_{ss}(\psi^2/Z_e + G\psi/Z_e))^{-1} Y''_{sp}.$$ (2.15)

In the general control scheme the measured output and the control input are given by $Y_o = V_s$ and $Y_i = U_{AB}$ with the FRFs $G_{op} = G_{sp} = (1 + Y''_{ss}\psi^2/Z_e)^{-1} Y''_{ss}$ and $G_{si} = G_{oi} = (1 + Y''_{ss}\psi^2/Z_e)^{-1} Y''_{ss}\psi/Z_e$.

Stability

Figure 2.12 shows the simulated (left) and measured (right) open loop FRF. A large number of loops due to the resonance frequencies of the plate lie in the positive real half plane. For increasing frequencies some loops also extend into the negative real half plane because of the additional phase shift due to the inductance. Spill-over is not expected because of the inductance effect since the locus is more than a distance of 1 away from the critical point. Measurements show at least one additional loop in the negative real half-plane due to internal resonances of the actuator that have also been observed in Figure 2.9. The amplitude of the open loop FRF at these resonances is reduced and the phase is shifted relative to the current command case because of the inductance-like effect. A different maximum stabilizing gain and spill-over at higher frequencies is hence expected.
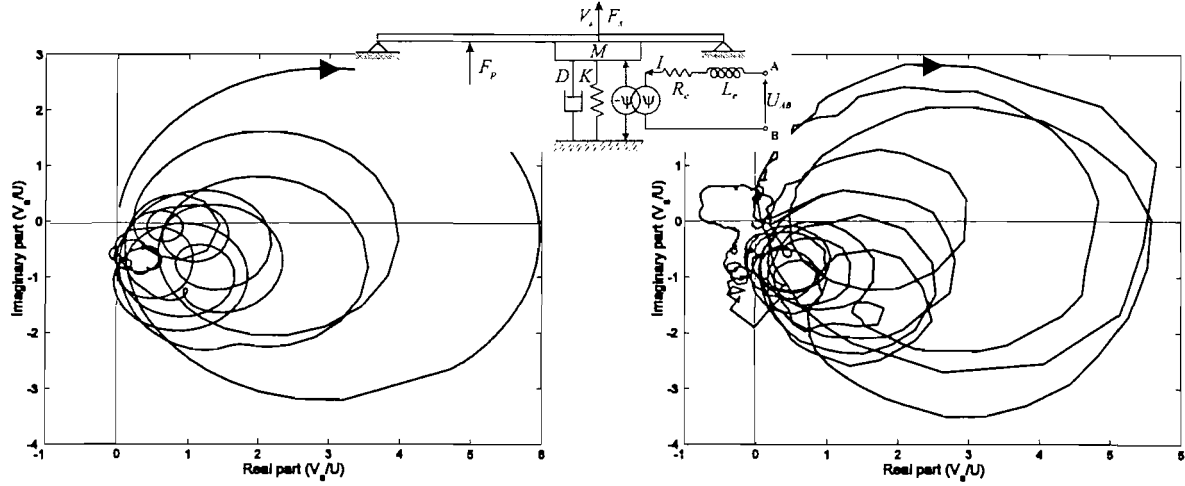
Figure 2.12: *Simulated (left) and measured (right) Nyquist plot of the FRF between the amplifier input voltage U and the time-integrated accelerometer output signal V_s.*

Performance

Figure 2.13 shows the simulated (left) and measured (right) FRF between the primary disturbance force and the plate velocity at the control actuator position in the open loop current command case (thick dashed line), in the voltage command case (thick solid line) and for direct velocity feedback with a gain used to plot Figure 2.12 (thin solid line). Because of the low-pass filter effect of the inductance that cuts off internal actuator resonance frequencies higher gains are realized in the voltage command closed loop case than in the current command closed loop case. Thus, higher vibration reductions are achieved in the first case. Despite the inductance effect no spill-over is visible in the chosen frequency range. Similar to Figure 2.4 the relative importance of the resonance peaks is also changed.
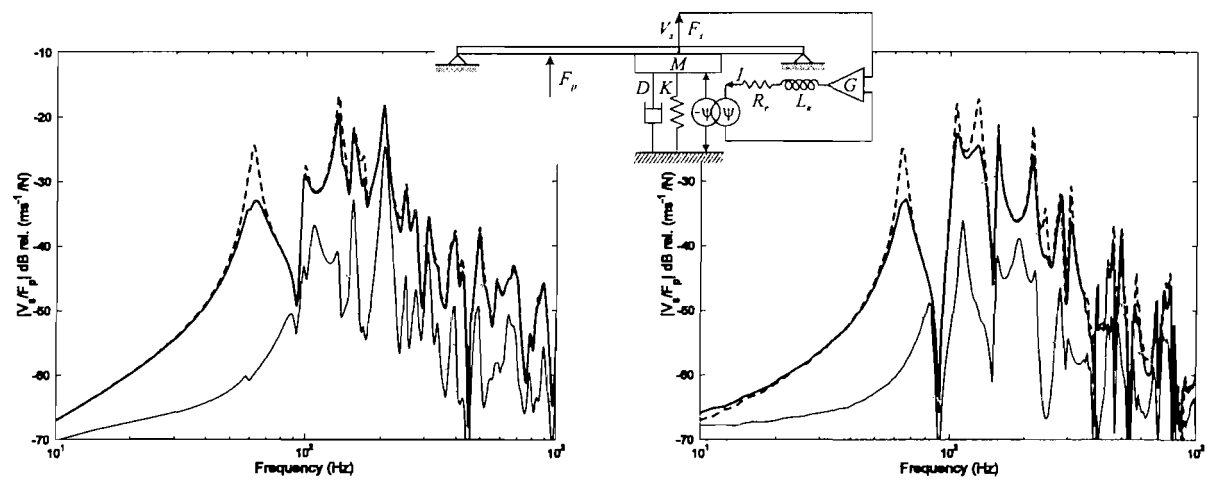
Figure 2.13: *Simulated (left) and measured (right) amplitude of the FRF between the primary disturbance force F_p and the plate velocity V_s at the control actuator position in the open loop case with current drive (thick dashed line), in the open loop case with voltage drive (thick solid line), and plate velocity feedback (thin solid line).*

33

The reactive voltage driven actuator in combination with a collocated accelerometer sensor hence could be used to implement optimum direct velocity feedback at lower frequencies for a thin plate.

Sometimes a velocity sensor is not available or a sensor cannot be placed collocated to the actuator. Therefore the following sections investigate control schemes with a self-sensing actuator.

2.3   Shunted resistor

A resistor R_l shunted to the connections of the self–sensing electrodynamic actuator in a configuration as shown in Figure 2.14 closes the electric circuit and allows a current flow I in the actuator.
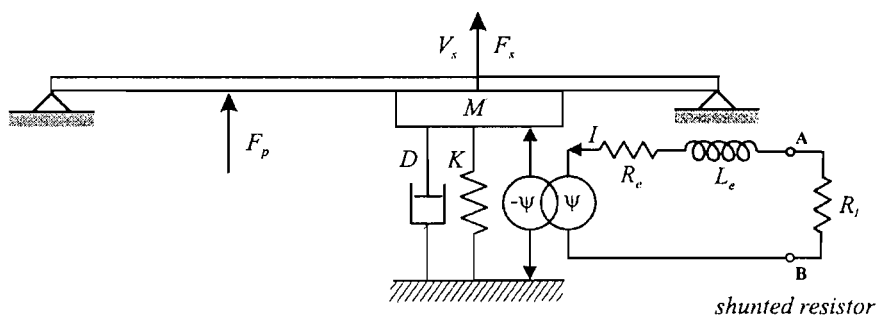
Figure 2.14: *Model of the electrodynamic reactive actuator connected to the plate and shunted with a resistor.*

The resistor implements negative current feedback to the actuator voltage

$$U_{AB} = - R_l I .$$ (2.16)

Stability of this passive scheme is assessed by the open loop FRF

$$\frac{I}{U_{AB}} = \frac{(1/Z_e)}{1 + \psi^2 / Z_e Y_{ss}''} .$$ (2.17)

The feedback gain $G = -R_l$ is changed by varying the value of the shunted resistor R_l. In the open circuit case the resistance tends to infinity whereas in the closed circuit case the resistance tends to zero. The closed loop FRF of the plate is

34

$$\frac{V_s}{F_p} = \frac{Y''_{sp}}{1 + \psi^2 / (R_l + Z_e) Y''_{ss}} \cdot \qquad (2.18)$$

The control input Y_i and output Y_o signals in the scheme of Figure 1.2 are given respectively by the voltage U_{AB} and the current I in the driving circuit of the RA. As a result the four transfer functions in the control framework in Figure 1.2 are given by the following relations: $G_{sp} = \dfrac{Y''_{sp}}{1 + \psi^2 / Z_e Y''_{ss}}$, $G_{si} = \dfrac{Y''_{ss}(\psi / Z_e)}{1 + \psi^2 / Z_e Y''_{ss}}$, $G_{op} = \dfrac{-Y''_{sp}(\psi / Z_e)}{1 + \psi^2 / Z_e Y''_{ss}}$ and

$$G_{oi} = \frac{(1/Z_e)}{1 + \psi^2 / Z_e Y''_{ss}} \cdot$$

Stability

Figure 2.15 shows the simulated (left plot) and measured (right plot) Nyquist plot of the open loop FRF between the input voltage U_{AB} and the coil current I. The current is measured using a measurement resistor in series to the RA. Measurements and simulations agree well up to about 1kHz, but they diverge for higher frequencies because of the non-ideal inductive behaviour. With this type of control scheme the locus lies in the right hand side so that unconditional stability is predicted as expected for a purely passive system. For low frequencies the locus starts at $1/R_e$ and it tends to the origin for high frequencies since an ideal inductance has been assumed. The loops at lower frequencies due to the induced voltage lie rather far away from the critical point so that the feedback current will be small and only a small amount of added damping is expected when the control loop with the shunted resistor is closed.
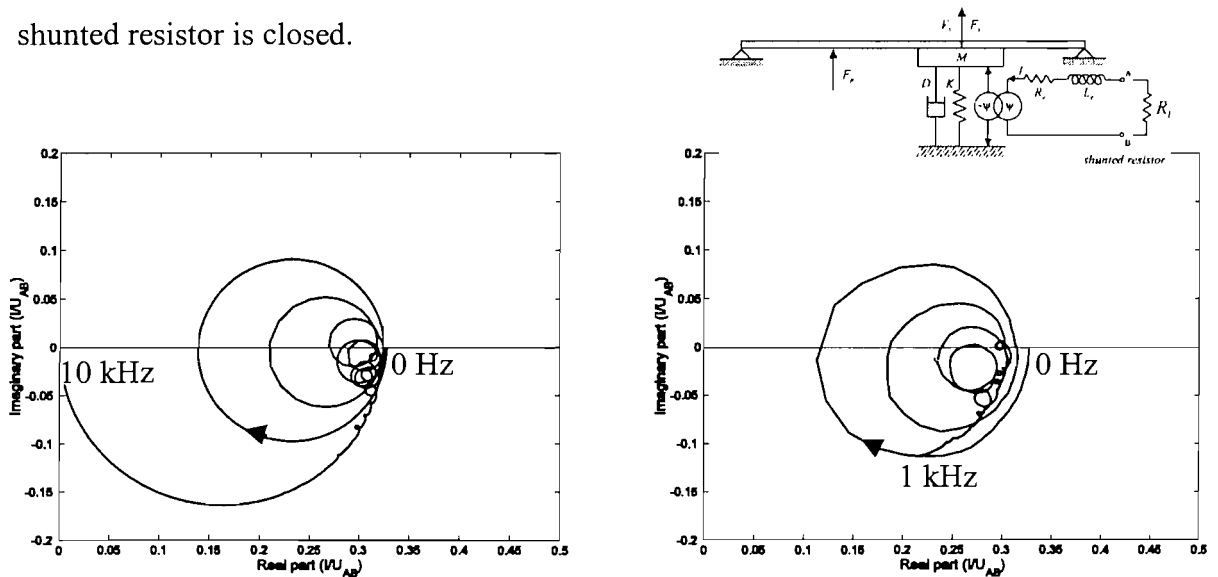
Figure 2.15: *Simulated (left plot) and measured (right plot) Nyquist plot of the open loop FRF between the voltage input U_{AB} to the control actuator and the coil current I.*

35

The two plots in Figure 2.16 show the simulated (left plot) and measured (right plot) vibration of the panel at the control position with reference to the primary disturbance excitation. The thick and thin solid lines give the vibration of the panel at the control position when the driving circuit of the control shaker is either left open or is closed with a small resistor R_l. Measurements below about 20Hz are not reliable due to small coherence values. Both plots show that only small damping can be added mainly at the first resonance frequency of the plate. Damping increases for decreasing value of the resistor since the current leading to an opposing secondary force is reduced less, i.e. the starting point of the locus of the Nyquist plot in Figure 2.15 moves towards the origin. Maximum passive damping is achieved when the connections of the shaker are closed without an intermediate shunting resistor effectively applying only the resistance of the connecting wire.
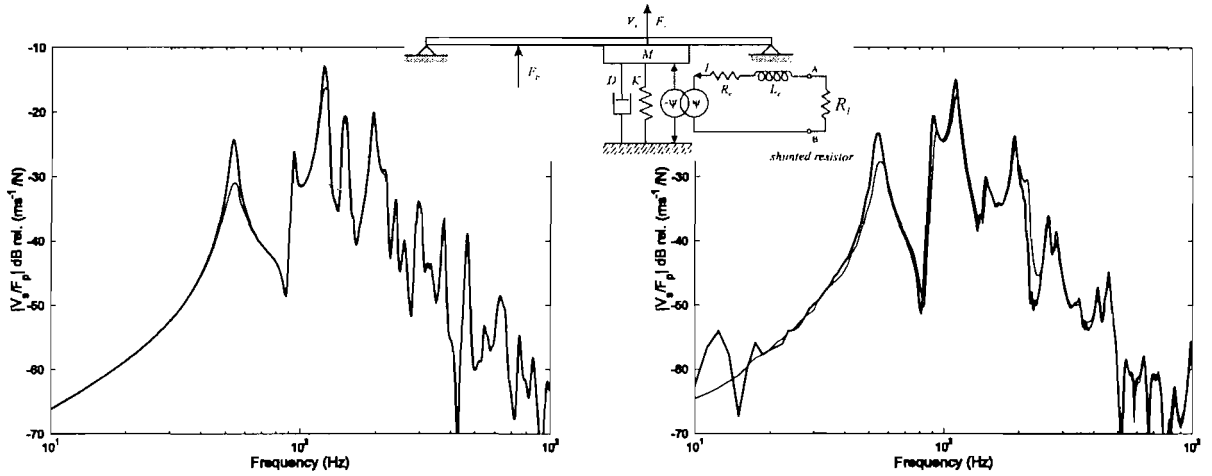
Figure 2.16: *Simulated (left plot) and measured (right plot) vibration level of the panel at the control actuator position with reference to the primary disturbance F_p in the open loop case (thick solid line) and for a 1ohms shunted resistor (thin solid line).*

2.4   positive current feedback

In order to further reduce the value of the shunted resistor a positive current feedback loop generating a negative resistance can be used. Then as shown in Figure 2.17 a measurement resistor R_l is added in series to the shaker so that a modified electrical impedance $Z'_e = R_l + Z_e$ results. Instead of directly feeding back the coil current I the voltage over the measurement resistor U_{BC} proportional to current is fed back to the shaker input via an amplifier. The input voltage becomes

$$U_{AC} = + GU_{BC} \qquad (2.19)$$

36

where G is a real positive feedback gain and the open loop FRF is

$$\frac{U_{BC}}{U_{AC}} = \frac{(R_l/Z_e')}{1+\psi^2/Z_e'Y_{ss}''} . \qquad (2.20)$$
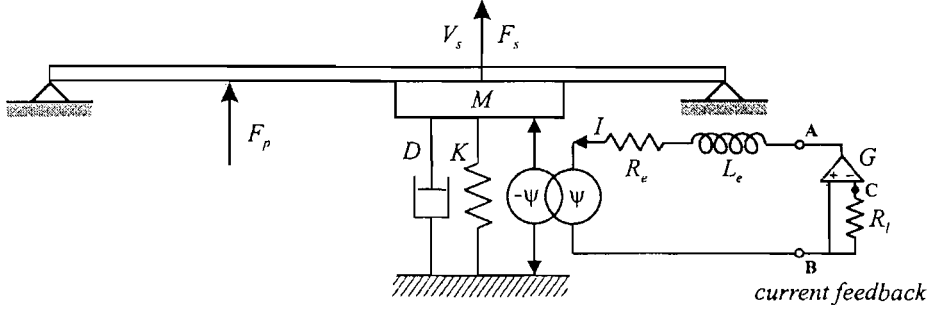
current feedback

Figure 2.17: *Model of the electrodynamic reactive actuator with positive current feedback and connected to the plate.*

Positive feedback is implemented since negative feedback would not be different from the shunted resistor case presented in the previous section. The closed loop FRF of the plate is

$$\frac{V_s}{F_p} = \frac{Y_{sp}''}{1+Y_{ss}''\psi^2/(Z_e'-GR_l)} \qquad (2.21)$$

where the feedback gain compensates for the real part of the electrical coil impedance, i.e. the resistive part. The signal output Y_o in the scheme of Figure 1.2 is the voltage drop U_{BC} over the measurement resistor, which is indeed proportional to the current in the driving circuit of the shaker, and the signal input Y_i is the driving voltage U_{AC} of the shaker. Therefore the transfer functions in the block diagram of Figure 1.2 remain proportional to those presented in Section 2.3 namely $G_{sp} = \frac{Y_{sp}''}{1+\psi^2/Z_e'Y_{ss}''}$, $G_{si} = \frac{Y_{ss}''(\psi/Z_e')}{1+\psi^2/Z_e'Y_{ss}''}$,

$G_{op} = \frac{-Y_{sp}''(\psi R_l/Z_e')}{1+\psi^2/Z_e'Y_{ss}''}$ and $G_{oi} = \frac{(R_l/Z_e')}{1+\psi^2/Z_e'Y_{ss}''}$. A Crown Electronics DC-300 amplifier is

used to implement the feedback gain G. Due to its small electrical output impedance R_l the amplifier already adds damping to the plate that is in the range of the shunted resistor case presented in Section 2.3.

Stability

The two plots in Figure 2.18 show the simulated (left plot) and measured (right plot) Nyquist plots of the open loop FRF between the amplifier output voltage U_{AC} and the

37

voltage over the measurement resistor U_{BC} for frequencies up to 10kHz in simulations. Measurements and simulations agree well up to about 1 kHz, but they diverge for higher frequencies. Compared to that in Figure 2.15 the locus has flipped into the left half plane so that the closed loop is predicted to be only conditionally stable. In the closed loop case, the voltage drop over the measurement resistor, which is proportional to the coil current, is predicted to be amplified. As a consequence the actuation force on the plate increases.
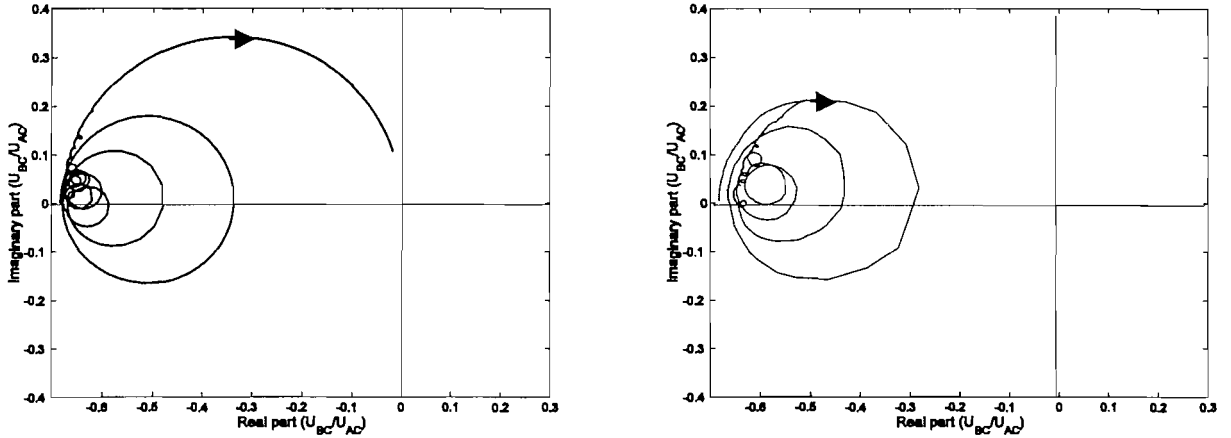
Figure 2.18: *Simulated (left plot) and measured (right plot) Nyquist plot of the FRF between the input voltage U_{AC} and the feedback voltage U_{BC}.*

This actuation force is opposite to the vibration velocity since for electrodynamic actuators the induced voltage, following Eq. (2.11) transformed into current, is of opposite sign to the current and the control force. Relatively more damping than in the passive shunted resistor case is predicted since the current is amplified electronically.

Performance

Figure 2.19 shows the simulated (left plot) and measured (right plot) vibration of the panel at the control position with reference to the primary disturbance excitation. The thick and thin solid lines give the vibration of the panel at the control position without the passive amplifier effect (thick solid line) and for a positive current feedback gain close to the stability limit (thin solid line). With reference to the shunted resistor case, a larger amount of damping of about 12dB is added to the first resonance frequency of the plate. Moreover about 4dB and 9dB damping is added to the second and third resonance frequencies. However, beyond about 200Hz spillover into higher modes occurs which will lead to instability if larger feedback gains are implemented.

38
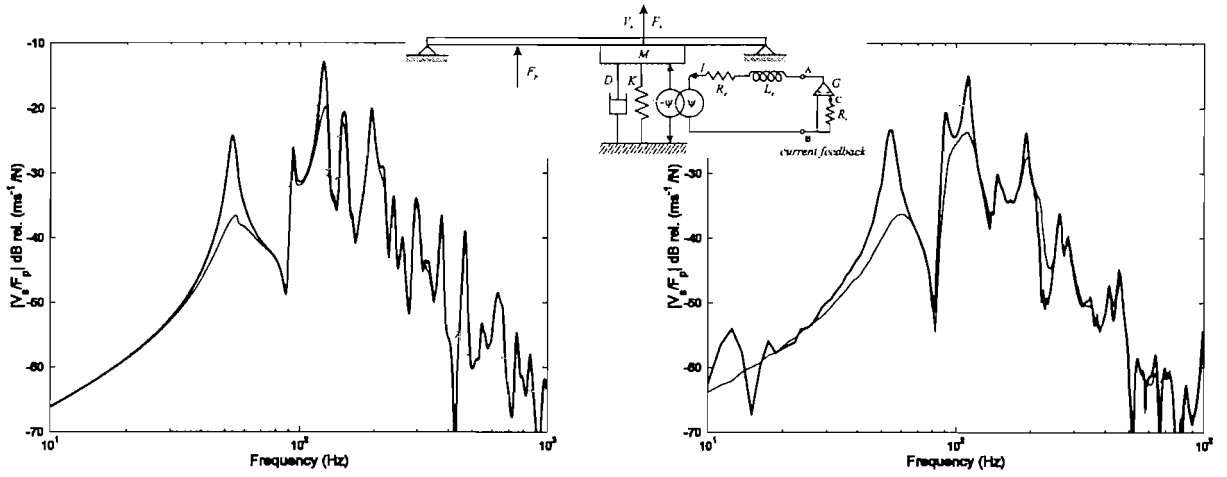
Figure 2.19: *Simulated (left plot) and measured (right plot) vibration level of the panel at the control actuator position with reference to the primary disturbance F_p in the open loop case (thick solid line) and for positive current feedback (thin solid line).*

2.5   Induced voltage feedback

In the previous case the current resulting from the feedback driving voltage is measured in addition to the current resulting from the induced voltage. In order to better estimate the induced voltage a Wheatstone bridge is added that partially compensates for the feed through from driving voltage to sensed current. As shown in Figure 2.20 one half of the bridge is formed by the electrical part of the shaker and a resistor R_l in series and the second half-bridge is formed by two resistors R_1 and R_2 in series in parallel to the first half-bridge.
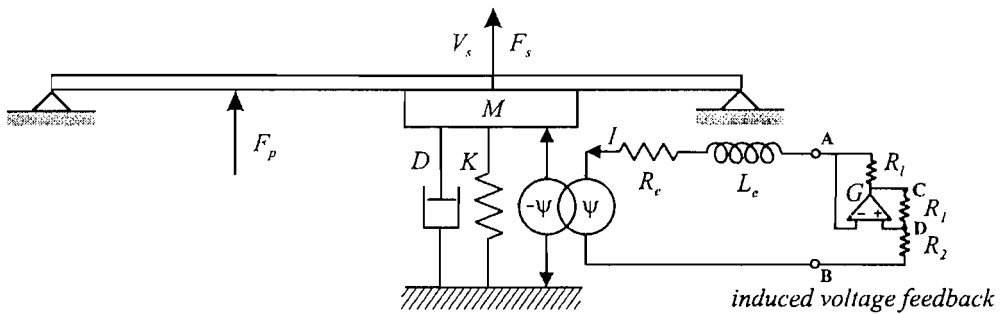
Figure 2.20: *Model of the electrodynamic reactive actuator with Wheatstone bridge for induced voltage feedback and connected to the plate.*

The voltage over each half of the bridge is given by

$$U_{BC}=(R_1+R_2)I_1=(Z_e+R_l)I+U_{ind} \tag{2.22}$$

where I_1 is the current in the second half-bridge. The input voltage to the feedback amplifier between the shaker input and the lower half of the second half-bridge is

39

$$U_{AD} = R_2 I_1 - Z_e I - U_{ind}. \qquad (2.23)$$

When the feedback amplifier implements direct feedback, i.e.

$$U_{BC} = -G\, U_{AD}, \qquad (2.24)$$

the open loop FRF is given by

$$\frac{U_{AD}}{U_{BC}} = \frac{R_2}{R_1 + R_2} - \frac{Z_e + \psi^2 Y_{ss}''}{Z_e' + \psi^2 Y_{ss}''}. \qquad (2.25)$$

This equation clearly shows that in comparison to Eq. (2.20) an additional feed through term can be cancelled. The closed loop FRF of the plate becomes

$$\frac{V_s}{F_p} = \frac{Y_{sp}''}{\left(1 + \psi^2 / (Z_e') Y_{ss}''\right)\left(1 - Y_{ss}'' / \left(GR_i\left(R_1 + R_2\right)/(R_1 + R_2 + R_2) - Z_e'\right)\right)}. \qquad (2.26)$$

U_{BC} simultaneously is the input voltage from the DC-300 amplifier and the control input Y_i. The output signal from the bridge, U_{AD}, is the bridge output voltage and the control output Y_o. In this case the four transfer functions in the control block diagram of Figure 1.2 are given by the following relations: $G_{sp} = \dfrac{Y_{sp}''}{1 + Y_{ss}'' \psi^2 / Z_e'}$, $G_{si} = \dfrac{Y_{ss}''(\psi / Z_e')}{1 + Y_{ss}'' \psi^2 / Z_e'}$,

$G_{op} = \dfrac{-\psi\, Y_{sp}'' / Z_e'}{1 + Y_{ss}'' \psi^2 / Z_e'}$ and $G_{oi} = \dfrac{R_2}{R_1 + R_2} - \dfrac{Z_e + \psi^2 Y_{ss}''}{Z_e' + \psi^2 Y_{ss}''}$.

Stability

The two plots in Figure 2.21 show the simulated (left plot) and measured (right plot) Nyquist plots of the open loop FRF between the bridge input voltage U_{BC} and the amplified bridge output voltage U_{AD} for frequencies up to 10 kHz. The simulated locus is completely in the right half plane, which indicates unconditional stability. Measurements up to 100 kHz show that for higher frequencies the electric circuit of the shaker does not behave like a real inductance. Probably for even higher frequencies the locus will enclose the critical point $(-1, 0j)$ at some gains. Therefore a steep 10 kHz low pass filter is used, so that closed loop stable feedback gains are implemented in practice.
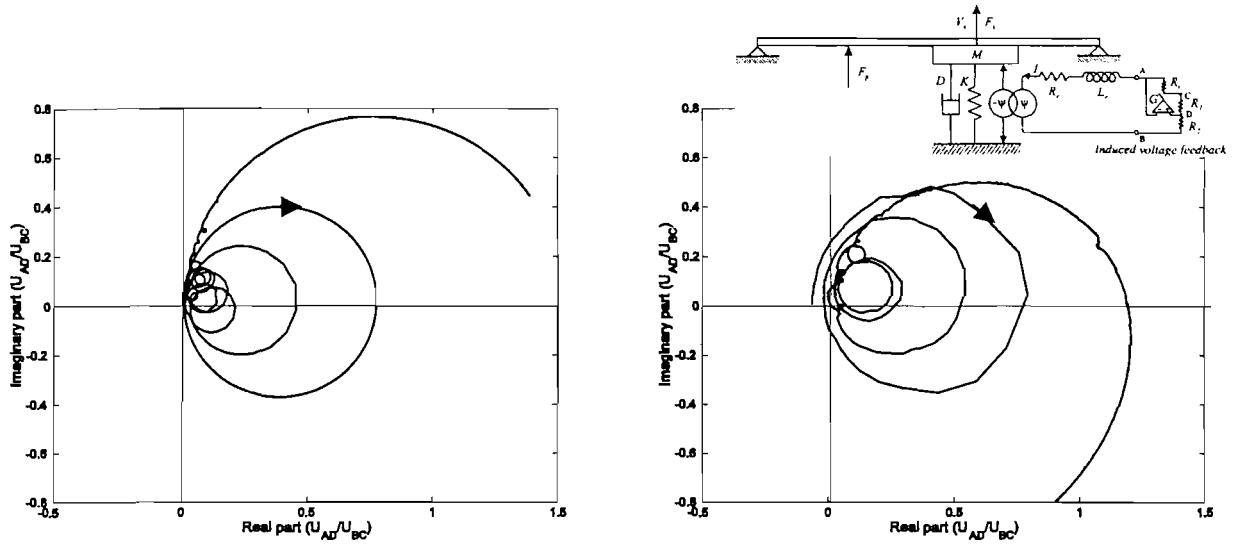
Figure 2.21: *Simulated (left plot) and measured (right plot) Nyquist plot of the FRF between the bridge input voltage U_{BC} and the amplified bridge output voltage U_{AD}.*

Performance

Figure 2.22 shows the simulated (left plot) and measured (right plot) vibration of the panel at the control position with reference to the primary disturbance excitation. The thick and thin solid lines give the vibration of the panel at the control position without the passive amplifier effect (thick solid line) and for two induced voltage feedback gains (thin solid and thick dashed lines).
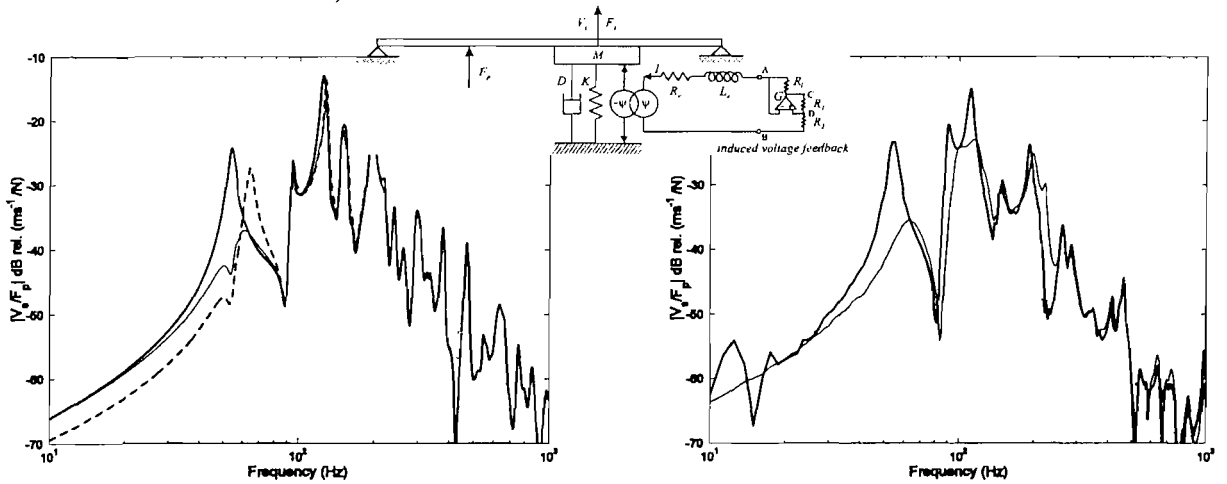
Figure 2.22: *Simulated (left plot) and measured (right plot) vibration level of the panel at the control actuator position with reference to the primary disturbance F_p in the open loop case (thick solid line) and for increasing bridge output voltage feedback gains (thin solid and thick dashed line).*

Due to risk of instability, because of measurement uncertainty, higher feedback gains have not been implemented in practice and thus only the thin solid line has been predicted in the right hand side plot. Comparable vibration reduction as in the positive current feedback case is achieved and, as found in the previous section, spillover, due to the uncorrected

41

inductance, appears at higher frequencies. In order to increase control bandwidth a bridge circuit should also compensate for the shaker inductance.

2.6   Induced voltage feedback with inductance compensation

Additional inductance compensation is achieved using a so-called Owens bridge. As shown in Figure 2.23 relative to a Wheatstone bridge, resistors are replaced by the reactive components $Z_1 = R_3 + \dfrac{1}{j\omega C}$ and $Z_2 = \dfrac{1}{j\omega C}$ with a capacitance C and a resistance R_3.

induced voltage feedback
with inductance compensation
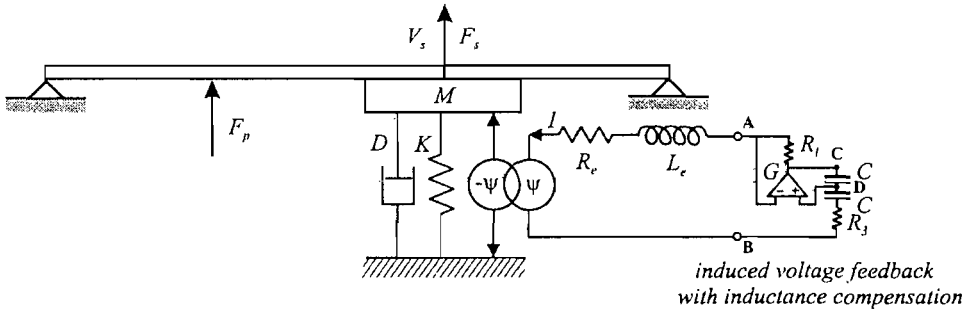
Figure 2.23: *Model of the electrodynamic reactive actuator with Owens bridge for induced voltage feedback with inductance compensation and connected to the plate.*

Eqs. (2.22) and (2.23) become

$$U_{BC}=(Z_1+Z_2)I_1=(Z_e+R_l)I+U_{ind} \tag{2.27}$$

and

$$U_{AD}=Z_1I_1-Z_eI-U_{ind}\, . \tag{2.28}$$

As in the previous case direct feedback is implemented by

$$U_{BC}= -G\, U_{AD} \tag{2.29}$$

so that also a frequency dependent feed through term can be compensated by the open loop FRF

$$\frac{U_{AD}}{U_{BC}} = \frac{Z_1}{Z_1+Z_2} - \frac{Z_e+\psi^2 Y_{ss}''}{Z_e'+\psi^2 Y_{ss}''}\, . \tag{2.30}$$

42

$$\frac{V_s}{F_p} = \frac{Y_{sp}''}{\left(1+\psi^2/(Z_e')Y_{ss}''\right)\left(1-Y_{ss}''/\left(GR_i\left(Z_1+Z_2\right)/\left(Z_1+Z_2+GZ_2\right)-Z_e'\right)\right)} \quad .(2.31)$$

U_{BC} is simultaneously the input voltage from the H&H VX-200 amplifier and the control input Y_i in the block diagram of Figure 1.2. U_{AD} is the bridge output voltage and the control output Y_o also in the block diagram of Figure 1.2. In this case the four transfer functions are given by the following expressions: $G_{sp} = \dfrac{Y_{sp}''}{1+\psi^2\,Y_{ss}''/Z_e'}$, $G_{si} = \dfrac{Y_{ss}''\,\psi/Z_e'}{1+\psi^2\,Y_{ss}''/Z_e'}$,

$$G_{op} = \frac{-\psi\,Y_{sp}''/Z_e'}{1+\psi^2\,Y_{ss}''/Z_e'} \qquad \text{and } G_{oi} = \frac{Z_1}{Z_1+Z_2} - \frac{Z_e+\psi^2 Y_{ss}''}{Z_e'+\psi^2 Y_{ss}''} \;.$$

Stability

The two plots in Figure 2.24 show the simulated (left plot) and measured (right plot) Nyquist plots of the open loop FRF between the bridge input voltage U_{BC} and the bridge output voltage U_{AD} for a tuned Owens bridge. The simulated locus is on the right hand side predicting unconditional stability. If the bridge is mistuned by less than 1% simulations predict that unconditional stability is no longer guaranteed. The measured locus on the right hand side indicates an important influence and phase shift of the amplifier at lower frequencies that spoils the tuning [122]. Also at higher frequencies the locus moves into the left half plane since the electrical circuit of the shaker does not behave like an ideal inductance at these frequencies. Hence, only conditional closed loop stability is predicted.
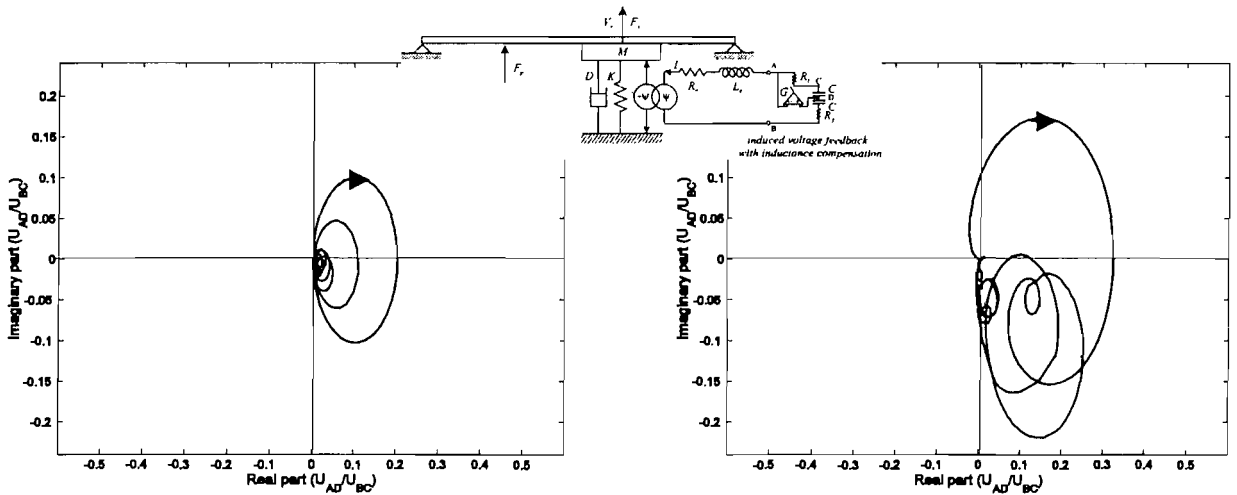
Figure 2.24: *Simulated (left plot) and measure (right plot) Nyquist plot of the FRF between the Owens bridge input U_{BC} and output voltage U_{AD}.*

43

Figure 2.25 shows the simulated (left plot) and measured (right plot) vibration of the panel at the control position with reference to the primary disturbance excitation. The thick and thin solid lines give the vibration of the panel at the control position without the passive amplifier effect (thick solid line) and for two induced voltage feedback gains (thin solid and thick dashed lines). High vibration reduction is predicted at lower frequencies and spill-over occurs only at higher frequencies beyond about 400Hz. The plot on the right hand side shows only one control case (thin solid line) close to the stability limit. For simulations and measurements in Figure 2.25 the secondary force transducer is removed for practical reasons so that the open loop amplitude is increased at higher frequencies relative to previous measurements and simulations. High vibration reduction up to 9dB is measured in the frequency range up to about 500Hz and the 11th visible mode. For higher frequencies spillover into higher modes occurs. Relatively less vibration reduction than that obtained with the resistive Wheastone bridge is obtained at the first resonance frequency because in the open loop case the small amplifier output impedance has already added damping. Measurements do not show a pure active damping effect since the locus of the open loop FRF in the Nyquist plot is rotated because of the high pass filter in the driving amplifier.
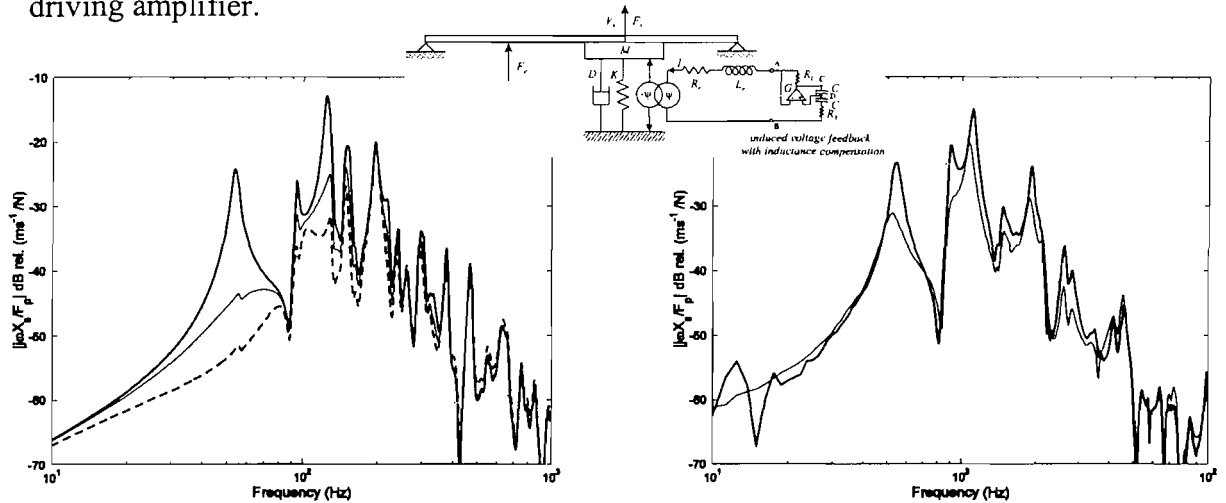
Figure 2.25: *Simulated (left plot) and measured (right plot) vibration level of the panel at the control actuator position with reference to the primary disturbance F_p in the open loop case (thick solid line) and for increasing Owens bridge output voltage feedback gains (thin solid and thick dashed line).*

2.7   Summary

The four control schemes shunted resistor (Figure 2.14), positive current feedback (Figure 2.17) and induced voltage feedback with (Figure 2.20) and without (Figure 2.23) inductance compensation have been investigated for vibration reduction of a clamped plate
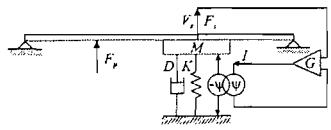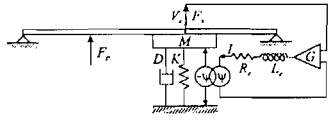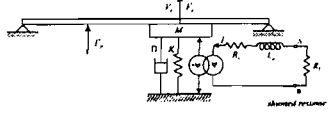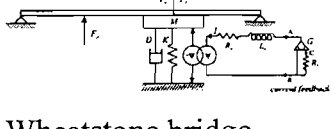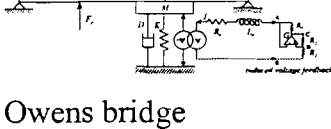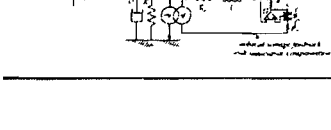
using a self-sensing, electrodynamic actuator reacting against a fixed environment (SSRA). They have been compared to direct velocity feedback a) with an ideal actuator and sensor (Figure 2.4), b) with an accelerometer and a current driven electrodynamic actuator (Figure 2.10) and c) with an accelerometer and a voltage driven electrodynamic actuator (Figure 2.13). A model of the plate and the electrical circuit has been developed and a general control framework has been presented in the frequency domain. Measurements at a test setup have shown reasonable agreement with the model up to about 1kHz.

Both in the direct velocity feedback case with accelerometer and voltage driven actuator and in the self-sensing actuator case, for higher frequencies, the electrical circuit of the shaker does not behave like an ideal inductance and dynamics of the electrical circuit interfere. Hence, duality between the actuation and sensing mechanisms is only guaranteed at lower frequencies resulting in spillover at higher frequencies in the closed loop case. In the case with accelerometer more vibration reduction is achieved than in the self-sensing actuator case because the inductance does not also limit the sensing bandwidth. Non-ideal collocation effects could not be distinguished because the mass effect of the force transducers dominates the frequency response at higher frequencies. In some cases at lower frequencies the amplifier characteristics interfere as well as low measurement coherence. Approximate vibration reductions for different control schemes are listed in Table 2.2. In the shunted resistor case vibration reductions of about 5dB at the first resonance frequency and about 2dB at the second and third resonance frequencies have been observed in simulations and measurements. For positive current feedback and induced voltage feedback without inductance compensation, vibration reduction of about 12dB at the first resonance frequency and about 4dB and 9dB at the second and third resonance frequencies are visible in measurements. However, spillover into higher modes occurs at about 200Hz. Induced voltage feedback with partial inductance compensation leads to measured vibration reduction of about 9dB at the first resonance frequency and of at least 5dB at each mode up to the 11th visible mode at 400Hz. Small spillover starts to appear at frequencies beyond about 500Hz. Higher vibration reduction at the first resonance frequency is anticipated if an appropriate amplifier is used. These vibration reductions are far away from those required for an optimum gain simulated in the ideal force actuator and velocity sensor case. Table 2.2 also lists the approximately achieved values when an accelerometer is used both in the current command and the voltage command case. When an accelerometer in combination with a sophisticated charge amplifier is used much more vibration reduction is achieved than with self-sensing vibration control.

With self-sensing vibration control further reduction could probably be obtained also using a sophisticated compensator that includes a more detailed model of the electrical shaker circuit at higher frequencies. For instance lumped parameter models are proposed in [169] to model higher frequency effects in ferrite inductors. Another way would be a non-physical model using for instance a digital compensator with a look-up table. The limited dynamic range and bandwidth / computation speed constitutes a technology limit when digital components are used. In Appendix B it is shown that compensation of the electrical impedance of the electrodynamic actuator leads to optimum kinetic energy reduction.

The used electrodynamic, reactive actuator (RA) weighs more than the plate and it requires a fixed reaction base. Therefore in the next chapter the design of a lightweight inertial actuator (IA) is considered that does not require any external reaction structure in addition to the plate.

Table 2.2: *Approximate, measured vibration reduction in dB at the first to 10th plate resonances for the studied control schemes in Chapter 2.*

Control	Res1	Res 2	Res 3	Res 4	Res 5	Res 6	Res 7	Res 8	Res 9	Res 10	Fig.2
DVFB acc. cc.	21	12	13	11	14	24	8	15	4	13	2.10
DVFB acc. vc.	24	18	19	20	22	33	14	24	10	21	2.13
Shunted resistor	5	3	3	-	-	-	-	1	-	-	2.16
Positive current FB	12	4	9	-	4	-	-	1	-	-	2.19
Wheatstone bridge	12	4	8	-1	1	-	-	1	-	1	2.22
Owens bridge	8	9	5	4	7	1	7	6	3	4	2.25

3. DESIGN OF A LIGHTWEIGHT, ELECTRODYNAMIC, INERTIAL ACTUATOR WITH INTERNAL VELOCITY SENSOR

In the previous chapter a rather heavy, unpractical, electrodynamic, reactive actuator (RA) has been used to study self-sensing vibration control. In order to reduce weight and allow its application to practical structures the design of a lightweight, electrodynamic, inertial actuator (IA) is presented in this chapter. An internal velocity sensor (IVS) is proposed as an alternative to self-sensing (SS) with the aim to improve the high-frequency sensing behaviour and reduce tuning effort. Potentially it is simpler and more robust to use a secondary sensing coil instead of compensating electronics.

Section 3.1 presents a number of considerations regarding the mechanical design of an inertial actuator (IA), the design of the electromagnetic circuit, the geometry of the suspension and self-sensing (SS) control. Section 3.2 shows validation measurements of the actuator force, its frequency response and the internal velocity sensor (IVS).

3.1   Design considerations

Following the discussion presented in Chapter 1, the out-of-plane force actuator for ASAC with a large number of collocated sensor-actuator pairs should be lightweight and self-contained. It should also allow vibration control in the acoustically perceivable frequency range between about 16Hz and 10kHz or at least between about 16Hz and 1kHz. A self-contained actuator is achieved by including an inertial mass in the actuator. The inertial actuator then acts on the structure and reacts against the inertial mass. Experiments with the model problem have shown that a primary 1kHz band limited white noise excitation force of about 4N is sufficient to generate a sound pressure level (SPL) of more than 80dB about 0.5m above the plate. It is assumed that a secondary actuator should be able to generate a control force transmitted on the plate also of 4N in order to cancel the primary disturbance. The electrodynamic actuation force should be at least as high despite a lightweight design. An inertial mass of 0.02 kg is chosen in order to be competitive with other means of active vibration reduction or passive treatments. For example four inertial actuators of 0.02kg could be compared to 16 patch actuators of more than 0.08grams [10].

In Section 3.1.1 it is investigated which suspension stiffness and stroke should be chosen for an inertial actuator in order to allow the required frequency range and transmitted force.

Section 3.1.2 determines the relation between the inertial mass of the actuator and the electrodynamic actuation force. Based on the electromagnetic circuit design and required suspension stiffness, compatible suspension geometries are investigated in Section 3.1.3. Section 3.1.4 highlights the advantages of an internal velocity sensor relative to a self-sensing approach.

3.1.1 Mechanical design

Figure 3.1 schematically shows an inertial actuator that consists of an inertial mass m, its suspension on the structure with stiffness K and viscous damping D and a force generation mechanism used to generate an actuation force F_a between the inertial mass and the structure.
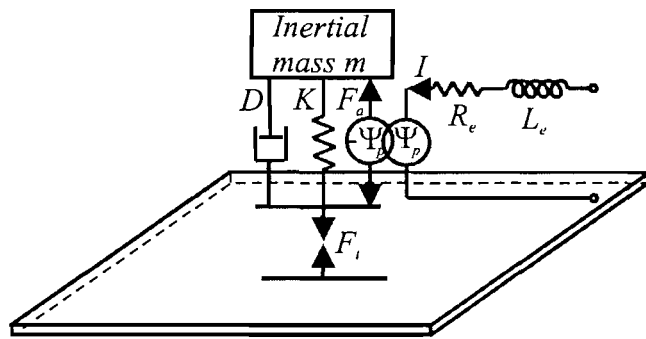
Figure 3.1: *Schematic view of an electrodynamic, inertial actuator on a lightweight plate.*

The relation between the transmitted force F_t on the structure and the generated actuation force is

$$\frac{F_t}{F_a} = \frac{j\omega m}{j\omega m + K/j\omega + D} \tag{3.1}$$

and results in a characteristic frequency response as shown in Figure 1.3. Below the undamped fundamental resonance frequency of the actuator $\omega_0 = \sqrt{K/m}$ there is hardly any force transmitted on the structure. At resonance the transmitted force is much greater than the actuation force. Moreover at frequencies below the fundamental resonance frequency the inertial mass and the structure vibrate out of phase whereas they vibrate in phase above this frequency.

In order to avoid an influence of the phase shift and amplification of the fundamental resonance on closed loop stability the lowest resonance frequency of the structure ω_1 should be higher than ω_0, for instance

$$\omega_1 > (3-5)\sqrt{K/m} \ . \tag{3.2}$$

An exact condition for a mechanical system with two degrees of freedom is given in Appendix E. Since the mass should be chosen as small as possible the stiffness of the suspension can be used to adjust this lower frequency bandwidth limit. An upper frequency bandwidth limit is given by internal resonances in the inertial actuator, which should not appear below the required upper frequency bandwidth limit of 1kHz.

For an inertial actuator the transmitted force is limited by the inertial mass m and the maximum stroke d. As shown in Figure 3.2 for steady state excitation this limit is important at lower frequencies below the saturation break frequency ω_b. Above the saturation break frequency there is reduced risk of stroke saturation since the actuation force F_a rather constitutes a limit.
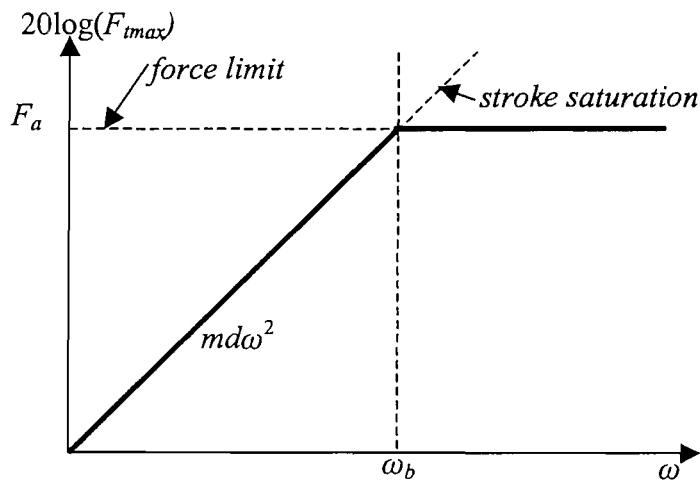
Figure 3.2: *Force Saturation Curve, +/- d maximum stroke* [53].

The saturation break frequency is defined as the frequency where the limit of the transmitted force due to stroke saturation is equal to the limit due to the actuation force. For maximum use of the actuator authority the control range should start at the saturation break frequency, i.e. the first resonance frequency of the structure to be controlled should lie at the saturation break frequency:

$$\omega_b = \sqrt{F_a/(md)} = \omega_1 \tag{3.3}$$

A maximum stroke d of about 0.002m results for an inertial mass m=0.02kg, an actuation force F_a=4N and the first flexible resonance frequency of the plate $\omega_1 = 2\pi$ 55 rad s^{-1}. This

stroke gives a limit on the actuator geometry that is important in the design of the force generation mechanism. Another limit on the geometry is given by the static sag $\delta=gm/K=g/\omega_0^2$ that depends on the fundamental resonance ω_0 and the gravity constant g. For the given values it lies in the order of the stroke. The static sag is compensated electronically in combination with offset compensation of the used operation amplifiers.

3.1.2 Electrodynamic design

The electrodynamic or Lorentz's force principle [170] has been chosen to generate the actuation force because of many reasons including

 a) its simplicity
 b) the large required stroke d=0.002m
 c) the rather small required force F_a=4N and
 d) the previous work about self-sensing, electrodynamic actuators.

Also, in contrast to other types of linear, electromagnetic actuators described in [68, 171], the heavy parts of the magnetic circuit (stator) can be included in the inertial mass. For an electrodynamic actuator the actuation force F_a depends linearly on the permanent magnetic field in the air gap B_g, the length of the wire in the air gap and the current in the wire I [170]. For given material properties, these three values depend on the geometry of the actuator and the electrical power input P that is considered to be a constant. The material properties limit the magnetic field that is generated by a permanent magnet. They also determine a saturation limit of the magnetic field in the magnetic circuit. The maximum temperature in the wire depends on material properties of the insulation and wire. Material properties also influence the actuator weight and leakage in the magnetic circuit. For a lightweight inertial actuator the geometry is constraint by the allowable weight of the inertial mass and the stroke although permanent magnet actuators favourably downscale in size [172]. The electrical power input partly dissipated into heat by the resistivity of the wire is constrained by the heat exchange with the environment that is only precisely known by experiments.

In this subsection the geometry of a typical electrodynamic design is first parameterised and the transmitted force, the magnetic field and the inertial mass are expressed as function of geometric and material parameters. Then the material of the permanent magnet is chosen. For a given material a finite element analysis (FEA) gives the relation between actuation force and inertial mass for a large number of dimensions without having to know a detailed magnetic leakage model. Finally a geometry with the required inertial mass and

maximum actuation force is chosen. A more detailed explanation of the design choices and equations is given in [57].

Figure 3.3 shows a cross section view of a design of an electrodynamic actuator axisymmetric about the vertical z-axis with a permanent magnet and a centring bore in the middle and coil in the air gap. B_m is the magnetic field generated by the permanent magnet, whereas B_w, B_{go} and B_{gi} are the magnetic fields in the outer yoke, the outer part of the air gap and in the inner part of the air gap respectively. A centring bore in the middle has been chosen in order to allow easy guidance of the actuator by a centred axis. As shown in [57] based on this geometry the actuation force is given by

$$F_a = \frac{B_r H_l p h_g \left(A + 2t\right) b \mu_0 \left(A^2 - A_i^2\right)}{4 H_l p h_g \left(A + 2t\right) b \mu_0 + B_r q \left(A^2 - A_i^2\right)} \frac{1}{s} \sqrt{\frac{P}{\rho_{wi}}} \sqrt{\frac{1}{2d + h_g}} \sqrt{\frac{\pi s}{\left(A + 2t + s\right)}} \quad (3.4)$$

where B_r, H_l, μ_0 are electromagnetic material properties, p, q are non-dimensional leakage factors depending on the actuator shape and ρ_{wi} is the current density of the wire. Apparently there is a non-linear dependence on the geometry that is further complicated because the shape factors p and q are only approximately known [173].
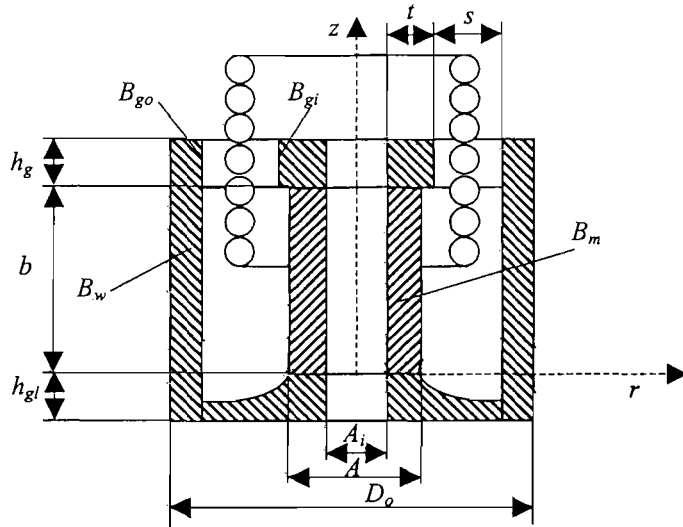
Figure 3.3: *Electrodynamic shaker design using a strong permanent magnet.*

This non-linear cost function to be maximised is constrained by the saturation of the magnetic field in the material assumed to follow

$$1T \geq B_{go} = \frac{\left(A^2 - A_i^2\right) B_r \left(H_l p \pi h_g \left(A + 2t\right) b \mu_0\right)}{4 h_g \left(A + 2s + 2t\right)\left(H_l p \pi h_g \left(A + 2t\right) b \mu_0 + B_r q s \left(A^2 - A_i^2\right) \pi/4\right)} \quad (3.5)$$

and

$$1.2T \geq B_{gi} = \frac{\left(A^2 - A_i^2\right)B_r\left(H_l p\pi h_g \left(A+2t\right)b\mu_0\right)}{4h_g\left(A+2t\right)\left(H_l p\pi h_g\left(A+2t\right)b\mu_0 + B_r qs\left(A^2-A_i^2\right)\pi/4\right)}. \tag{3.6}$$

Moreover it is assumed that this analysis is no longer valid because of important leakage in the magnetic circuit if

$$s \leq 0.5\left(1.2\left(A+2t\right)-A-2t\right), \tag{3.7}$$

$$b > 3s \tag{3.8}$$

are not fulfilled. Additionally the magnetic field in the permanent magnet has to be smaller than the remanence of the used material:

$$B_m = \frac{B_r}{1+\dfrac{B_r q\left(A^2-A_i^2\right)\,s}{4H_l p h_g\left(A+2t\right)b\mu_0}} < B_r. \tag{3.9}$$

The remanence B_r is a material property that describes the permanently remaining magnetic B-field in a material after a magnetic field has been consecutively applied and removed [170]. Finally the inertial mass equivalent to the stator of the actuator is given by

$$m = \rho_{mag}\pi\left(A^2-A_i^2\right)b/4 + \rho_{fe}\left(\left(A+2t\right)^2 - A_i^2\right)\pi h_g/4 + \\ \rho_{fe}\left(\pi\left(2t+2s\right)/4+\left(A^2-A_i^2\right)\pi/\left(16A\right)+\left(b+2h_g\right)\pi/4\right)\left(D_o^2-\left(A+2t+2s\right)^2\right) \tag{3.10}$$

Hence for a large number of dimensions compatible with $d=0.002\text{m}$ Eqs. (3.4) and (3.10) can be plotted in an actuation force – inertial mass diagram. Also, the actual magnetic field in the air gap

$$B_g = B_m \frac{A^2 - A_i^2}{4h_g\left(A+2t+s\right)} \tag{3.11}$$

can be assessed for each parameter combination, material properties and estimated leakage factors. As expected calculations show that when the magnetic field in the air gap is small, there tends to be a rather high air gap with more wire, whereas a high magnetic field tends to lead to a small amount of wire in the air gap. At a given geometry the magnetic field

depends on the material properties. Figure 3.4 shows typical *H-B* curves in the demagnetisation region for different materials. Interpolating past development of permanent magnets into the future shows that today's HB$_{max}$ products are still halfway from a theoretical limit [174] promising even stronger electrodynamic actuators in the future. Since the remanent magnetic field B_r should be high anisotropic AlNiCo materials should be chosen. But these materials also show a low coercitivity H_l, which could be a problem for high currents. The coercitivity is a material property and describes the magnetic field of opposite polarity that has to be applied to a material to compensate for the remanence B_r [170]. If high currents lead to a $H>H_l$ and a knee is encountered in the *H-B* curve the permanent magnet is irreversibly demagnetised and the remanent magnetic field is reduced, too [175]. For high temperatures this behaviour is even more critical since the shown curves move to the right [176]. For small actuators the possible current density [177] tends to increase. Therefore sintered Nd-Fe-B magnets with a high HB_{max} product and a knee far in the 3rd quadrant should be chosen. The manufacturer of the Nd-Fe-B magnets gives a temperature limit of about 80°C [178]. Since these magnets contain iron Fe they are prone to corrosion and a Ni coating should be applied.

(a) anisotropic ALNICO
(b) isotropic ALNICO
(c) sintered anisotropic ferrite
(d) polymer bonded Sm-Co
(e) polymer bonded Nd-Fe-B
(f) sintered Sm-Co
(g) sintered Nd-Fe-B

H (kA/m)
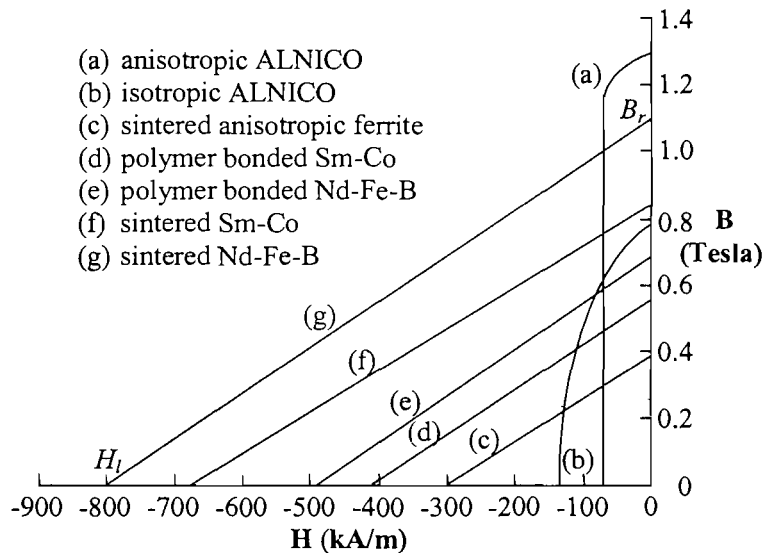
Figure 3.4: *Typical B/H curves in the demagnetisation region* [179].

The shown materials are hard magnetic materials that do not easily change with the direction of the magnetic field [180]. Their application in variable magnetic fields results in rather high core losses. Permanent magnets also have a relative permeability close to 1 and therefore they should not be used to guide and concentrate the magnetic flux in the air gap. In order to reduce dissipation in a time-varying magnetic field and to guide the magnetic flux soft magnetic materials should be used for the yoke constituting the magnetic circuit [181]. Soft, low-carbon ferritic steel is chosen and treated with an oil film in order to protect it from corrosion.

In this design procedure, uncertainty still remains because the saturation values of the soft magnetic material and leakage factors are not precisely known. Therefore a finite element analysis including saturation properties of the material is carried out for a large number of dimensions. The actuation force is calculated with reference to the air gap geometry that determines the amount of wire and the magnetic field in the air gap. In Figure 3.5 the actuation force and the magnetic field in the air gap are plotted as a function of the inertial mass for a larger number of parameter values. For the chosen design in Figure 3.3 there seems to be a large region with quasi-linear behaviour between the maximum actuation force and the inertial mass. Also, the magnetic field in the air gap is rather small with values between 0.2 and 0.3 T. As expected rather higher currents are reasonable for small actuators. Higher current densities are realizable for smaller actuators since, because of the high surface per volume, heat is more easily evacuated from these actuators [86].
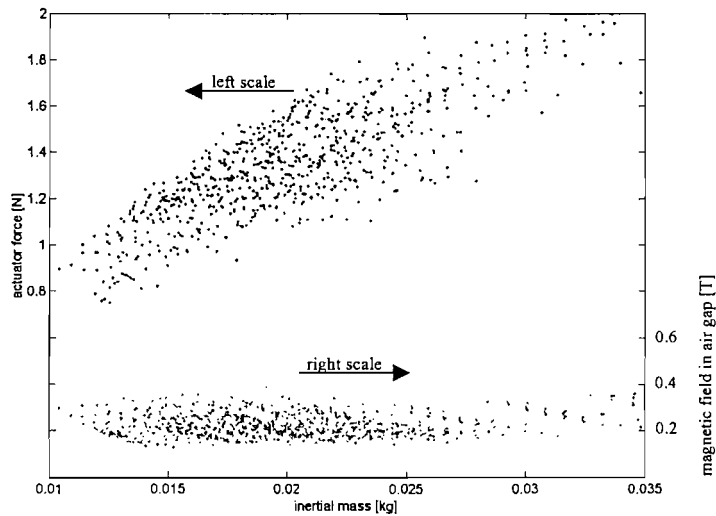
Figure 3.5: *Actuator force as a function of the inertial mass with different parameter combinations $(A,s,h_g,b,A_i=2mm)$.*

The highest actuation force for an inertial mass of 0.02kg is about 1.6N at an electrical power input of 1 Watts. Although this actuation force is below the required 4N it could well be accceptable since the exact electrical power input is not known a priori. It depends very much on the heat transfer with the environment that cannot be easily determined without experiments. The chosen design point corresponds to an electromagnetic circuit shown in Figure 3.6 where a rather large air gap with a small magnetic field is visible. Figure 3.6 shows a cross-section view of the magnetic circuit axisymmetric about the z-axis. The corresponding parameter values are compiled in Table 3.1. These geometric values constitue the input to the suspension design described in the next subsection.

Design	A	A_i	h_g	s	b	D_o	B_g (T)	m (g)	F_a (N)	h_{gl}
final	12.5	2	4	3	4.8	23.5	0.2972	20.3	1.6362	2.3
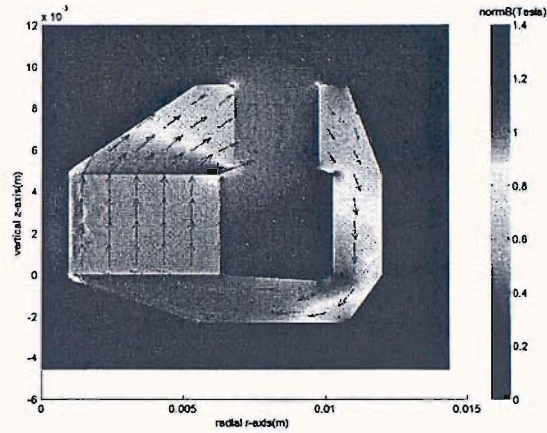
Figure 3.6: *Finally chosen magnetic circuit design.*

3.1.3 Suspension design

After having determined the geometry of the inertial mass in Subsection 3.1.2 the geometry of the surrounding mechanical components, e.g. suspension, guide and cover, are chosen. The suspension should guarantee a high stiffness in horizontal direction and a vertical stiffness that, together with a moving mass of $m=0.02$kg, results in a main resonance frequency of about $\omega=2\pi 15$rad s^{-1} so that a frequency bandwidth starting at about 55Hz is achieved as explained in Subsection 3.1.1. Figure 3.7 shows a selection of possible springs for a dominant dimension in either vertical or horizontal direction. A spring in postbuckling depends much on its geometric boundary conditions [182] and requires prestressing. A metal bellow [183] requires a large height for the required small stiffness of $K=\omega_0^2 m$ so that at low frequencies internal resonance frequencies in bending are introduced. Since the resonance frequencies of all remaining spring versions are not beyond the upper bandwidth limit of 1kHz the internal stress becomes the decisive criterion. All spring versions also have a very small weight so that the internal resonance

| postbuckling | metal bellow | 3 leaves | 2 leaves membrane |
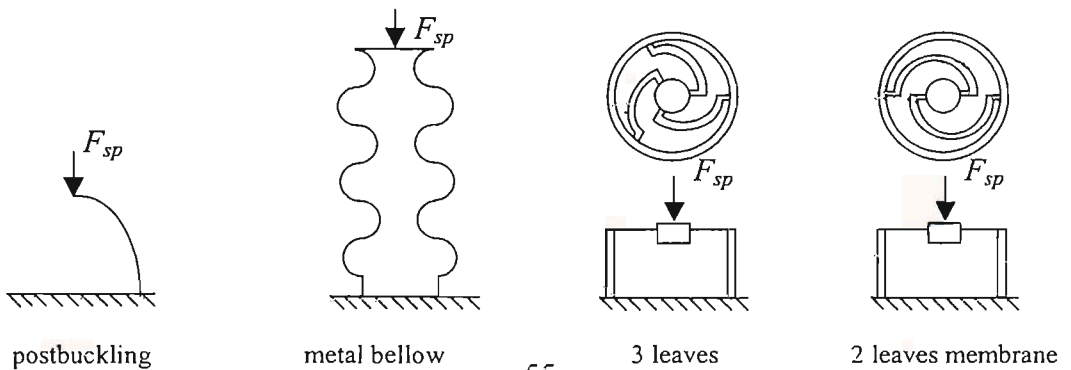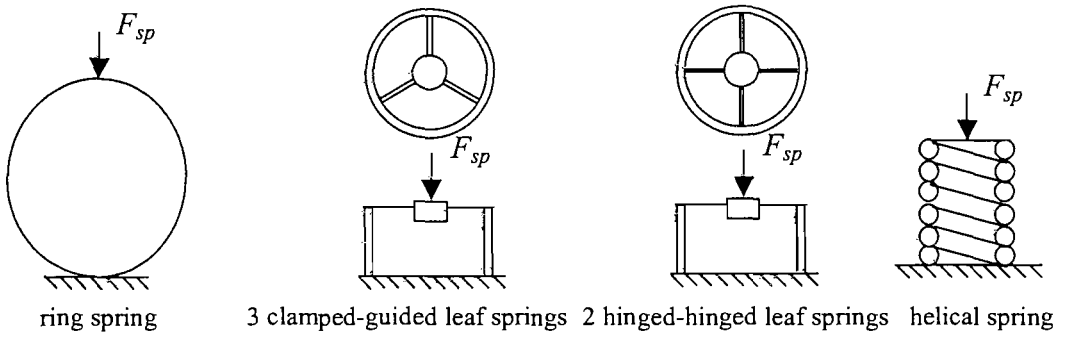
Figure 3.7: *Different options for the suspension of the moving mass with suspension force F_{sp}.*

frequencies are estimated to not be very important. Different membrane springs are not considered here since FEAs have shown that high internal stresses are induced at these dimensions and strokes.For other spring types there are analytical expressions for the maximum internal stress. Three ring springs of radius R with a Young's modulus E_s that are used to generate a stiffness K have a maximum internal stress [184]

$$\sigma_d = \frac{0.318R\left(I_d 4/\pi\right)^{0.25} 0.2}{3I_d} \tag{3.12}$$

with $I_d = \dfrac{3R^3 K}{20 E_s 3}$. Three clamped-guided leaf springs used to generate the same stiffness have an internal stress

$$\sigma_b = \frac{0.2R\left(I_b 4/\pi\right)^{0.25}}{3I_b} \tag{3.13}$$

with $I_b = \dfrac{R^3 K}{12 E_s 3}$. The maximum internal stress in two hinged-hinged leaf springs is

$$\sigma_c = \frac{0.2R\left(I_c 4/\pi\right)^{0.25}}{2I_c} \tag{3.14}$$

with $I_c = \dfrac{(2R)^3 K}{48 E_s 2}$. Theoretically instead of three clamped-guided springs three ideal cantilever springs are considered for comparison only. They cannot be implemented here

because in this case the centre needs to be guided in vertical direction. Three ideal cantilever beams would have a maximum stress of

$$\sigma_a = \frac{0.2R\left(I_a 4/\pi\right)^{0.25}}{3I_a}$$ (3.15)

with $I_a = \frac{R^3 K}{3E_s 3}$. For a constant moment of inertia it is clear that ring springs have the smallest internal stress followed by three ideal cantilever beams and three clamped-guided springs. Two hinged-hinged leaf springs are worst. However, as mentioned before three ideal cantilever beams cannot be implemented since the inertial mass needs to be guided in vertical direction. Figure 3.8 shows the internal stress in the springs as function of the spring radius for a fundamental resonance frequency of 20Hz and beryllium copper springs. In comparison to two hinged-hinged leaf springs or cantilever beams three ring springs have a lower internal stress at all diameters. Three clamped-guided leaf springs show the highest internal stress. Also in comparison to 3 leaves and 2 leaves membranes ring springs have a lower internal stress. The results of a verification using FEA for possible designs are indicated with a star * and a plus + and they even indicate smaller values with the ring springs more favourable than the next best 2 leaves membrane. Only helical springs show a smaller internal shear stress, but the material yield strength against torsion is much smaller than for bending. Additionally resonance frequencies of helical springs are not well known [185] and they require pre-stressing in order to be used.
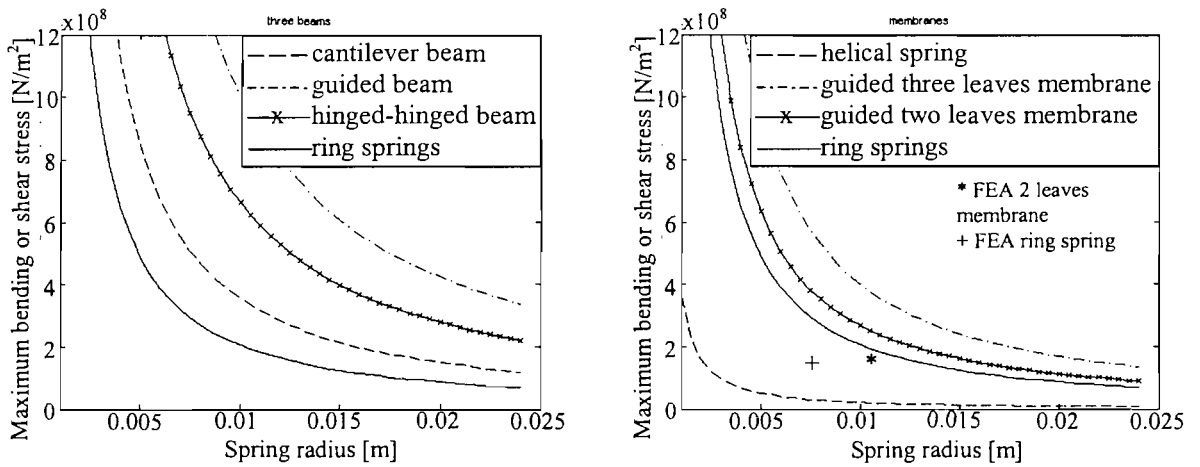
Figure 3.8: *Internal stress at* 316N/m *suspension stiffness as function of spring radius and for various spring configurations, material: beryllium bronze.*

In addition Table 3.2 shows some resonance frequencies of selected spring versions calculated by a FEA and compatible to the electromagnetic circuit design. Although non of the first resonance frequencies lies beyond 1kHz ring springs seem to have the highest

resonance frequencies. Because of the small weight of the suspension none of the internal resonance frequencies should have a substantial effect at low frequencies. Hence, ring springs are used for the suspension although the actuator becomes a bit bigger in diameter.

Table 3.2: *First four internal resonance frequencies of various spring versions in Hz.* [57]

Spring	1st res. freq.	2nd res. freq.	3rd res. freq.	4th res. freq.
Ring	652	855	2263	2341
Two leaves	187	749	1540	2643
Trefoil	254.56	362.34	362.43	759.39
Spiral	165	290	309	395

Figure 3.9 shows the inertial mass as a light shape with ring springs designed for a resonance frequency of 20Hz at its outer diameter. The dark shape shows the deformation shape at the main vertical resonance frequency that is predicted to lie at about 30Hz. The FEA shows that the resonance frequency is different from the one predicted with formulae from [184] because the boundary conditions at the connection point with the environment have a big influence. Additionally a rotary resonance frequency at 34 Hz is simulated with a FEA. It should not be important for vibrations in vertical direction because of the small weight of the springs. Simulations also show that it is vital to restrict the vibration into vertical directions by using an appropriate guide since there is a number of modes in the frequency range between 40Hz and 1kHz that might be excited.
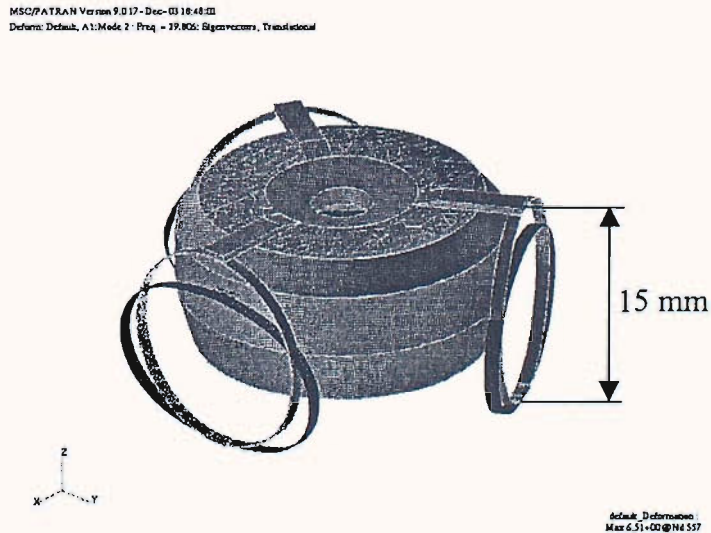
Figure 3.9: *1st mode shape if centre is constraint to only move in z direction; dark: deformed shape; light: not deformed shape.*

In combination with the inertial mass the internal resonance frequencies of the ring spring itself lie at frequencies beyond 1kHz for a rigid connection to ground, but they shift to

lower frequencies if boundary conditions change. The rotary resonance frequency can be found at very low frequencies (3Hz) if the ring spring is connected to the ground by just one element.

3.1.4 Self-sensing design

It has been found in the previous chapter that the self-inductance of the coil should be as small as possible in order to allow a large control bandwidth. Also, in Appendix B it is shown at the example of an actuator model with a single mechanical degree of freedom that the transducer coefficient should be big to allow critical damping. But both the self-inductance and the electrodynamic transducer coefficient (the Bl product) increase with the number of coil windings and depend on the material properties of the magnetic circuit. Hence, the increase in electrodynamic transducer coefficient, increasing sensing sensitivity, and decrease in self-inductance, increasing sensing bandwidth, have to be balanced. For a required bandwidth there is a maximum sensitivity.

Moreover in Section 2.4 it has been shown that the internal coil resistance determines the amount of positive current feedback, i.e. negative resistance, required. Figure 3.10 shows the root locus of the FRF between the vibration velocity V_S and the input voltage to the actuator U_{fb} for an actuator model with a single mechanical degree of freedom as in Appendix B [31].
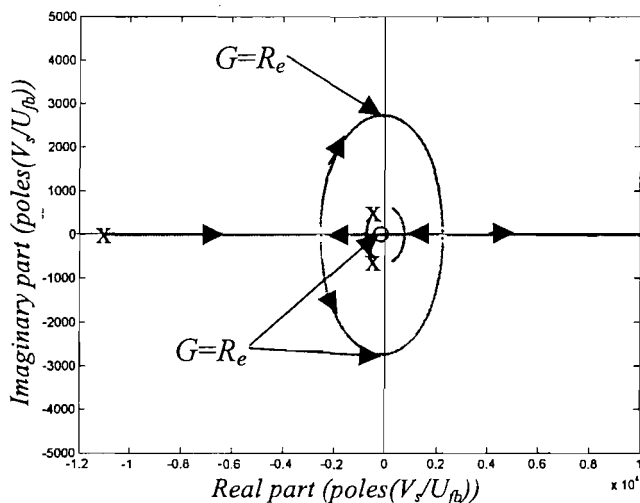
Figure 3.10: *Root locus plot of the FRF between the actuator vibration velocity V_s and the actuator input voltage U_{fb} for positive current feedback gains $G=1$ to 2000 and an actuator model as in Appendix B.*

When the positive current feedback gains are bigger than the coil resistance R_e the poles of the FRF move into the right half-plane and the actuator becomes unstable. The bigger the

resistance relatively less important are small variations in the feedback gain and the feedback loop is more robust. In conclusion, the higher the internal coil resistance the higher active feedback gains and hence power consumption and the higher also robustness. Therefore power consumption and robustness also have to be balanced.

As an alternative to a self-sensing electrodynamic actuator an electrodynamic actuator with primary driving and secondary sensing coil is proposed and schematically shown in Figure 3.11. The primary driving coil could be designed for minimum power consumption by choosing a small resistance whereas the secondary coil could be designed for a high sensing bandwidth with relatively high resistance and small inductance.
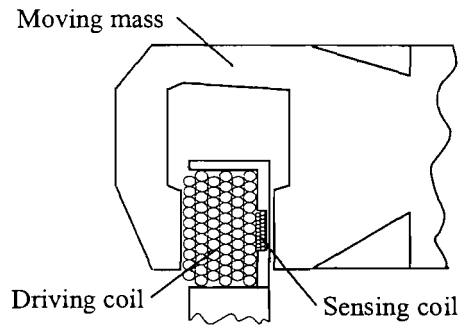
Figure 3.11: *Cross section sketch of moving, inertial mass and coils.*

However, since both coils are aligned a current in the driving coil I_c will also induce a voltage

$$U_s = \frac{N_s A_s \mu N_p}{h_p} j\omega I_c \tag{3.16}$$

in the secondary coil depending on the number of windings of the secondary coil N_s and the primary coil N_p, the cross section of the secondary coil A_s, the height of the primary coil h_p and an equivalent permeability of the magnetic circuit μ. Because of the velocity of the inertial mass relative to the coil the induced voltage in the secondary coil is given by

$$U_{inds} = \pi \left(A + 2t + s \right) N_s B_g j\omega d \ . \tag{3.17}$$

This voltage induced in the secondary coil is bigger than the voltage U_s due to the coupling between the two coils if

$$I_c < \frac{4B_g h_p d}{(A + 2t + s)\mu N_p} \qquad (3.18)$$

This equation shows that for high displacements and low driving currents the sensing coil can be used effectively. Geometric values can only be adjusted partially because they also influence the transducer coefficient that should be as big as possible for a high sensitivity. Validation measurements should show whether a better balance between sensitivity and bandwidth could be achieved. Power consumption can be reduced without compromising robustness since the driving coil can be designed for small power consumption without affecting the robustness of the sensing coil.

3.2   Validation

In order to validate the simulated actuator characteristics a prototype actuator and the driving and sensing electronics have been designed and manufactured. Design drawings can be found in reference [57] and an exploded top view of the prototype is shown in Figure 3.12. An axis with bushings in the centre guides a moving mass that comprises the magnetic circuit and that is suspended by three ring shaped springs. An upper cover and lower cover protect the assembly and prevent any small particles from intruding and blocking the air gap. The lower cover is also used as the former for the primary and the secondary coils. The ends of the coil wires are guided through the lower cover via cable seals and they are electrically connected to a connector plate for easy connection to the electrical driving and sensing circuits. Tight tolerances have to be respected for some parts and the most important manufacturing issues are summarized in Appendix D. Figure 3.13 shows the final result without upper cover on a plate. In order to prevent the inertial mass from leaving the central axis a copper sheet is glued to its upper ending. It has been found that in a laboratory environment small particles do not pose a threat to the actuator so that the upper cover is removed for most experiments. Characteristic values are compiled in Table 3.3.
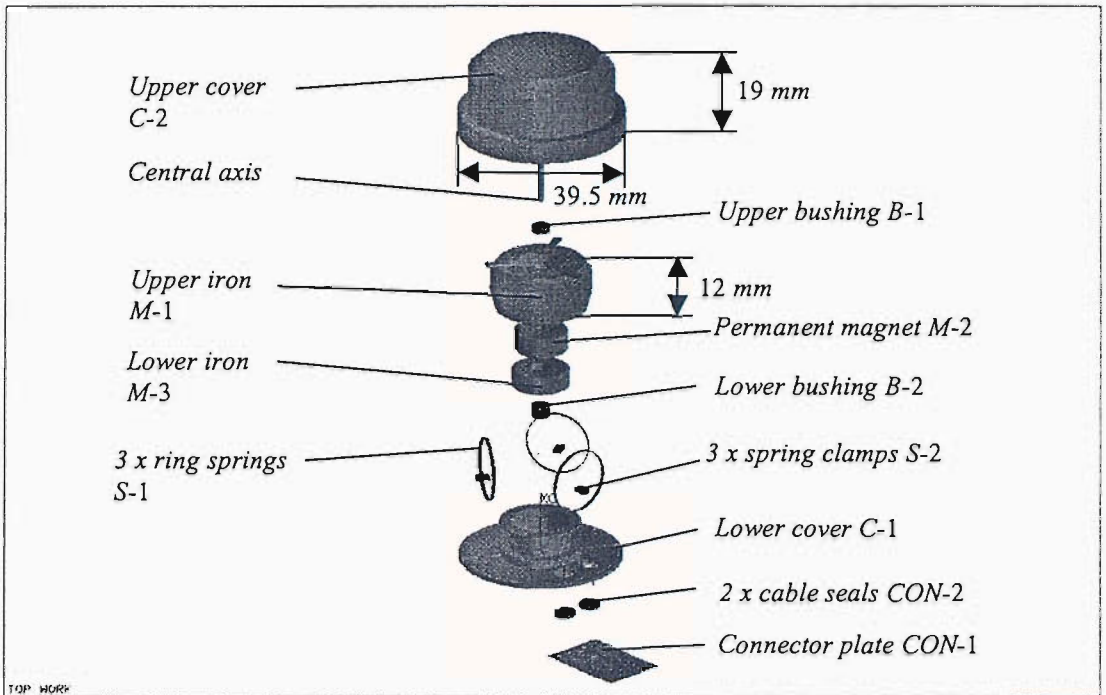
Figure 3.12: *Exploded top view of the designed actuator.*
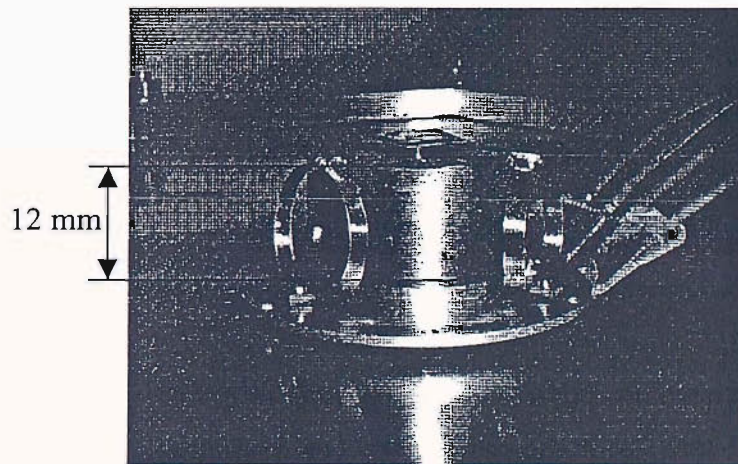
Figure 3.13: *Photograph of the miniaturised, inertial actuator without cover.*

This section deals with the validation of some characteristics of the prototype inertial actuator. The dimensions and mass values given in Table 3.3 have been taken during the assembly of the actuator. Subsection 3.2.1 deals with the electrical parameters, e.g. coil resistance, maximum electrical input power and transducer coefficient. In Subsection 3.2.2 the mechanical behaviour with special focus on the suspension is determined. The final Subsection 3.2.3 investigates the internal velocity sensor in more detail.

Value	Description
0.0395m	overall diameter
0.0207m	overall height
0.019m	diameter of the flange
0.0017m	height of the flange
0.046kg	total mass
0.012kg	mass of the lower cover and coils
0.012kg	mass of the upper cover
0.022kg	approximate moving mass
~2.5N/A	primary transducer coefficient
~2.2W	maximum DC power input
~2.5N	maximum continuous actuation force, $\Delta T = 60°C$
~4.2N	peak actuation force, 10 sec.
+/-0.002m	maximum stroke
~22Ω	secondary coil resistance
~1.8Ω	primary coil resistance

3.2.1 Electrical Characteristics

In order to obtain an idea about reasonable current and voltage inputs the maximum electric power input is measured. It is limited by heating of the actuator [65]. The actuator is placed into a closed box to allow only a small, constant heat exchange with the environment, i.e. quasi adiabatic conditions. A DC voltage is applied to the actuator so that the inertial mass does not move from a reached equilibrium position. Therefore no induced voltage disturbs measurements. A voltmeter in parallel and an ammeter in series to the actuator measure voltage and current. The product of voltage and current gives the input power and the ratio of voltage and current gives the internal resistance R_0 of the actuator at DC. When higher power values are input into the actuator it is heated up by ΔT and as a result the value of the resistance changes by

$$\Delta R_e = R_0 \alpha_{20} \Delta T \qquad (3.19)$$

where $R_0 = 1.68\Omega$ is the resistance at 20°C and $\alpha_{20} = 4.3 \times 10^{-3} 1/K$ is the linear temperature coefficient of the specific resistance of copper [176]. By measuring the increase in resistance the temperature increase is determined. Measurements are carried out for several DC voltages i.e. power inputs. The measured temperature increase and power input results are plotted in Figure 3.14. The dissipated power is assumed to be proportional to the rise in

temperature [180] so that a line may be used to extrapolate the measurement points (circles) for which an increase in temperature is measured. Thus, information about the input power at temperatures close to the material limit is obtained without risking destroying the actuator. Different points at a similar power input indicate that small changes are possible even when having waited over an hour until a stabilisation of the voltage and current.
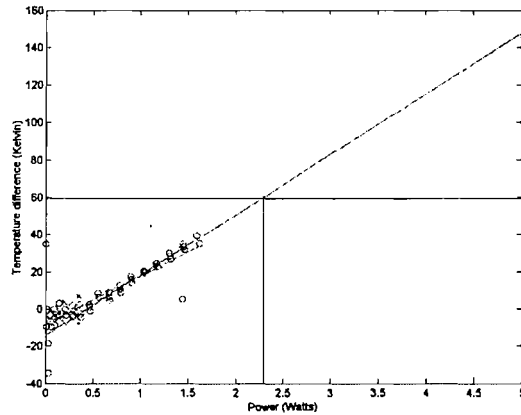
Figure 3.14: *Measured (o) and extrapolated (-) temperature increase of the driving coil for different DC power inputs.*

This is due to the influence of the environment that could not completely be eliminated, which indicates that the test has not been carried out under adiabatic conditions. In particular only small differences in the temperature of the environment lead to a different 0K position as is shown by measurement points marked by a cross and a dot in Figure 3.14. Assuming an environmental temperature of 20°C an increase by about 60K in the wire is acceptable since the supplier of the permanent magnet material gives a temperature limit of 80°C [178]. Hence, a maximum input power of 2.2 Watts at an input current of 1.1A is predicted. Higher temperatures are possible with reversible change of the demagnetisation line to lower H values since the knee of the demagnetisation curve of the permanent magnet lies far in the 3rd quadrant. An ultimate limit with reduction of the static magnetic field in the air gap is given by the melting temperature of the wire insulation at 155°C leading to a short term ultimate power input limit of about 4.7Watts or a current input limit of 1.33A.

The transducer coefficient of the primary driving coil is determined by adding a known weight on top of the moving mass and increasing the coil current until the top mass moves to an equilibrium position. Careful manual adjustment is necessary since small changes in the current may move the mass from its equilibrium position. The measurement is carried

out for several current inputs from 0A to the 1A close to the current limit since the current at the equilibrium position is difficult to find with just one measurement. The average transducer coefficient is found to be 2.52 N/A where a maximum mass of 247g is lifted to an equilibrium position at about 1A DC input. Together with the current and power limits for 60K and 135K temperature increase a maximum continuous actuation force F_a=2.7N and a maximum 10s peak force F_{ap}=4.2N are predicted, when the actuator resistor does not have time to heat up. These values are only approximate as for example the driving coil resistance is 1.8Ω when measured with a conventional Ohmmeter instead of 1.68Ω. The force values approximately agree with the prediction in Table 3.2, when considering a power input of 2.2 W instead of 1W.

3.2.2 Mechanical Characteristics

In order to characterize the dynamic, mechanical behaviour of the actuator the FRF between the primary current, proportional to the actuation force, and the transmitted force is measured. Ideally this FRF should look like the one in Figure 1.3 with a -180° phase shift at the spring-mass resonance frequency and no further internal suspension dynamics. The set-up depicted in Figure 3.15 is used to measure the FRF at the prototype with a PCB208 force transducer below the actuator and a measurement resistor in series to the actuator. The electronics of the used ICP force transducer incorporate a high pass filter at lower frequencies so that only measurements above approximately 10Hz are related to the mechanics of the actuator. Therefore a sine sweep voltage between 10Hz and 10kHz is input to the actuator. As explained in Appendix F this is different from the excitation method in Chapters 2, 4 and 5 where a white noise signal band limited at 1kHz is used.
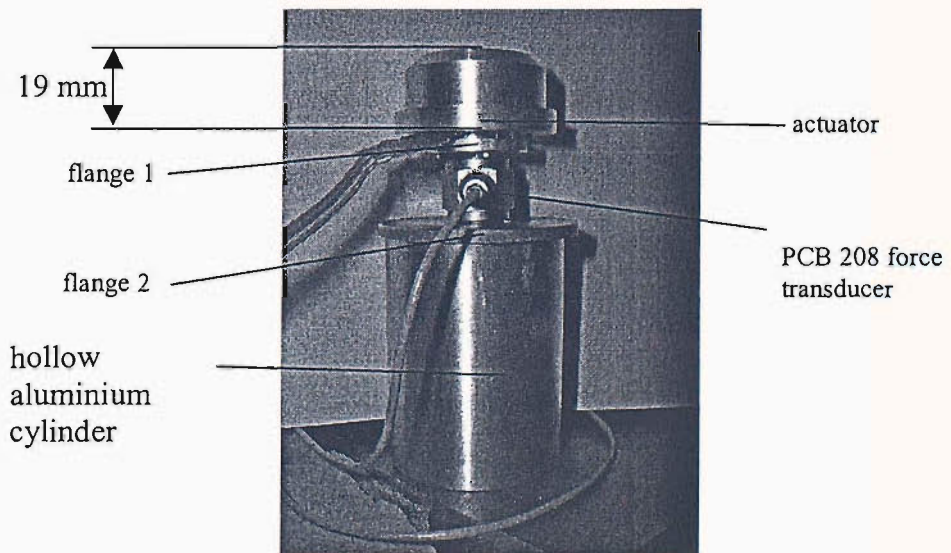
Figure 3.15: *Set-up for the measurement of the FRF between the primary current I_c and the transmitted force F_t.*

65

The phase plot of the measured FRF, shown in the lower half of Figure 3.16, hints at the expected -180° phase shift from +180° to 0°. Since the actuator is well damped the fundamental resonance is not as peaky as simulated in Figure 1.3. At about 25Hz a very small influence of a secondary resonance appears that possibly is the main rotational resonance about the z-axis predicted in simulations. Then a flat response up to about 1kHz follows indicating that internal spring resonance frequencies are of small importance. For higher frequencies the stiffening effect of the upper cover plays a role. In Figure 3.16 the thick solid line indicates measurements without upper cover C-2 and the faint solid line is from measurements with mounted upper cover C-2. There is an additional resonance frequency at about 3200Hz that is shifted to about 3500 Hz when the cover stiffens the actuator. Higher resonance frequencies shown in Figure 3.16 are not shifted by the cover.
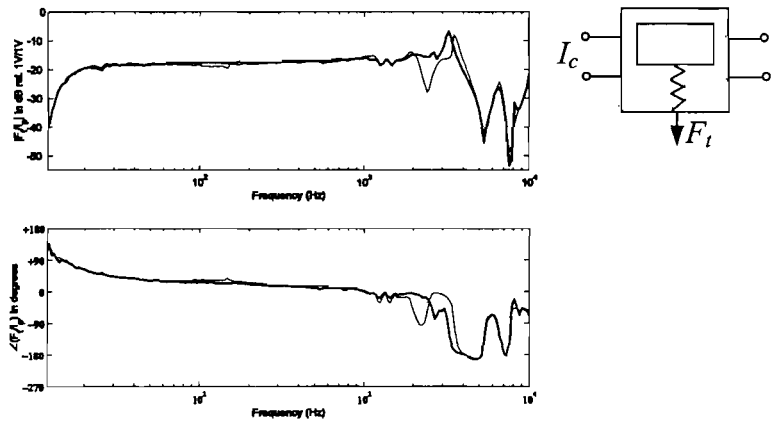
Figure 3.16: *FRF between primary current I_c and transmitted force F_t with upper cover (faint solid line) and without upper cover (thick solid line).*

Another resonance anti-resonance combination appears at 2000Hz when the cover is mounted. The exact positions of these resonance frequencies depend on the mounting of the actuator relative to the force transducer, but they usually lie beyond 1kHz. In particular it is not absolutely clear in how far resonances of the chosen set-up in Figure 3.15 interfere. For active vibration control a high order low-pass filter at about 1kHz is recommended in order to limit the control bandwidth. For higher excitation currents there is stroke saturation around the spring-mass resonance below 15Hz since the moving mass hits the cover. In order to prevent this effect further damping could be added to the fundamental resonance for example by using feedback of the velocity signal in the secondary coil.

3.2.3 Internal velocity sensor

As shown in Figure 3.11 a secondary sensing coil aligned to the primary driving coil has been included in the actuator so that the self-sensing approach potentially is not limited by the self-inductance of the primary coil.

As will be explained in more detail in Chapter 4, Eq. (4.42), the voltage in the secondary coil U_s per current input in the primary coil I_c is

$$\frac{U_s}{I_c} = \frac{L_{sp}j\omega + \dfrac{\Psi_s \Psi_p}{1/Y_m + Z}}{1 + \left(L_s j\omega + \dfrac{\Psi_s^2}{1/Y_m + Z} \right)/Z_s} \tag{3.20}$$

where L_{sp} is the mutual coupling inductance between the primary and the secondary coil, L_s is the self-inductance of the secondary coil, Z_s is the electrical input impedance of the sensing circuit connected to the sensing coil and Ψ_s and Ψ_p are the transducer coefficients of the secondary and the primary coil. Neglecting the self-inductance of the secondary coil L_s this FRF is simulated as a bold dashed line in Figure 3.17 for parameter values compiled in Table 3.4. Several parameter combinations lead to a similar curve in Figure 3.17 and the chosen combination need not necessarily be the most physical one. The parameter estimation does not explicitly include the fact that the driving current amplifier might add negative damping because of positive current feedback.
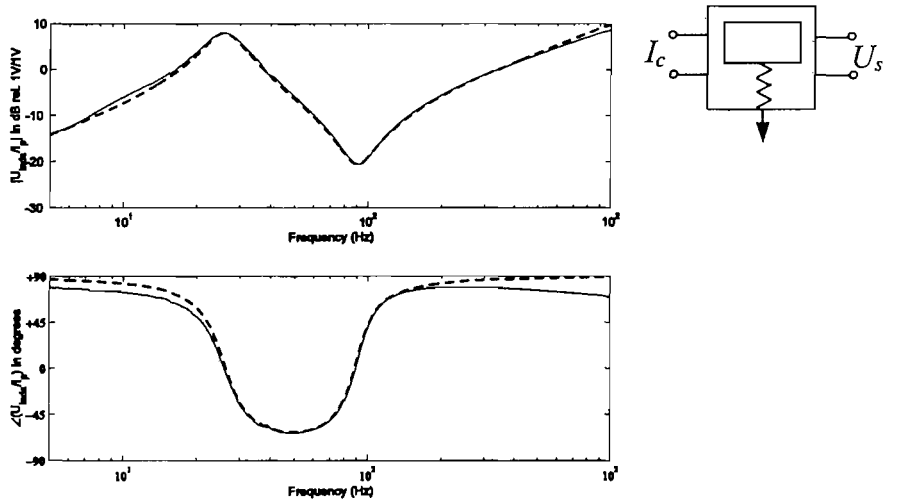
Figure 3.17: *FRF between the primary current I_c and the secondary coil voltage U_s without upper cover and with stiff suspension.*

Measurements and simulations fit well in the important frequency range around the fundamental resonance of the actuator, for this spring version at about 25Hz, and the anti-resonance frequency due to the coupling inductance at about 90Hz. The fundamental resonance frequency of the actuator is different from the one measured in Figure 3.16 because of a slightly different installation of the clamps and spring geometry. For higher frequencies neglecting the self-inductance of the secondary coil, core losses [186] or non-linear effects [187] lead to differences due to the permanent magnet and the iron within the coil. Figure 3.17 clearly shows that the sensing bandwidth is limited by the coupling between the secondary and primary coil that gives a limit at about 100Hz. Measurement bandwidth could be increased by compensating for direct feed through between the coils with a circuit similar to the one described in [33] for self-sensing actuators.

Table 3.4: *Parameter values used for simulations in Fig.* 3.17.

Parameter	Value	Description
Z_s	-0.57Ω	Resistance of secondary coil and measurement equipment
L_{sp}	0.0005H	Coupling inductance
M	0.0203kg	Weight of the moving mass
D	3.5Ns/m	Damping factor
K	540N/m	Spring stiffness
Ψ_p	2.6N/A	Transducer coefficient of the driving coil
Ψ_s	1.146N/A	Transducer coefficient of the measurement coil

3.3   Summary

This chapter has discussed practical issues related to the design and validation of a lightweight, electrodynamic, inertial actuator prototype. An investigation of the mechanical part has shown that the fundamental resonance of the actuator constitutes a low frequency bandwidth limit due to the high-pass filter behaviour of the inertial actuator (IA). Also, stroke saturation has to be considered at lower frequencies that also limits the achievable transmitted force on the structure. Considering an actuator with an inertial mass of 0.02kg for a transmitted force of 4N a stroke of 0.002m is expected to be sufficient. A challenge for the electrodynamic design is to generate a high electromagnetic actuation force of 4N at the given inertial mass. A finite element analysis has given a relation between the actuation force and the inertial mass by investigating a large number of different geometrical parameter values. An electromagnetic circuit with maximum actuation force at a given inertial mass has been chosen where the magnetic field in the air gap is rather small and the amount of wire is rather big. Because of the high magnetic field a large transducer coefficient and big self-inductance result. This increases sensitivity of self-sensing control,

but also decreases self-sensing control bandwidth as is also illustrated in Appendix B. A challenge for the suspension is to allow a low stiffness, in order to guarantee the necessary low fundamental resonance frequency for a given small inertial mass, at a high stroke of 0.002m and acceptable internal stress. Additional internal resonance frequencies of the suspension should lie beyond 1kHz. Ring springs have been chosen that guarantee a low resonance frequency at compatible dimensions and acceptable mechanical internal stress. Moreover an alternative to self-sensing (ss) control has been incorporated in the prototype by using a secondary sensing coil. The validation study has shown that the best electrodynamic design has been approximately achieved since a transducer coefficient of 2.5N/A approximately corresponds to a predicted low magnetic field of about 0.2T in the air gap. Additionally a continuous power input of 2.2 W or up to an approximate peak of 5W means a required continuous force of 2.2 N or a 4.2N peak force. The frequency response has been found to show the fundamental resonance at about 20Hz, that could be reduced to about 13Hz using spring steel instead of beryllium copper. Only a very small influence of a rotational resonance is visible at about 20Hz and all unfavourable resonance frequencies lie beyond 1kHz. The validation of the secondary sensing coil has shown that suitable relative velocity measurements can be carried out below about 100Hz without being limited by the mutual coupling inductance between the primary and secondary coil.

In conclusion, the prototype of a lightweight (34grams), inertial actuator has been designed and manufactured that can be used in a broad frequency range for practical applications and especially the model problem used in this study. It also incorporates an alternative secondary sensing coil whose bandwidth is not limited by the self-inductance of the primary coil, that reduces tuning effort and that allows current driving of the primary coil.

A further miniaturization of an electrodynamic, inertial actuator down to microscale dimensions is investigated in Appendix C.

4. VIBRATION CONTROL OF A PLATE WITH AN INERTIAL ACTUATOR

In the previous section the design and construction of a new lightweight electrodynamic, inertial actuator (IA) has been discussed in detail. In this section the performance of this prototype self-sensing, inertial actuator (SSIA) is investigated with special focus on how it can be used for active damping on the model problem considered in this study. As for the reactive configuration studied in Chapter 2, collocation - duality and the self-sensing behaviour at higher frequencies are considered in this chapter. Additionally internal direct velocity feedback with the secondary sensing coil as internal velocity sensor (IVS) and an alternative to self-sensing is considered. Special focus is on its behaviour at higher frequencies. For completeness the effect of passive control in addition to active control is also highlighted.

The reference cases ideal internal and ideal external direct velocity feedback are investigated where either the relative velocity between the inertial mass and the base of the actuator or just the plate velocity are fed back. Then a practical implementation of external direct velocity feedback with an accelerometer sensor and the lightweight, electrodynamic, inertial actuator (IA) is studied. Internal direct velocity feedback is implemented using a self-sensing configuration of the IA. There are several ways of generating broadband damping with self-sensing electrodynamic inertial actuators (SSIA) mounted on structures, for example using:

1) Eddy currents
2) a shunted resistance
3) proportional current feedback
4) induced voltage feedback without inductance compensation
5) induced voltage feedback with inductance compensation.

1) and 2) are passive ways, whereas 3) to 5) are active means that require an additional power source. Complexity of the control circuit increases from 1) to 5). As an alternative to self-sensing control additionally direct velocity feedback with the secondary sensing coil internal velocity sensor (IVS) with and without compensator for the mutual coupling inductance is considered for the implementation of direct internal velocity feedback.

Whenever possible both simulation and experimental results are shown for the model problem where the electrodynamic IA is connected to a clamped plate at the same position where the control RA described in Chapter 2 was mounted. As schematically shown in Figure 4.1 a primary force is generated on the panel in such a way as to excite most of the low frequency resonant modes of the panel. A force transducer measures the primary force and a velocity sensor measures the plate velocity to be reduced.
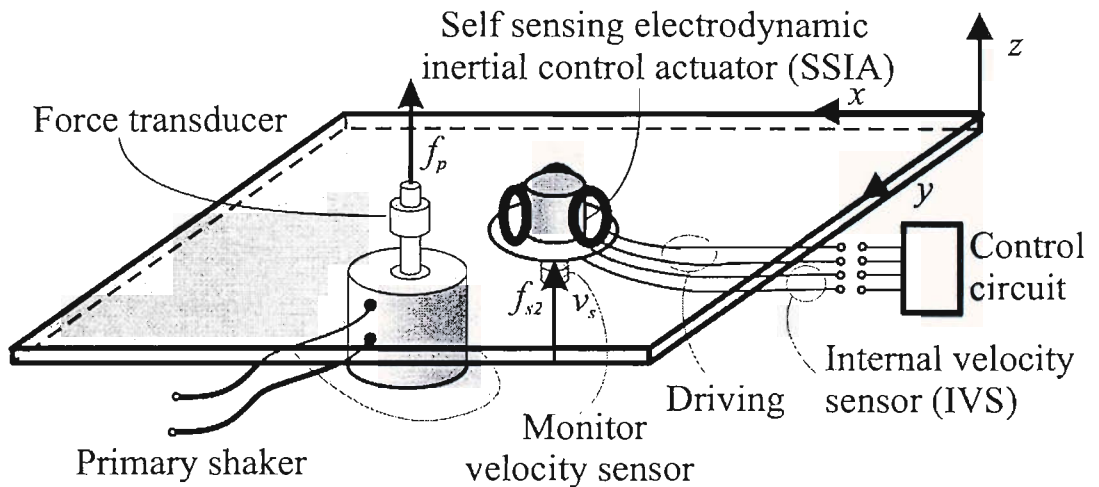
Figure 4.1: *Sketch of the model problem where a test panel is connected to a self sensing electrodynamic inertial actuator which is set to control the vibrations generated by a primary force disturbance.*

Section 4.1 considers an ideal inertial force actuator and a) an ideal external velocity sensor mounted at the base of the actuator in order to implement external velocity feedback or b) an ideal internal velocity sensor that measures the relative velocity between the base and the inertial mass of the actuator in order to implement internal velocity feedback. The effect of Eddy currents is also considered. As a reference case Section 4.2 investigates direct external velocity feedback with the lightweight, electrodynamic, inertial actuator and an accelerometer sensor. Both current command and voltage command of the inertial actuator are considered in simulations and measurements. Sections 4.3 to 4.6 contrast simulated and experimental results with a shunted resistor, positive current feedback and induced voltage feedback with and without inductance compensation. Sections 4.7 and 4.8 focus on internal velocity feedback with a secondary sensing coil with and without inductance compensation. In each section first the model is presented and the FRFs for the general control framework shown in Figure 1.2 are given. Second the stability of the feedback control schemes is investigated with reference to the open loop sensor-actuator response function. Finally the active damping performance is evaluated considering the vibration reduction of the panel at the control position with reference to the primary disturbance force. If different from simulations measured vibration reduction is considered.

4.1 Direct velocity feedback

This section presents a model of an inertial actuator mounted on a plate and shows simulations regarding stability and performance of direct internal and external velocity feedback. The model considers an ideal actuation force, ideal current command amplifier and ideal plate velocity or relative velocity sensors. In comparison to the simulations presented in Chapter 2 the effect of the inertial actuator is assessed.

4.1.1 Model

The same model problem as in Chapter 2 is considered in order to illustrate the active damping effects produced by a self-sensing, electrodynamic inertial actuator connected to the panel. The material and geometrical properties of the panel test rig and self-sensing inertial actuator valid for Sections 4.1 to 4.6 are summarised in Table 4.1. In comparison to the model presented in Chapter 2 viscous instead of hysteretic damping is assumed so that non-dimensional damping can be adjusted for each mode individually.

Table 4.1: *Parameter values used for simulations in Section 4.1 to 4.6.*

Para-meter	Value	Description	Para-meter	Value	Description
l_x	0.414m	Plate length	ρ	2700kg/m^3	Mass density of plate
l_y	0.314m	Plate width	K_1	1.2037	Coefficient to adjust for boundary conditions
h	0.001m	Plate thickness	K_2	0.7042	Coefficient to adjust for boundary conditions
x_p	0.345m	X coordinate of primary shaker	$\zeta_{1,n}$	0.01	Viscous damping coefficient
y_p	0.254m	Y coordinate of primary shaker	$\zeta_{2,12,19,20,22}$	0.04	Viscous damping coefficient
x_s	0.225m	X coordinate of control actuator	ζ_3	0.0001	Viscous damping coefficient
y_s	0.12m	Y coordinate of control actuator	$\zeta_{4,30}$	0.1	Viscous damping coefficient
ζ_{11}	0.08	Viscous damping coefficient	R_e	1.8Ω	Resistance of actuator coil
ζ_{28}	0.02	Viscous damping coefficient	L_e	1.4mH	Inductance of actuator coil
ζ_{38}	0.001	Viscous damping coefficient	R_1	1/26/1/7.2Ω	Shunted/ Measurement resistor
E	71 10^{9}N/m^2	Young's modulus of plate	R_2	1Ω	Bridge resistor 2
v	0.33	Poisson's ratio	R_1	1.8Ω	Bridge resistor 1
M_p	0.028kg	Added force transducer mass	C	0.1μF	Capacitance of Owens bridge
M	0.01kg	Housing mass of inertial actuator	R_3	$L_e/Z_1C\times1.5$	Resistance of Owens bridge
m	0.0203kg	Moving mass of inertial actuator	Ψ_p	2.6N/A	Transducer coefficient of actuator
K	135N/m	Suspension stiffness			
D	1 or 0.3 Ns/m	Suspension damping			

As in Chapter 2 the steady state response of the panel has been derived assuming harmonic disturbances and responses. The phasor of the complex velocity at the error sensor, $V_s(\omega)$,

can be expressed in terms of the phasors of the primary, $F_p(\omega)$, and secondary, $F_{s2}(\omega)$, force excitations with the following mobility relation

$$V_s = Y_{sp}F_p + Y_{ss}F_{s2} \qquad (4.1)$$

where the two mobility functions, $Y_{sp}(\omega)$ and $Y_{ss}(\omega)$, have been derived with the following modal expansions

$$Y_{sp} = j\omega \sum_{n=1}^{N} \frac{\phi_n(x_s, y_s)\phi_n(x_p, y_p)}{\rho l_x l_y h \left[\omega_n^2 + 2\xi_n \omega_n j\omega - \omega^2 \right]} \quad Y_{ss} = j\omega \sum_{n=1}^{N} \frac{\phi_n(x_s, y_s)\phi_n(x_s, y_s)}{\rho l_x l_y h \left[\omega_n^2 + 2\xi_n \omega_n j\omega - \omega^2 \right]} \qquad (4.2)$$

where ξ_n is the viscous damping factor of the nth-mode. In contrast to the model in Chapter 2 an individual damping factor can be associated to each mode so that a better fit between simulations and measurements is expected. The secondary force at position (x_s, y_s) is generated by the electrodynamic inertial actuator that reacts against a moving mass m suspended on a spring with stiffness K and damping D'. Because of the mass of the actuator housing and the moving coil M the point mobility of the plate at the control position (x_s, y_s) is modified to be $Y'_{ss} = \dfrac{Y_{ss}}{1 + j\omega M Y_{ss}}$. Considering the lumped parameter model of the actuator shown in Figure 4.2 the velocity of the actuator mass m is given by

$$V_a = Y_m F_{s1} \qquad (4.3)$$

where $Y_m = 1/(j\omega m)$ is the mobility of the actuator mass and F_{s1} is the force between the actuator mass m and the actuator suspension. The transmitted force on the plate and by the actuator mass are combined in a vector

$$\mathbf{f}_s = \left\{ \begin{matrix} F_{s2} \\ F_{s1} \end{matrix} \right\} = - \begin{bmatrix} Z & -Z \\ -Z & Z \end{bmatrix} \left\{ \begin{matrix} V_s \\ V_a \end{matrix} \right\} + \left\{ \begin{matrix} F_a \\ -F_a \end{matrix} \right\} = -\mathbf{Z}\mathbf{v}_s + \mathbf{f}_a \qquad (4.4)$$

where $Z = \dfrac{K}{j\omega} + D'$ is the impedance of the coil suspension system here modelled as a stiffness K and viscous damper D' in parallel to an actuation force $\mathbf{f}_a = \left\{ \begin{matrix} F_a \\ -F_a \end{matrix} \right\}$.
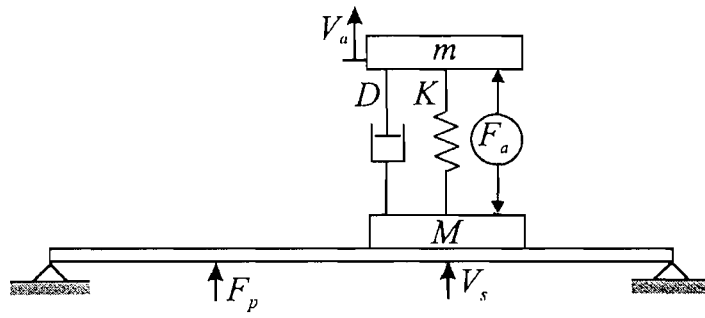
Figure 4.2: *Schematic plate model with disturbance force F_p, inertial actuator with parameters m, M, K and D and secondary velocity sensor V_s.*

Taking into account the mass and suspension effects of the inertial actuator, Eq. (4.1) is modified to become

$$\mathbf{v}_s = \left(\mathbf{I} + \mathbf{Y}_{ss}^m \mathbf{Z}\right)^{-1} \mathbf{y}_{sp}^m F_p + \left(\mathbf{I} + \mathbf{Y}_{ss}^m \mathbf{Z}\right)^{-1} \mathbf{Y}_{ss}^m \mathbf{f}_a \tag{4.5}$$

where the transfer and point mobility matrices are $\mathbf{y}_{sp}^m = \begin{Bmatrix} Y_{sp} \\ 0 \end{Bmatrix}$, $\mathbf{Y}_{ss}^m = \begin{bmatrix} Y_{ss}' & 0 \\ 0 & Y_m \end{bmatrix}$, $\mathbf{v}_s = \begin{Bmatrix} V_s \\ V_a \end{Bmatrix}$

and $\mathbf{I}$ is a 2x2 identity matrix. Even when there is no explicit feedback force the actuation force

$$F_a = \Psi_{ec} I_{ec} = \Psi_{ec} / R_{ec} U_{ec} = \Psi_{ec}^{\;2} / R_{ec} \{-1 \; 1\} \mathbf{v}_s \tag{4.6}$$

is proportional to Eddy currents I_{ec} generated by the induced voltage U_{ec} in the metal parts of the actuator by the motion of the moving actuator mass relative to the coil. The resulting viscous damping coefficient $D_{ec} = \Psi_{ec}^{\;2} / R_{ec}$, with equivalent transducer coefficient Ψ_{ec} and electrical resistance of the metal R_{ec}, is incorporated into the suspension damping so that a general damping coefficient $D = D' + D_{ec}$ replaces D'.

Direct velocity feedback to the actuation force can be implemented either by feedback of the plate velocity external to the actuator or by feedback of the relative velocity between the plate velocity and the velocity of the inertial mass of the actuator that is internal to the actuator.

4.1.2 External direct velocity feedback

In a first case direct external velocity feedback with a real feedback gain G leads to an actuation force

74

$$F_a = -GV_s.$$
(4.7)

Stability of direct external velocity feedback is assessed by investigating the open loop FRF

$$V_s/F_a = \{1\ 0\}(\mathbf{I}+\mathbf{Y'''}_{ss}\mathbf{Z})^{-1}\mathbf{Y'''}_{ss}\{1\ -1\}^{\mathrm{T}}.$$
(4.8)

Closed loop vibration reduction performance is then evaluated by the FRF

$$\frac{V_s}{F_p} = \{1\quad 0\}\left(1+G\{1\quad 0\}\mathbf{Y}_{ss}''\{1\quad -1\}^{\mathrm{T}}\right)^{-1}\mathbf{y}_{sp}''$$
(4.9)

for different feedback gains G where $\mathbf{Y}_{ss}'' = (\mathbf{I}+\mathbf{Y}_{ss}'''\mathbf{Z})^{-1}\mathbf{Y}_{ss}'''$ and $\mathbf{y}_{sp}'' = (\mathbf{I}+\mathbf{Y}_{ss}'''\mathbf{Z})^{-1}\mathbf{y}_{sp}'''$. Direct external velocity feedback can be put in the form of the general framework in Figure 1.1 with $Y_o = V_s$, $Y_i = F_a$ and the FRFs $G_{oi} = G_{si} = \{1\ 0\}\mathbf{Y'''}_{ss}\{1\ -1\}^{\mathrm{T}}$ and $G_{sp} = G_{op} = \{1\ 0\}\mathbf{y'''}_{sp}$.

Stability

Figure 4.3 shows the simulated open loop FRF between the actuation force and the plate velocity. The loops due to the plate modes lie in the positive real half-plane and only one loop due to the fundamental actuator resonance lies in the negative real half-plane. Therefore direct velocity feedback with inertial actuators is not unconditionally stable in contrast to direct velocity with ideal force actuators as in Section 2.1.2.
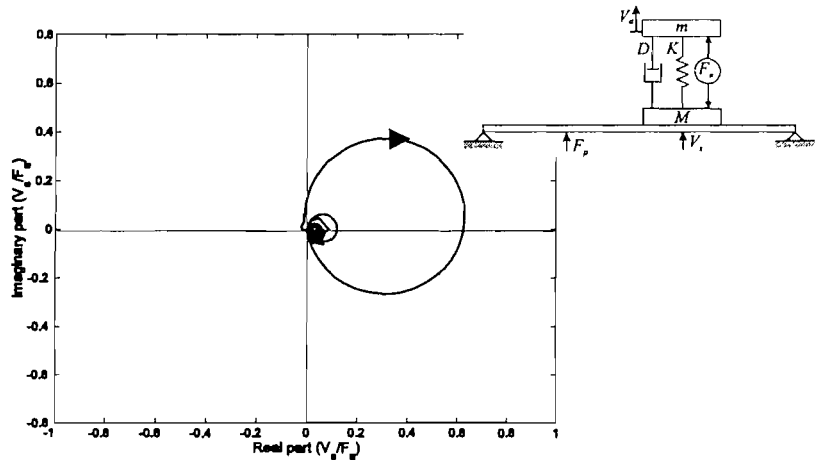
Figure 4.3: *Simulated Nyquist plot of the FRF between the actuation force and the plate velocity at the control actuator position.*

75

Additionally in the closed loop case spill-over into the fundamental actuator resonance and at slightly higher frequencies is expected. Still high vibration reduction is expected at the resonance frequencies of the plate and it would be interesting to know whether the optimum feedback gain simulated in Figure 2.6 could be implemented as is studied in the next paragraph.

Performance

Figure 4.4 shows the simulated FRF between the primary disturbance force and the plate velocity at the position of the inertial actuator in the open loop case (thick solid line) and for external velocity feedback gains of 1 (thin solid line), 5 (thick dashed line) and 50 (thin dashed line). As expected because of control spillover there is vibration amplification around the fundamental resonance frequency of the IA and vibration reduction at the plate resonance frequencies. In comparison to Figure 2.4 similar vibration reduction is possible at the plate resonance frequencies as in the optimum feedback gain case. Additionally the relative importance of modes also changes. However, the optimum gain is close to the stability limit so that robustness is no longer guaranteed. High vibrations at the fundamental resonance may also lead to stroke saturation and fatigue problems.
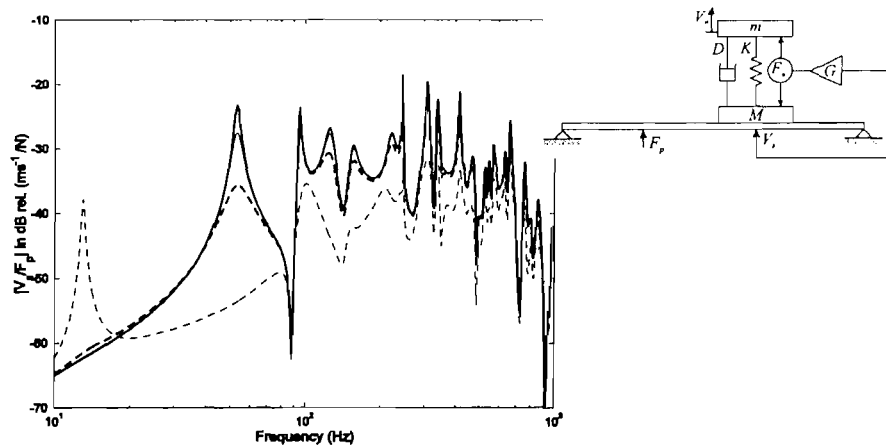
Figure 4.4: *Amplitude of the simulated FRF between the primary disturbance force and the plate velocity at the control actuator position in the open loop case (thick solid line), for external velocity feedback gains of 1 (thin solid line), 5 (thick dashed line) and 50 (thin dashed line).*

4.1.3 Internal direct velocity feedback

In a second case internal velocity feedback with a real feedback gain g results in an actuation force

$$F_a = -g(V_a - V_s). \tag{4.10}$$

Stability of direct internal velocity is assessed by investigation the open loop FRF

$$(V_a - V_s)/F_a = \{-1 \ 1\}(\mathbf{I} + \mathbf{Y'''}_{ss}\mathbf{Z})^{-1}\mathbf{Y'''}_{ss}\{1 \ -1\}^\mathbf{T}. \tag{4.11}$$

The closed loop FRF becomes

$$V_s/F_p = \{1 \ 0\}(1 + g\{-1 \ 1\}\mathbf{Y''}_{ss}\{1 \ -1\}^\mathbf{T})\mathbf{y''}_{sp.} \tag{4.12}$$

and the input and output signals in the general control framework are $Y_o = V_a - V_s$ and $Y_i = F_a$ with the FRFs $G_{oi} = \{-1 \ 1\}\mathbf{Y''}_{ss}\{1 \ -1\}^\mathbf{T}$, $G_{si} = \{1 \ 0\}\mathbf{Y''}_{ss}\{1 \ -1\}^\mathbf{T}$, $G_{op} = \{-1 \ 1\}\mathbf{y''}_{sp}$ and $G_{sp} = \{1 \ 0\}\mathbf{y''}_{sp}.$

Stability

Simulating Eq. (4.11) in Figure 4.5 shows that the open loop FRF completely lies in the positive real half-plane so that the closed loop FRF is predicted to be unconditionally stable. Simulations show that he first loop is associated to the fundamental resonance of the inertial actuator at about 13Hz whereas all following loops are due to plate resonances. More active damping hence is predicted at the fundamental resonance than at plate resonances. In other words the main effect of relative velocity feedback is to damp the fundamental resonance of the actuator and to produce a relatively smaller damping effect on the plate [188, 189].
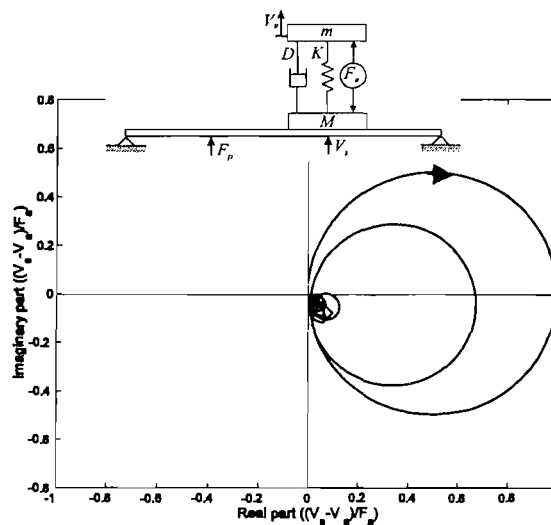
Figure 4.5: *Simulated Nyquist plot of the FRF between the actuation force and the velocity between actuator housing and moving mass.*

Figure 4.6 shows the FRF between the primary disturbance force and the plate velocity at the inertial actuator position in the open loop case (thick solid line) and for internal velocity feedback gains of 1 (thin solid line), 5 (thick dashed line) and 50 (thin dashed line). As expected there is increasing vibration reduction at higher plate resonances for increasing feedback gains and the fundamental resonance is very much damped so that there is no spillover around this frequency. At higher resonances vibration reduction is similar to the case with an ideal actuator-sensor combination in Figure 2.4. The relative importance of resonance peaks is changed very slightly. However, vibrations are not always reduced, but at some frequencies new peaks appear that actually have higher vibration amplitude. Those peaks usually are at a lower frequency as a corresponding open loop peak. This would mean that either the apparent plate stiffness was reduced or the apparent mass of the plate was increased. Simulations show that for very high feedback gains the plate behaves like a plate with a point mass attached at the actuator position. The effect of the internal feedback gain is to gradually fix the inertial mass of the actuator to the plate effectively increasing the mass of the plate. Correspondingly the higher frequency vibration reduction converges to the mass effect of the attached inertial mass. Also, for each resonance frequency there is a best gain for which the resonance peak is minimum. In general this optimum gain is different for each resonance and also from the optimum gain in Figure 2.6. Maximum reduction in kinetic energy over a frequency range up to 1kHz also is smaller than in Figure 2.6. Apparently internal velocity feedback cannot be used to add optimum damping at lower frequencies, although substantial damping at single or high resonance frequencies is possible. Only in the limiting case when the fundamental resonance is very small does internal velocity feedback converge to external velocity feedback with an ideal fore actuator so that large optimum kinetic energy reduction is possible. In comparison to external direct velocity feedback simulated in Figure 4.4 similar vibration reduction is possible at higher frequencies. At lower frequencies external velocity feedback leads to spillover into the fundamental resonance frequency, which might lie outside the audible range, but it is only conditionally stable. At lower frequencies internal velocity feedback leads to vibration amplification at frequencies close to the first resonance frequency of the plate and smaller vibration reduction although unconditional stability is guaranteed. A combination of direct external and internal velocity feedback studied in Chapter 5 could allow to balance vibration reduction performance and robustness of the feedback loop between these two extremes.

Figure 4.6: *Amplitude of the simulated FRF between the primary disturbance force and the plate velocity at the control actuator position in the open loop case (thick solid line), for internal velocity feedback gains of 1 (thin solid line), 5 (thick dashed line) and 50 (thin dashed line).*

4.2 Direct velocity feedback with accelerometer sensor

The results presented in the previous section cannot be measured because in practice the force transducer and sensor add substantial weight and additional dynamics. Therefore in this section a model of a real setup shown in Figure 4.7 is first described. Figure 4.7 shows the lightweight, electrodynamic inertial actuator attached to the plate at the same position as the reactive control actuator (RA) discussed in Chapter 2. In order to facilitate attachment of the inertial actuator to the plate this time the velocity sensor is attached beneath the plate. The same primary shaker with force transducer as in Chapter 2 is used.

Figure 4.7: *Photography of the experimental set-up with the primary shaker below the plate in the background and the inertial actuator above the plate in the foreground.*

The reference case external velocity feedback is implemented with an accelerometer and successively with a current command and a voltage command inertial actuator. In Subsection 4.2.1 the case for current command is considered and in Subsection 4.2.2 direct external velocity feedback with voltage command is investigated.

79

4.2.1 current command

In addition to the model in Section 4.1 the primary force generated by a primary shaker is measured with a force transducer that adds a mass M_p to the plate at position (x_p, y_p) so that the transfer mobility of the plate is modified to be $Y'_{sp} = \dfrac{Y_{sp}}{1 + j\omega M_p Y_{pp}}$. Then the transfer and point mobility vector and matrix in Eq. (4.5) become $\mathbf{y}_{sp} = \left\{ \begin{array}{c} Y'_{sp} \\ 0 \end{array} \right\}$ and $\mathbf{Y}_{ss} = \begin{bmatrix} Y'_{ss} & 0 \\ 0 & Y_m \end{bmatrix}$. As indicated in Figure 4.8 the actuation force for the electrodynamic control actuator

$$F_a = \Psi_p I_c \tag{4.13}$$

is proportional to the primary coil current, where the transducer coefficient Ψ_p is the proportionality constant.
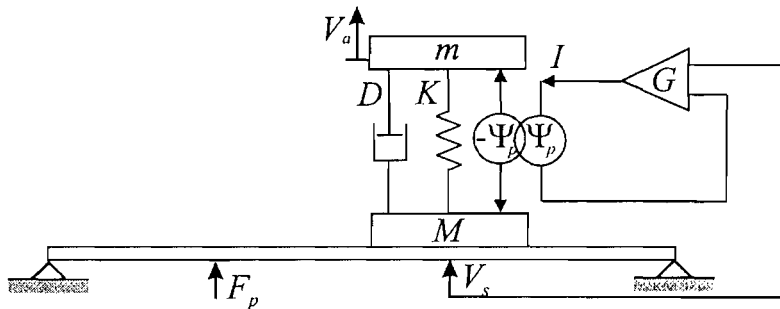
Figure 4.8: *Model of the electrodynamic current driven inertial actuator connected to the plate.*

When amplifier and sensor dynamics do not introduce phase shifts in the control range, direct external velocity feedback implements a feedback current

$$I_c = -GV_s \qquad . \tag{4.14}$$

Closed loop stability of direct external velocity feedback with a current command actuator is determined by the open loop FRF

$$V_s/I_c = \{1 \ 0\}(\mathbf{I} + \mathbf{Y'}_{ss}\mathbf{Z})^{-1}\mathbf{Y'}_{ss} \ \psi_p{}^{\mathbf{T}} \tag{4.15}$$

where $Y'_{ss} = (I + Y_{ss}Z)^{-1} Y_{ss}$ and the transducer coefficients of the primary coil are compiled in a vector $\psi_p = \{\psi_p \; -\psi_p\}$. The closed loop FRF is

$$V_s/F_p = \{1 \; 0\}(1 + G\{1 \; 0\}Y'_{ss} \; \psi_p{}^T) y'_{sp} \qquad (4.16)$$

where $y'_{sp} = (I + Y_{ss}Z)^{-1} y_{sp}$. In the generalized control scheme in Figure 1.2 the input and output signal are given by $Y_o = V_s$ and $Y_i = I$ with the associated FRFs $G_{oi} = \{1 \; 0\}Y'_{ss} \; \psi_p{}^T$, $G_{si} = \{1 \; 0\}Y'_{ss} \; \psi_p{}^T$ and $G_{op} = G_{sp} = \{1 \; 0\}y'_{sp}$.

Stability

Figure 4.9 show the simulated (left) and measured (right) FRF between the driving current of the primary coil and the plate velocity at the inertial actuator position. As indicated by simulations in Figure 4.3 closed loop unconditional stability is not guaranteed because of inertial actuator dynamics. Vibration reduction is predicted at higher plate resonance frequencies that lie completely in the positive real half-plane. Moreover, measurements show a distortion effect at very low frequencies that is not predicted by simulations. At even lower frequencies not shown in these measurements there is at least one more loop in the negative real half-plane. This probably is a result of the high-pass filter and non-ideal time integrator in the charge amplifier of the accelerometer. Since the associated loop in the negative real half-plane lies within the loop due to the inertial actuator effect, in this case it does not influence stability considerations.
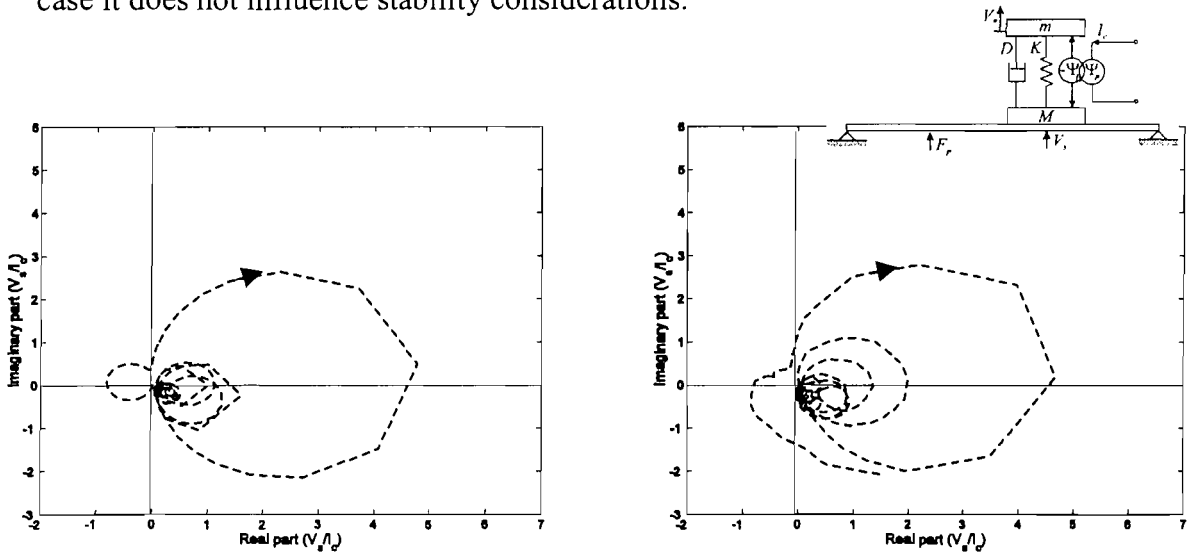
Figure 4.9: *Simulated (left) and measured (right) Nyquist plot of the FRF between the driving current I_c and the time-integrated accelerometer output signal V_s.*

Figure 4.10 shows the simulated (left) and measured (right) FRF between the primary force and the plate velocity at the secondary actuator position in the open loop case (thick solid line) and for external velocity feedback (thick dashed line) with a feedback gain used to plot Figure 4.9. In comparison to Figure 4.4 the mass effect of the additional force transducer is visible. Also, as expected there is substantial spill-over into the fundamental resonance, which will lead to instability for higher feedback gains. At the same time there is some vibration reduction at higher frequencies that, however, is much smaller than in the optimum case in Figure 4.4 because the influence of the inertial actuator is more constraining than indicated by those simulations. An important factor is the internal actuator damping that has been found about three times smaller than in the initial simulations in Figure 4.4. Therefore here the feedback gains that can be implemented in practice are not large enough to change the relative importance of modes as would be necessary for a substantial reduction in kinetic energy of the whole plate.
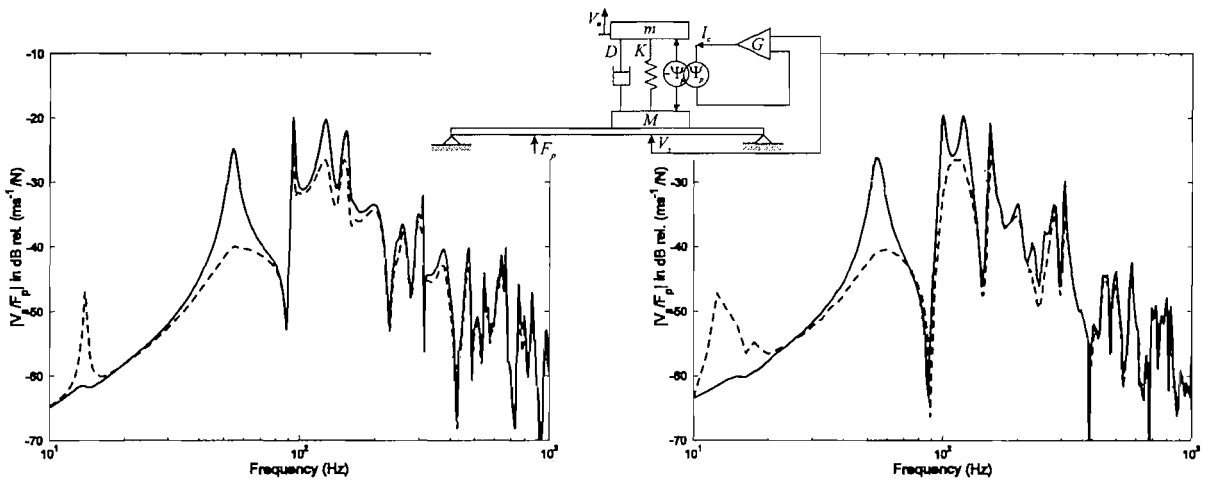
Figure 4.10: *Simulated (left) and measured (right) amplitude of the FRF between the primary disturbance force F_p and the plate velocity V_s at the control actuator position in the open loop case (thick solid line) and for medium plate velocity feedback gains (thick dashed line).*

4.2.2 voltage command

As shown in Figure 4.11 in the voltage command case, the current in the control coil is

$$I_c = \frac{1}{Z_e}\left(U_{AB} - U_{ind}\right) \tag{4.17}$$

where $Z_e = R_e + j\omega L_e$ is the electrical impedance of the shaker and R_e, L_e are the resistance and self-inductance of the driving coil.

82
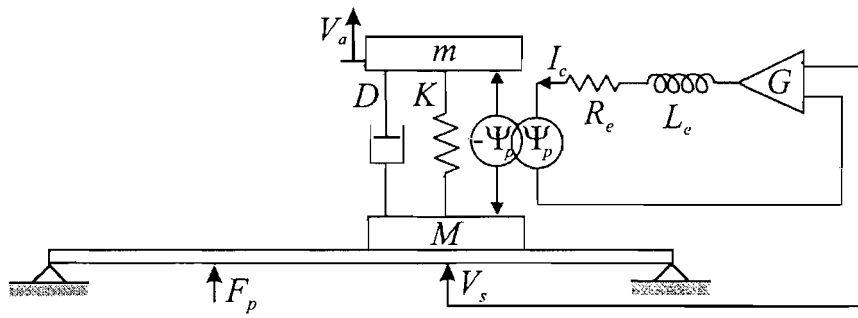
Figure 4.11: *Model of the electrodynamic inertial voltage driven actuator connected to the plate.*

U_{AB} is the driving voltage applied to the inertial actuator and U_{ind} is the induced voltage in the driving circuit generated by the back electromotive force due to the vibration of the coil relative to the moving actuator mass:

$$U_{ind} = \Psi_p \{1 \quad -1\} \mathbf{v}_s .$$ (4.18)

When a feedback voltage

$$U_{AB} = - GV_s$$ (4.19)

is applied to the electrical connections of the actuator driving coil, stability of this external velocity feedback with voltage command is determined by the FRF

$$V_s/U_{AB} = \{1\ 0\}(\mathbf{I} + \mathbf{Y'}_{ss}\ \mathbf{\psi}_p{}^{\mathrm{T}}/Z_e\mathbf{\psi}_p)^{-1}\mathbf{Y'}_{ss}\ \mathbf{\psi}_p{}^{\mathrm{T}}/Z_e$$ (4.20)

and the FRF

$$V_s/F_p = \{1\ 0\}(\mathbf{I} + \mathbf{Y'}_{ss}\ \mathbf{\psi}_p{}^{\mathrm{T}}/Z_e(\mathbf{\psi}_p + G\{1\ 0\}))^{-1}\mathbf{y'}_{sp}$$ (4.21)

gives an indication about the closed loop performance. In the generalized control framework the output and input signals are $Y_o = V_s$ and $Y_i = U_{AB}$ with the FRFs $G_{oi} = G_{si} = \{1\ 0\}(\mathbf{I} + \mathbf{Y'}_{ss}\ \mathbf{\psi}_p{}^{\mathrm{T}}/Z_e\mathbf{\psi}_p)^{-1}\mathbf{Y'}_{ss}\ \mathbf{\psi}_p{}^{\mathrm{T}}/Z_e$ and $G_{op} = G_{sp} = \{1\ 0\}(\mathbf{I} + \mathbf{Y'}_{ss}\ \mathbf{\psi}_p{}^{\mathrm{T}}/Z_e\mathbf{\psi}_p)^{-1}\mathbf{y'}_{sp}.$

Stability

Figure 4.12 shows the simulated (left) and measured (right) open loop FRF between the input voltage to the actuator voltage command amplifier, proportional to U_{AB} in the considered frequency range, and the plate velocity at the inertial actuator position. Both simulations and measurement results show a loop due to the fundamental resonance of the

inertial actuator which lies in the negative real half-plane. Therefore conditional stability and spillover around the fundamental resonance frequency is predicted. At even lower frequencies measurements indicate the influence of the used electronics. Further measurements show that the loop due to electronics in the negative real half-plane is smaller than the loop due to the fundamental resonance. Therefore actuator dynamics rather limit the feedback gains. Both measurement and simulation results indicate that for a large number of plate resonances the loop lies in the positive real half-plane indicating substantial vibration reduction. At higher frequencies the inductance effect of the driving coil is visible since a number of resonance loops are rotated in such a way as to enter into the negative real half-plane. Hence, spillover into some higher modes is predicted. In comparison to Figure 4.9 loops are bigger so that more vibration reduction is expected in the voltage command case.
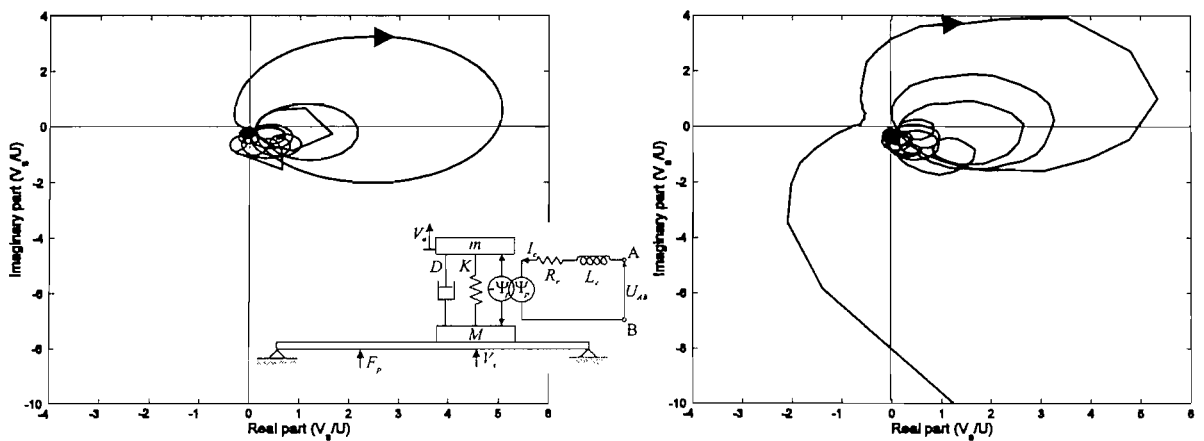
Figure 4.12: *Simulated (left) and measured (right) Nyquist plot of the FRF between the amplifier input voltage U and the time-integrated accelerometer output signal V_s.*

Performance

Figure 4.13 shows the simulated (left) and measured (right) FRF between the primary disturbance force and the plate velocity at the inertial actuator position in the open loop voltage command case (thick solid line), in the open loop current command case (thick dashed line) and for plate velocity feedback with the gain used to plot Figure 4.12 (thin solid line). In comparison to the current command case there already is some damping in the open loop for voltage command because of the coil resistance that is not compensated by a current command amplifier. As expected both simulations and measurements show substantial spillover at the fundamental resonance frequency and small spillover at some higher resonance frequencies when direct external velocity feedback is investigated. Despite limited feedback gains there is some change in the relative importance of modes although not by far as much as in Figure 4.4.

84

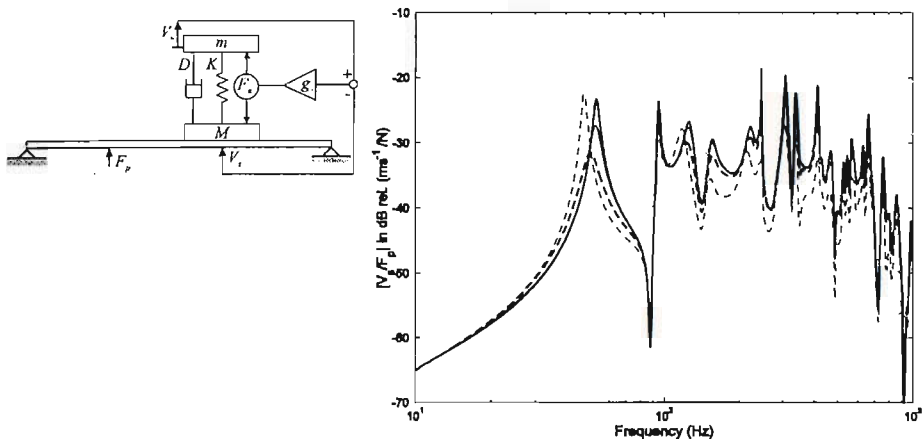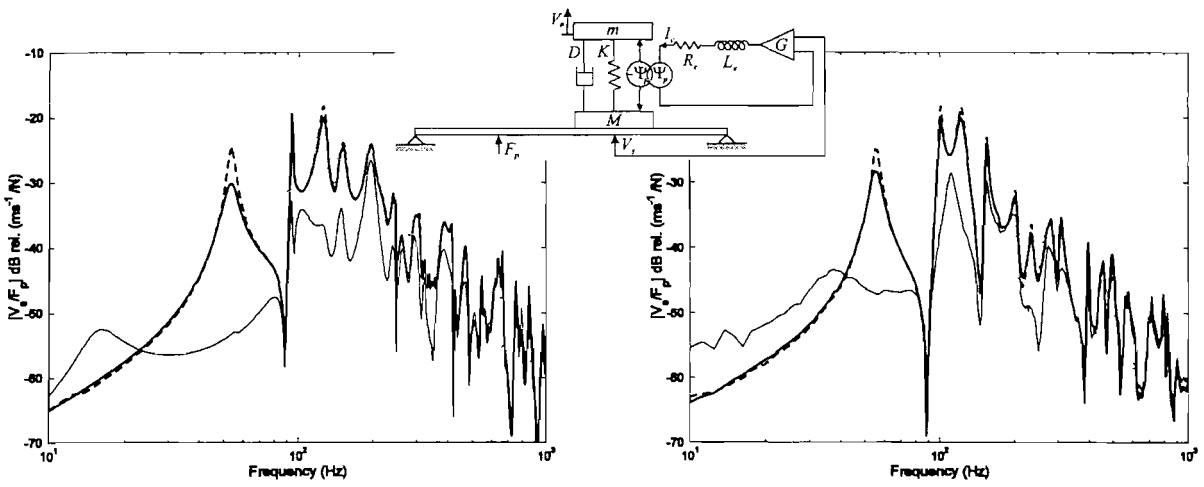**Figure 4.13:** *Simulated (left) and measured (right) amplitude of the FRF between the primary disturbance force F_p and the plate velocity V_s at the control actuator position in the open loop case with current drive (thick dashed line), in the open loop case with voltage drive (thick solid line) and for plate velocity feedback (thin dashed line).*

In comparison to the current command case, voltage command already adds internal damping because of a shunted resistor effect. In the following sections this effect and other control schemes with a self-sensing inertial actuator are investigated.

4.3   Shunted resistor

For active damping the circuit connected to the connections of the primary actuator coil should be designed in such a way that the applied voltage results in an actuation force that is proportional, but of opposite sign, to the relative velocity and hence the induced voltage U_{ind}. When feedback is implemented using a shunted resistor R_l as is schematically shown in Figure 4.14 a voltage

$$U_{AB} = -R_l I. \tag{4.22}$$

is generated across the electrical connections of the control actuator.
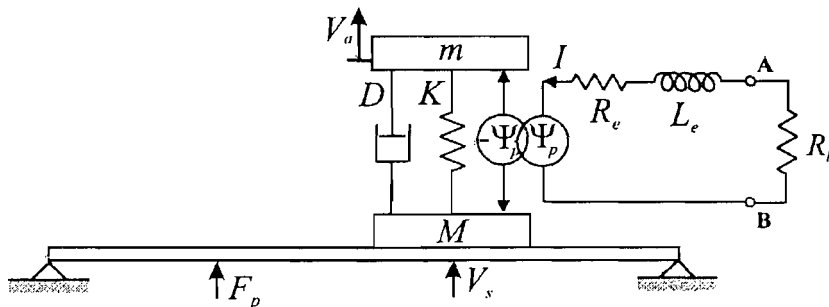
Figure 4.14: *Model of the electrodynamic inertial voltage driven actuator with a shunted resistor and connected to the plate.*

The open loop FRF for a resistor shunted to the electrical connections is

$$\frac{I}{U_{AB}} = \frac{1/Z_e}{1 + \psi_p \mathbf{Y}'_{ss} \psi_p^{\mathrm{T}}/Z_e} \quad . \tag{4.23}$$

Then the feedback gain $g = R_l$ is changed by varying the value of the shunted resistor R_l. In the open circuit case of the actuator connections the resistance tends to infinity whereas in the closed circuit case the resistance tends to zero. Closed loop performance is investigated with the FRF

$$\frac{V_s}{F_p} = \frac{\mathbf{y}'_{sp}}{1 + \psi_p \mathbf{Y}'_{ss} \psi_p^{\mathrm{T}}/(R_l + Z_e)} \quad . \tag{4.24}$$

Note the similarity of the second part of the second term in the denominator with the Eddy current damping coefficient in Eq. (4.6). For eddy currents the metal resistance R_{ec} that is determined by the actuator geometry takes the place of the shunted resistor R_l. For large eddy currents and hence high damping a small resistance, implying a thick cylindrical aluminium coil former of small circumference, seems to be advantageous. In the general control scheme in Figure 1.2 the output and input signals are given by $Y_o = I$ and $Y_i = U_{AB}$

with the FRFs $G_{sp} = \{1 \quad 0\} \mathbf{D} \, \mathbf{y}'_{sp}$, $G_{si} = \{1 \quad 0\} \mathbf{D} \, \mathbf{Y}'_{ss} \psi_p^{\mathrm{T}} \dfrac{1}{Z_e}$, $G_{op} = \dfrac{1/Z_e}{1 + \psi_p \mathbf{Y}'_{ss} \psi_p^{\mathrm{T}}/Z_e} \psi_p \mathbf{y}'_{sp}$

and $G_{oi} = \dfrac{1/Z_e}{1 + \psi_p \mathbf{Y}'_{ss} \psi_p^{\mathrm{T}}/Z_e}$ where $\mathbf{D} = \left(\mathbf{I} + \mathbf{Y}'_{ss} \psi_p \dfrac{1}{Z_e} \psi_p^{\mathrm{T}} \right)^{-1}$.

Stability

Figure 4.15 shows the simulated (left) and measured (right) Nyquist plots of the open loop FRF between the input voltage U_{AB} and the coil current I. The current is measured using a measurement resistor in series to the shaker. Measurements and simulations show the same trend with motional impedance loops at lower frequencies and convergence to the origin for high frequencies. With this type of control scheme the locus lies in the right hand side so that as expected unconditional stability is predicted. For low frequencies the locus starts at $1/R_e$ and it tends to the origin for high frequencies since an ideal inductance has been assumed. The loops at lower frequencies due to the induced voltage lie rather far away from the critical point so that the current decreases relative to the closed circuit case without shunted resistor and only a small amount of added damping is expected when the control loop with the shunted resistor is closed. The biggest loop is associated to the fundamental actuator resonance so that a lot of damping is expected at this resonance.
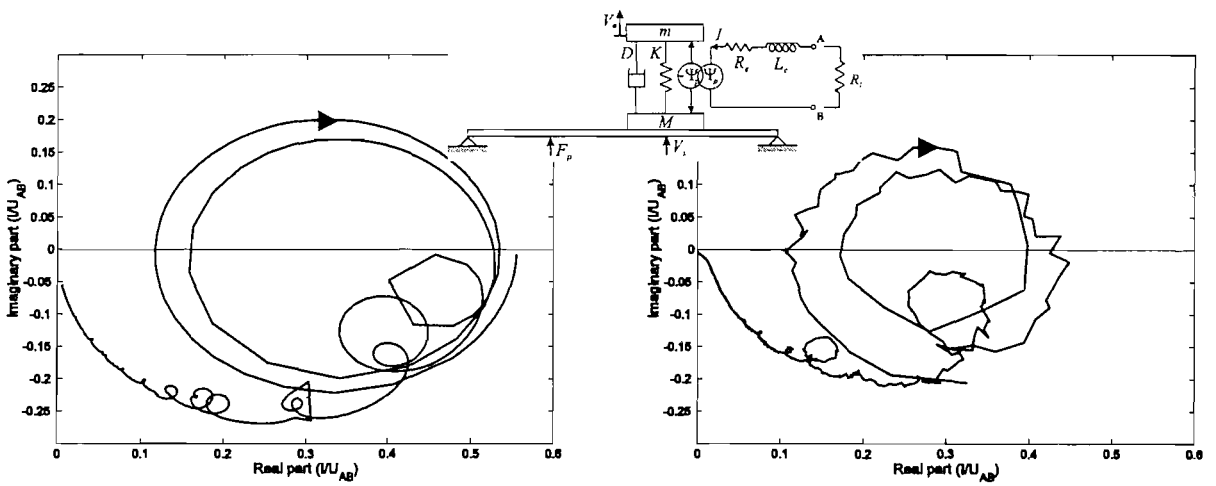
Figure 4.15: *Simulated (left plot) and measured (right plot) Nyquist plot of the open loop FRF between the voltage input U_{AB} to the inertial actuator and the coil current I.*

Performance

The two plots in Figure 4.16 show the simulated (left) and measured (right) vibration of the panel at the control position with reference to the primary disturbance excitation. The thick and thin solid lines give the vibration of the panel at the control position when the driving circuit of the control actuator is either left open or is closed with a small resistor R_l. The dashed line indicates plate vibrations without the inertial actuator. Measurements below about 20Hz are not reliable due to small coherence values. Both plots clearly show the passive mass–effect of the force transducer used to measure the primary force excitation and the actuator weight by a shift of the first resonance frequency of the panel to lower values when the actuator is added. This downward shift is reduced by the suspension system in the control actuator. Furthermore the amplitude of the response of the panel decreases at higher frequencies.

Figure 4.16: *Simulated (left plot) and measured (right plot) vibration level of the panel at the control position with reference to the primary disturbance F_p in the open loop case without actuator (thick dashed line), with actuator (thick solid line) and for a small shunted resistor (thin solid line).*

87

About 6dB damping is added to the first plate mode just by applying the actuator that shows both Eddy current and increased internal actuator damping. Only small additional damping can be added by shunting the actuator mainly at the fundamental actuator resonance and at the first resonance frequency of the plate. Damping increases for decreasing value of the resistor since the current leading to an opposing secondary force is increased i.e. the starting point of the locus of the Nyquist plot in Figure 4.15 moves towards the origin. Maximum passive damping is achieved when the connections of the actuator are closed without an intermediate shunting resistor.

4.4 Positive current feedback

In order to further reduce the value of the shunted resistor a positive current feedback loop can be used. This generates a negative resistance. As schematically shown in Figure 4.17 the driving current is measured by a resistor R_l in series to the driving coil of the inertial actuator.
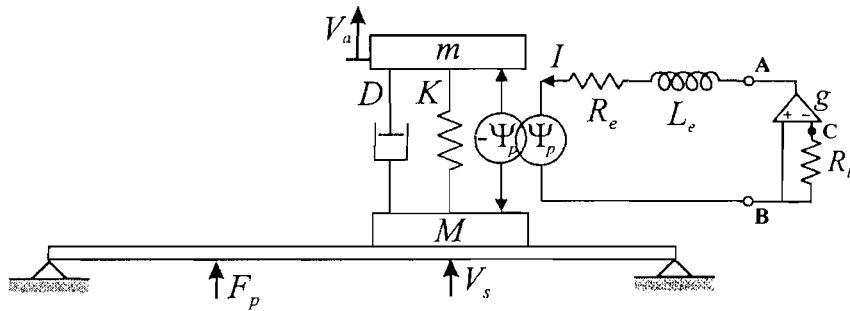
Figure 4.17: *Model of the electrodynamic inertial voltage driven actuator with positive current feedback and connected to the plate.*

For this control scheme the feedback voltage is

$$U_{AC} = + g U_{BC} . \tag{4.25}$$

The open loop FRF between the input voltage to the actuator and the voltage of the measurement resistor is

$$\frac{U_{BC}}{U_{AC}} = \frac{(R_l / Z'_e)}{1 + \psi_p Y'_{ss} \psi^T_p / Z'_e} . \tag{4.26}$$

A Crown Electronics DC-300 amplifier is used to implement the feedback gain g. Due to its small electrical output impedance R_l the amplifier already adds damping to the plate that is in the range of the shunted resistor case presented in Section 4.3. The closed loop FRF

$$\frac{V_s}{F_p} = \frac{\mathbf{y}'_{sp}}{1 + \mathbf{\psi}_p \mathbf{Y}'_{ss} \mathbf{\psi}^T_p / (Z'_e - gR_l)} \tag{4.27}$$

is used to evaluate vibration reduction performance. The signal output Y_o in the scheme of Figure 1.2 is the voltage drop U_{BC} over the measurement resistor which is indeed proportional to the current in the driving circuit of the shaker and the signal input Y_i is the driving voltage U_{AC} of the shaker. Therefore the transfer functions in the block diagram of Figure 1.2 remain proportional to those given in the previous section when Z_e is replaced by $Z_e' = Z_e + R_l$ so that $G_{sp} = \{1 \quad 0\} \mathbf{D}' \mathbf{y}'_{sp}$, $G_{si} = \{1 \quad 0\} \mathbf{D}' \mathbf{Y}'_{ss} \mathbf{\psi}^T_p \dfrac{1}{Z'_e}$,

$G_{op} = \dfrac{R_l / Z'_e}{1 + \mathbf{\psi}_p \mathbf{Y}'_{ss} \mathbf{\psi}^T_p / Z'_e} \mathbf{\psi}_p \mathbf{y}'_{sp}$ and $G_{oi} = \dfrac{R_l / Z'_e}{1 + \mathbf{\psi}_p \mathbf{Y}'_{ss} \mathbf{\psi}^T_p / Z'_e}$ where $\mathbf{D}' = \left(\mathbf{I} + \mathbf{Y}'_{ss} \mathbf{\psi}_p \dfrac{1}{Z'_e} \mathbf{\psi}^T_p \right)^{-1}$.

Stability

The two plots in Figure 4.18 show the simulated (left) and measured (right) Nyquist plots of the open loop FRF between the amplifier output voltage U_{AC} and the voltage over the measurement resistor U_{BC} for frequencies up to 100kHz for measurements and 1kHz for simulations. Measurements and simulations show the same trend, but measurements clearly indicate non-ideal inductive behaviour at higher frequencies. Compared to that in Figure 4.15, the locus has flipped into the left half plane so that the closed loop is predicted to be only conditionally stable. At a given gain the higher the internal coil resistance the further away is the loop from the critical point. Amplitude variations are relatively less important for high resistance so that robustness is increased. In the closed loop case, the voltage drop over the measurement resistor, which is proportional to the coil current, is predicted to be amplified. As a consequence the actuation force on the plate increases. This actuation force is opposite to the vibration velocity since for electrodynamic actuators the induced voltage is of opposite sign to the current and the secondary force. Relatively more damping than in the shunted resistor case is predicted since the current is amplified electronically.
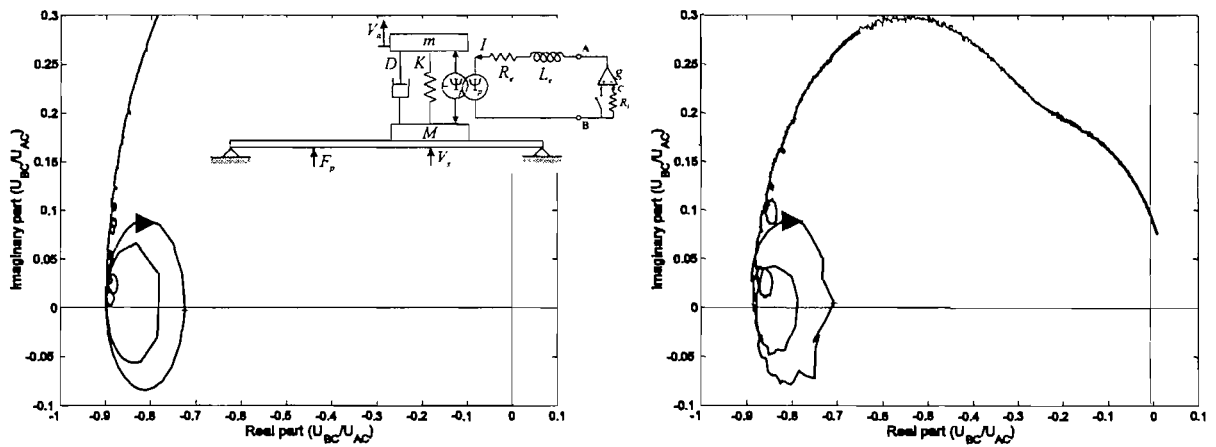
Figure 4.18: *Simulated (left plot) and measured (right plot) Nyquist plot of the FRF between the input voltage U_{AC} and the feedback voltage U_{BC}..*

Performance

Figure 4.19 shows the simulated (left) and measured (right) vibration of the panel at the control position with reference to the primary disturbance excitation. The thick and thin solid lines give the vibration of the panel at the control position without the passive amplifier effect (thick solid line) and for two positive current feedback gains (thin solid and thick dashed lines). In comparison to the shunted resistor case, a larger amount of damping is added to the first resonance of the plate. Moreover about 3 to 4dB vibration reduction is added to the second and third resonances. The lower amplitude of the closed loop measurements at about 200Hz is due to relatively small measurement coherence and does not illustrate vibration reduction. Simulations show that for higher gains spillover is expected at these frequencies due to the self-inductance of the actuator.
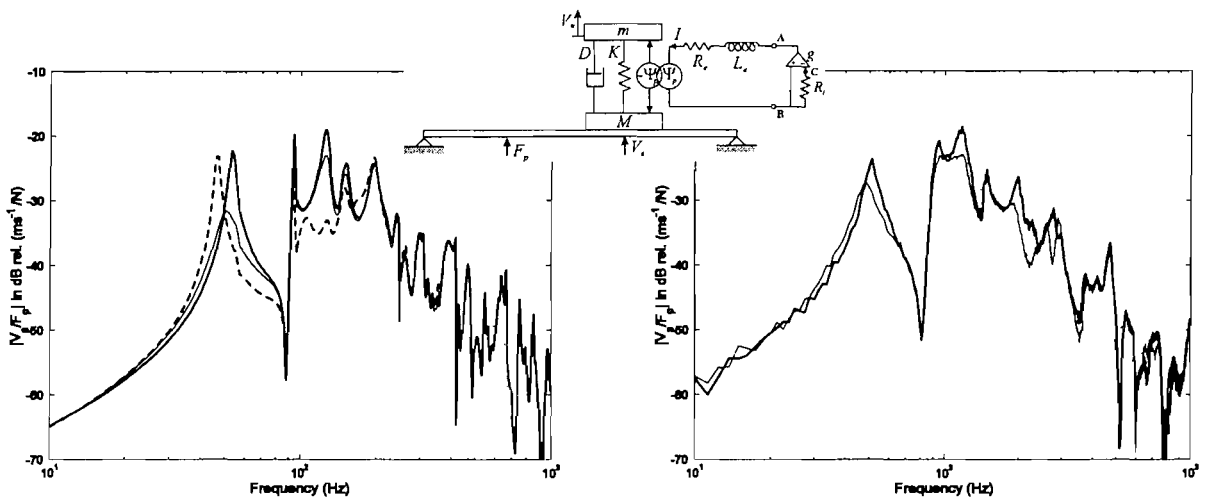
Figure 4.19: *Simulated (left plot) and measured (right plot) vibration level of the panel at the control position with reference to the primary disturbance F_p in the open loop case (thick solid line) and for one or two positive current feedback gains (thin solid and thick dashed line).*

90

Also, vibration reduction due to the first big loop at the internal actuator resonance at about 13Hz is not visible in this plot. Because of the fundamental resonance of the actuator spillover into lower frequencies is expected for higher gains as indicated by the dashed line in simulations. These gains have not been implemented because they are extremely close to the stability limit. For feedbacks at the stability limit theoretically leading to infinite damping the plate would behave as if the actuator mass was firmly attached at the connection point as illustrated by simulations in Figure 4.6.

4.5 Induced voltage feedback

In order to better estimate the induced voltage a Wheatstone bridge is added as shown in Figure 4.20.
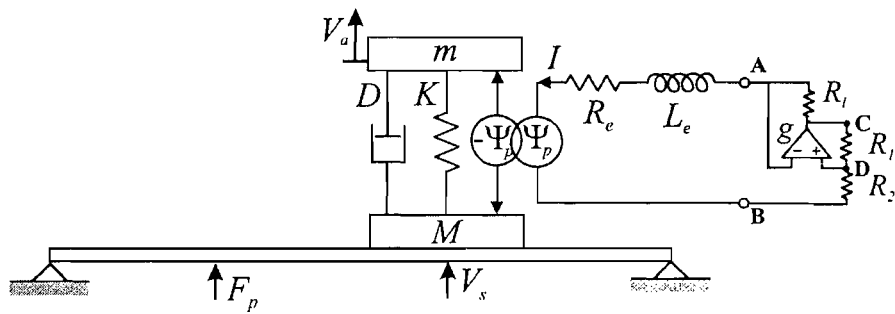
Figure 4.20: *Model of the electrodynamic inertial voltage driven actuator with induced voltage feedback and connected to the plate.*

The bridge partially compensates for a feed through path. In comparison to the formulation presented in Section 2.5 Eqs. (2.22) to (2.26) only U_{ind} is changed which is now proportional to the relative velocity between the inertial mass and the plate and not the plate velocity at the inertial actuator position. As in Eq. (2.22) the voltage over each half-bridge is given by

$$U_{BC}=(R_1+R_2)I_1=(Z_e+R_l)I+U_{ind} \qquad (4.28)$$

and the input voltage to the feedback amplifier is

$$U_{AD}=R_2I_1-Z_eI-U_{ind}. \qquad (4.29)$$

When a voltage

$$U_{BC}=-g\,U_{AD} \qquad (4.30)$$

91

is fed back, the open loop FRF is slightly changed from Eq. (2.25) to become

$$\frac{U_{AD}}{U_{BC}} = \frac{R_2}{R_1 + R_2} - \frac{Z_e + \psi_p Y'_{ss} \psi_p^T}{Z'_e + \psi_p Y'_{ss} \psi_p^T} \; . \tag{4.31}$$

The closed loop FRF of the plate becomes

$$\frac{V_s}{F_p} = \frac{\{1\,0\}\mathbf{y}_{sp}}{\left(\mathbf{I} + \mathbf{Y}_{ss}\left(\mathbf{Z} + \psi_p\left(\dfrac{R_1 + R_2 + gR_2}{-Z'_e(R_1 + R_2 + gR_2) + gR_1(R_1 + R_2)}\right)\psi_p^T\right)\right)} \; . \tag{4.32}$$

Regarding the control scheme in Figure 1.2 U_{BC} is both the input voltage from the DC-300 amplifier and the control input Y_i. The output signal from the bridge, U_{AD}, is the output voltage and the control output Y_o. In this case the four transfer functions in the control block diagram of Figure 1.2 are given by the following relations: $G_{si} = \{1 \quad 0\}\,\mathbf{D'}\,\mathbf{Y}'_{ss}\psi_p^T\dfrac{1}{Z'_e}$,

$$G_{sp} = \{1 \quad 0\}\,\mathbf{D'}\,\mathbf{y}'_{sp}, \quad G_{op} = \frac{R_l \psi_p \mathbf{y}'_{sp}}{Z'_e + \psi_p \mathbf{Y}'_{ss}\psi_p^T} \text{ and } G_{oi} = \frac{-R_2}{R_1 + R_2} + \frac{R_l}{Z'_e + \psi_p \mathbf{Y}'_{ss}\psi_p^T} \; .$$

Stability

The two plots in Figure 4.21 show the simulated (left) and measured (right) Nyquist plots of the open loop FRF between the bridge input voltage U_{BC} and the bridge output voltage U_{AD} for frequencies up to 1 kHz with a 500Hz cut-off filter.
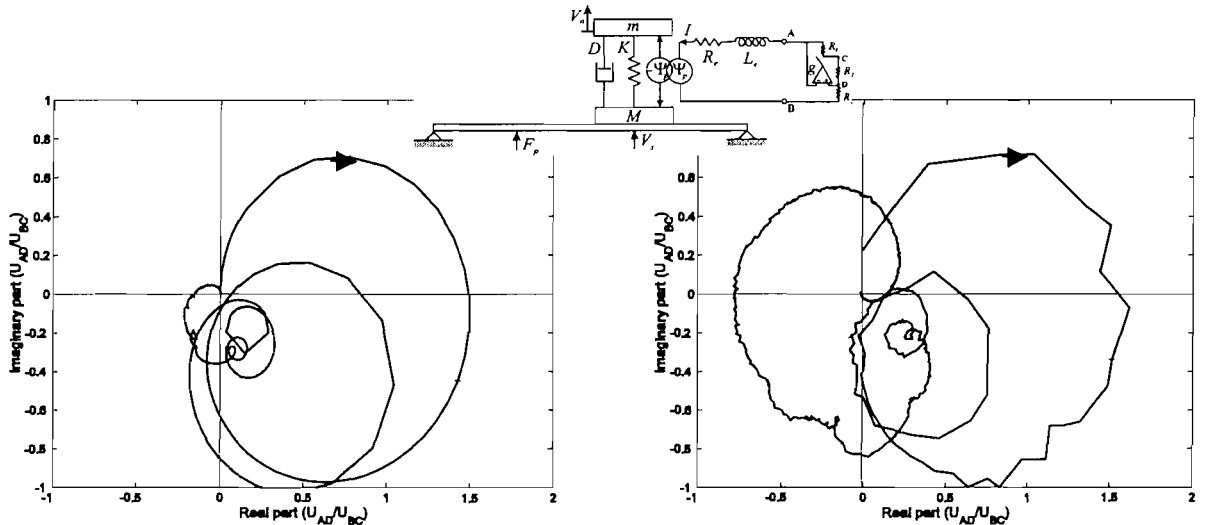
Figure 4.21: *Simulated (Left plot) and measured (right plot) Nyquist plot of the FRF between the bridge input voltage U_{BC} and the bridge output voltage U_{AD}.*

Measurements up to 100 kHz without filter show that for high frequencies the electric circuit of the inertial actuator does not behave like a real inductance and that because of circuit dynamics the locus encircles the critical point. Therefore a steep 500Hz low pass filter is used, so that closed loop stable feedback gains are implemented in practice. Since only two major loops are visible in the positive real half-plane additional vibration reduction is expected at the internal actuator resonance frequency and at the first resonance of the plate.

Performance

Figure 4.22 shows the simulated (left) and measured (right) vibration of the panel at the control position with reference to the primary disturbance excitation. The thick and thin solid lines give the vibration of the panel at the control position without the passive amplifier effect (thick solid line) and for two induced voltage feedback gains (thin solid and thick dashed lines). Due to risk of instability because of measurement uncertainty, higher feedback gains have not been implemented in practice and therefore only measurements for medium gains are shown. More vibration reduction than in the positive current feedback case is observed at the first flexible plate resonance, but, as expected, only very small reduction is visible at higher resonances. Additionally simulations predict that spillover occurs into lower frequencies because of the fundamental actuator resonance. In order to increase control bandwidth to higher frequencies the bridge circuit should also compensate for the self-inductance of the driving coil in the inertial actuator. Spillover into lower frequencies can probably be reduced by decreasing the fundamental resonance frequency and properly adjusting actuator damping.
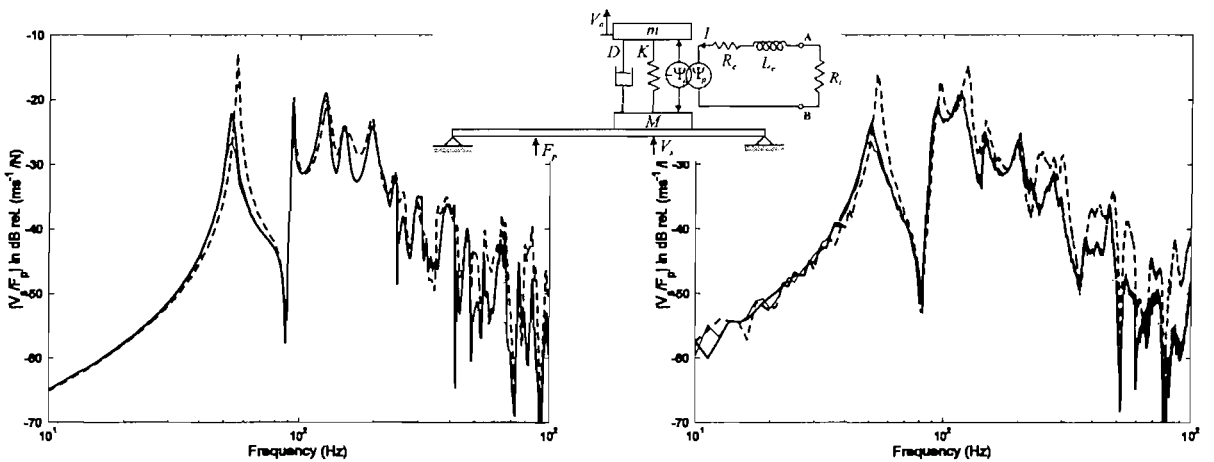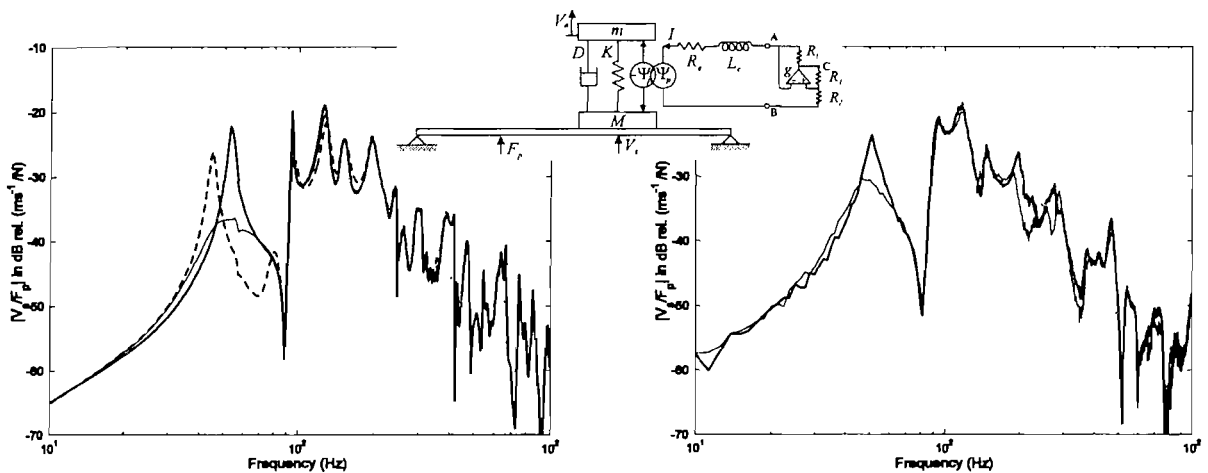

Figure 4.22: *Simulated (left plot) and measured (right plot) vibration level of the panel at the control position with reference to the primary disturbance F_p in the open loop case (thick solid line) and for increasing bridge output voltage feedback gains (thin solid and thick dashed line).*

93

4.6 Induced voltage feedback with inductance compensation

Additional inductance compensation is achieved using a so-called Owens bridge as also presented in Section 2.6 and as schematically shown in Figure 4.23.
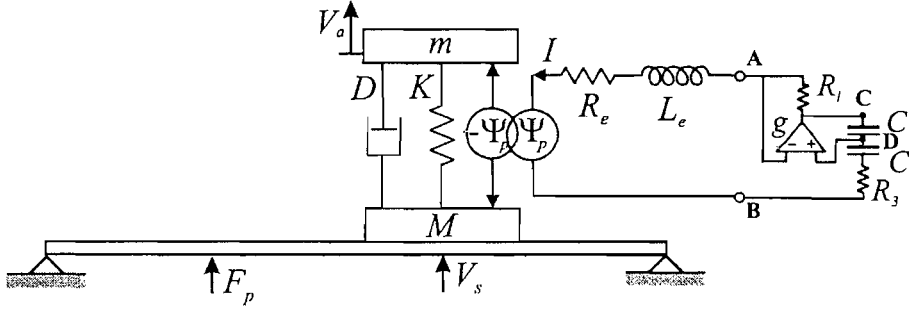
Figure 4.23: *Model of the electrodynamic inertial voltage driven actuator with induced voltage feedback with inductance compensation and connected to the plate.*

As before the voltage over each half-bridge is

$$U_{BC}=(Z_1+Z_2)I_1=(Z_e+R_l)I+U_{ind} \tag{4.33}$$

and the input voltage to the feedback amplifier is

$$U_{AD}=Z_1I_1-Z_eI-U_{ind} \tag{4.34}$$

where $Z_1 = R_3 + \dfrac{1}{j\omega C}$ and $Z_2 = \dfrac{1}{j\omega C}$. When a direct feedback voltage

$$U_{BC}=-g\,U_{AD} \tag{4.35}$$

is implemented, closed loop stability is investigated with the FRF

$$\frac{U_{AD}}{U_{BC}} = \frac{Z_1}{Z_1+Z_2} - \frac{Z_e+\psi_p Y'_{ss}\psi_p^T}{Z'_e+\psi_p Y'_{ss}\psi_p^T} \cdot \tag{4.36}$$

Closed loop performance is evaluated by the FRF

94

$$\frac{V_s}{F_p} = \frac{\{1\ 0\}\mathbf{y}_{sp}}{\left(1+\mathbf{Y}'_{ss}\left(\mathbf{Z}+\mathbf{\psi}_p\left(\dfrac{Z_1+Z_2+gR_2}{-Z'_e\left(Z_1+Z_2+gZ_2\right)+gR_l\left(Z_1+Z_2\right)}\right)\mathbf{\psi}_p^{\mathrm{T}}\right)\right)} \quad . (4.37)$$

U_{BC} simultaneously is the input voltage from the amplifier and the control input Y_i in the block diagram of Figure 1.2. U_{AD} is the bridge output voltage and the control output Y_o also in the block diagram of Figure 1.2. In this case the four transfer functions are given by the following expressions: $G_{sp} = \{1\ \ 0\}\mathbf{D}'\,\mathbf{y}'_{sp}$, $G_{si} = \{1\ \ 0\}\mathbf{D}'\,\mathbf{Y}'_{ss}\mathbf{\psi}_p^{\mathrm{T}}\dfrac{1}{Z'_e}$, $G_{op} = \dfrac{R_l\mathbf{\psi}_p\mathbf{y}'_{sp}}{Z'_e + \mathbf{\psi}_p\mathbf{Y}'_{ss}\mathbf{\psi}_p^{\mathrm{T}}}$

and $G_{oi} = \dfrac{-Z_1}{Z_2+Z_1} + \dfrac{R_l}{Z'_e + \mathbf{\psi}_p\mathbf{Y}'_{ss}\mathbf{\psi}_p^{\mathrm{T}}}$.

Stability

Slightly different parameter values and offsets are used for the open loop and the closed loop case probably due to the influence of used amplifiers. The two plots in Figure 4.24 show the simulated (left) and measured (right) Nyquist plots of the open loop FRF between the bridge input voltage U_{BC} and the bridge output voltage U_{AD} for a tuned Owens bridge with a cut-off filter at 7kHz. If no filter is used the locus encircles the critical point because the Owens bridge cannot completely compensate the non-ideal inductive behaviour of the inertial actuator. So even if the bridge is not ideally tuned simulations and measurements show that more motional impedance loops lie in the right real half-plane than for the Wheatstone bridge case. Hence, vibration reduction is predicted at higher resonance frequencies than in the case of the Wheatstone bridge.
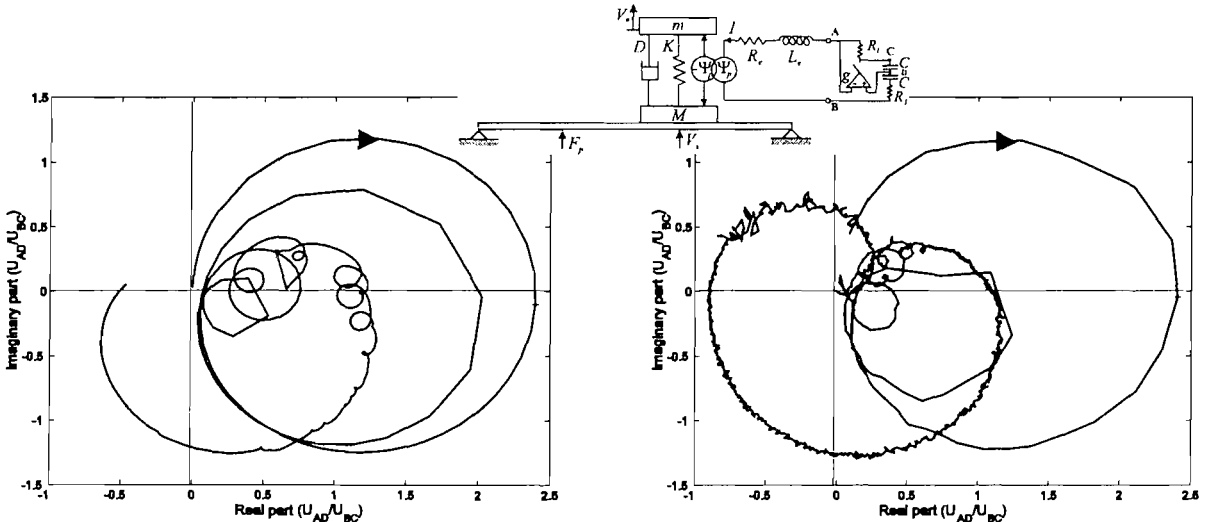
Figure 4.24: *Simulated (left plot) and measured (right plot) Nyquist plot of the FRF between the Owens bridge input U_{BC} and output voltage U_{AD}.*

Figure 4.25 shows the simulated (left) and measured (right) vibration of the panel at the control position with reference to the primary disturbance excitation. The thick and thin solid lines give the vibration of the panel at the control position without the passive amplifier effect (thick solid line) and for two induced voltage feedback gains (thin solid and thick dashed lines). The plot on the right shows only one control case (thin solid line) already close to the stability limit.
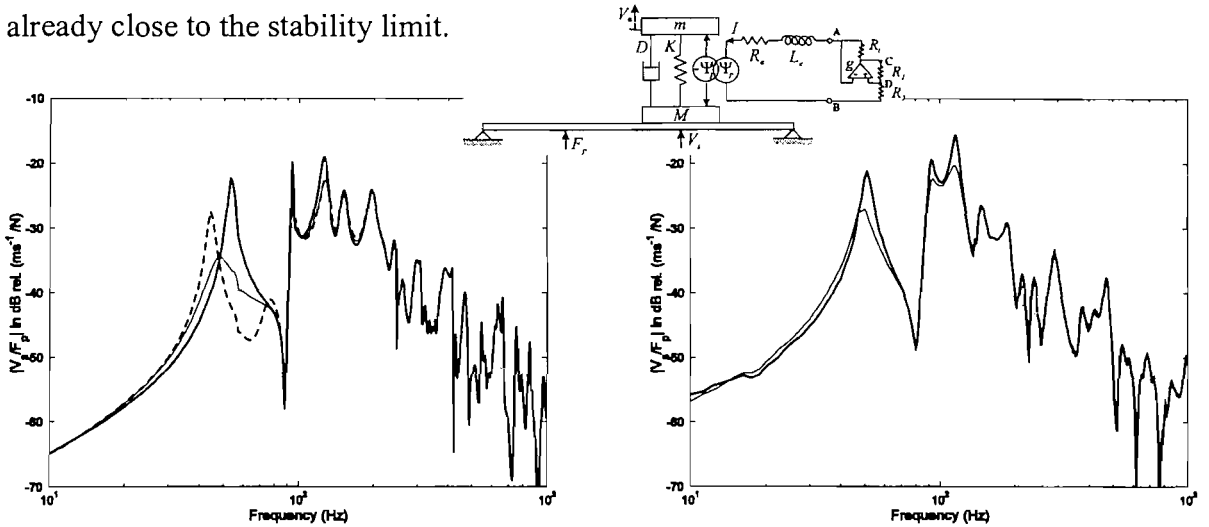
Figure 4.25: *Simulated (left plot) and measured (right plot) vibration level of the panel at the control position with reference to the primary disturbance F_p in the open loop case (thick solid line) and for increasing Owens bridge output voltage feedback gains (thin solid and thick dashed line).*

Additional 7dB vibration reduction at the first plate resonance and about 5dB at the 2nd and 3rd modes or 13 dB and 7dB relative to the case without actuator are measured. Note that for this set of measurements open loop damping is decreased relative to previous ones so that the difference rather than the absolute vibration amplitude should be considered in these plots. There is not more vibration reduction at the first plate resonance also because of the influence of the fundamental actuator resonance as indicated by simulations.

4.7 Secondary coil voltage feedback

In order to increase internal velocity feedback gains the use of an internal sensor to implement internal velocity feedback is investigated in this subsection. Using a secondary sensing coil as schematically shown in Figure 4.26 as an internal sensor should give two important advantages [190]: First increased sensing bandwidth is targeted since the sensing coil might have a different self-inductance than the primary one. Second when a secondary sensing coil is used, a current command amplifier can drive the primary coil, so that spillover also should be reduced.

Also, in the double coil case the moving mass consists of a permanent magnet and an axisymmetric iron yoke arranged in such a way that a constant horizontal magnetic field B_g is created in the air gap in which two coils of lengths l_p and l_s are immersed. Both coils are connected to the housing mass so that a current in the primary driving coil I_c and in addition to the formulation in Eq. (4.13) also in the sensing coil I_s, both in radial direction, will generate a vertical actuation force

$$F_a = \psi_p I_c + \psi_s I_s \qquad (4.38)$$

between the moving mass m and the housing mass M connected to the plate. Additionally, following Biot-Savart's law [170], the currents in the coils will also generate a varying magnetic B field in predominantly vertical direction

$$B_V = \mu N_p / h_p I_c + \mu N_s / h_s I_s \qquad (4.39)$$

that depends on the number of windings $N_{s,p}$ and height $h_{s,p}$ of the secondary sensing s and primary driving coil p as well as on the material permeability μ of the magnetic circuit. Since the resulting vertical magnetic field is time-varying and the coils move in a constant horizontal B field a voltage

$$U_s = j\omega B_v A_s + \psi_s \mathbf{v}_s = L_s j\omega I_s + L_{sp} j\omega I_c + \psi_s \mathbf{v}_s \qquad (4.40)$$

will be induced in the sensing coil where $L_s = \mu N_s A_s / h_s$ is the self-inductance of the sensing coil, $L_{sp} = \mu N_p A_s / h_p$ is the coupling or mutual inductance between the primary driving and the secondary sensing coil, $\psi_s = \{\Psi_s \; -\Psi_s\}$ and A_s is the cross section of the sensing coil. As indicated in Figure 4.26 the driving coil is connected to a primary electrical circuit whose current I_c is controlled by a current command amplifier here included in the controller. The sensing coil circuit is connected to the electrical input impedance of the controller $Z_s = -U_s / I_s$ that in the simplest case is a resistance.
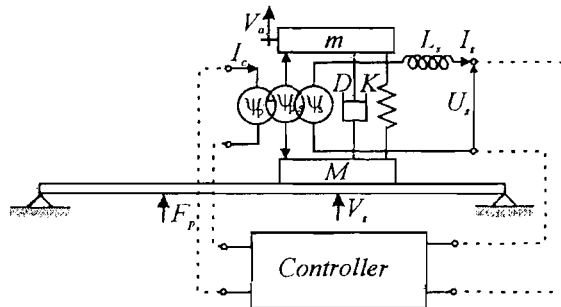
Figure 4.26: *Model of the electrodynamic, inertial actuator connected to the plate.*

Therefore, using Eqs. (4.5) with $F_p=0$, (4.38) and (4.40), only the voltage in the sensing coil,

$$U_s = \frac{\overset{(i)}{L_{sp}j\omega} + \overset{(ii)}{\psi_s Y'_{ss}\psi_p^T}}{1+\underset{(iii)}{\frac{L_s j\omega}{Z_s}}+\underset{(iv)}{\frac{\psi_s Y'_{ss}\psi_s^T}{Z_s}}}I_c \tag{4.41}$$

and not the induced voltage in the driving coil is considered. When the sensing coil voltage is fed back and the driving coil current is used as control input, Equation (4.41) gives the open loop frequency response function (FRF) that is to be considered for stability. The denominator shows the influence of the self-inductance of the secondary sensing coil (iii) that will reduce control bandwidth at higher frequencies. Figure 4.27 shows the amplitude (top plot) and phase shift (bottom plot) of the FRF between the sensing coil voltage and the driving coil current as in Eq. (4.41) (thick solid line) or when the sensing coil inductance is neglected (thin solid line). Clearly the self-inductance of the sensing coil adds phase shift at higher frequencies.
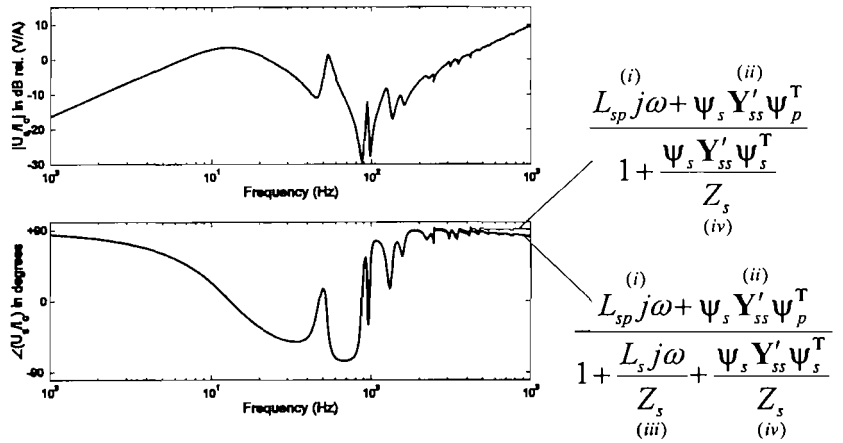
Figure 4.27: *Simulated FRF between the sensing coil voltage and driving coil current with (thick solid line) and without (thin solid line) sensing coil inductance.*

Also, Eq.(4.41) shows a motional impedance term (iv) due to the shunted resistance in the sensing coil that adds a small amount of damping to the plate. Figure 4.28 shows the amplitude (top plot) and phase shift (bottom plot) of the FRF between the voltage in the sensing coil and the current in the driving coil as in Eq.(4.41) (thick solid line) or when the motional impedance term (iv) due to the shunted resistance in the sensing coil is neglected

98

(thin solid line). Clearly term (iv) adds damping to the plate, so that it is also used to simulate damping due to the Eddy current effect.

$$\frac{\overset{(i)}{L_{sp}j\omega} + \overset{(ii)}{\psi_s \mathbf{Y}'_{ss} \psi_p^T}}{1 + \dfrac{L_s j\omega}{Z_s}}$$
(iii)

$$\frac{\overset{(i)}{L_{sp}j\omega} + \overset{(ii)}{\psi_s \mathbf{Y}'_{ss} \psi_p^T}}{1 + \underset{(iii)}{\dfrac{L_s j\omega}{Z_s}} + \underset{(iv)}{\dfrac{\psi_s \mathbf{Y}'_{ss} \psi_s^T}{Z_s}}}$$
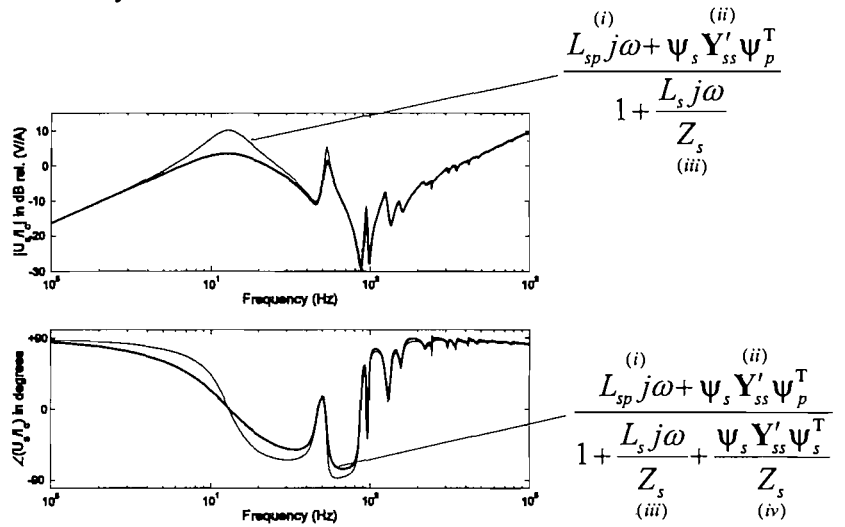
Figure 4.28: *Simulated FRF between the sensing coil voltage and driving coil current with (thick solid line) and without (thin solid line) back-emf influence of the sensing coil.*

The second term (ii) in the numerator shows the influence of the relative velocity between the moving mass and the plate on the sensing coil voltage. Additionally there is the influence of the mutual inductance indicated by the first term (i) that dominates at higher frequencies. Figure 4.29 shows the amplitude (top plot) and phase shift (bottom plot) of the FRF between the driving coil current and the sensing coil voltage (thick solid line) in comparison to terms (i) (thin solid line) and (ii) (thin dashed line) of Eq. (4.41). At higher frequencies the mutual inductance term (i) dominates, whereas at lower frequencies the relative velocity between the inertial mass and the plate can be well sensed.

$$\overset{(i)}{L_{sp}j\omega}$$

$$\frac{\overset{(i)}{L_{sp}j\omega} + \overset{(ii)}{\psi_s \mathbf{Y}'_{ss} \psi_p^T}}{1 + \underset{(iii)}{\dfrac{L_s j\omega}{Z_s}} + \underset{(iv)}{\dfrac{\psi_s \mathbf{Y}'_{ss} \psi_s^T}{Z_s}}}$$

$$\overset{(ii)}{\psi_s \mathbf{Y}'_{ss} \psi_p^T}$$
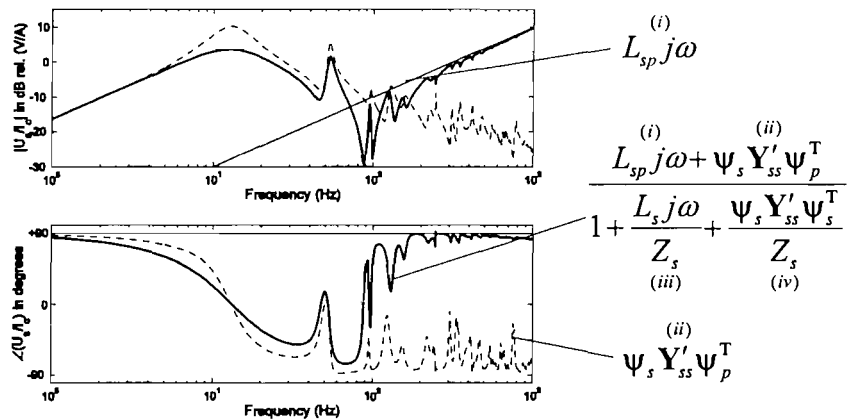
Figure 4.29: *Simulated FRF between the sensing coil voltage and driving coil current (thick solid line), term (i) (thin solid line) and term (ii) (thin dashed line) of Eq. (4.41).*

In Section 4.8 an electronic circuit is proposed that aims to eliminate the mutual inductance term (i) so that the sensing term (ii) becomes dominant. Another way to reduce term (i)

would be the reduction of the coupling inductance L_{sp}. Decreasing the height, the coil length and the number of windings in the driving coil does not give an additional effect to self-sensing where the self-inductance $L_p=\mu N_p A_p/h_p$ limits the control bandwidth. When a sensing coil is used the cross section of the sensing coil A_s can also be reduced to reduce L_{sp}. The simultaneous reduction in L_s is beneficial for increased control bandwidth and can be increased by increasing the sensing coil height or decreasing the number of windings of the sensing coil. In addition to increasing the control bandwidth, sensing sensitivity would be decreased by reducing the coil length of the sensing coil. Therefore it might be preferable to change the placement of the sensing coil relative to the driving coil so that the coupling magnetic flux between both coils is minimized. For minimum coupling they should be placed at an angle of 90 degrees to one another, whereas for sensing and driving the same mechanical degree of freedom they should lie on the same axis. A 45 degrees compromise does not seem to be feasible.

In order to check closed loop performance of sensing coil voltage feedback Equations (4.5), (4.38), (4.40) and the feedback current

$$I_c = - gU_s \tag{4.42}$$

are used to obtain the FRF between the primary disturbance force and the plate velocity at the control actuator position

$$\frac{V_s}{F_p} = \{1 \quad 0\} \frac{y'_{sp}}{1 + \psi_s Y'_{ss}\left(g\psi_p^T + \frac{1}{Z_s}\psi_s^T\right)\bigg/\left(1 + L_{sp}j\omega g + L_s j\omega/Z_s\right)} . \tag{4.43}$$

In this section Eqs. (4.41) and (4.43) are investigated for a purely real feedback gain $G=g$. In the following Section 4.8 a feedback control function $G=G(j\omega)$ compensating for the mutual inductance is considered. The model parameters that give reasonable agreement with measurements with the test set-up are compiled in Table 4.2. A current command amplifier consisting of an OPA 549 operation amplifier in series with a Crown Electronics DC400 amplifier is used to drive the inertial actuator. This combination allows a flat FRF between the amplifier input voltage U_{in} and the coil current I_c up to about 12kHz. A KEMO Benchmark VBF8 variable 4th order filter is used to steeply cut-off the feedback signal at the appropriate frequency.

When the output and input signals $Y_o=U_s$ and $Y_i=I_c$ are considered in the control scheme in Figure 1.2 are

$$G_{sp} = \{1 \quad 0\}\frac{\left(1+\dfrac{L_s j\omega}{Z_s}\right)\mathbf{y}'_{sp}}{1+\dfrac{L_s j\omega}{Z_s}+\dfrac{\mathbf{\psi}_s \mathbf{Y}'_{ss}\mathbf{\psi}_s^{\mathbf{T}}}{Z_s}} \quad , \quad G_{si} = \{1 \quad 0\}\frac{\mathbf{Y}'_{ss}\left(\mathbf{\psi}_p^{\mathbf{T}}\left(1+\dfrac{L_s j\omega}{Z_s}\right)+\mathbf{\psi}_s^{\mathbf{T}}\dfrac{L_{sp} j\omega}{Z_s}\right)}{1+\dfrac{L_s j\omega}{Z_s}+\dfrac{\mathbf{\psi}_s \mathbf{Y}'_{ss}\mathbf{\psi}_s^{\mathbf{T}}}{Z_s}} \quad ,$$

$$G_{op} = \frac{\mathbf{\psi}_s \mathbf{y}'_{sp}}{1+\dfrac{L_s j\omega}{Z_s}+\dfrac{\mathbf{\psi}_s \mathbf{Y}'_{ss}\mathbf{\psi}_s^{\mathbf{T}}}{Z_s}} \quad \text{and} \quad G_{oi} = \frac{L_{sp} j\omega + \mathbf{\psi}_s \mathbf{Y}_{ss}\mathbf{\psi}_p^{\mathbf{T}}}{1+\dfrac{L_s j\omega}{Z_s}+\dfrac{\mathbf{\psi}_s \mathbf{Y}_{ss}\mathbf{\psi}_s^{\mathbf{T}}}{Z_s}} \quad .$$

Table 4.2: *Parameter values used for simulations in Sections 4.7 and 4.8.*

Parameter	Value	Description
l_x	0.414m	Plate length
l_y	0.314m	Plate width
h	0.001m	Plate thickness
x_p	0.345m	X coordinate of primary force position
y_p	0.254m	Y coordinate of primary force position
x_s	0.225m	X coordinate of secondary force position
y_s	0.12m	Y coordinate of secondary force position
ρ	2700kg/m^3	Mass density of plate
K_1	1.2037	Coefficient to adjust for boundary conditions
$\xi_{1,n}$ all other n not specified	0.01	Viscous damping coefficient
$\xi_{2,12,19,20,22}$	0.04	Viscous damping coefficient
ξ_3	0.0001	Viscous damping coefficient
$\xi_{4,30}$	0.1	Viscous damping coefficient
ξ_{11}	0.08	Viscous damping coefficient
ξ_{28}	0.02	Viscous damping coefficient
ξ_{38}	0.001	Viscous damping coefficient
E	71 10^{9}N/m^2	Young's modulus of plate
K_2	0.7042	Coefficient to adjust for boundary conditions
v	0.33	Poisson's ratio
M_p	0.028kg	Added mass of primary shaker
M	0.01kg	Housing mass of inertial actuator
m	0.0203kg	Moving mass of inertial actuator
K	135N/m	Suspension stiffness of inertial actuator
D	1Ns/m	Suspension damping of inertial actuator
Ψ_p	2.6 N/A	Transducer coefficient of primary driving coil
Z_s	1.22 Ω	Shunted impedance to secondary coil
L_s	0.03 mH	Secondary coil inductance
L_{sp}	0.5 mH	Mutual inductance between primary and secondary coil
Ψ_s	1.146 Vs/m	Transducer coefficient of secondary sensing coil
R_3C	L_{sp}*0.6	Characteristic frequency of compensating high-pass filter

Stability

Proportional secondary sensing coil voltage feedback is equivalent to implementing a constant feedback gain g. However, in order to guarantee stability, despite amplifier dynamics and the mutual inductance effect, a 4th order low-pass filter with a 500Hz cut-off frequency has been used in the feedback loop so that a constant feedback gain g is only implemented in a limited frequency band. Figure 4.30 shows the simulated (left plot) and

101

measured (right plot) Nyquist plots of the open loop FRF between the input voltage to the current command amplifier U_i and the filtered sensing coil voltage gU_s. Simulations show the influence of the mechanical modes on the FRF by characteristic loops as do measurements. The first mode that is due to the fundamental actuator resonance is rather big, but structural damping keeps the size of the loops for the plate modes relatively small. The mutual inductance effect would tend to increase amplitudes and produce additional phase shifts at frequencies higher than about 200Hz so that the locus would encircle the critical point of instability (-1,0j). However, measurements and simulations predict well the effect of the 4th order filter that reduces the amplitude at higher frequencies so that the locus does not encircle the critical point. Therefore closed loop conditional stability is predicted. Some smaller loops are also visible in a circle of radius 1 around the critical point beyond about 260Hz in measurements and about 266Hz in simulations so that spillover at higher resonance frequencies is expected in the closed loop case.
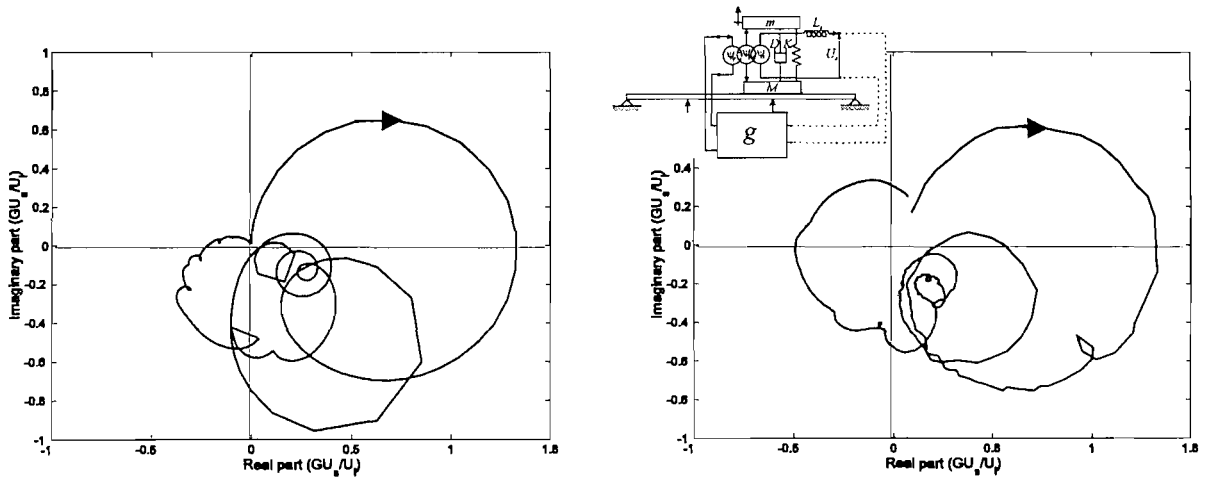
Figure 4.30: *Nyquist plot of the simulated (left) and measured (right) FRF between the input voltage to the current command amplifier and the filtered secondary coil voltage with a cut-off filter at 500Hz.*

Performance

Figure 4.31 shows the amplitude of the simulated (left plot) and measured (right plot) FRF between the primary disturbance force F_p and the plate velocity at the actuator position V_s in the open loop case (thick solid line) and for secondary sensing coil voltage feedback (thin solid line) at a gain margin of 6dB. Simulations may predict the general trend of the FRF with a number of modes identifiable, but modal damping generally differs from measurements. Moreover, neither in the open loop nor in the closed loop case, the resonance peak for the fundamental actuator mode is visible because of relatively high internal actuator damping. Hence, vibration reduction due to the first big loop in Figure 4.30 is not apparent in Figure 4.31, but it is clearly visible during measurements. Vibration reduction up to 8dB is found at the (1,1) plate mode in measurements and simulations, but

102

only small vibration reduction of about 1-2 dB can be obtained at the second and the third peaks. Spillover already appears at the 4th mode at about 145Hz in measurements and at the 5th mode at about 195Hz in simulations. These frequencies are different from the ones predicted by the open loop in Figure 4.30 because Figure 4.31 shows the FRF V_s/F_p and not V_s/F_s and the actuator behaviour is slightly different for large currents used in open loop measurements and for small currents implemented in closed loop measurements.
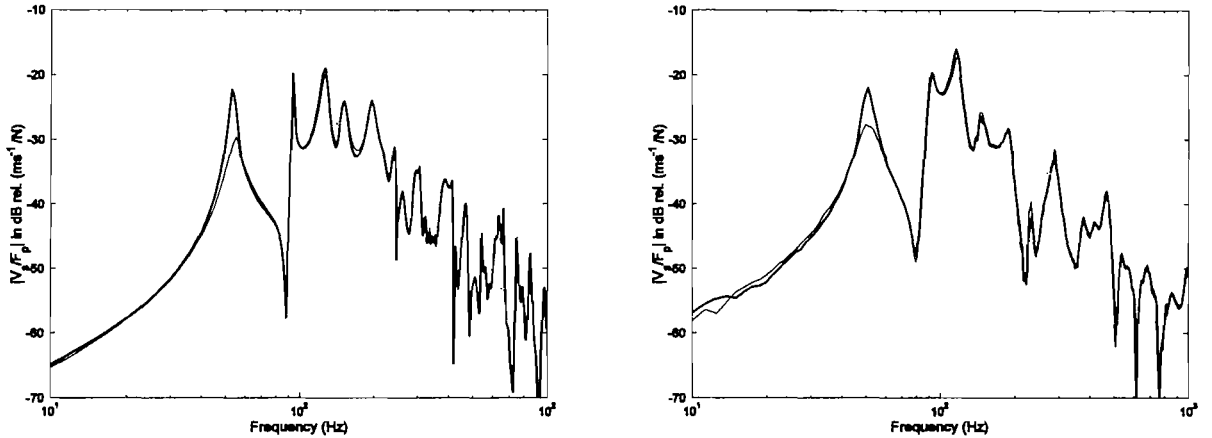
Figure 4.31: *Bode plot of the simulated (left) and measured (right) FRF between the primary disturbance force and the plate velocity at the control actuator in the open loop case (thick solid line) and for filtered secondary voltage feedback (thin solid line).*

4.8   Compensated secondary coil voltage feedback

In order to compensate for the mutual inductance between the two coils that increases amplitudes and adds phase shift at higher frequencies, an electronic circuit similar to the one in [33], is proposed. It consists of a resistor for sensing a voltage proportional to the primary coil current and three operational amplifier circuits that consecutively implement a first order high pass filter to simulate an inductance, an adjustable gain and subtraction of both from the secondary coil voltage as explained in [190]. Up to about 600Hz the FRF of the compensator is therefore given by the following expression

$$G(j\omega)=gCR_3j\omega/(1+CR_3j\omega)L_c/U_s-1.\qquad(4.44)$$

The implementation requires precise tuning and a high operation amplifier bandwidth because of the high pass filter behaviour with high amplitudes at high frequencies. In this circuit the used LM324 operation amplifier adds an additional electrical resonance frequency at about 1kHz so that a low cut-off filter at about 700 Hz has to be used. Alternatively video amplifiers with a higher gain bandwidth product such as the THS4081 could have been implemented.

103

Stability

Figure 4.32 shows the Nyquist plot of the simulated (left) and measured (right) open loop FRF between the input voltage to the current command amplifier U_{in} and the feedback filter output voltage $G(j\omega)U_s$ with a 4th order cut-off filter at 700Hz. For the first fundamental actuator resonance, simulations and measurements agree well and for higher frequencies simulations follow the general measurement trend. Especially in both simulation and measurement plots more loops are visible in the positive real half plane than in Figure 4.30 so that vibration reduction at higher natural frequencies of the plate is expected. The measurement coherence of measurements beyond about 400Hz is very low, firstly because of the effect of low operation amplifier bandwidth and secondly because of actuator non-linearity. In fact the induced voltage in the secondary coil depends on the oscillations of the mass that might be distorted by stick-slip and stroke saturation at some frequencies. The coil voltage is subtracted from a slightly distorted and offset signal of the compensation circuit that is not influenced by stick-slip or stroke saturation. These non-linearities hence stay in the signal and lead to a small coherence at higher frequencies. The compensation circuit is manually tuned to obtain a large control bandwidth that is illustrated by the cut-off filter of 700Hz used for measurements in Figure 4.32. In comparison to the case without compensation a larger control bandwidth is achieved. Nevertheless a gain margin of about 6dB comparable to the one in Figure 4.30 is selected in order to compare performance. Because of the non-ideal inductance behaviour of the actuator, ideal tuning and inductance compensation is not achieved so that the locus in Figure 4.32 lies within a circle of radius 1 around the critical point for several frequency ranges. In these ranges spillover is predicted.
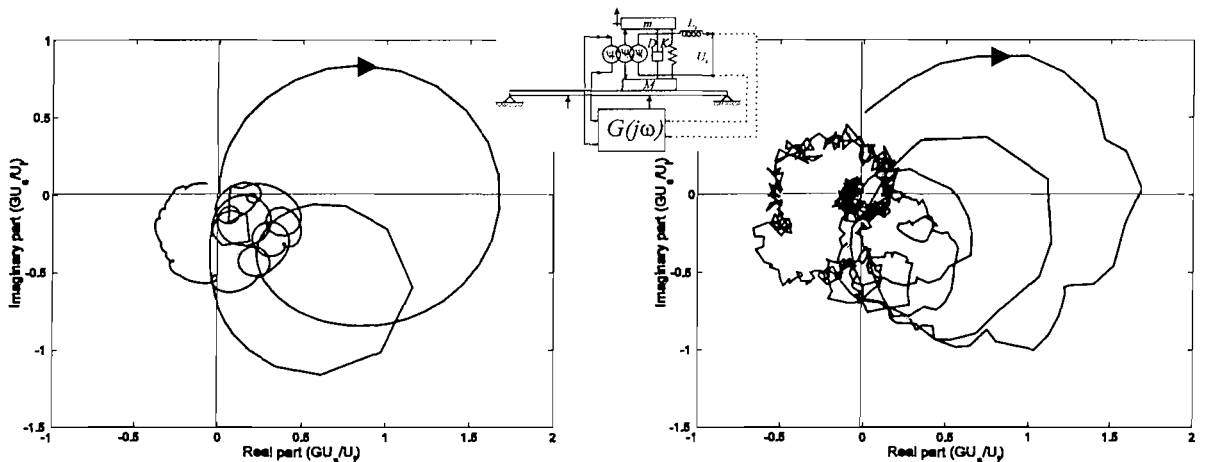
Figure 4.32: *Nyquist plot of the simulated (left) and measured (right) open loop FRF between the input voltage to the current amplifier and the filtered compensator output voltage using a 700Hz filter.*

Performance

Figure 4.33 shows the amplitude of the simulated (left) and measured (right) FRF between the primary disturbance force F_p and the plate velocity at the actuator position V_s in the open loop case (thick solid line) and for compensated secondary coil voltage feedback (thin solid line).
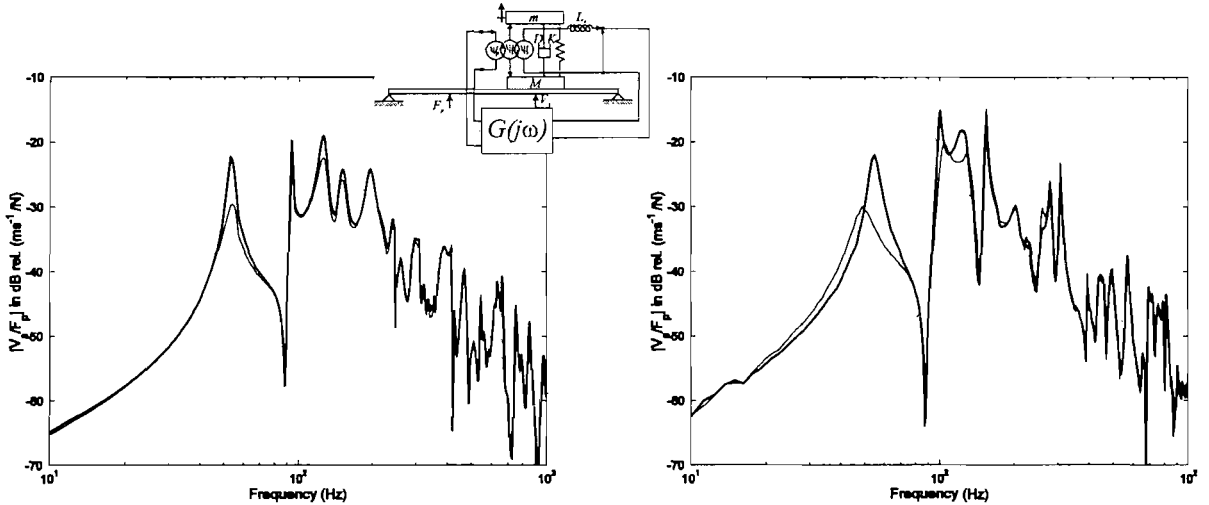
Figure 4.33: *Amplitude of the simulated (left) and measured (right) FRF between the primary disturbance force F_p and the plate velocity at the actuator position V_s in the open loop case (thick solid line) and for compensated secondary coil voltage feedback (thin solid line).*

Simulations and measurements predict vibration reduction of about 8dB at the first plate mode, about 2 to 3dB at the second and third modes and smaller reduction at higher modes. Measurements show slightly larger vibration reduction of the second and third modes since loops are slightly larger in the measurements in Figure 4.32 than in Figure 4.30. There is already spillover into the 4th mode, but vibrations are attenuated at the 5th and 6th mode and spillover prevails for resonance frequencies beyond about 260Hz in measurements and about 346Hz in simulations. This is coherent with predictions in Figure 4.32 where the locus repeatedly enters in the circle of radius 1 around the critical point. Both in simulations and measurements vibration reduction due to the large first loop in Figure 4.32 at the mode associated to the fundamental inertial actuator resonance is not visible.

4.9 Summary

The four control schemes shunted resistor (Fig. 4.14), positive current feedback (Fig. 4.17) and induced voltage feedback with (Fig. 4.20) and without (Fig. 4.23) inductance compensation have been investigated for vibration reduction of a clamped plate using a lightweight, electrodynamic, self-sensing, inertial actuator (SSIA). They have been

105
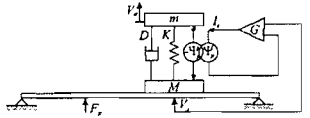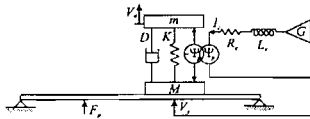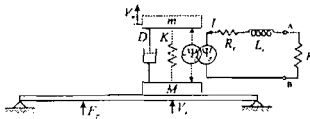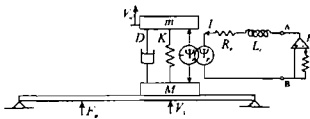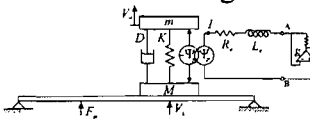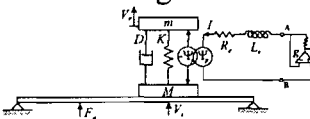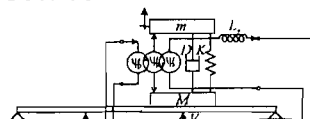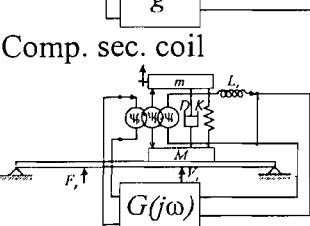
compared to direct velocity feedback a) with an ideal plate velocity sensor (Fig.4.2) b) with an ideal relative velocity sensor (Fig. 4.2) c) with an accelerometer and a voltage driven actuator (Fig. 4.11), d) with an accelerometer and a current driven actuator (Fig. 4.8) and e) with an internal coil sensor (Fig. 4.26) with and without inductance compensation and a current driven actuator. A numerical model of the plate and the electrical circuit has been developed and a general control framework has been presented in the frequency domain. Measurements have shown reasonable agreement with the model up to about 1kHz. Table 4.3 lists the approximately achieved vibration reduction values of the FRF plate velocity at the inertial actuator position relative to a primary force disturbance of the plate. The best result is achieved with an accelerometer and a voltage driven actuator. The best result without accelerometer is achieved with the internal velocity sensor and mutual inductance compensation.

Simulations show that direct external plate velocity feedback with an inertial actuator is not unconditionally stable. Direct feedback of the internal relative velocity between the inertial mass and the plate velocity is unconditionally stable and an inertial actuator is dual to a relative velocity sensor. But lower frequency vibrations may be amplified since some plate resonances are not directly targeted by internal velocity feedback. When the fundamental resonance of the actuator is very small, internal velocity feedback effectively converges to external velocity feedback. Measurements and simulations of direct external plate velocity feedback with the inertial actuator show that the fundamental resonance frequency of the actuator constitutes a lower control bandwidth limit despite collocation of actuator and sensor. This limit is less severe when there is additional passive internal actuator damping. Additionally as in Chapter 2 when a voltage driven actuator is used, the self-inductance effect of the driving coil leads to spillover at higher frequencies in the closed loop case. The self-inductance also limits control bandwidth when a self-sensing inertial actuator is used. Even when using compensation for the self-inductance with an Owens bridge, duality cannot be achieved at higher frequencies. Therefore a secondary coil is proposed as an internal velocity sensor (IVS). The vibration reduction is comparable to the self-sensing (ss) case at lower frequencies and the mutual inductance between the primary driving and the secondary sensing coil limits the control bandwidth. Tuning is easier than with self-sensing and the mutual inductance can be more easily adjusted by dimensioning of the cross-section of the secondary sensing coil.

Increased vibration reduction could probably be achieved by either reducing the fundamental resonance of the inertial actuator using for example a suspension in post-

buckling or by varying internal actuator damping as proposed in [49]. Some indications about the importance of the fundamental resonance frequency are given in Appendix E for a 2DOF analytical model. The influence of internal actuator damping on external velocity feedback is investigated in Chapter 5. The higher frequency limit could be shifted by better compensating for either the self-inductance of the primary driving coil or the mutual inductance between the primary driving and the secondary sensing coil, for example see Section 2.7. Additionally the geometry and the position of the secondary coil could be changed to find an appropriate balance between sensing bandwidth and sensitivity.

Table 4.3: *Approximate measured vibration reduction in dB at the first to 10th plate resonances for the studied control schemes in Chapter 4.*

Control	Res.1	Res.2	Res.3	Res.4	Res.5	Res.6	Res.7	Res.8	Res.9	Res.10	Fig.
DVFB acc. cc.	14	6	6	1	2	4	3	2	6	-	4.10
DVFB acc. vc.	18	9	9	6	3	12	5	9	-	-	4.13
Shunted resistor	3	-	-	-	-	-	-	-	-	-	4.16
Positive current FB	4	3	5	-	-	-	-	-	-	-	4.19
Wheatstone bridge	6	2	1	-	-	-	-	-	-	-	4.22
Owens bridge	5	3	5	-	-	2	2	-	-	-	4.25
Sec. coil	6	1	1	-1	-	2	1	-	-	-	4.31
Comp. sec. coil	6	5	4	-2	-	2	5	1	3	-	4.33

5. VIBRATION CONTROL OF A PLATE WITH AN INERTIAL ACTUATOR AND A DOUBLE LOOP

In the previous chapter it has been found that external direct velocity feedback adds more damping than internal direct velocity feedback when an inertial actuator (IA) with a high fundamental resonance frequency is used. This chapter investigates how far internal direct velocity feedback can be beneficial to stabilize external direct velocity feedback with this kind of inertial actuators (IA). Eddy current damping, internal velocity feedback with self-sensing (ss) actuators or a secondary sensing coil as an internal velocity sensor (IVS) could be used to add internal actuator damping that has also been proposed in [49]. In this chapter all three means in combination with external velocity feedback are investigated. The aim is to find a best combination between internal and external velocity feedback that would lead to relatively large reduction of the plate vibrations. Additionally a combination of internal and external velocity feedback is compared to alternative means of stabilizing inertial actuators in an external velocity feedback loop and purely passive treatments.

Measurements and simulations are carried out on the same model problem of a clamped plate as in Chapters 2 and 4 where the monitor velocity sensor is now used as a control sensor as shown in Figure 5.1.
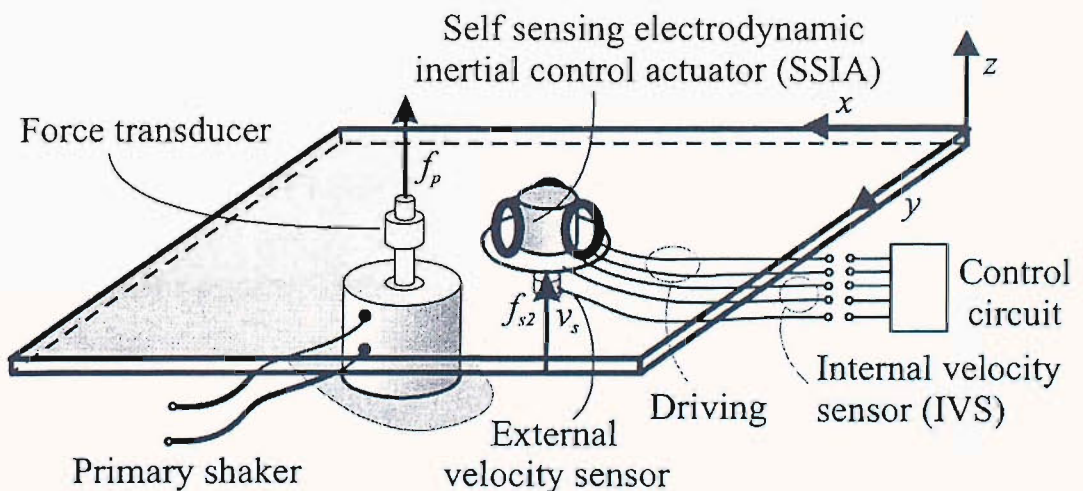
Figure 5.1: *Sketch of the model problem where a test panel is connected to a double-coil, self-sensing electrodynamic inertial actuator which is set to control the vibrations generated by a primary force disturbance.*

Section 5.1 investigates direct external and internal velocity feedback for an inertial actuator with ideal primary force sensor and ideal internal and external velocity sensors. The influence of internal velocity feedback on an external velocity feedback loop is studied

as well as the notion of a best combination of feedback gains. Section 5.2 studies stability and performance of external velocity feedback with a self-sensing actuator and accelerometer in simulations and measurements. Section 5.3 focuses on internal velocity feedback with a secondary sensing coil internal velocity sensor (IVS) and external velocity feedback with an accelerometer. Measurements of the stability behaviour, performance and the effect of a best combination of gains are contrasted to simulations. Section 5.4 considers alternative means of stabilising an inertial actuator used for an external direct velocity feedback loop such as a compensator for the fundamental actuator resonance and a high-pass filter. Stability and performance is investigated in both measurements and simulations. Finally active control is compared to a passive inertial actuator with high internal Eddy current damping and a passive treatment of a similar weight as the actuator.

5.1 Direct internal and external velocity feedback

Figure 5.2 shows a lumped parameter model of the inertial actuator on a plate with internal and external direct velocity feedback. Internal velocity feedback has been found to be unconditionally stable in Section 4.1.3 so that closed loop stability need not be investigated again.
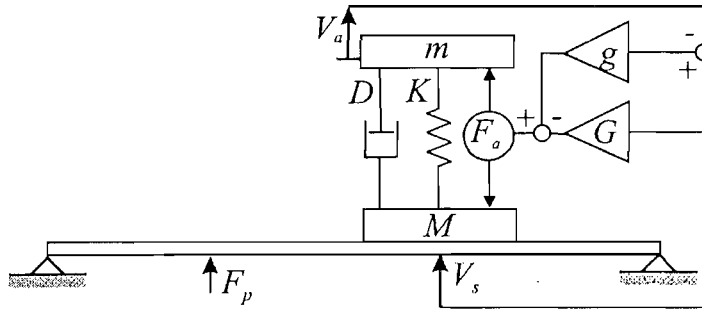
Figure 5.2: *Model of the electrodynamic, inertial actuator connected to the plate.*

For external direct velocity feedback the actuation force is given by

$$F_a = - G\, V_s \qquad\qquad (5.1)$$

and when the internal velocity feedback loop is closed with a feedback gain g, stability of external velocity feedback is investigated with the following FRF:

$$\frac{V_s}{F_a} = \{1 \quad 0\}\left(\mathbf{I} + \mathbf{Y}_{ss}^m\left(\mathbf{Z} + \begin{bmatrix} g & 0 \\ 0 & g \end{bmatrix}\right)\right)^{-1}\mathbf{Y}_{ss}^m\begin{Bmatrix} 1 \\ -1 \end{Bmatrix}. \qquad\qquad (5.2)$$

The closed loop FRF used to evaluate performance is

$$\frac{V_s}{F_p} = \{1 \quad 0\}\left(I + Y_{ss}^m\left(Z + \begin{bmatrix} G+g & 0 \\ -G & g \end{bmatrix}\right)\right)^{-1} y_{sp}^m.$$ (5.3)

This control scheme is not put in the generalized control framework of Figure 1.2 which does not enable the analysis of a double loop feedback control system.

5.1.1 Influence of internal velocity feedback on stability of external velocity feedback

Figure 5.3 shows the simulated FRF between the actuation force and the plate velocity at the control actuator position for several internal velocity feedback gains g, when its amplitude is tuned to a gain margin of 1.25 using G. The gain margin is given by the absolute value of the inverse of the smallest real part of the locus at the intersection point with the real axis [168]. The absolute value of this real part, the inverse of the gain margin, is marked by δ_1 in Figure 5.3. Internal velocity feedback gains are higher in the right plot than in the left plot and they are higher for the simulations marked by a dashed line than for the solid line ones. For increasing internal velocity feedback gains larger parts of the locus move into the negative real half-plane at lower frequencies and the size of loops at higher frequencies in the positive real half-plane seems to increase at constant gain margin. Although the amplitude at the fundamental resonance is decreased relative to the amplitude at the plate resonances, there is an additional phase shift that rotates the loops due to lower frequency plate modes around the origin. As shown in Appendix E for a two degrees of freedom system this phase shift is only observable if structural damping is considered. For increasing feedback gains more and more loops are rotated until, for infinite internal velocity feedback gains, all loops are rotated by $-90°$ and the fundamental resonance is negligible. As stated before for infinite internal velocity feedback gains the model problem behaves like a plate with a point mass at the inertial actuator position. When additionally direct external velocity feedback to the actuation force is implemented, acceleration feedback with an actuator closely attached to the plate results. Since the goal of using a number of decentralised force actuator velocity sensor pairs is to add damping to the plate by direct velocity feedback very large internal velocity feedback gains should not be implemented. The loop due to plate resonances should just be amplified and not substantially rotated into the negative real half-plane. As shown in Figure 5.3 considering the example of the first plate resonance, $n=1$, the real part of the locus at the intersection

110
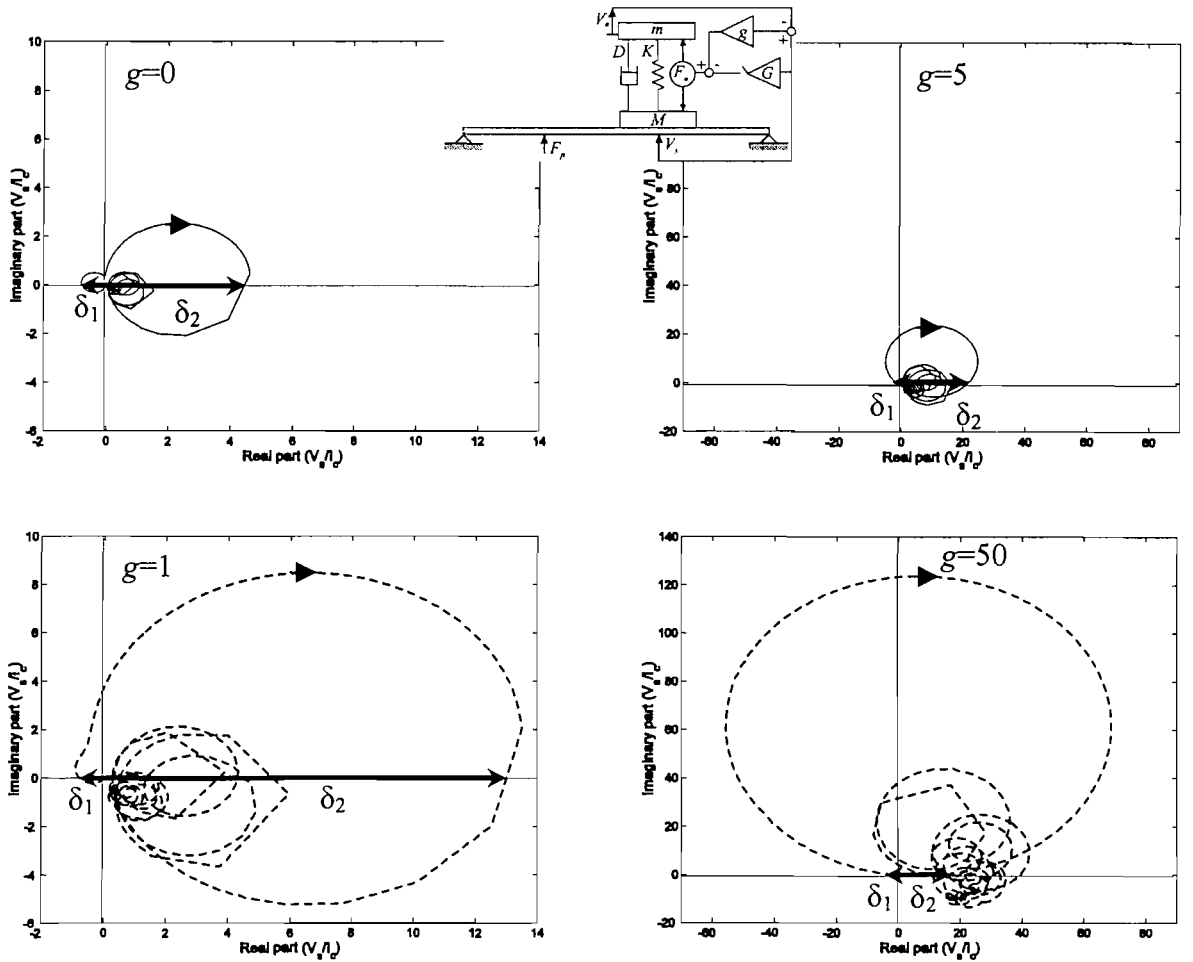
Figure 5.3: *Nyquist plot of the simulated FRF between the actuation force and the plate velocity at the control actuator position for increasing internal velocity feedback gains from solid line to dashed line and from left to right tuned to an external velocity feedback gain margin of* 1.25.

point with the positive real axis δ_{n+1} is a measure for the size of the loop associated to the nth plate mode. The ratio δ_1/δ_{n+1} gives the relative importance of the fundamental resonance peak to the resonance peak at the nth resonance frequency of the plate. When it is minimum, maximum vibration reduction should be achieved at the nth resonance frequency for a given amplification at the fundamental actuator resonance frequency.

Alternatively stability could be assessed by investigating the weighted sum of the open loop FRFs between the actuation force and the internal and external velocities. The weights of each FRF are given by the internal and external velocity feedback gains. In that case the interpretation of internal velocity feedback as internal damping that could also be implemented in a passive way for example by increasing the existing Eddy current damping is lost.

5.1.2 Performance

Figure 5.4 shows the simulated FRF between the primary disturbance force and the plate velocity at the inertial actuator position in the open loop case (thick solid line) and for the same internal velocity feedback gains as in Figure 5.3 at constant gain margins for external velocity feedback (thin solid and thick dashed lines). In the left plot it is obvious that for similar amplification at the fundamental resonance frequency more vibration reduction is achieved at resonance frequencies of the plate, when a higher internal velocity feedback gain is chosen. However, the frequency for which there is spillover has shifted to higher frequencies. As shown in the right plot, even more vibration reduction at resonance frequencies of the plate is achieved, when the internal velocity feedback gain is further increased. In these cases spillover at the fundamental resonance might be bigger since it is not longer linked to δ_1, but rather to the minimum distance of the locus from the critical point. There is a change in the relative importance of the resonance frequencies of the plate so that the optimum direct velocity feedback gain mentioned in Section 2.1.3 might be obtained if the internal velocity feedback was properly chosen.
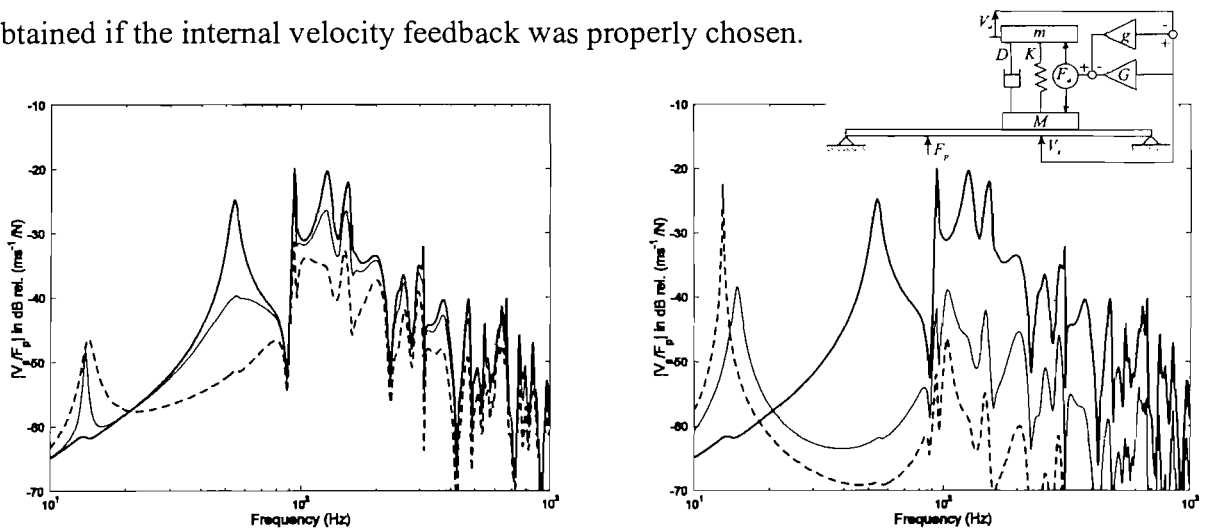
Figure 5.4: *Amplitude of the simulated FRF between the disturbance force and the plate velocity at the control actuator position in the open loop case (thick solid line) and for internal velocity feedback gains 0 (left plot, thin solid line), 1 (left plot, thin dashed line), 5 (right plot, thin solid line) and 50 (right plot, thin dashed line) and external velocity feedback gains tuned to a gain margin of 1.25.*

5.1.3 Best internal and external velocity feedback gain

Instead of directly calculating the kinetic energy as measure for vibration reduction the ratio of δ_1/δ_{n+1} is considered in the open loop. The advantage of this measure is that it can be easily verified experimentally and it does not mean extra effort since before closing the direct velocity feedback loop δ_1 has to be checked in all cases to decide whether closed loop stability is guaranteed. Figure 5.5 shows the simulated ratio δ_1/δ_{n+1} where δ_{n+1}

consecutively is taken for the first, $n=1$, (thick solid line), second, $n=2$, (thin solid line) and fourth, $n=4$, (thick dashed line) resonance frequency of the plate. As expected the ratio decreases for increasing direct internal velocity feedback gains, but beyond a best gain it increases again. This best gain seems to be at higher values for higher resonance frequencies because as shown in Figure 5.3 higher plate resonances are only affected by the additional phase shift, i.e. rotation of loops, for higher internal velocity feedback gains. A best gain for maximum kinetic energy reduction hence depends on the considered resonances and frequency range. Figure 5.5 also implies that the maximum achievable vibration reduction is different at each resonance peak.
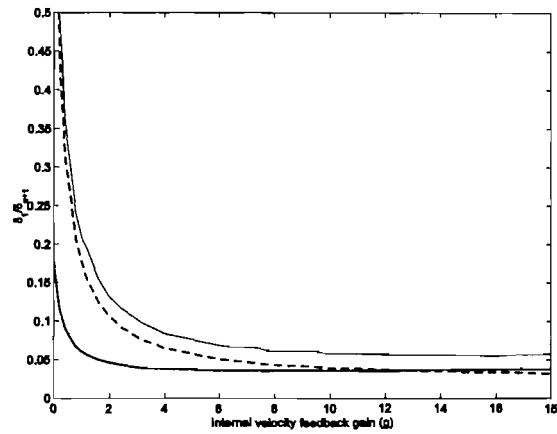
Figure 5.5: *Simulated ratio of δ_1 and δ_2 in Figure 5.3 for the first (thick solid line), second (thin solid line) and fourth (thick dashed line) plate resonance and different internal velocity feedback gains.*

For example, Figure 5.6 shows the simulated amplification at the fundamental resonance peak and vibration reduction at the second resonance peak of the plate in the closed loop case for different internal and external velocity feedback gains. Positive values indicate vibration reduction, whereas negative values effectively mean vibration amplification.
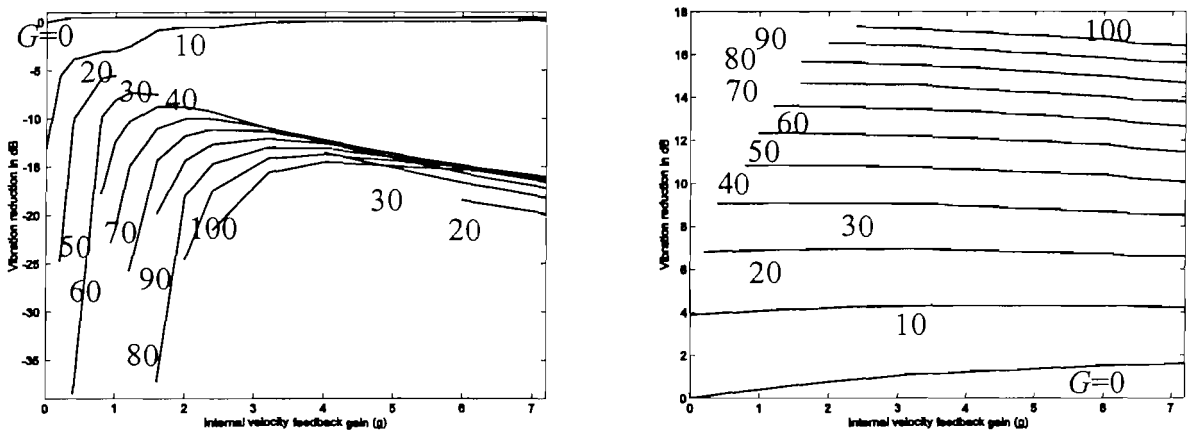
Figure 5.6: *Simulated vibration reduction as function of the internal velocity feedback gain g for different external velocity feedback gains G at the fundamental resonance of the actuator (left plot) and the second plate resonance (right plot).*

113

For a given external velocity feedback gain there is a worst internal velocity feedback gain for which maximum vibration amplification at the fundamental resonance is achieved. Also, at a given external velocity feedback gain there is a best internal velocity feedback gain for which maximum vibration reduction at the second resonance peak is achieved. In general these internal velocity feedback gains do not correspond for different external velocity feedback gains. For increasing external velocity feedback gains the worst internal velocity feedback gain shifts to higher values whereas the best internal velocity feedback gain becomes smaller. For too high external velocity feedback gains the best gain lies at the stability limit. The higher the external velocity feedback gains the higher internal velocity feedback gains have to be implemented in order to guarantee stability. In general more vibration reduction at the second resonance and more amplification at the fundamental resonance result for increasing external velocity feedback gains. Therefore an external velocity feedback gain exists for which vibration amplification at the fundamental resonance would lead to stroke saturation for any internal velocity feedback gain.

5.2 Internal induced voltage and external velocity feedback with accelerometer sensor

Internal velocity feedback could be implemented for example with a pair of relatively heavy accelerometers. In order to reduce weight and complexity the self-sensing arrangement considered in the previous chapter is used for the internal relative velocity feedback loop. Figure 5.7 shows a lumped parameter model where the internal velocity is measured by a Wheatstone bridge and the external velocity by an accelerometer.
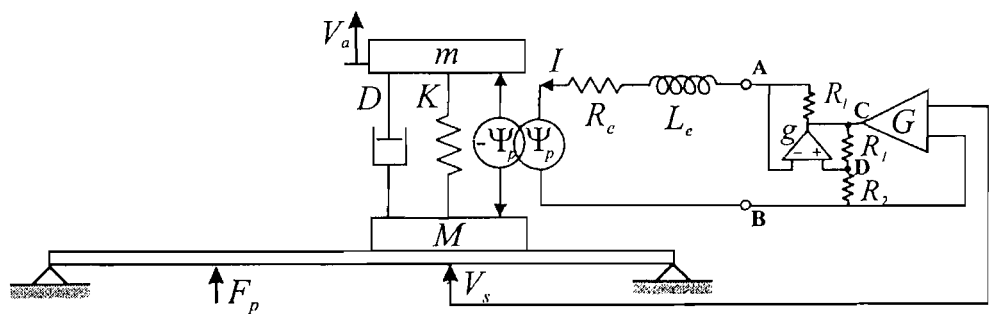
Figure 5.7: *Model of a self-sensing, electrodynamic, inertial actuator connected to a clamped plate.*

Closed loop stability of external velocity feedback to the voltage over one half-bridge

$$U_{BC} = - G\, V_s \qquad\qquad (5.4)$$

is assessed by the open loop FRF

$$\frac{V_s}{U_{BC}} = \frac{\{10\}\mathbf{Y}_{ss}\,\boldsymbol{\psi}_p^{\mathrm{T}}/Z_e'}{\left(\mathbf{I}+\mathbf{Y}_{ss}\left(\mathbf{Z}+\boldsymbol{\psi}_p\left(\dfrac{R_1+R_2+gR_2}{-Z_e'(R_1+R_2+gR_2)+gR_1(R_1+R_2)}\right)\boldsymbol{\psi}_p^{\mathrm{T}}\mathbf{I}\right)\right)} \;,\;(5.5)$$

when the internal induced voltage feedback loop is closed. The closed loop FRF

$$\frac{V_s}{F_p} = \frac{\{10\}\mathbf{y}_{sp}}{\left(\mathbf{I}+\mathbf{Y}_{ss}\left(\mathbf{Z}+\boldsymbol{\psi}_p\left(\left(\dfrac{R_1+R_2+gR_2}{-Z_e'(R_1+R_2+gR_2)+gR_1(R_1+R_2)}\right)\boldsymbol{\psi}_p^{\mathrm{T}}\mathbf{I}+\begin{bmatrix}G&0\\-G&0\end{bmatrix}\Big/Z_e'\right)\right)\right)} \quad (5.6)$$

is investigated for vibration reduction.

Stability

Figure 5.8 shows the simulated (left) and measured (right) FRF between the current in the driving coil or the proportional input voltage to the current amplifier and the plate velocity at the inertial actuator position, when internal velocity feedback is implemented.

Figure 5.8: *Nyquist plot of the simulated (left) and measured (right) FRF between the actuator driving voltage proportional to the driving current and the plate velocity for induced voltage feedback.*

In comparison to the case without internal velocity feedback shown in Figure 4.12 the locus is rotated in clockwise direction about the origin. Since the self-inductance of the primary coil has not been compensated the locus lies in the negative real half-plane for some loops at higher frequencies. At low frequencies measurements show the additional effect of the accelerometer and charge amplifier dynamics. The feedback gain has been

chosen so that the dip in the FRF due to the interaction between the inertial actuator and the measurement electronics lies on the real axis.

Performance

Figure 5.9 shows the FRF between the primary force and the plate velocity at the inertial actuator position in the open loop case (thick solid line) and for combined internal and external velocity feedback with the same feedback gains as in Figure 5.8 (thin solid line). In comparison to Figure 4.13, no significantly more damping is possible, which indicates that Eddy currents already add substantial damping in the case of an open internal velocity feedback loop. Passive damping thus is used to increase stability of active vibration control in a hybrid control architecture. Additionally there is spillover at higher frequencies because the primary coil in the self-sensing actuator is not current driven.
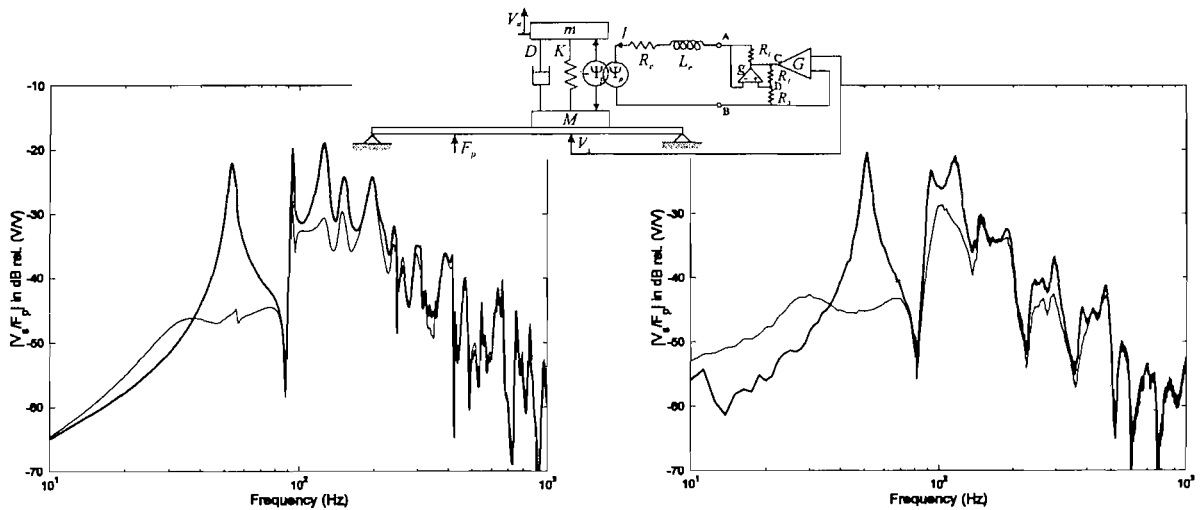
Figure 5.9: *Simulated (left) and measured (right) amplitude of the FRF between the primary force and the plate velocity at the control actuator position in the open loop case (thick solid line) and for combined induced voltage external velocity feedback (thin solid line).*

5.3 Internal sensing coil and external velocity feedback with accelerometer sensor

Instead of using a self-sensing actuator to add internal damping the secondary coil is used for internal velocity feedback [191]. As is schematically shown in Figure 5.10 the primary driving coil is then current driven and both the voltage in the secondary sensing coil and the time-integrated output signal of the accelerometer are fed back. For external velocity feedback a current

$$I_c = - G \, V_s \tag{5.7}$$

116

proportional to the plate velocity is implemented. When internal velocity feedback is implemented by a feedback gain g, stability of direct external velocity feedback is evaluated by

$$\frac{V_s}{I_c} = \{1 \quad 0\} \frac{\mathbf{Y}'_{ss}\mathbf{\psi}_p^T}{1 + \mathbf{\psi}_s \mathbf{Y}'_{ss}\left(g\mathbf{\psi}_p^T + \frac{1}{Z_s}\mathbf{\psi}_s^T \right) \Big/ \left(1 + L_{sp}j\omega g + L_s j\omega/Z_s \right)}. \quad (5.8)$$

The closed loop FRF is

$$\frac{V_s}{F_p} = \{1 \quad 0\} \frac{\mathbf{y}_{sp}}{\mathbf{I} + \mathbf{Y}_{ss}\left[\mathbf{Z} + \mathbf{I}\mathbf{\psi}_s\left(g\mathbf{\psi}_p^T + \frac{1}{Z_s}\mathbf{\psi}_s^T \right) \Big/ \left(1 + L_{sp}j\omega g + L_s j\omega/Z_s \right) + \mathbf{\psi}_p \begin{bmatrix} G & 0 \\ -G & 0 \end{bmatrix} \right]}. \quad (5.9)$$
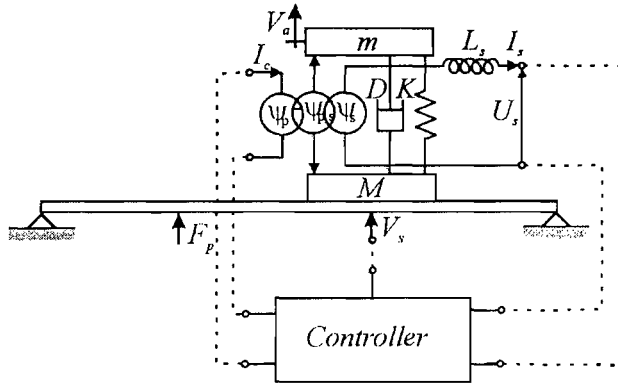
Figure 5.10: *Model of the double-coil electrodynamic actuator connected to a plate.*

5.3.1 Stability

Fig. 5.11 shows the Nyquist plot of the simulated (left) and measured (right) FRF between the primary coil current and the plate velocity at the control actuator position for high internal velocity feedback gains (thin solid line) and for medium internal velocity feedback gains (dash-dotted line) between 1Hz and 160Hz. Considering the measured FRF, the loops due to plate resonances do not significantly move into the left half-plane at high frequencies. In contrast, simulations show small spillover into the negative real half-plane because the simulated filter in the internal velocity feedback loop does not cut-off as steeply as the one used in experiments. At low frequencies again the influence of the accelerometer and its electronics are visible in measurements.

117
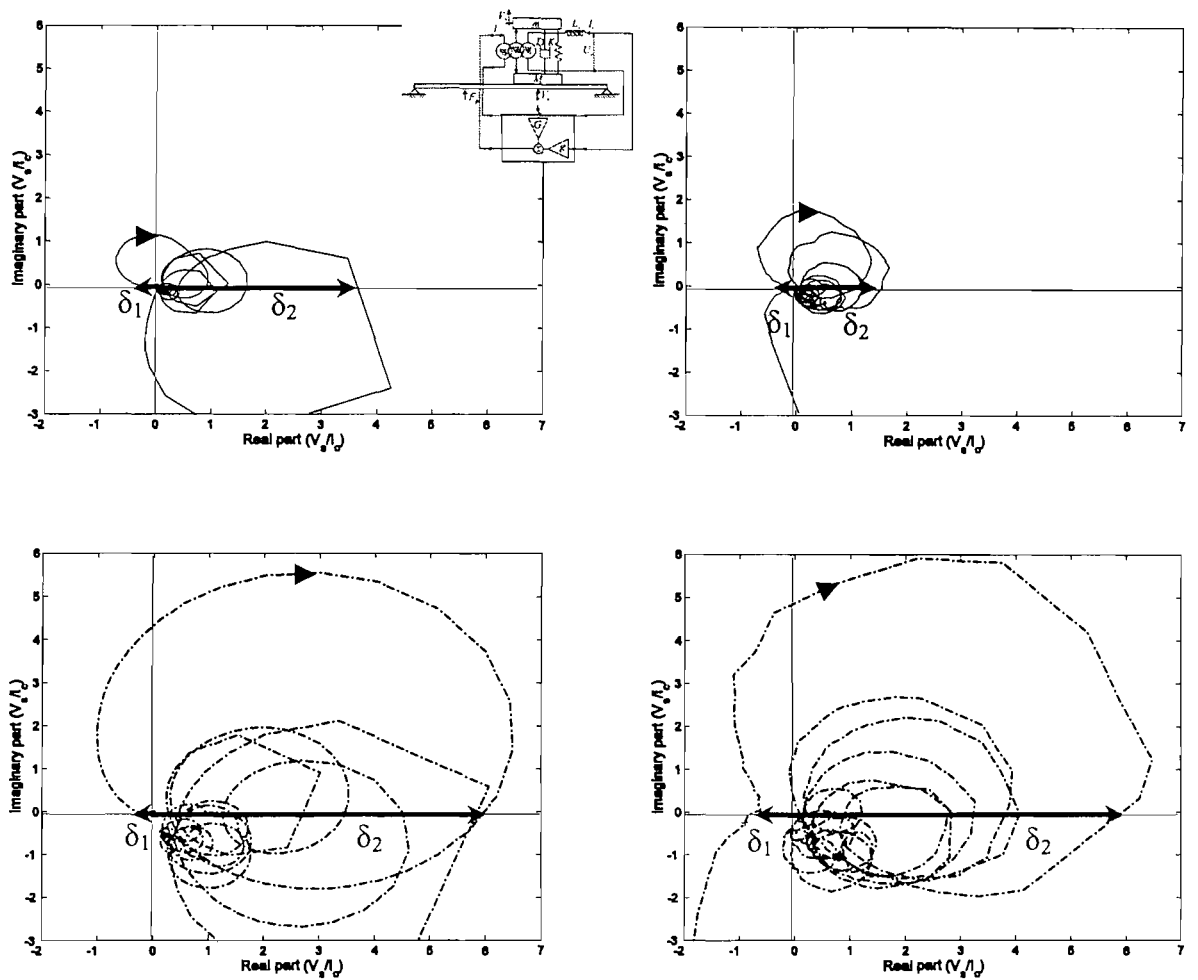
Figure 5.11: *Nyquist plot of the simulated (left) and measured (right) FRF between the primary coil current and the plate velocity at the control actuator position between* 1*Hz and* 160*Hz for high (thin solid line) and medium (thick dash dotted line) internal velocity feedback gains.*

The beneficial effect of additional internal damping using internal relative velocity feedback is clearly visible when the plate is lightly damped since $|\delta_1|$ decreases at similar size of the loops due to plate resonances. Inversely at equal gain margin $1/|\delta_1|$, when medium internal feedback gains (dash-dotted line) are implemented, the part of the loops due to the resonance frequencies of the plate in the positive real half-plane is bigger than in the purely external feedback case shown in Fig. 4.12. Since the farther away the locus in the positive real half-plane is from the critical point the more vibration reduction is achieved [26, 168], larger vibration reduction is predicted at the nth resonance of the plate. For high internal relative velocity feedback (thin solid line) the size of the loops due to the resonance frequencies of the plate in the positive real half-plane decreases at equal gain margin. As also found in simulations in Figure 5.1 this type of behaviour indicates the existence of an optimum control gain. Similar to Section 5.1 the vibration reduction generated by the external velocity feedback loop at the nth resonance of the plate is approximated by the amplitude of the FRF locus at the intersection point with the positive

118

real axis δ_{n+1} which is indicated by δ_2 in Fig.5.11 for the first plate mode. The smaller is the ratio $|\delta_1|/\delta_{n+1}$ the larger is the closed loop vibration reduction predicted at the nth plate mode for a given gain margin or the less spillover is predicted at an expected vibration attenuation. Since this criterion does not consider the smallest distance between the locus and the critical point it also does not guarantee robustness.

5.3.2 Performance

Fig. 5.12 shows the amplitude of the simulated (left) and measured (right) FRF between the primary disturbance force F_p and the plate velocity V_s in the open loop case (thick solid line), for high internal / medium external (thin solid line) and for medium internal / high external velocity feedback gains (thick dashed line).
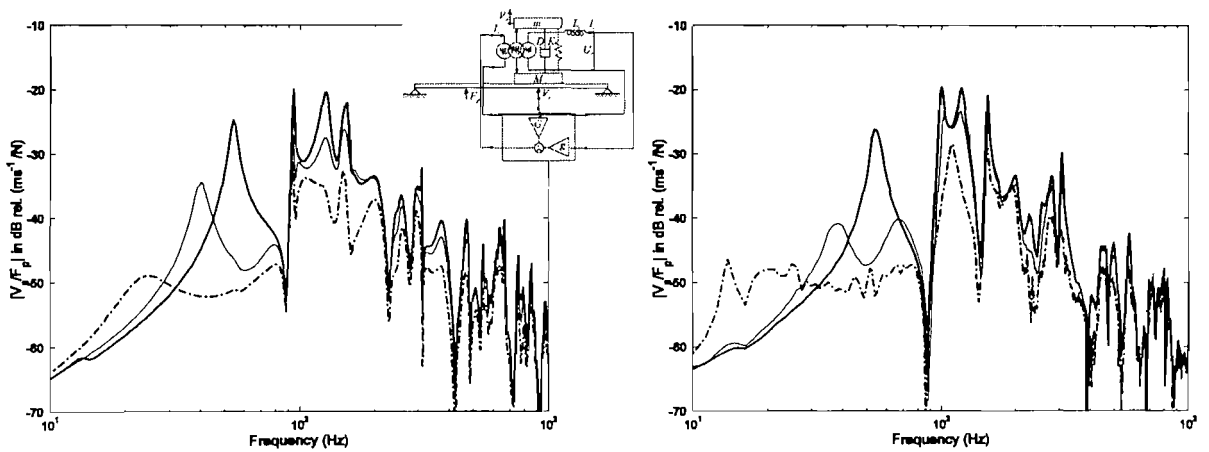
Figure 5.12: *Amplitude of the simulated (left) and measured (right) FRF between the disturbance force and the plate velocity at the control actuator position in the open loop case (thick solid line), internal high gain and external velocity feedback (thin solid line) and internal medium gain and external velocity feedback (thick dashed line).*

Although for a relatively high internal feedback gain these plots show discrepancies between predictions and measurements the trend for significant spillover at frequencies below the first plate resonance is clearly visible. This trend would even be enhanced when larger external velocity feedback gains were implemented. As shown in Appendix E the frequency at which spillover appears also depends on the internal velocity feedback gain. In this case, where the mass of the inertial actuator is smaller than the equivalent mass of the first plate resonance and the first plate resonance frequency is more than four times bigger than the fundamental actuator resonance frequency, increasing internal velocity feedback apparently does not reduce the frequency at which spillover ω_{so} occurs. Larger vibration reductions of up to 21 dB and up to 10 dB at higher plate resonances are possible

119

even with only a medium internal and a high external velocity feedback gain. Higher external velocity feedback gains cannot be implemented because of stability limits due to the non-ideal time integrator of the charge amplifier.

5.3.3 Best gain internal sensing coil and external velocity feedback with accelerometer sensor

Figure 5.12 indicates that there is a best internal velocity feedback gain for which maximum vibration reduction can be achieved at a targeted resonance peak. In this section the best internal control gain with reference to maximum vibration reduction at the first resonance frequency of the plate is considered.

Figure 5.13 shows the measured (dots) and simulated (lines) ratios $|\delta_1|/\delta_2$ in the case with coupling inductance between the primary and the secondary coils (solid line) and for ideal internal relative velocity feedback (dashed line).
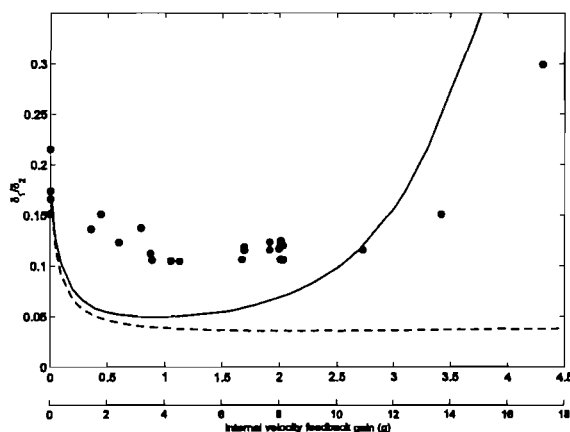
Figure 5.13: *Simulated (lines) and measured (dots) ratio between δ_1 and δ_2 in Figure 5.11 for the first resonance frequency of the plate and different internal velocity feedback gains with secondary coil voltage feedback (solid line and upper x-axis) and relative velocity feedback (dashed line and lower x-axis).*

Both measurements and simulations show that in the case with coupling inductance there is a best gain for which this ratio becomes minimum i.e. maximum vibration reduction is expected at the first plate resonance for a given gain margin. This gain margin also determines the amount of spillover at the fundamental resonance frequency. The measurement results are distorted by the non-ideal integrator in the charge amplifier. In the case without coupling inductance between the primary and the secondary coils (dashed line), but with plate damping, this minimum is smaller; it lies at much higher gains and is much shallower.

120

Figure 5.14 shows the simulated (left) and measured (right) vibration reduction at the first plate resonance for different internal and external velocity feedback gains. The measurements in Figure 5.12 correspond to the highest and lowest external velocity feedback gains implemented experimentally. If no external velocity feedback is used high internal velocity feedback gains have to be implemented to achieve about 12 dB vibration reduction at the first resonance frequency. For higher gains vibration reduction levels off or is even reduced since the frequency for which spillover occurs approaches the resonance frequency of the targeted first plate mode. If only external velocity feedback is implemented vibration reduction of about 16dB is possible before the actuator becomes unstable.
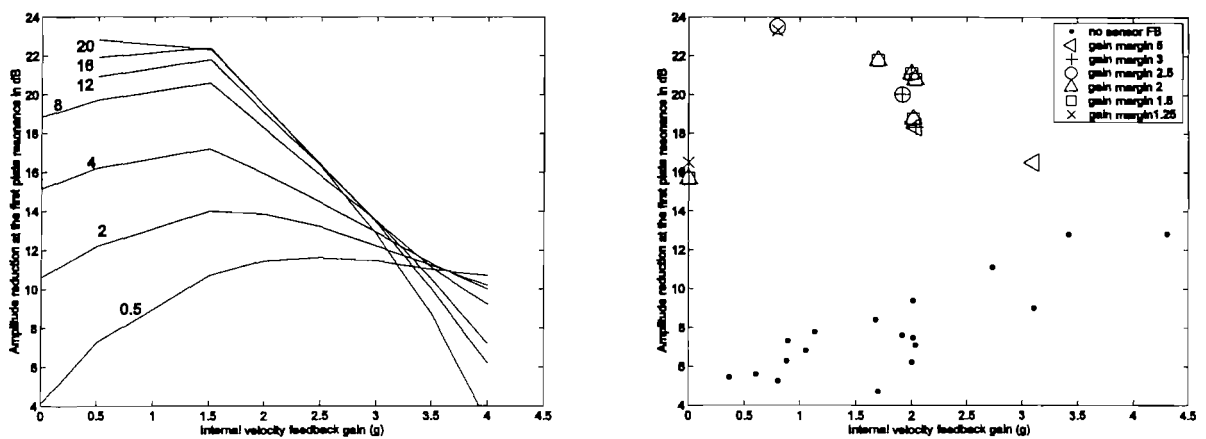
Figure 5.14: *Simulated (left) and measured (right) vibration reduction at the resonance frequency of the first plate resonance as function of the internal velocity feedback gain g for different external velocity feedback gains.*

Internal actuator damping is increased by applying internal, relative velocity feedback with a secondary coil so that higher external velocity feedback gains can be implemented. If, for a given external velocity feedback gain, not enough internal damping is added, the closed loop will become unstable. If too much internal damping is added, following the formulae in Appendix E, if $\xi_0 \gg \xi_1 \omega_1/\omega_0$ and $1+m/M_1+\xi_1/\xi_0\omega_1/\omega_0+G_1/4/M_1/\xi_0 \rightarrow 1$, spillover appears at frequencies close to the resonance frequency of the first plate mode so that vibration reduction decreases again. Hence, as indicated in Figure 5.13, there is a best combination of internal and external velocity feedback gains for which maximum vibration reduction is achieved when the first resonance of the plate is considered. The necessary high external velocity feedback gain has not been implemented experimentally because of the additional phase shift due to the non-ideal integrator in the charge amplifier of the accelerometer that is used to sense the plate vibration. Even for the high external velocity feedback gain measurements in Fig. 5.12

(dashed line) very low frequency vibrations are present that reduce measurement coherence due to stroke saturation.

5.4 Comparison to alternative means of stabilisation and vibration reduction

According to the results presented in the previous sections internal velocity feedback enables the implementation of external velocity feedback control loops with relatively large control gains without the need of additional compensators. In this section different compensators, also presented in [192], are investigated with reference to their ability to stabilize inertial actuators used in a direct velocity feedback loop. For comparison measurements with a passive treatment and the passive inertial actuator only are also presented. Parameter values used for additional simulations in Section 5.4 are listed in Table 5.1.

Table 5.1: *Parameter values used for simulations in Section 5.4.*

Parameter	Value	Description
G_1	2	Proportional feedback gain in compensator for inertial actuator
$C_1 R_4$	0.0094	Cut-on frequency for integrated displacement feedback
$C_2 R_5$	0.0210	Damping in compensator for inertial actuator
ω_{co}	9.3621 rad/s	Cut-on frequency for high-pass filter in compensator
ω_{hp}	43.982 rad/s	Cut-on frequency for high-pass filter

5.4.1 Compensator for the fundamental actuator resonance

In order to compensate for the fundamental resonance an inverted version of Eq. (3.1) shown in Figure 1.3 is implemented electronically. In simulations the FRF

$$\frac{I_c}{U_{in}} = \left(G_1 + \left(\frac{1}{j\omega C_1 R_4} \right)^2 + \frac{1}{j\omega C_2 R_5} \right) \left(\frac{j\omega}{j\omega + \omega_{co}} \right)^6 \qquad (5.10)$$

is multiplied in series to the current command amplifier of the primary driving coil and the time integrating charge amplifier of the accelerometer. Depending on the gains G_1, the value of the resistors R_4 and R_5 the direct external velocity, the integrated displacement and the displacement feedback gain can be adjusted to give the inverse of the FRF shown in

Figure 1.3. The capacitors C_1 and C_2 have fixed values that can be easily implemented. The additional approximately 6th order high pass filter with cut-on frequency ω_{co} is added in order to prevent saturation in the electronics because of high amplitudes at very low frequencies. Figure 5.15 shows the simulated (left) and measured (right) FRF of the compensator that approximately follows the inverse behaviour of Figure 1.3 where the damping is adjusted to fit the value observed at the inertial actuator. Measurements and simulations clearly show that the high-pass filter at lower frequencies severely distorts the compensator at lower frequencies up to the fundamental actuator resonance. This compensator also does not consider changes in frequency and amplitude of the fundamental resonance for example due to fatigue, temperature changes, etc.
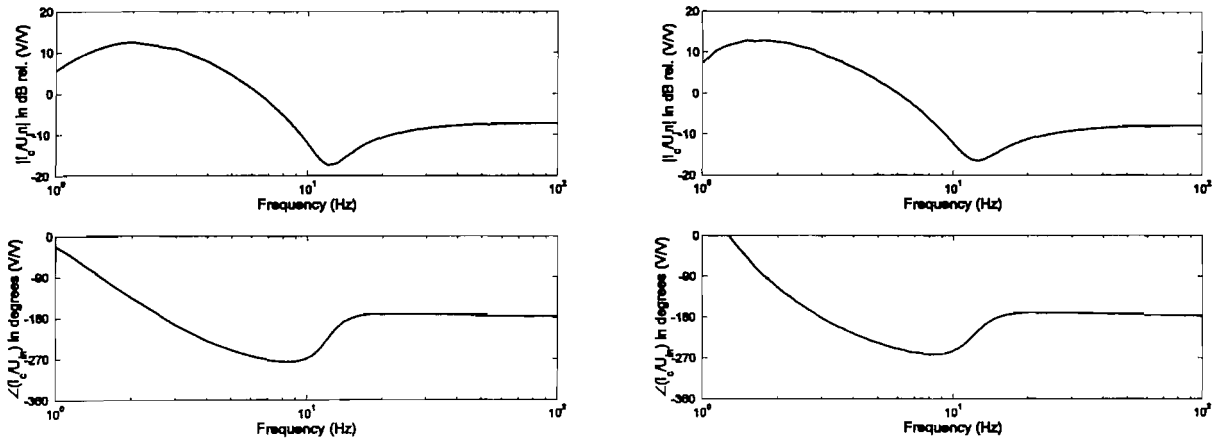
Figure 5.15: *Simulated (left) and measured (right) Bode plot of the compensator FRF between compensator input and output voltage.*

When the electronic compensator is inserted in the feedback loop, closed loop stability is investigated with the FRF between the input voltage to the current driving amplifier and the plate velocity at the inertial actuator position

$$\frac{V_s}{U_{in}} = \left\{ 1 \quad 0 \right\} \mathbf{Y}'_{ss} \boldsymbol{\psi}_p^T \left(G_1 + \left(\frac{1}{j\omega C_1 R_4} \right)^2 + \frac{1}{j\omega C_2 R_5} \right) \left(\frac{j\omega}{j\omega + \omega_{co}} \right)^6. \tag{5.11}$$

Figure 5.16 shows this simulated (left) and measured (right) FRF that shows that in comparison to the current command case, shown in Figure 4.9, and even to the voltage command case, shown in Figure 4.12, the fundamental actuator resonance is partly compensated. Since current command has been used, the loops at higher frequencies do not move into the negative real half-plane in contrast to the voltage command case in Figure 4.12. Additionally, the measured locus shows high amplitudes at lower frequencies.

123
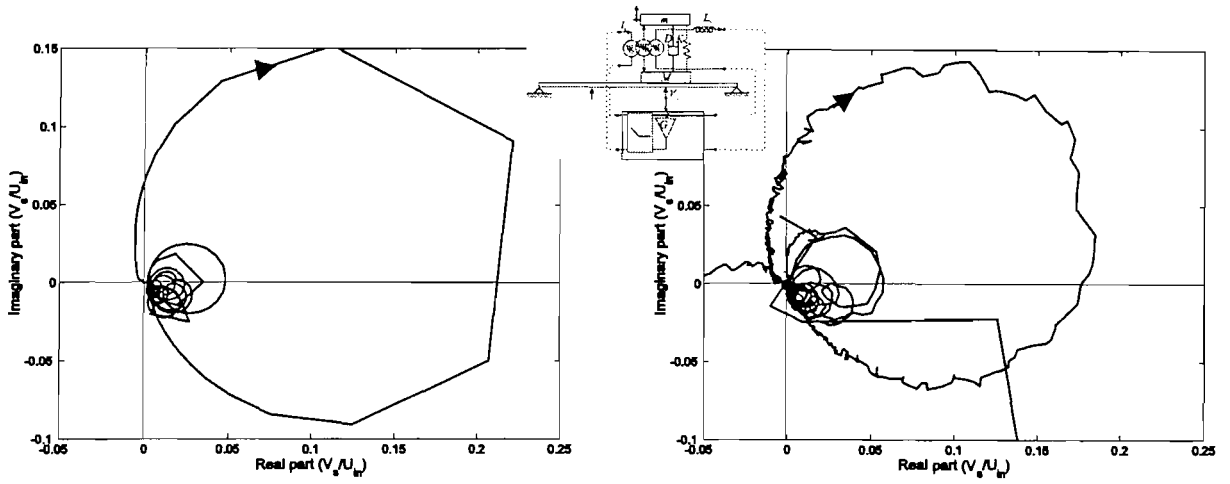
Figure 5.16: *Simulated (left) and measured (right) Nyquist plot of the FRF between the input voltage of the compensator to the plate velocity at the control actuator position; zoom at the origin.*

The locus shown in Figure 5.16 is actually part of a bigger loop as shown in Figure 5.17. This additional loop at lower frequencies is not predicted by simulations.
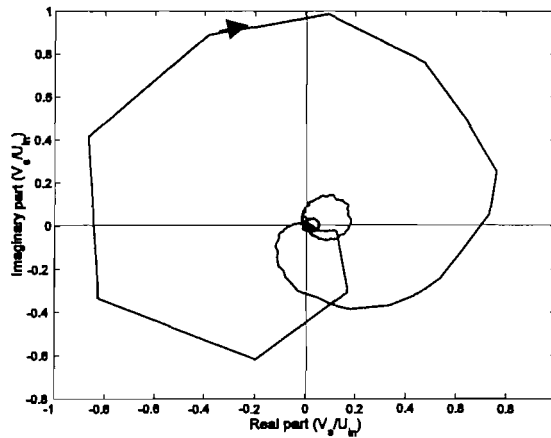
Figure 5.17: *Measured Nyquist plot of the FRF between the input voltage of the compensator to the plate velocity at the actuator position including lower frequencies.*

Dynamics of the measurement equipment, accelerometer and charge amplifier, at lower frequencies are probably responsible for this behaviour that severely limits direct velocity feedback gains. For instance, the previous measurements presented in this chapter the charge amplifier showed high additional amplitudes and phase shifts at frequencies below the inertial resonance frequency. When the external velocity is fed back to the input voltage of the current drive amplifier

$$U_{in} = - G \, V_s \quad , \qquad (5.12)$$

124

the closed loop FRF of the plate is

$$\frac{V_s}{F_p} = \frac{\{1 \quad 0\}\mathbf{y}'_{sp}}{1 + G\{1 \quad 0\}\mathbf{Y}'_{ss}\mathbf{\psi}_p^T\left(G_1 + \left(\dfrac{1}{j\omega C_1 R_4}\right)^2 + \dfrac{1}{j\omega C_2 R_5}\right)\left(\dfrac{j\omega}{j\omega + \omega_{co}}\right)^6} . \quad (5.13)$$

Figure 5.18 shows the simulated (left) and measured (right) FRF between the primary disturbance force F_p and the plate velocity at the control actuator position V_s in the open loop case (thick solid line) and for compensated velocity feedback (thin solid line). Due to changes in boundary conditions and variations in the primary force excitation, resulting in a reduced influence of the force transducer, measurements and simulations no longer agree well.
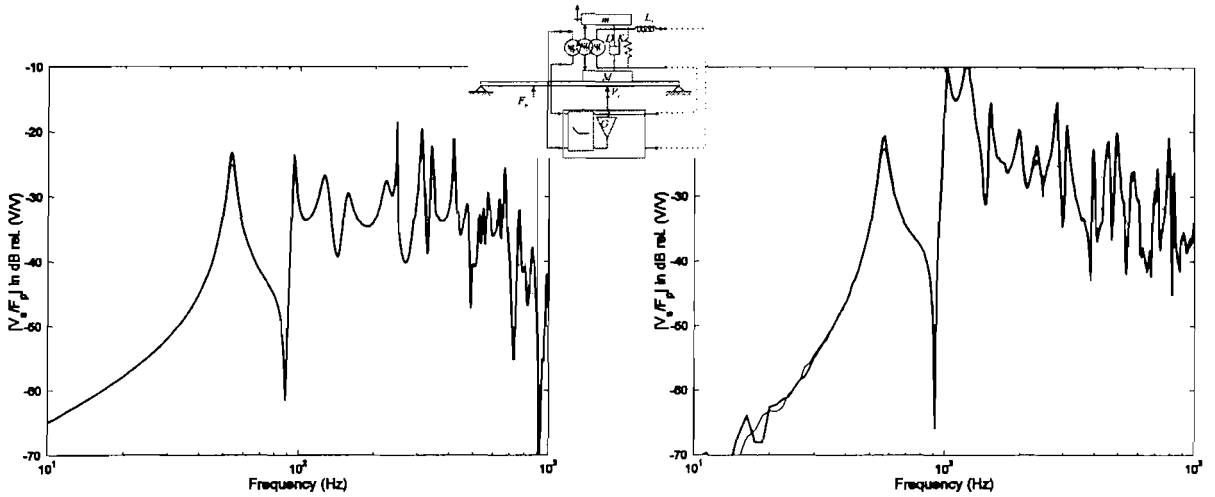
Figure 5.18: *Simulated (left) and measured (right) amplitude of the FRF between the primary force and the plate velocity at the control actuator position in the open loop case (thick solid line) and for external velocity feedback with compensator (thin solid line).*

These variations illustrate the effect of uncertainties on the FRF. Since direct velocity feedback is used, there is a small risk of instability due to changes in the plate structure. However, as explained before, only small feedback gains can be realized with the chosen compensator circuit. As a result only small vibration reduction is visible at the first plate resonance.

5.4.2 High-pass filter

Because of the difficult implementation of twice integrated velocity feedback a high-pass filter had to be added. As a simplification it is proposed to only use a high-pass filter that

125

cuts-off the actuator dynamics at lower frequencies below 5Hz. When direct external velocity feedback to the input voltage of the current command amplifier

$$U_{in} = - G \, V_s \quad (5.14)$$

is to be implemented, the open loop FRF between the input voltage to the current command amplifier and the plate velocity at the inertial actuator position is then

$$\frac{V_s}{U_{in}} = \left(\frac{j\omega}{j\omega + \omega_{hp}} \right)^6 \{1 \quad 0\} \, \mathbf{Y}'_{ss} \mathbf{\psi}^{\mathrm{T}}_p . \quad (5.15)$$

The closed loop FRF is

$$\frac{V_s}{F_p} = \frac{\{1 \quad 0\} \, y'_{sp}}{1 + G \left(\dfrac{j\omega}{j\omega + \omega_{hp}} \right)^6 \{1 \quad 0\} \, \mathbf{Y}'_{ss} \mathbf{\psi}^{\mathrm{T}}_p} . \quad (5.16)$$

Figure 5.19 shows the simulated (left) and measured FRF when the high-pass filter is used in series to the charge amplifier of the accelerometer. The loop due to the fundamental actuator resonance is very much cut off, but also the loops due to the resonance frequencies of the plate and the measurement electronics are rotated about the origin because of the phase shift associated to the high-pass filter. Therefore spillover is still expected in the closed loop.
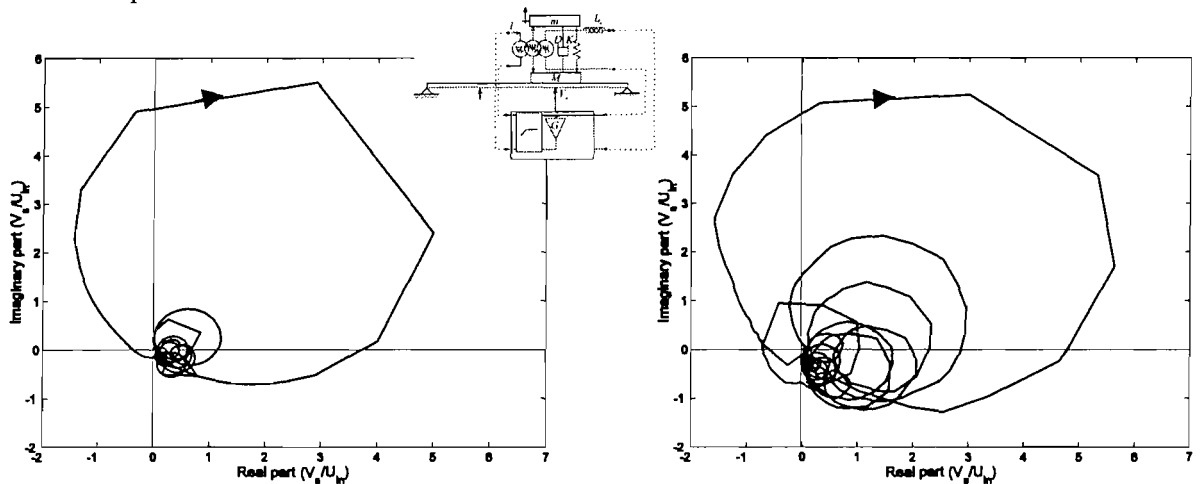
Figure 5.19: *Simulated (left) and measured (right) Nyquist plot of the FRF between the actuator driving current and the plate velocity including a 5Hz high-pass filter.*

Figure 5.20 shows the simulated (left) and measured (right) FRF between the primary disturbance force F_p and the plate velocity V_s at the secondary actuator position in the open loop case (thick solid line) and for velocity feedback with a 5Hz high-pass filter in the feedback loop. Comparable vibration reduction as in the direct velocity feedback case shown in Figure 4.13 is achieved. But spillover at lower frequencies now occurs at higher frequencies in the audible range.
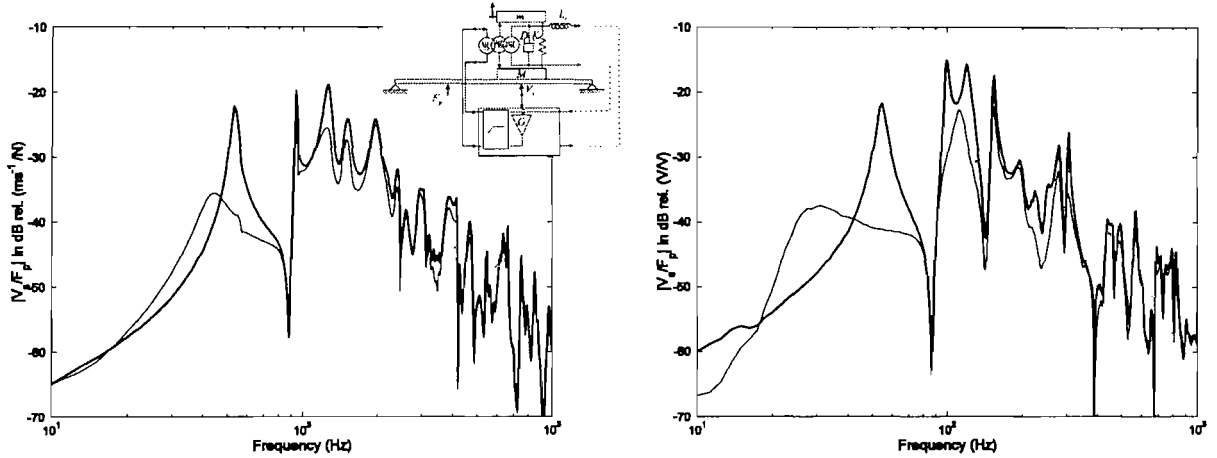
Figure 5.20: *Simulated (left) and measured (right) amplitude of the FRF between the primary force and the plate velocity at the control actuator position in the open loop case (thick solid line) and for external velocity feedback with 5Hz high-pass filter (thin solid line).*

5.4.3 Passive means

Figure 5.21 shows the FRF between the primary force and the plate velocity at the control actuator position in the case without actuator (thick solid line), in the case with inertial actuator (thin solid line) and in the case without actuator when a passive damping treatment is applied centred at the inertial actuator position (dashed line).
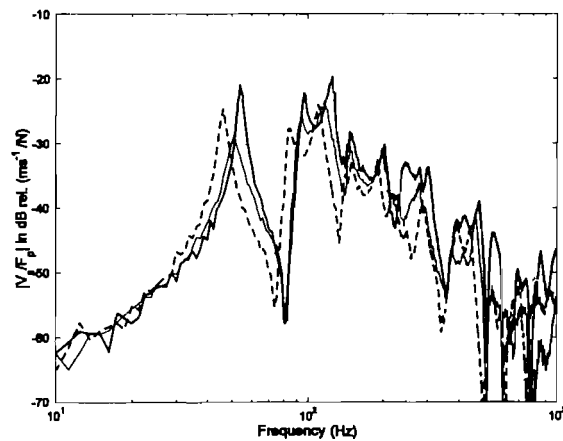
Figure 5.21: *Amplitude of the FRF between the disturbance force F_p and the plate velocity V_s without actuator (thick solid line) with actuator (thin solid line) and using a passive damping treatment of 55 grams (thick dashed line).*

127

The clamped plate with the passive treatment of 0.055kg and dimension 0.2mx0.06mx0.003m is shown in Figure 5.22.
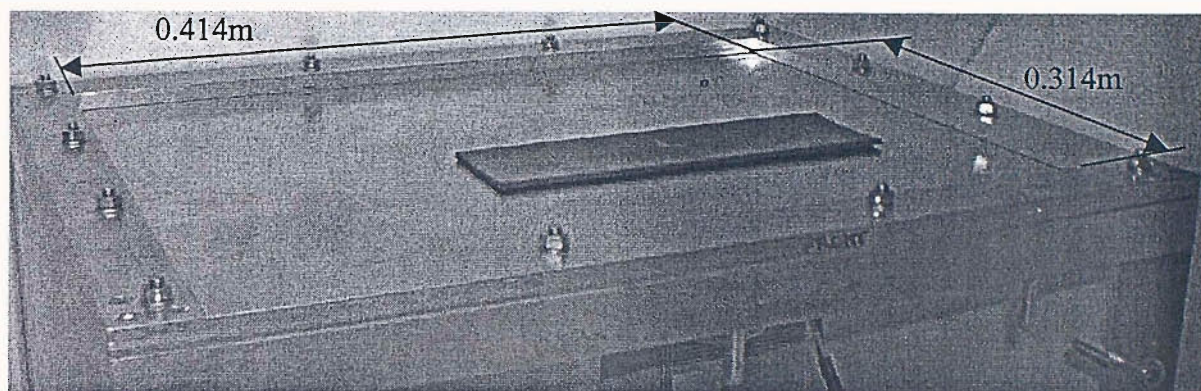
Figure 5.22: *Photograph of the experimental set-up with the primary shaker below the plate in the background and the passive treatment above the plate in the foreground.*

Considering the case without actuator, the mass effect of the primary force transducer of 0.028kg produces the characteristic roll-off at higher frequencies. The velocity sensor does only add little additional mass of about 0.005kg. When the actuator is added, relatively high additional vibration reduction is visible at the lowest flexible resonance frequency of the plate and to a lesser extent also at higher resonance frequencies. At higher frequencies the additional mass effect of the actuator is visible since the roll-off of the FRF is more pronounced. The fundamental resonance of the inertial actuator at about 13Hz does not show a significant effect on the FRF because of the high passive, internal actuator damping. The passive treatment is mainly effective at higher frequencies due to its mass effect, whereas vibration reduction at lower frequencies is limited. Also, due to its higher weight, the resonance frequencies of the plate are more shifted to lower frequencies than in the cases with and without actuator.

5.5   Summary

In this chapter active vibration control with a lightweight, electrodynamic, inertial actuator on a plate using an internal and an external velocity feedback loop has been investigated.

Simulations assuming ideal external, internal and force sensor behaviour have shown that there is a best combination of internal and external velocity feedback gains for vibration reduction at a targeted resonance frequency. Despite internal velocity feedback, the external velocity feedback gain is limited by the amplification at the fundamental actuator

resonance that could lead to stroke saturation for high amplitudes. Also, at high external velocity feedback gains the best internal velocity feedback gain is close to the stability limit.

Simulations and measurements using an accelerometer and an inertial actuator for external velocity feedback on the model problem have shown that passive means such as eddy currents induced in the coil former may implement high internal damping. When using a self-sensing actuator to implement internal velocity feedback, the self-inductance of the actuator leads to spillover at higher frequencies. Also, the dynamics of the accelerometer and its time-integrated charge amplifier distort the internal damping effect at lower frequencies. These dynamics limit external velocity feedback gains when a secondary coil is used to implement internal velocity feedback. Still when considering the coupling inductance between the primary and the secondary coil, there is a best internal velocity feedback gain. As shown in Table 5.2 more vibration reduction is observed when best internal and external velocity feedback gains are implemented than with just external velocity feedback and high passive internal eddy current damping.

Using a compensator for the fundamental actuator resonance or cutting it off with a high-pass filter is less effective than the combined internal and external velocity feedback. Finally in most active control cases larger vibration reduction is achieved than when a passive treatment of 55grams is applied or when only the passive effect of the inertial actuator of 34grams is used.

In comparison to the results in Chapter 4 more vibration reduction is achieved when the internal direct velocity feedback loop is properly adjusted, but simple external velocity feedback can give more vibration reduction than some other more complicated active vibration control schemes.

Table 5.2: *Approximate measured vibration reduction in dB at the first to 10th plate resonances for the studied control schemes in Chapter 5.*

Ext. FB gain	Int. FB gain	Res.1	Res.2	Res.3	Res.4	Res.5	Res.6	Res.7	Res.8	Res.9	Res.10	Fig.
High	Med. ind. vol.	22	5	9	1	1	3	2	6	6	-	5.9

Med.	High coil FB	14	4	4	6	2	5	3	2	6	2	5.12

High	Med. coil FB	21	9	9	8	2	6	5	6	12	3	5.12

Integrated displacement FB		3	-	-	-	-	1	-	-	-	-	5.18

High-pass filter		20	8	7	5	2	7	7	4	9	1	5.20

With actuator*		8	3	4	2	1	5	3	6	6	6	5.21
55g passive*		3	5	4	5	3	5	6	6	-	2	5.21

* relative to plate without actuator

6. CONCLUSION

The main goal of this thesis is to investigate, design and realize a lightweight, self-contained force actuator velocity sensor device that can be used to reduce the structural response at resonance frequencies. In particular it should be suitable for application in a decentralised active damping scheme with a large number of collocated force actuator velocity sensor units on a mechanical structure [25].

As illustrated in the introduction, a self-sensing, electrodynamic, inertial actuator (SSIA) seems to be a promising approach since it potentially allows both collocation and duality in practice. Two major challenges with this approach have been identified and tackled in this thesis. First the inductance behaviour of an electrodynamic actuator which constitutes a bandwidth limit at higher frequencies for a self-sensing electrodynamic actuator. Second the fundamental actuator resonance which constitutes a bandwidth limit for an inertial actuator at lower frequencies when the actuator is used in a direct velocity feedback loop.

Analytical two degrees of freedom models of a self-sensing actuator presented in Appendices B and E illustrate these bandwidth limits and show possible ways they can be influenced. A model with an electrical and mechanical degree of freedom (DOF) shows that critical damping can be added to the mechanical DOF if the self-inductance of the actuator coil is chosen sufficiently small relative to a) the transducer coefficient, b) the moving mass and c) the damped resonance frequency of the actuator. However, in general a high transducer coefficient and a low self-inductance are contradicting requirements. In order to minimize the vibration amplitude of the mechanical DOF it is important to compensate for the resistance and inductance of the actuator. A model with a mechanical DOF representing the inertial mass on the actuator suspension and a mechanical DOF representing a mode of the structure where the actuator is mounted shows that the fundamental actuator resonance frequency should be smaller than a certain bound to guarantee a certain gain margin for external velocity feedback. This bound depends on the resonance frequency of the structure to be controlled and on internal actuator damping if damping of the structural mode is neglected. Additionally the model shows that the frequency at which spillover appears at lower frequencies depends in a characteristic way on internal actuator damping as well as mass and resonance frequency ratios.

In the thesis the bandwidth limits have been examined at the example of a model problem, a thin clamped plate similar to an aircraft panel. A numerical model based on the exact

solution of a clamped plate and lumped parameters of the actuator has been developed where passive effects and active control are modelled in the same feedback scheme. Wherever possible, simulations based on the model are compared to measurements at an experimental set-up showing satisfactory agreement. Achieved vibration reductions are compiled in a table in the conclusion section of each respective chapter.

In Chapter 2 the bandwidth limit of a reactive, self-sensing, electrodynamic actuator at higher frequencies is investigated. Although the self-sensing actuator applies a force and senses a velocity on the same degrees of freedom the collocation-duality property tends to be lost at higher frequencies. Non-ideal collocation is not observed because the mass effect of a primary force transducer provides vibration attenuation at higher frequencies. Despite non-duality simulations indicate that the direct velocity feedback gain necessary for optimum overall vibration reduction of the structure to be controlled might be obtained as in [25]. Some broadband vibration reduction is achieved on the test set-up and in simulations, when a passive resistor is shunted to the actuator, a negative resistor or induced voltage feedback is actively implemented. In order to improve duality by changing the way the self-sensing actuator applies a force and senses a velocity on the same degrees of freedom of the structure to be controlled, the actuator inductance is compensated by an Owens bridge circuit. As a result the control bandwidth is increased and more vibration reduction is observed, although complete compensation of the non-ideal self-inductance is not achieved.

Chapter 3 deals with the design of a lightweight, electrodynamic, inertial actuator. Considering the higher bandwidth limit, special attention is focused on how to balance the value of the self-inductance and transducer coefficient for a specific design under a given weight constraint. Because of the required actuation force for a given weight of the actuator a high transducer coefficient with a rather high self-inductance results from a finite element analysis (FEA) for a large number of dimensions. The FEA also gives an indication of the force-mass relationship for the chosen design type of electrodynamic actuator. As an alternative to a self-sensing actuator, a secondary sensing coil is proposed. By using the secondary coil there is minor additional design freedom to adjust the sensing bandwidth. Both compensated and uncompensated inductance feedbacks lead to a similar vibration reduction result as in the self-sensing case. Considering the lower bandwidth limit, the inertial actuator suspension is designed as to provide a low fundamental resonance frequency for a given weight using a specific spring design. It is found that lightweight actuators tend to have a high fundamental resonance frequency. A high amount

of internal actuator damping is also added by Eddy current damping. The main characteristics of the innovative, lightweight, inertial actuator prototype are listed in Table 3.3. Considerations for further miniaturization are discussed in Appendix C and manufacturing issues encountered at a prototype are described in Appendix D.

Chapter 4 targets the upper bandwidth limit of internal, direct velocity feedback with the designed lightweight, electrodynamic, inertial actuator. It also shows that direct external velocity feedback does not guarantee collocation. Collocation of actuator and sensor is only guaranteed if the internal relative velocity is fed back to the actuation force. But then, the reduction of vibration may decrease or vibrations may even be amplified at lower frequencies since the structural velocity is no longer directly targeted. Eddy current damping, a shunted passive resistor, an active negative resistor or induced voltage feedback implement internal velocity feedback in a limited frequency range and add some damping to the structure. Compensating for the coil inductance by an Owens bridge can extend the internal velocity feedback control bandwidth. The alternative secondary coil velocity sensor allows similar damping to the induced voltage feedback case or the Owens bridge case if the mutual inductance between the primary and secondary coil is compensated. In contrast to a bridge circuit, tuning is not required for the secondary coil that is determined during the design stage. The studied internal velocity feedback control schemes only provide as much structural damping as external velocity feedback at frequencies far above the fundamental actuator resonance. Therefore for inertial actuators with a high fundamental resonance frequency a self-sensing actuator should be rather used as an add-on to external direct velocity feedback.

Chapter 5 targets the lower bandwidth limit of external, direct velocity feedback with the designed, lightweight, electrodynamic, inertial actuator. As found in Appendix E in the analytical two DOFs system, internal actuator damping is beneficial for the stabilisation of external direct velocity feedback in some cases because of its influence on the mentioned lower bandwidth limit. In the lightweight, electrodynamic, inertial actuator a lot of internal damping is provided by Eddy current damping that can be enhanced by the active schemes described in Chapter 4. A simulation study shows that there is a best combination of direct internal and external velocity feedback gains and that the maximum achievable external velocity feedback gain is limited by stroke saturation due to high amplitudes at the fundamental resonance frequency. For high external velocity feedback gains leading to high reduction of the structural response at resonances, the best internal velocity feedback gain is close to the stability limit, which implies reduced robustness. When dynamics of the

secondary coil sensor and distortion by the weight of a force transducer are taken into account, a best internal velocity feedback gain is also found in measurements. Measurements and simulations with internal and external velocity feedback show more vibration reduction than with each feedback scheme separately, a compensator for the fundamental actuator resonance, a high-pass filter cutting off the fundamental resonance and a passive treatment heavier than the designed lightweight, inertial actuator.

A lightweight, self-contained, electrodynamic actuator accelerometer sensor unit has been designed that allows large direct velocity feedback gains in the range necessary to obtain the wanted vibration reduction of the structure under control as discussed in [23]. A best control scheme has been proposed in combination with an inertial actuator. An external velocity feedback loop with a high control bandwidth controls vibration at high frequencies, but it also leads to spillover at low frequencies. Internal velocity feedback counteracts this spillover and reduces vibrations including the spillover from the external feedback loop. The controller could also be implemented as a hybrid active/passive system. Still driving, feedback and measurement amplifiers are needed that add substantial weight, but less amplifiers would be needed if the proposed self-sensing control was improved.

Future work could focus on

- a better compensation of either the self-inductance in the self-sensing case or the mutual inductance in the secondary coil case. More sophisticated electronics such as the electronic implementation of inverse lumped parameter models or a digital compensator with a look-up table have the potential to make the internal velocity sensor as sophisticated as the used accelerometer sensor with non-ideal time integrator. For example geophones [193] show a measurement bandwidth up to 600Hz.

- further miniaturization of the lightweight actuator to an array of actuators with each one tenth of the size and the force of the prototype actuator as discussed in Appendix C. A technology limit is given by the magnetic field strength of the permanent magnets that is predicted to increase in the future [174] and, when making the assumptions of Appendix C, also by the achievable stroke. Giant microeletromechanical systems (MEMS) using the traditional MEMS manufacturing processes in the upper 100μm range seem to be necessary.

- the application and investigation of several prototype actuators on the model problem in order to come closer to the theoretically investigated case in [25] and to design a smart panel competitive to the one proposed in [10] that uses piezoelectric patch actuators.

APPENDIX A: A data collection of recent electrodynamic actuator designs

These values have been found on the electronic homepages of the respective manufactures [72-77, 194] and in a number of publications [78-85].

Type	Stroke (+/-mm)	Maximum force (N)	Continuous force (N)	Total mass (grams)	Maximum Power (W)
BEIKIMCO [72]					
LA05-05-000A	0.508	0.7	0.35	9.407	5.83
LA08-10-000A	2.03	6.7	2.13	34.41	40.1
LA10-12-027A	4.57	13.3	4.6	70.59	63.4
LA12-17-000A	3.81	44.5	15.6	45.9	102.8
LA13-30-000A	17.5	13.3	5.1	437.3	73.6
LA14-17-000A	5.08	22.2	7.1	201.81	104
LA15-16-020A	5.08	33.8	11.6	220.56	153
LA15-16-024A	3.18	89	24.47	228.21	232
LA15-65-000A	50.8	66.7	18.9	87.2	276
LA16-27-000A	3	60	13.9	238	267
LA17-28-000A	7.6	71.2	28.5	496.7	107.2
LA18-12-000A	3	44.5	15.1	219.5	84.9
LA19-40-000A	22.86	22.24	8.54	811.4	88
LA24-20-000A	8.26	111.21	44.93	740	220
LA25-42-000A	12.7	266.89	86.30	1520	375
LA30-43-000A	12.7	445	164	2626	531
LA100-90-001	25.4	2447.5	1299.4	10300	807
TIRA [73]					
TV50009	3	9		1500	
TV50018	5	18		4500	
TV51075	10	75	40	18000	
TV51115-IN		150	75	13000	
LDS [74]					
V101/2	2.5		8.9	910	
V201/3	5	26.7	17.8	1810	
V406/8	17.6	196	98	14100	
Unholtz-Dickie [75]					
S032	51	1330	445	1300	
S062	51	4400	2700	4500	

Type	Stroke (+/-mm)	Maximum force (N)	Continuous force (N)	Total mass (grams)	Maximum Power (W)
S202	51	9800	4400	282000	
S452	51	26700	20000	294700	
S802	51	38000	26700	721000	
Aurasound [76]					
AST-2B-4		132	89	1300	50
Micromega Dynamics [77]					
IA-01	1	3.2	1.6	85	
ADD-45N	3	45		3000	
LMS [194]					
E-Misha		2.5		150	50
Miscellaneous					
[78]		50		1100	20
[79]	3	54		46	300
[80]	20	95		10400	
[81]	4	60			
[82]	(rotary)	20000		1350	
[83]	3	10			
[84]	1		9	1100	3.5
[85]	1.5	15			

APPENDIX B: Conditions for critical damping of a single degree of freedom (SDOF) system using self-sensing control

In a very much simplified model of an electrodynamic actuator reacting against a fixed base and a plate as in Chapter 2, the first plate mode and connected parts of the actuator are modeled by a single degree of freedom (SDOF) system as depicted on the right side in Figure B.1 with mass M, stiffness K and damping D, a natural frequency of $\omega_1 = \sqrt{K/M}$, non-dimensional damping ratio $\xi_1 = D/(2\sqrt{KM})$ and damped natural frequency $\omega_d = \omega_1\sqrt{1-\xi^2}$. When a harmonic primary disturbance force $F_p(\omega)$ oscillating at frequency ω is exerted and the electrodynamic coupling of the actuator is neglected, the structure starts to vibrate with velocity $V_s(\omega)$ so that

$$Z_m V_s(\omega) = F_p(\omega) \tag{B.1}$$

where $Z_m = j\omega M + D + \dfrac{K}{j\omega}$ and $j = \sqrt{-1}$ is the blocked mechanical impedance of the structure and actuator.
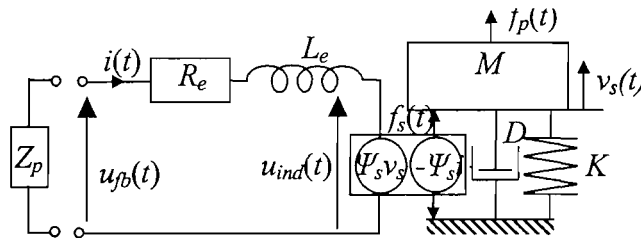
Figure B.1: *Model of a shunted electrodynamic actuator attached to a SDOF resonant structure.*

When the electrodynamic coupling of the actuator, as modeled in the center of Figure B.1, is also considered, a voltage

$$U_{ind}(\omega) = \Psi_s V_s(\omega) \tag{B.2}$$

is induced in the coil which moves in the magnetic B field of the actuator. The transducer coefficient

$$\Psi_s = B_g l_c \tag{B.3}$$

is considered to be constant in the working range and it depends on the amplitude of the magnetic field B_g perpendicular to the direction of the coil movement and the length of the coil wire l_c in the magnetic field.

When, as depicted on the left side of Figure B.1, an electrical impedance Z_p is shunted with the coil having an inductance L_e and a resistance R_e an electrical current

$$I(\omega) = \frac{1}{Z_e}\left(U_{fb}(\omega) - U_{ind}(\omega)\right) = -\frac{\Psi_s}{Z_e + Z_p}V_s(\omega) \tag{B.4}$$

results in the coil so that electrical energy is dissipated over the coil resistance R_e as well as over a shunt resistance R_s=Re(Z_p). Z_e=R_e+$L_e$$j\omega$ is the open loop electrical impedance of the electrodynamic actuator and $U_{fb}(\omega)$=-$Z_p$$I(\omega)$ is the voltage over the shunt impedance. The resulting current in the moving coil leads to a secondary force

$$F_s(\omega) = \Psi_s I(\omega) \tag{B.5}$$

in addition to the primary force $F_p(\omega)$ on the vibrating structure. Following Lentz's rule this force is in opposite direction to the primary disturbing vibration velocity $V_s(\omega)$ leading to vibration reduction. By appropriately choosing the shunt impedance Z_p a goal such as adding critical damping to the mechanical DOF or minimizing the kinetic energy of the mechanical DOF might be obtained. The reduction in amplitude of the FRF from the primary excitation force $F_p(\omega)$ to the vibration velocity of the SDOF system

$$\frac{V_s(\omega)}{F_p(\omega)} = \frac{1}{Z_m + \dfrac{\Psi_s^2}{Z_e + Z_p}} = \frac{Z_e + Z_p}{Z_m\left(Z_e + Z_p\right) + \Psi_s^2} \tag{B.6}$$

is then a measure of vibration reduction. In the following, the FRF due to an added primary current $I_p(\omega)$ proportional to the primary excitation force

$$F_p(\omega) = \Psi_p I_p(\omega) \tag{B.7}$$

is considered. First proportional secondary current feedback control is investigated. By feeding back a voltage

to the electrical input of the actuator the real part of the shunt impedance can be tuned in order to change the apparent shunt resistance. The case of a negative current feedback gain is equivalent to using a resistor as shunt impedance with $Z_p = G$ so that the total resistance of shunt and actuator electrical circuits increases. According to equation (B.6) vibrations also increase for a given primary force. In contrast when a positive current feedback gain G is used, a negative shunt impedance $Z = -G$ results that reduces the total resistance of shunt and actuator electrical circuits. As a result, a higher current leading to a higher secondary force opposing the primary force is applied on the structure. The FRF from the primary current to the vibration velocity of the structure hence becomes

$$\frac{V_s(\omega)}{I_p(\omega)} = \frac{\Psi_p}{Z_m + \dfrac{\Psi_s^2}{R_e + L_e j\omega - G}} = \frac{\Psi_p\left(R_e + L_e j\omega - G\right)}{Z_m\left(R_e + L_e j\omega - G\right) + \Psi_s^2}. \qquad \text{(B.9)}$$

The simulated FRF using the parameter values in Table B.1 for different values of the negative feedback gain G is shown in Figure B.2.

Table B.1: *Parameter values used for simulations in Appendix B.*

Parameter	low	high electrical cut-off frequency
Spring constant K	56 kNm^{-1}	56 kNm^{-1}
Damping coefficient D	2.667 Nsm^{-1}	2.667 Nsm^{-1}
Plunger and plate mass M	0.15 kg	0.15 kg
Primary transducer coefficient Ψ_P	3.65	3.65
Secondary transducer coefficient Ψ_S	3.4	3.4
Coil inductance L_e	1 mH	0.02 mH
Coil resistance R_e	3.3 Ω	3.3 Ω
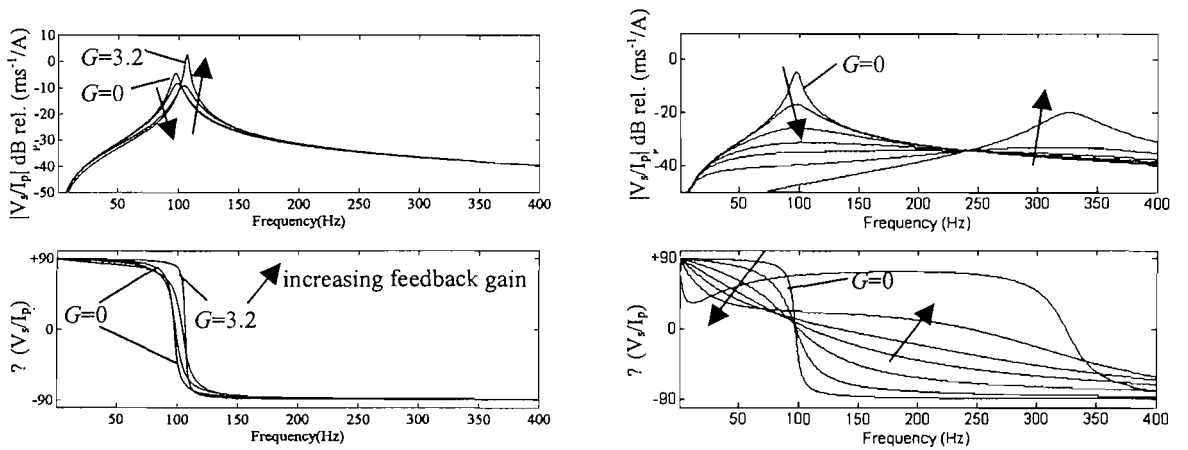
Figure B.2: *FRF from the primary current to the vibration velocity for different proportional current feedback gains G, left: actuator with low electrical cut-off frequency, right: with high electrical cut-off frequency.*

Simulations hardly show any effect in the case when the actuator has a low electrical cut-off frequency R_e/L_e. The control scheme seems to be very efficient in the case of an

actuator with a high electrical cut-off frequency R_e/L_e. However, for higher gains in both cases a secondary peak appears in the FRF that limits possible feedback gains. The root locus plot of the denominator of equation (B.9) shown in Figure B.3 for increasing feedback gains G shows that this secondary peak is due to the interaction of the mechanical poles with the electrical pole. Actuators with a high cut-off frequency show a range of feedback gains where the two mechanical poles and the electrical pole are real and all three poles are critically damped. In contrast at actuators with a low cut-off frequency the mechanical poles are far from reaching the critically damped state.
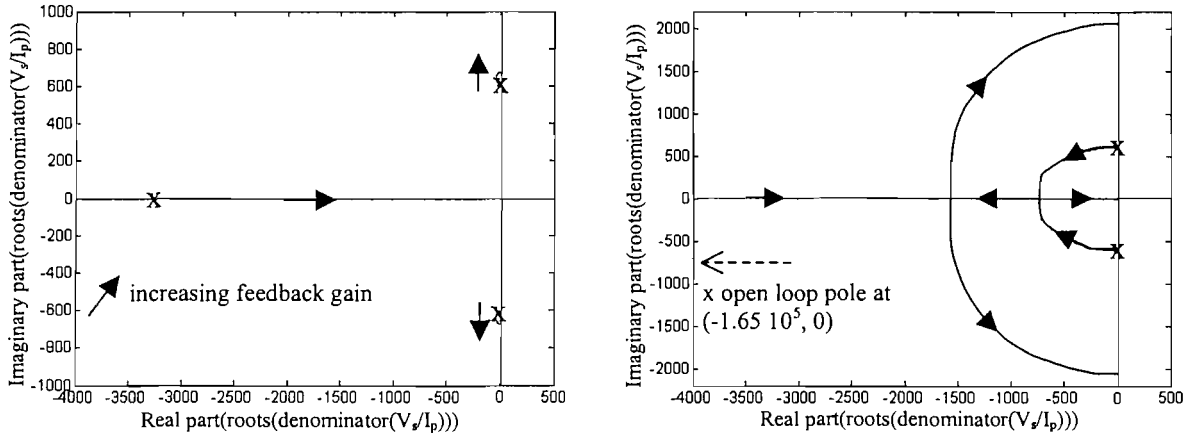
Figure B.3: *Root locus plot of the denominator of the FRF from the primary current to the vibration velocity plotted for the stable range, left: actuator with low electrical cut-off frequency, right: actuator with high electrical cut-off frequency, x open loop pole position.*

Electrodynamic actuators with a high electrical cut-off frequency hence are actuators where there exists a feedback gain G for which the closed loop mechanical poles and the electrical poles are real, i.e. when all three roots of

$$y = s^3 + s^2 \left(D/M + R_e/L_e - G/L_e\right) + s\left(D/M\left(R_e/L_e - G/L_e\right) + \omega_1^2 + \Psi_s^2/\left(L_e M\right)\right) + \\ + \omega_1^2\left(R_e/L_e - G/L_e\right)$$
(B.10)

with $s = j\omega$ are real. Applying a result from [195] this is verified if

$$D = b_1^2 - 2b_1 b_2 + b_2^2 - \frac{D}{M}b_1 + \frac{D}{M}b_2 - 3\left(\omega_1^2 + b_3\right) + \left(\frac{D}{M}\right)^2 > 0$$
(B.11)

where $b_1 = R_e/L_e$, $b_2 = G/L_e$ and $b_3 = \Psi_s/(L_e M)$. In the limiting case, where $D=0$, the quadratic equation in two variables (B.11) describes two parallel lines [195] in the b_1–b_2 plane if

$$L_e < \frac{\Psi_s^2}{M\omega_d^2}.$$
(B.12)

Hence, there is a real gain G so that equation (B.10) has three real poles if equation (B.12) is verified. For a given actuator resistance, condition (B.12) translates into a condition for the electrical cut-off frequency of the actuator R_e/L_e. Taking values from Table B.1 condition (B.12) is true for the actuator with a high electrical cut-off frequency, but not for the actuator with a low electrical cut-off frequency, which explains the different results in Figures B.2 and B.3. When there is the possibility to design the magnetic circuit of the actuator there still is a balance to be made between L_e and Ψ_s since changes in the magnetic circuit increasing Ψ_s usually also increase L_e as explained in Chapter 3. If there is no or only partial inductance compensation this balance between actuator parameters transforms into a balance between control bandwidth and sensitivity of a self-sensing, electrodynamic actuator. If there is a possibility for compensation, the compensator could be chosen in such a way that the kinetic energy of the mechanical DOF is minimized. The kinetic energy is proportional to

$$\mathrm{Re}\left\{Z_m V_s^2\right\} = \frac{1}{Z_m}F_p^2 + \frac{\Psi_s^2}{Z_m}I^2 + \frac{2\Psi_s}{Z_m}F_p I \tag{B.13}$$

where V_s is given by Eqs. (B.1) and (B.5). A condition for an optimal current is

$$\frac{\partial\left(Z_m V_s^2\right)}{\partial I} = 2\frac{\Psi_s^2}{Z_m}I + 2\frac{\Psi_s}{Z_m}F_p = 0 \tag{B.14}$$

leading to an optimum current of

$$I = -1/\Psi_s\, F_p. \tag{B.15}$$

When a shunted impedance is implemented following Eqs. (B.4), (B.1) and (B.5) the coil current is given by

$$I = \frac{1}{Z_e}\left(-Z_p I - \frac{\Psi_s}{Z_m}\left(F_p + \Psi_s I\right)\right) = \frac{-\Psi_s/Z_m}{Z_p + Z_e + \dfrac{\Psi_s^2}{Z_m}}F_p \tag{B.16}$$

that is identical to Eq. (B.15) if $Z_p = -Z_e$. Hence, in order to achieve minimization of the kinetic energy of the mechanical DOF the shunted circuit should compensate for the electrical impedance of the coil and implement a negative impedance. Pure resistance compensation as proposed before should be complemented by electronic inductance compensation.

APPENDIX C: Scaling analysis of lightweight, electrodynamic, inertial actuators.

As shown in Chapter 3 the transmitted force, the actuation force and the suspension stiffness are important factors that have to be considered in the miniaturization of an electrodynamic actuator. In the following a scaling analysis using these three variables is carried out when first assuming that all three dimensions scale homogeneously and when second assuming that the stroke direction is larger than the two other plane dimensions. Finally a numerical example of an array of 10 x 10 actuators occupying the space of a single prototype actuator gives ideas about manufacturing issues associated to a further miniaturization.

First when assuming that all three dimensions in a Cartesian space scale like a length l, the transmitted force at lower frequencies as in Figure 3.2 behaves like

$$F_t = \rho_{\mathrm{mag}}\, l^4 \omega^2 \tag{C.1}$$

at a given frequency ω and given mass density of the inertial mass ρ_{mag}. At higher frequencies the transmitted force is limited by the maximum actuation force that scales like l^2, l^3 or l^4 depending on whether the current density increases or the power or current density remain constant for changing dimensions [86]. In the particular case of Chapter 3 , when assuming that the result in Figure 3.5 can be extrapolated to lower masses, the actuation force behaves like

$$F_a = 125 \rho_{\mathrm{mag}}\, l^3. \tag{C.2}$$

Since the transmitted force in Eq. (C.1) becomes faster smaller with decreasing l than the actuation force in Eq. (C.2) the saturation break frequency ω_b as defined in Chapter 3 increases with decreasing dimensions. It actually scales like $l^{1/2}$. Consequently the lowest controllable resonance frequency of the mechanical structure also moves to higher values.

More importantly the fundamental resonance frequency of the actuator increases even faster since it scales like

$$\omega_0 = \sqrt{\frac{E_s I_d}{l^3 \rho_{mag} l^3}} \sim l^{-3} \tag{C.3}$$

when assuming that the moment of inertia of the suspension I_d can always be at an even smaller size than l. In Eq. (C.3) the suspension stiffness is assumed to be realized by a spring loaded in bending.

When all dimensions are scaled equally, the significantly smaller inertial mass and the significantly higher fundamental resonance frequency of the actuator reduce control authority and bandwidth.

Second when assuming that the dimension in stroke direction scales like L and the other two plane dimensions scale like l the transmitted force scales like

$$F_t = \rho_{\mathrm{mag}} l^2 L^2 \omega^2. \tag{C.4}$$

There is especially a difference to the previous case when assuming that L can be approximately kept constant. This assumption is reasonable when considering that miniaturization is especially aimed on the surface of a structure to better spatially control distributed vibrations and not in a direction perpendicular to the surface. Since the actuation force in Figure 3.5 scales like

$$F_a = 125 \rho_{\mathrm{mag}} \, l^2 L. \tag{C.5}$$

similar to the transmitted force the saturation break frequency does not change significantly with varying l. The control bandwidth is only shifted to higher frequencies by the fundamental resonance frequency of the actuator. When assuming that a spring in predominantly vertical direction is used, the fundamental resonance frequency scales like

$$\omega_0 = \frac{\sqrt{E_s I_d}}{L^2 l} \tag{C.6a}$$

or when a spring with predominant extension in horizontal direction is used the fundamental resonance frequency scales like

$$\omega_0 = \sqrt{\frac{E_s I_d}{l^5 L}} \, . \tag{C.6b}$$

When the dimension of the actuator stroke is considered constant during scaling, the actuator authority is limited by either the actuation force or the transmitted force, whichever is smaller, and the bandwidth is reduced by l^{-1}. Clearly for an inertial actuator the stroke should not be reduced as much as the other two dimensions of the actuator and a suspension with dominant extension in the stroke direction should be used. In this case in the following some possible manufacturing issues are suggested.

A further miniaturization of the prototype actuator could be to appropriately adjust the actuator dimensions so that the feedback force observed at the model problem is just obtained. Alternatively it could be tried to replace the prototype actuator by a larger number of smaller actuators that in sum generate the same force and in total cover the same

area as the prototype actuator. In the first case a similar study as the one presented in Chapter 3 could be carried out whereas in the second case more serious technology challenges are predicted. Considering the case, when one inertial actuator of a surface of about 0.04m x 0.04m with F_t=2.5N is to be replaced by an array of 100 0.025N actuators of a surface each of about 0.004 x 0.004m. The same control bandwidth with the lowest resonance frequency at ω_b=50Hz is aimed. First in order to generate a sufficient transmitted force the stroke d is to be increased to compensate for the reduced mass. At a mass density of the inertial mass of ρ_{mag}=7400kgm^{-3} and approximate dimensions l x l = 0.004m x 0.004m a stroke of

$$d = \sqrt{\frac{F_t/100}{\omega_b^2 \rho_{mag} 2l^2}} \approx 0.001\text{m} \qquad (C.7)$$

seems to be sufficient that is not much different from the one used in the prototype actuator. When considering that Figure 3.5 can be extrapolated to lower inertial masses, an actuation force of

$$F_a = 125 \ l^2 \ L \approx 0.03\text{N} \qquad (C.8)$$

should be possible when L=2d=0.002m. When assuming a constant magnetic field B=0.2T in the air gap an even bigger force

$$F_a = B\pi AN_p \sqrt{\frac{P}{R_e}} = B\pi AN_p \sqrt{\frac{PlL}{\rho_{wi}\pi AN_p^2}} = B\sqrt{\frac{\pi APlL}{\rho_{wi}}} \qquad (C.9)$$

of up to 0.067N should be realizable for each actuator where ρ_{wi}=0.017 10^{-6}Ωm is the specific resistivity of the copper wire, l=0.001m is the characteristic dimension air gap width and A=0.0015m is the diameter of the permanent magnet that determines the radius of the coil. At a power input of 0.1W a current of 0.35A and a coil resistance of 0.8Ω seem reasonable provided that coils with a diameter of 100μm with a large number of windings can be realized. As mentioned in Chapter 3 and implied in [87] the temperature increase and the maximum input power can only be precisely known at the actual design.

An estimation of the stiffness of the actuator suspension

$$K=\omega_0^2 m \approx 0.987\text{Nm}^{-1} \qquad (C.10)$$

at a fundamental resonance ω_0=10Hz and an inertial mass m=2.5 10^{-4}kg given by the stroke in Eq. (C.7) and the required transmitted force at 50Hz shows that an extremely small suspension stiffness is required. When a spring is used in bending for the suspension, its moment of inertia is in the order of

$$I_d = K l^3 E_s \qquad \text{(C.11)}$$

that leads to a radius of about 15μm of the circular cross section of the spring, when assuming a realization in polysilicon with a Young's modulus E_s=201×10^3 MPa and a characteristic dimension l=0.002m. It is questionable whether the materials that can be used in the manufacturing process have enough yield strength to support the static and especially dynamic internal stress since displacements in the mm range are required for a suspension of tens of μms. A suspension in post-buckling could allow low suspension stiffness although non-linearity would be a concern.

This appendix has indicated that a further miniaturization seems to be possible by either using the proposed design methodology in Chapter 3 and slightly reduce actuator force and weight (top-down approach) or to implement a large number of small actuators with each a much smaller force replacing the prototype actuator (bottom-up approach); but it has also highlighted technological limits that are just being explored. For instance, an electrodynamic actuation force requires a microscale coil and magnetic circuit. Coil circuits on a microscale are studied in [196-198, 87]. The generation of permanent magnetic layers is investigated in [199]. Non-linear dynamics of a suspension of a proof-mass actuator are considered in [200-202]. A combination of these different components to a MEMS electrodynamic actuator is presented in [203, 204] with dimensions in the 10μm range. The electrodynamic actuator principle has been used previously with less sophisticated components [205, 206]. Implementing the coil and suspension on one chip and the magnetic circuit on another chip could be a way to implement an inertial actuator in flip-chip technology [206] potentially increasing actuator dimensions.

The proposed miniaturized actuator design is situated in a technology gap between microelectromechanical systems (MEMS) manufacturing technology and more conventional manufacturing technology as also shown in [207]. The first technology can reach dimensions of a couple of 100μm only under certain circumstances whereas the latter may easily manufacture parts in the range of 1000μm. Hence, at the current (2005) stage of technological development, due to manufacturing considerations on a microscale, other force generation principles might be more interesting [208].

Because of the required small size and weight dimensions of the inertial actuator tend to be small so that there are some manufacturing challenges using conventional machine tools that are also explained in [57]. Tight tolerances are demanded for the air gap in order to allow a maximum number of coil windings. For the same reason the wall thickness of the former should be as small as possible requiring special care during manufacturing. Additionally a special device has been built for winding the primary and the secondary coil. The ring springs also require special care during manufacturing. Finally the assembly of the complete prototype actuator needs to follow an order, too.

Because of the tight tolerances and the thin wall thickness of the former special care is required for manufacturing. Figure D.1 shows the lower cover part C-1 during machining of the small groove for the measurement wire. The part is clamped on the left hand side in the chuck of a lathe. The PTFE cylinder on the right hand side is used to clamp the part when the clamping cylinder on the left hand side is removed once the coil is wound. It also stabilizes the cylinder with 0.1mm wall thickness during machining of the groove for the measurement wire and during winding of the coil. Once the coil is wound and glued the former itself should have sufficient stability on its own.
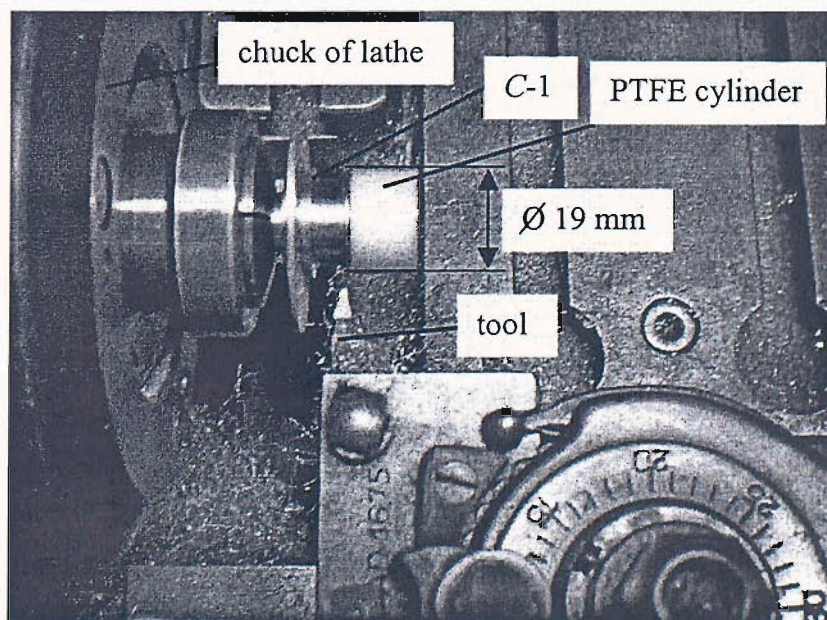
Figure D.1: *Lower cover part during machining* [209].

Figure D.2 shows a selection of tools that are manufactured to drill the hole for press fitting the axis into the lower cover and the hole in the upper cover to guide the axis. A DIN 6325 steel pin of length 32mm is ground to the required dimensions. The aluminium

cylinder in Figure D.2 is used to guide the tool horizontally and one of the tools is actually used to machine the guiding hole in the aluminium cylinder.
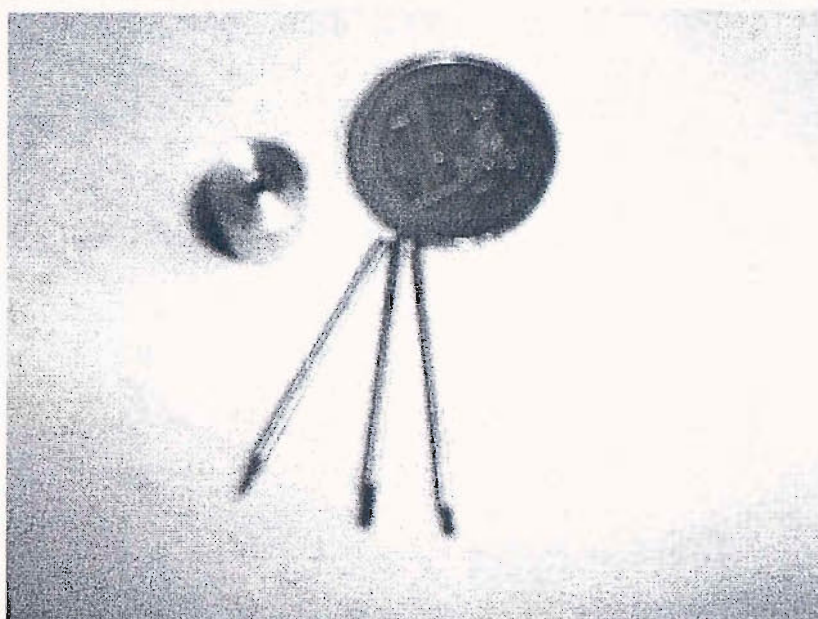
Figure D.2: *Tools for drilling holes into the lower cover.*

Figure D.3 shows the procedure to drill the six holes of diameter 1.2mm at 60 degrees distance that is also used to drill the M1 threads into the upper cover. Note the use of a magnifying glass.
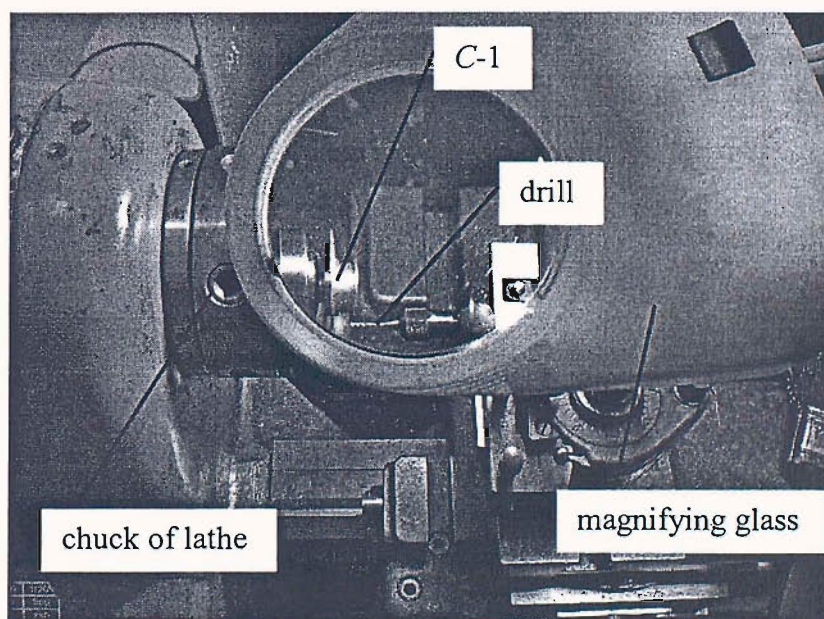
Figure D.3: *Drilling diameter* 1.2mm *holes in the lower cover* [209]

In order to be able to wind coils on a common lathe a special coil-winding device depicted in Figure D.4 has been designed and built. The screw is used to adjust the friction force and hence the tension in the coil wire during winding so that there is limited control over the density of the coil package. A soft Teflon inlet with minimum friction is used to guide the wire.
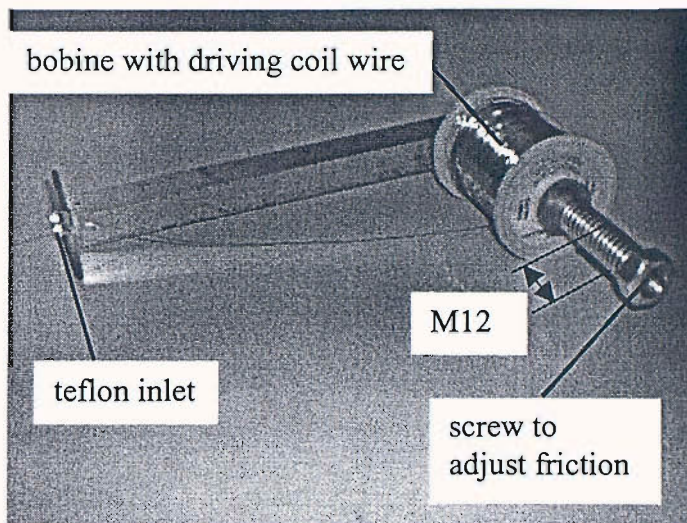
Figure D.4: *Coil winding device to be used at a common lathe.*

The coil winding is first carried out at a test part of the lower cover part in order to determine practical problems during the procedure and acquire the necessary skills. The same part is also used to approximately determine the coil coupling without influence of the magnetic circuit. Figure D.5 shows the test part during winding of the driving coil. A plastic stick can be used to increase the density of the coil package when it is wound manually. For more than four layers winding by turning the lathe chunk manually instead of using the lathe advance at very low speeds is recommended because it allows easier control of crossing wires. Wires should not cross in order to prevent compensation of the driving magnetic field during operation and increase lifetime.
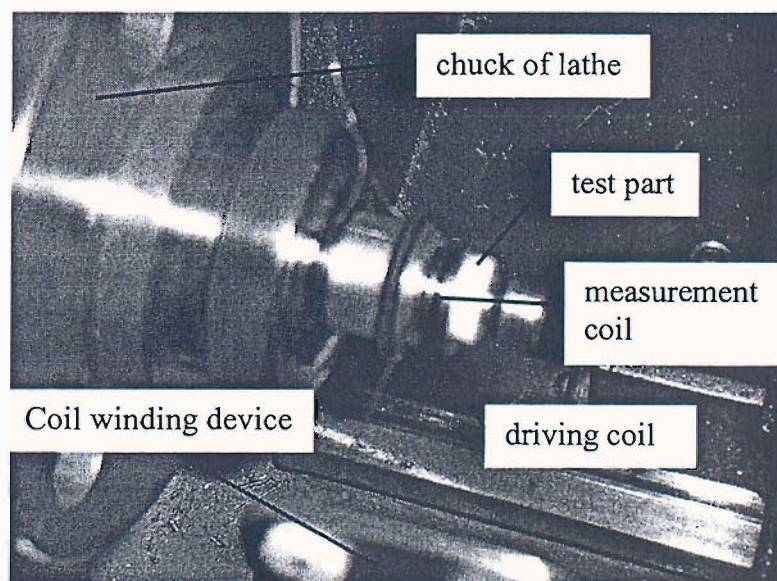
Figure D.5: *Winding of the driving coil at a test part.*

During the test winding it has been found that the big wire of the driving coil damages the tiny wire of the measurement coil as is shown in Figure D.6. Therefore grooves that allow
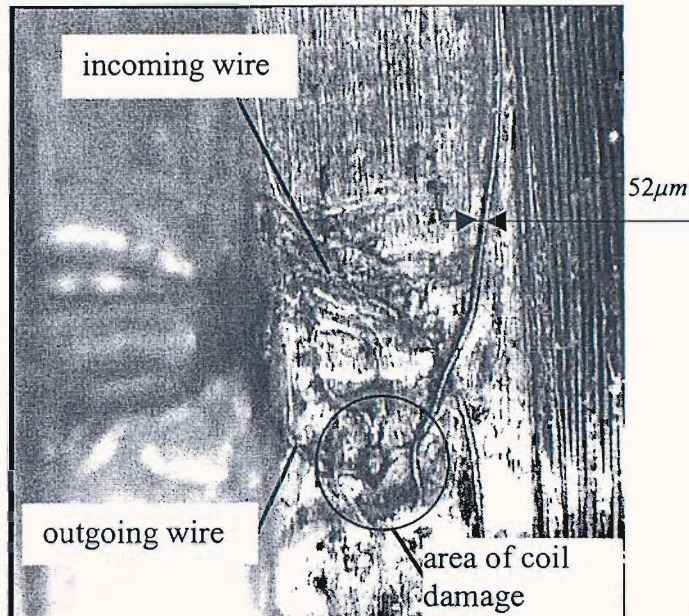
Figure D.6: *Damaged measurement coil wound on test former, magnified by light microscope.*

protecting the small wire are machined in part C-1 with an electro discharge machine (EDM) as depicted in Figure D.7. These grooves are not included in drawing C-1. Additionally before winding the big wire the small wire is wound and glued into the main groove with two connecting ends sticking out at a length of about 0.1m each. Then those two ends are put into the grooves for additional protection and glued again so that the used low viscosity epoxy glue provides additional protection. The procedure is repeated on the

Figure D.7: *Grooves machined into part C-1 for the protection of the measurement wire, magnified by light microscope.*

real part. Then the big wire is wound and glued. Just some drops of the glue are sufficient. The ends of the wire are soldered to 0.3mm diameter metal pins that pierce the Teflon wire guiding parts. In order to be able to solder the measurement wire its insulation is to be

etched away. Salicylic acid generated by an Aspirin® when exposed to the 350° C of a soldering iron is a convenient etching agent.

The ring springs are manufactured of bronze strips (Cu98Be2) with a wire electro discharge machine (wire-EDM). Special care is to be taken to correctly choose manufacturing parameters and to ensure good positioning of the raw material that is clamped between two 1mm aluminium plates. Otherwise vibration of the raw material leads to errors as depicted in Figure D.8.
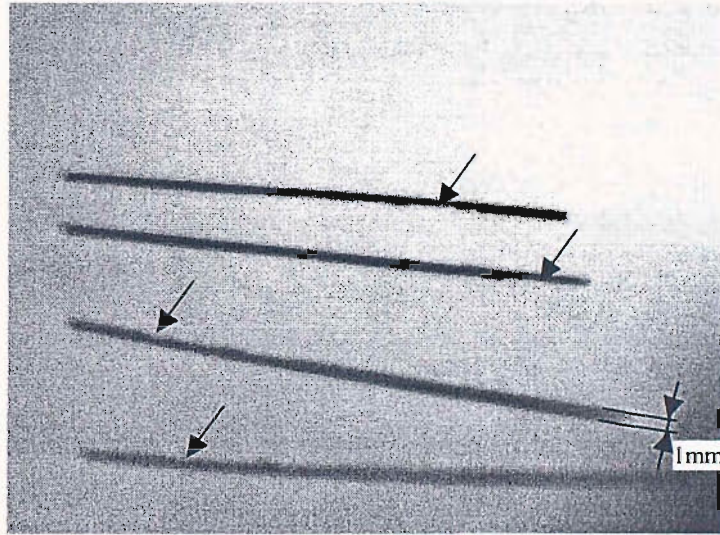
Figure D.8: *Manufacturing error at bronze strips for ring spring.*

Alternatively strips can also be manufactured with common manual cutting tools. This is the only manufacturing option if another material like DIN 17222 Ck101 spring steel is chosen in order to profit from the increased yield strength. In addition to an increased safety factor the dynamic behaviour of steel parts is more widely known than the one of bronze parts. The maximum allowable stress σ_H in a DIN2093 steel with $E_{st}=206\times10^9 Pa$ at a given number of load cycles and at a lower stress σ_u as well as peak stress σ_o can be found in diagrams. Three ring springs of radius $r=0.0075m$ should statically support the moving mass resulting in a static moment [184]

$$M_{st}=0.318\times r\times M/3\times9.81m/s^2=1.6\times10^{-4}Nm \tag{D.1}$$

in a single ring spring. In order for the resulting static stress to be smaller than R_m/S_{st} where $R_m=640MPa$ is the yield strength of the material and $S_s=1.5$ is a safety factor the spring width is to be chosen to be superior to

$$b_{sp} \geq \frac{M_{st}6}{h_{rs}^2 S_s R_m} =7.6\times10^{-4}m, \tag{D.2}$$

where h_{rs}=0.06mm is the available material thickness. Moreover the ring spring stiffness given by [184] is equal to the required stiffness K if

$$b_{sp} = \frac{KR^3 9}{5h_{rs}^3 E_s} = 17.96 \times 10^{-4} \text{m},$$ (D.3)

so that a spring width b_{sp}=1.8mm is chosen. At this spring width a dynamic moment

$$M_d = 0.318 \times K \times 2 \times d \times r = 5 \times 10^{-4} \text{Nm}$$ (D.4)

with the required stroke d leads to a dynamic stress σ_{dy}=464.9MPa. Together with the static stress and a safety factor S_d it should be smaller than the maximum allowable stress $\sigma_H(\sigma_u)$=700MP from a dynamic stress - load cycle diagram at the lower stress $\sigma_u=\sigma_{st}-\sigma_{dy}/2$=-88.05MPa. For the chosen spring width a theoretical safety factor S_d=1.5 is realized that is a reasonable value for bending load. However, these calculations are just approximate since the required dimensions can only be realized with tolerances due to the manual production process. Bronze springs should be used when material failure is not critical, but the influence on the magnet field is important. Steel springs can be more reliably designed against dynamic failure except if stress peaks occur at discontinuities, but they still are influenced by the magnetic field.

The metal strips, either phosphor bronze or spring steel, are bent to ring springs using a special forming tool that is manufactured with close tolerances. It consists of an inner cylinder of diameter 15 (0,-0.1) with a groove to carry the 1mm x 0.1mm bronze or 1.8mm x 0.06mm steel and 50mm long strips and an outer hollow cylinder of diameter 15 (+0.1, 0) that presses the metal strip into the groove as is depicted in Figure D.9. A small groove is filed into the outer cylinder so that the ends of the metal strip may overlap for better soldering. While being clamped in this tool the ring springs are soldered one after the other to the moving mass piece using soldering fat. A circular shape of the ring springs results.
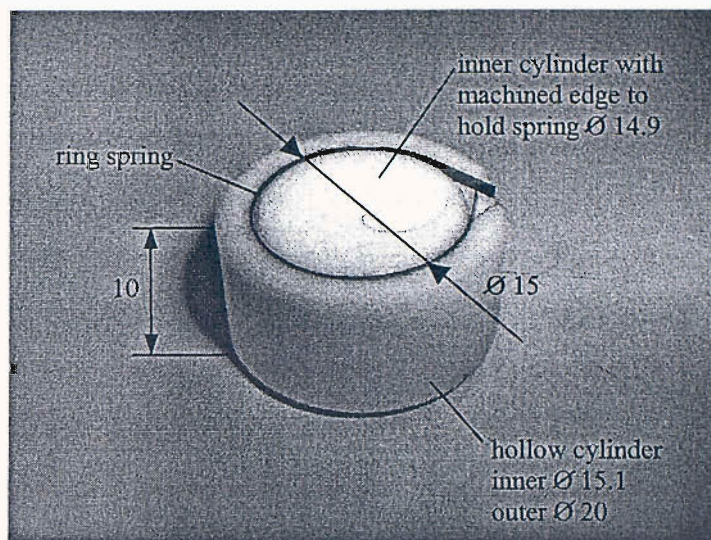
Figure D.9: *Ring spring forming tool.*

After winding the two coils, fixing them with low-viscosity epoxy glue and connecting them to the metal pins in the wire outlet the interior of the moving mass part M-1 is machined so that it fits over the wound coil. Since the winding process does not allow very dense packages for more than about four layers the air gap is to be widened considerably. A clamping tool shown in Figure D.10 is built so that the part M-1 may be clamped into the chunk of a lathe.
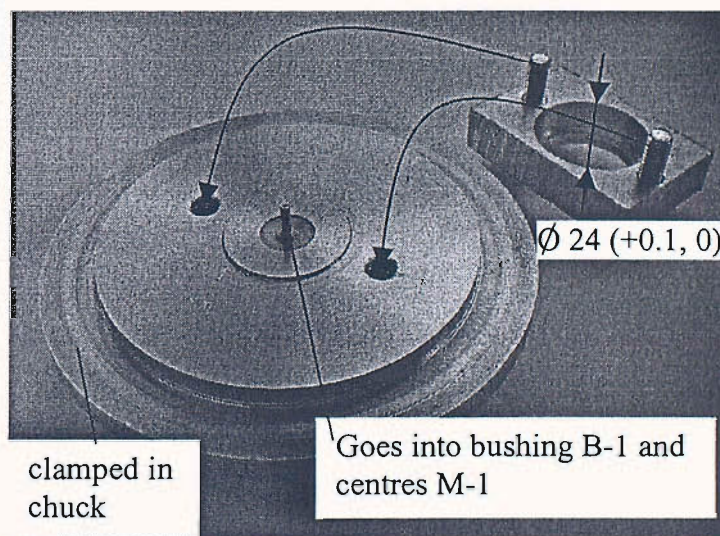
Figure D.10: *Clamping tool to allow machining of part M-1.*

The inner diameter forming the outer part of the air gap is widened from diameter 19.5 to diameter 19.9 to fit over the coil with a small gap. Then the bushings B-1 and B-2 are mounted into the parts M-1 and M-3 by press fitting with the smaller outer diameter of parts B-1 and B-2 going first. In order to mount the permanent magnet M-2 and the iron M-3 a hollow cylindrical PTFE mounting device with close tolerances is machined for each of the parts. M-2 is connected to M-1 as depicted in Figure D.11 with a small layer of glue that also serves as heat insulator. After hardening the glue part M-3 is mounted on and glued to M-2. The axis is used to align parts M-1 and M-3 before the glue is hardened.

Then the three ring springs are soldered to M-1 using the ring spring forming tool. Before clamping the ring springs to the lower cover and adding the moving mass assembly together with the guiding axis the lower cover is brought into its final shape by removing the clamping cylinder on its bottom side and the PTFE cylinder on its upper side. During removal of the PTFE cylinder using its internal thread care is to be taken to not damage the 0.1mm thick former supporting the coils. Finally after the upper cover is connected to the lower cover using 6 M1 screws and centred on the central axis, the actuator is ready for testing.
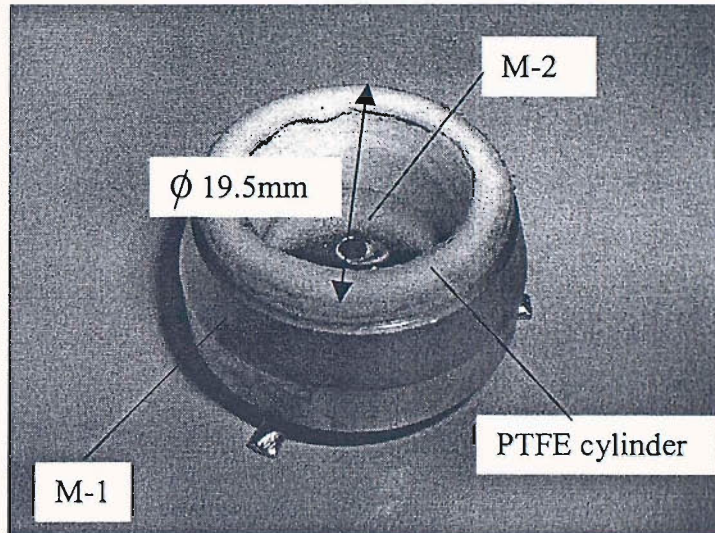
Figure D.11: *Mounting M-2 in M-1.*

APPENDIX E: Spillover frequency and highest inertial actuator resonance frequency for a two degrees of freedom system.

In order to simplify the interpretation of the results in Chapter 5, in particular the beneficial influence of the internal actuator damping on a given mode of the panel, in this appendix a simplified two degrees of freedom (DOF) model will also be considered. In this model the response of the rth mode of the panel is represented by a modal mass $M_r = \rho l_x l_y h / \phi_r^2 (x_s, y_s)$, modal stiffness $K_r = \omega_r^2 M_r$ and viscous damping $D_r = 2\xi_r \sqrt{K_r M_r}$. The dynamics of the actuator are represented by its axial suspension stiffness K, damping D and inertial mass m. The response of such a simplified system is derived from the second part of Eq. (4.5) when only the rth mode of the plate, i.e. $N=r$ and $n=r$ in Eq. (4.2b), and the fundamental resonance of the inertial actuator are used. In order to check the closed loop performance and stability, the open loop frequency response function (FRF) between the actuation force and the vibration velocity of this simplified model

$$
\frac{V_s}{F_a} = \frac{-\omega^4 / j\omega M_r}{\left(\omega_r^2 + 2\xi_r \omega_r j\omega + \left(\omega_0^2 + 2\xi_0 \omega_0 j\omega \right) \frac{m}{M_r} - \omega^2 \right)\left(\omega_0^2 + 2\xi_0 \omega_0 j\omega - \omega^2 \right) - \left(\omega_0^2 + 2\xi_0 \omega_0 j\omega \right)^2 \frac{m}{M_r}} \tag{E.1}
$$

is investigated where $\xi_0 = D / \left(2\sqrt{Km} \right)$ is the viscous damping coefficient and $\omega_0 = \sqrt{K/m}$ the undamped natural frequency of the inertial actuator. Similar to Figures 4.3 and 5.3 this simplified 2 DOF analytical model has one loop in the left real half-plane due to the fundamental resonance of the inertial actuator with resonance frequency ω_0 and a single loop in the right real half-plane due to the rth plate mode with resonance frequency ω_r.

According to the Nyquist criterion, closed loop stability is guaranteed if the locus of the open loop FRF in the real – imaginary plane does not encircle the critical point (-1,0j). Defining δ_1 as the real part of the FRF where its locus intersects with the negative real axis as shown in Fig. 5.3, in the studied case, it is sufficient that $|\delta_1|<1$. The amplitude of the FRF at this point $|\delta_1|$ is inversely proportional to the gain margin and hence a measure for stability [26, 168]. The smaller the gain margin the closer the locus is to the critical point and more spillover is expected in the closed loop case.

In measurements there is an additional phase shift at very low frequencies due to the electronic integrator in the charge amplifier. Hence, because of the inertial actuator resonance leading to $\delta_1 < 0$ and because of the charge amplifier distortion only a limited range of control gains is predicted to guarantee closed loop stability. Also, spillover effects are anticipated in the vicinity of the fundamental resonance frequency since the locus enters the circle with radius 1 about the critical point.

In the analytical model the locus of the FRF in Eq.(E.1) intersects with the real axis at

$$\bar{\omega}_{r,0}^2 = 0.5\left(\left(\omega_r^2 + 4\xi_r\xi_0\omega_r\omega_0 + \omega_0^2\left(1+\frac{m}{M_r}\right)\right) \pm \sqrt{\left(\omega_r^2 + 4\xi_r\xi_0\omega_r\omega_0 + \omega_0^2\left(1+\frac{m}{M_r}\right)\right)^2 - 4\omega_0^2\omega_r^2}\right) \quad \text{(E.2)}$$

where $\bar{\omega}_0$ and $\bar{\omega}_r$ indicate the modified fundamental resonance frequency and the rth resonance frequency of the plate when the 2DOF model is considered. The amplitude of Eq. (E.1) at these intersection points is given by

$$\delta_{1,r+1} = \frac{\bar{\omega}_{0,r}^2}{\bar{\omega}_{0,r}^2\left(2\xi_0\omega_0\left(1+\frac{m}{M_r}\right)+2\xi_r\omega_r\right) - \omega_r^2 2\xi_0\omega_0 - \omega_0^2 2\xi_r\omega_r}. \quad \text{(E.3)}$$

In the special case where the plate damping is neglected, i.e. $\xi_r=0$, and the mass of the inertial actuator is much smaller than the modal mass of the plate $m/M_r \ll 1$ Eq. (E.3) can be simplified to the following expression

$$\delta_1 = \frac{1}{2M_r\xi_0\omega_0\left(1-\frac{\omega_r^2}{\omega_0^2}\right)}. \quad \text{(E.4)}$$

The advantageous effect of internal damping is clearly observable in Eq. (E.4) since the gain margin increases with increasing ξ_0. Closed loop stability for external velocity feedback of V_s is guaranteed if $\delta_1 > -1$ and thus

$$\omega_r^2 > \omega_0^2 + \frac{\omega_0}{M_r 2\xi_0}. \quad \text{(E.5)}$$

(Note that $\delta_1<0$ because of the fundamental actuator resonance.) Since ω_r and M_r are given by the structure to be controlled, the resonance frequency of the inertial actuator ω_0 should be chosen as small as possible. In particular the condition has to be fulfilled for the lowest resonance frequency of the plate ω_1. However, there are practical limitations [51] for the reduction of $\omega_0 = \sqrt{K/m}$. For example m should be kept as small as possible so that the inertial actuator is lighter than other passive means that could be used to increase the damping of the structure to be controlled. Also the suspension stiffness K must be kept large enough in order to provide the necessary static support of the inertial mass. In conclusion the addition of internal damping ξ_0 is proposed in order to either increase the gain margin or performance at a given gain margin. In order to add internal damping, internal relative velocity feedback at the model problem is investigated in Chapter 4.

Even when closed loop stability is achieved there will be spillover for frequencies where $|1+GV_s/F_a|<1$. For instance considering Eq. (E.1) for $r=1$, the cut-off frequency for spillover is found to be

$$\omega_{so} = \omega_0 \sqrt{\frac{\left(\dfrac{\omega_1}{\omega_0}\right)^2 + \dfrac{\xi_1}{\xi_0}\dfrac{\omega_1}{\omega_0}}{\left(1+\dfrac{m}{M_1}\right) + \dfrac{\xi_1}{\xi_0}\dfrac{\omega_1}{\omega_0} + \dfrac{G_1}{4M_1\xi_0}}} \;. \tag{E.6}$$

Thus the higher the frequency ratio ω_1/ω_0 is the higher the spillover frequency will be. In general the spillover frequency can be further brought up by the internal damping effect although this effect tends to fade away as the ratio ω_1/ω_0 decreases. Because of limits in the design of low stiffness suspensions [57] small frequency ratios tend to occur in systems with lightweight, inertial actuators. For such systems, where additionally m is important relative to M_1, increased ξ_0 can help to reduce ω_{so}. External velocity feedback also reduces the frequency range in which spillover occurs.

In conclusion, there is an optimum internal velocity feedback gain for which, despite the negative spillover effects of the external velocity feedback at some frequencies, large vibration reductions are achieved at other frequencies so that an overall reduction results in the frequency band of interest. This notion of best internal velocity feedback gain is studied in Chapter 5.

APPENDIX F: Measurement apparatus and procedures.

Measurements in Chapters 2, 4 and 5 are carried out with an Advantest R9211C FFT Servo Analyzer.

For open loop measurements to assess stability its signal output is used to apply a band limited white noise voltage to the respective driving amplifier. The 0-10Hz, 0-100Hz, 0-1kHz, 0-10kHz and 0-100kHz are excited successively. Measurements are shown in a frequency range that is sufficient to assess stability depending on the control scheme. In the case of the inertial actuator in Chapters 4 and 5 the power supply of the driving amplifier from [57] limits the maximum current to 1A. In the reactive actuator case in Chapter 2 an additional ammeter in series between the driving amplifier, either a Crown Electronics DC300, a H&H VX-200 voltage or a no-name current amplifier, allows to monitor the driving current. The signal output voltage of the servo analyser is adjusted in order to obtain a sufficient coherence in the respective frequency band. The driving and the measurement amplifiers are used to adjust the feedback gain. Open loop measurements are non-calibrated. In some cases indicated in the text additionally a KEMO Benchmark VBF8 4th order filter with adjustable high-pass or low-pass up to 100kHz is used to amplify, invert and/or filter a feedback signal. Time integration of the B&K 4375 accelerometer signal is carried out with a B&K charge amplifier with high-pass filter setting at 10Hz. The open loop FRF between the input on channel a and output on channel b mentioned in each section is measured with the transducers, inverter and amplifiers in series. 30 successive measurements are carried out and the FRF, with a resolution of 800 lines in each frequency range, is automatically averaged by the servo analyser. For the estimation of the FRF between channel a an b the frequency analyser internally digitalizes the data, calculates the power spectral density of the input signal in channel a and the cross spectral density between channel *a* and channel *b*. The Nyquist plot directly displayed by the analyser can be analysed for stability by investigating the number of circles around the critical point (1, 0j). When stability is guaranteed the open loop is closed by disconnecting the cables from channel a and b and directly connecting them with a BNC connector. Usually instability is either directly visible or audible by harmonic movement of the actuator. However, care has to be taken that the frequency band close to the critical point lies in an audible or visible range because otherwise the circuit might become unstable and destroy components before being directly noticeable.

For closed loop measurements to assess performance the primary shaker is driven via the DC-300 amplifier by the signal output of the servo analyzer. The force exerted on the plate by the shaker is measured with the intermediate B&K 8230 force transducer connected via a B&K 2635 charge amplifier to channel a. Channel b is connected via another integrating B&K 2635 charge amplifier to the B&K 4375 monitor accelerometer on the plate. Measurements as in the case of stability assessment are carried out in a frequency range up to 1kHz in the open loop and closed loop case. Plots in the thesis for performance assessment show calibrated measurements where the amplification of the charge amplifiers for accelerometer and force transducer is removed.

Measurements in Chapter 2 are carried out with a HP frequency analyser, a current amplifier from [57] and a PCB208 force transducer with ICP electronics that have a high pass filter at 10Hz. A sine sweep voltage between 10Hz and 10kHz is input to the actuator and the frequency analyser calculates the FRF between the input to the current amplifier and the output of the ICP amplifier.

LIST OF REFERENCES

[1] Fahy F.J. (1994) *Sound and Structural Vibration*, London, Academic Press.

[2] L.L. Beranek (1954).*Acoustics*. New York, McGraw-Hill.

[3] Heckl M. and Müller H.A. (1995) *Taschenbuch der Technischen Akustik*. Berlin, Springer, 2nd Edition.

[4] Fuller C.R., Elliott S.J. and Nelson P.A. (1997) *Active Control of Vibration*. London, Academic Press, 2nd printing.

[5] Lagö T.L. (2002) Industry Overview of Active Control Methods and Applications. *Adaptronic Congress 2002*, 23.-24.04.

[6] Gardonio P. (2002) Review of Active Techniques for Aerospace Vibro-Acoustic Control. *Journal of Aircraft* **39**(2), 206-214.

[7] Elliott, S.J. (2001) *Signal Processing for Active Control*. London, Academic Press.

[8] Elliott S.J., Serrand M. and Gardonio P. (2001) Feedback Stability Limits for Active Isolation Systems with Reactive and Inertial Actuators. *Transactions of the ASME. Journal of Vibration and Acoustics* **123**, 250-261.

[9] Beard A.M., von Flotow A.H. and Schubert D.W. (2000) A practical product implementation of an active/passive vibration isolation system. *Proceedings of Stable Control of Active Isolation Systems*, 101-108.

[10] Gardonio P., Bianchi E. and Elliott S.J. (2004) Smart panel with multiple decentralised units for the control of sound transmission. Part I: theoretical predictions. *Journal of Sound and Vibration* **274** (1-2), 163-192.

[11] Nelson P.A., Elliott, S.J. (1996) *Active Control of Sound*. London, Academic Press.

[12] Roure A. (1985) Self-adaptive broadband active sound control system. *Journal of Sound and Vibration* **101** (3), 429-441.

[13] Rafaely B. and Jones M. (2002) Combined feedback-feedforward active noise-reducing headset-The effect of the acoustics on broadband performance. *Journal of the Acoustical Society of America* **112** (3), 981-989.

[14] Elliott S.J., Nelson P.A., Stothers I.M. and Boucher C.C. (1990) In-flight Experiments on the Active Control of Propeller-induced Cabin Noise. *Journal of Sound and Vibration* **140** (2), 219-238.

[15] Swanson D. and Potter J. (2005) Active Systems in Rotary and Fixed Wing Aircraft Applications. *Adaptronic Congress 2005, Göttingen*, 31.05./01.06. Paper No.17.

[16] Fuller C.R. and Silcox R.J. (1992) Active Structural Acoustic Control. *Journal of the Acoustical Society of America* **91** (1), 519.

[17] Bianchi E. (2003) Smart panel with an array of decentralised control systems for active structural acoustic control. *ISVR. University of Southampton. Ph.D. thesis*.

[18] Jakob A. (1999) Aktive Minderung der Schallabstrahlung schwingender Platten. *Fortschritt-Berichte VDI, Reihe 11, No.280*. Düsseldorf, VDI.

[19] Petitjean B. and Legrain I. (1996) Feedback Controllers for Active Vibration Suppression. *Journal of Structural Control* **3** (1-2), 111-127.

[20] Gardonio P. and Elliott S.J. (2004) Smart panels for active structural acoustic control. *Smart Mater. Struct.* **13**, 1314-1336.

[21] Johnson M.E. and Elliott S.J. (1995) Active control of sound radiation using volume velocity cancellation. *Journal of the Acoustical Society of America* **98** (4), 2174-2186.

[22] Gardonio P., Lee Y.-S., Elliott S.J. and Debost S. (2001) Analysis and measurement of a matched volume velocity sensor and uniform force actuator for active structural acoustic control. *Journal of the Acoustical Society of America* **100** (6), 3025-3031.

[23] Henrioulle K. and Sas P. (2003) Experimental validation of a collocated PVDF volume velocity sensor/actuator pair. *Journal of Sound and Vibration* **265**, 489-506.

[24] De Man P. (2004) Contrôle actif du rayonnement acoustique des plaques : une approche à faible autorité. *Université Libre de Bruxelles, Ph.D. Thesis.*

[25] Elliott S.J., Gardonio P., Sors T.C. and Brennan M.J. (2002) Active vibroacoustic control with multiple local feedback loops. *Journal of the Acoustical Society of America* **111** (2), 908-915.

[26] Preumont A. (2002) *Vibration Control of Active Structures.* Dordrecht, Kluver Academic Publishers, 2nd Edition.

[27] Sun J.Q. (1996) Some observations on physical duality and colocation of structural control sensors and actuators. *Journal of Sound and Vibration* **194** (5), 765-770.

[28] Yang S.M. and Lee Y.J. (1993) Vibration suppression with optimal sensor/actuator location and feedback gain. *Smart Mater. Struct.* **2**, 232-239.

[29] Holterman J. and De Vries T.J.A. (2005) Active Damping Based on Decoupled Collocated Control. *IEEE/ASME Transactions on Mechatronics* **10** (2), 135-145.

[30] Gardonio P. and Elliott S.J. (2005) Smart panels with velocity feedback control systems using triangularly shaped strain actuators. *Journal of the Acoustical Society of America* **117** (4), 2046-2064.

[31] Paulitsch C., Gardonio P. and Elliott S.J. (2003) Investigation of an Electrodynamic Actuator for Self-Sensing Active Vibration Control. *ISVR Technical Memorandum No.* 917.

[32] Inman D.J., Dosch J.J. and Garcia E. (1992) A self-sensing piezoelectric actuator for collocated control. *J. of Intell. Mater. Syst. and Struct.* **3**, 166-185.

[33] Okada Y., Matsuda K. and Hashitani H. (1995) Self-sensing Active Vibration Control using the Moving-Coil-Type Actuator. *Transactions of the ASME. Journal of Vibration and Acoustics* **117**, 411-415.

[34] Clark R.L., Saunders W.R. and Gibbs G.P. (1997) *Adaptive Structures.* New York, Wiley.

[35] Den Hartog J.P. (1948) *Mechanics.* New York, Dover.

[36] Crawley E.F. and de Luis J. (1987) Use of Piezoelectric Actuators as Elements of Intelligent Structures. *AIAA Journal* **25** (10), 1373-1385.

[37] Dimitriadis E.K., Fuller C.R. and Rogers C.A. (1991) Piezoelectric Actuators for Distributed Vibration Excitation of Thin Plates. *Transactions of the ASME. Journal of Vibration and Acoustics* **113**, 100-107.

[38] Ehmann C. (2004) Methoden und Komponenten für die Realisierung aktiver Schwingungsdämpfung. *Forschungsberichte Mechatronik & Maschinenakustik, D17.* Aachen, Shaker.

[39] Dehandschutter W. and Sas P. (1998) Active Control of Structure-Borne Road Noise Using Vibration Actuators. *Transactions of the ASME. Journal of Vibration and Acoustics* **120**, 517-523.

[40] Huang Y.M. and Fuller C.R. (1998) Vibration and Noise Control of the Fuselage via Dynamic Absorbers. *Transactions of the ASME. Journal of Vibration and Acoustics* **120**, 496-502.

[41] Garcia E., Webb S. and Duke J. (1995) Passive and Active Control of a Complex Flexible Structure Using Reaction Mass Actuators. *Transactions of the ASME. Journal of Vibration and Acoustics* **117**. 116-122.

[42] Hallauer W.L. and Lamberson S.E. (1989) Experimental active vibration damping of a plane truss using hybrid actuation. *AIAA Paper* 89-1169-CP, April, 80-90.

[43] Ham F.M., Greeley S.W. and Henniges B.L. (1989) Active Vibration Suppression for the Mast Flight System. *IEEE Control Systems Magazine* **9**. 85-90.

[44] Juang J. (1984) Optimal Design of a Passive Vibration Absorber for a Truss Beam. *AIAA Journal of Guidance, Control and Dynamics* **7**(6), 733-739.

[45] Miller D.W. and Crawley E.F. (1988) Theoretical and Experimental Investigation of Space-Realizable Inertial Actuation for Passive and Active Structural Control. *AIAA Journal of Guidance, Control and Dynamics* **11**(5), 449-458.

[46] Matunaga S., Yimei Y. and Ohkami Y. (1997) Vibration Suppression Using Acceleration Feedback Control with Multiple Proof-Mass Actuators. *AIAA Journal* **35**(5), 856-862.

[47] Spanos J.T. (1989) Control-Structure Interaction in Precision Pointing Serco Loops. *AIAA Journal of Guidance, Control and Dynamics* **12**(2), 256-263.

[48] Rankers A.M. and van Eijk J. (1994) The Influence of Reaction Forces on the Behaviour of High Performance Motion Systems. *Second International Conference on Motion and Vibration Control, Yokohama*, August 30-September 3, 711-716.

[49] Inman D.J. (1990) Control/Structure Interaction: Effects of Actuator Dynamics chapter 20 in: *Mechanics and Control of Large Structures* ed. J.L. Junkins, **29**(4), 507-533.

[50] Balas M.J. (1979) Direct Velocity Feedback Control of Large Space Structures. *AIAA Journal of Guidance and Control* **2**, 252-253.

[51] Paulitsch C., Gardonio P., Elliott S.J., Sas P. and Boonen R. (2004) Design of a Lightweight, Electrodynamic, Inertial Actuator with Integrated Velocity Sensor for Active Vibration Control of a Thin Lightly-Damped Panel. *Proceedings of ISMA 2004, Katholieke Universiteit Leuven, Belgium,* 20-22 September.

[52] Benassi L. and Elliott S.J. (2004) Active vibration isolation using an inertial actuator with local displacement feedback control. *Journal of Sound and Vibration* **278**, 705-724.

[53] Lindner D.K., Celano T.P. and Ide E.N. (1991) Vibration Suppression Using a Proofmass Actuator Operating in Stroke/Force Saturation. *Transactions of the ASME. Journal of Vibration and Acoustics* **113**, 423-433.

[54] Lindner D.K., Zvonar G.A. and Borojevic D. (1994) Performance And Control Of Proof-Mass Actuators Accounting For Stroke Saturation. *AIAA Journal of Guidance, Dynamics and Control* **17**(5). 1103-1108.

[55] Scruggs J. and Lindner D.K. (1999) Optimal sizing of a proof-mass actuator. *AIAA Paper* 99-1288.

[56] Lindner D.K., Zvonar G.A. and Borojevic D. (1997) Nonlinear control of a proof-mass actuator. *AIAA Journal of Guidance, Control and Dynamics* **20**(3). 464-470.

[57] Paulitsch C., Gardonio P., Boonen R., Sas P. and Elliott S.J. (2004) Design of an Inertial, Electrodynamic Actuator with Internal Velocity Sensor for Active Vibration Damping of Lightweight, Flexible Structures. *ISVR Technical Memorandum No. 940.*

[58] Janocha H. (1992) *Aktoren Grundlagen und Anwendungen.* Berlin, Springer.

[59] Lee Y.K. and Shimoyama I. (2000) A micro rubber artificial muscle driven by a micro compressor for artificial limbs. *Actuator 2000. 7th International Conference on New Actuators, Bremen,* 19-21 June. pp.272-275.

[60] Janocha, H. (1999) *Adaptronics and Smart Structures.* Berlin, Springer.

[61] Busch-Vishniac I.J. (1998) *Electromechanical Sensors and Actuators.* New York, Springer.

[62] Brennan M.J., Garcia-Bonito J., Elliott S.J., David A. and Pinnington R.J. (1999) Experimental investigation of different actuator technologies for active vibration control. *Smart Material and Structures* **8**, 145-153.

[63] Silva E.C.N., Nishiwaki S. and Kikuchi N. (2000) Topology Optimization Design of Flextensional Actuators. *IEEE Transactions on Ultrasonics, Ferroelectrics and Frequency Control* **47**(3), 657-671.

[64] Product brochure. CEDRAT SA, 15, Chemin de Malacher – ZIRST, 38246 Meylan, France. www.cedrat.fr.

[65] Petricevic R. and Gurka M. (2005) High Performance Piezoelectric Composites. *Adaptronic Congress 2005, Göttingen,* 31.05./01.06. Paper No.19.

[66] BS ISO 5344:2004 (2004) Electrodynamic vibration generating systems – Performance characteristics. BSI, London.

[67] Wildi T. (2002) *Electrical Machines, Drives and Power Systems,* Upper Saddle River, Prentice Hall.

[68] Stölting H.-D., Kallenbach, E. (2002) *Handbuch Elektrische Kleinantriebe.* Munich, Hanser.

[69] Paulitsch C., Okamoto K.-I. and Utsunomiya K. (2003) Self-sensing Active Damping Guide Roller for Elevators. *VDI-Berichte* 1753. Düsseldorf, VDI, 91-110.

[70] Okada Y., Matsuda K. and Hashitani H. (1995) Self-sensing Active Vibration Control using the Moving-Coil-Type Actuator. *Transactions of the ASME. Journal of Vibration and Acoustics* **117,** 411-415.

[71] Heinrich J., Hermann R., Eccarius M. and Kallenbach E. (2000) Optimal application fields for electromagnetic and piezoceramic actuators. *Actuator 2000,* Bremen. Paper P67.

[72] Product brochure BEI Kimco Magnetics Division 2470 Coral Street, Building "D", Vista, CA 92081-8430. USA. www.beikimco.com

[73] Product brochure TIRA GmbH, Eisfelder Straße 23/25, 96528 Schalkau. Germany. www.tira-gmbh.de

[74] Product brochure LDS Test and Measurement Ltd, Heath Works Baldock Road, Royston Herts, SG8 5BQ. UK. www.lds-group.com

[75] Product brochure Unholtz-Dickie Corporation, 6 Brookside Drive, Wallingford, CT 06492. USA. www.udco.com

[76] Product brochure Aurasound Inc., 11839 East Smith Avenue, Santa Fe Springs, CA 90670. USA. www.aurasound.com

[77] Product brochure Micromega Dynamics SA, Liege Science Park, Rue des Chasseurs Ardennais, B-4031 Angleur. Belgium. www.micromega-dynamics.com

[78] She T. (1992) Active vibration control by eigenstructure assignment. *Department of Mechanical Engineering, Katholieke Universiteit Leuven, Ph.D. thesis.*

[79] Roschke T. (2002) Miniaturised bipolar electromagnetic actuators for space applications. *Actuator 2002. 8th International Conference on New Actuators, 10-12 June, Bremen,* 664-667.

[80] Kim Y.-B., Hwang W.-G., Kee C.-D. and Yi H.-B. (2001) Active vibration control of a suspension system using an electromagnetic damper. *Proc. Instn. Mech. Engrs. Part D* **215**, 865-873.

[81] Hartwig C., Hasse H., Hofmann M. and Karkosch H.-J. (2000) Electromagnetic actuators for active engine vibration cancellation. *Actuator 2000. 7th International Conference on New Actuators, Bremen,* B5.4.

[82] Kjellqvist P., Sadarangani C. and Östlund, S. (2001) Design of a Permanent Magnet Synchronous Machine for an Electromechanical Active Suspension Actuator. *IEEE IEMDC 2001,* Cambridge, Ma, June 17-20, 534-541.

[83] Bendel K., Brechlin E. and Storz A. (2000) Electromagnetic vibration excitation of moments and forces with minimal mass loading. *Proceedings of ISMA25, Vol. 2,* 967-972.

[84] Foshage J., Davis T., Sullivan J., Hoffmann T. and Das A. (1996) Hybrid active/passive actuator for spacecraft vibration isolation and suppression. *Proceedings of SPIE Vol. 2865,* 104-122.

[85] Hanieh A.A. (2003) Active Isolation and Damping of Vibrations via Stewart Platform. *Université Libre de Bruxelles, Ph.D. thesis.*

[86] Minotti P. (2001) An approach to Smart Structure Design using MEMS Technology in: *Responsive Systems for Active Vibration Control* ed. A. Preumont, Dordrecht, Kluwer Academic Publishers, 325-378.

[87] Kallenbach E., Eick R., Quendt P., Ströhla T., Feindt K. and Kallenbach M. (2003) *Elektromagnete.* Stuttgart, Teubner, 2nd edition.

[88] Hunt F.V. (1954) *Electroacoustics. Transduction and Its Historical Background.* Harvard University Press.

[89] Pratt J. and Flatau A.B. (1993) Development and Analysis of a Self-sensing Magnetostrictive Actuator Design. *SPIE/ASME/SEM North American Conference on Smart Structures.*

[90] Clephas B. and Janocha H. (2000) Extended Performance of Hybrid Actuators. *International Journal of Applied Mechanics and Engineering* 5(1), 157-168.

163

[91] Montie D. and Maslen E. (2001) Experimental Self-Sensing Results for a Magnetic Bearing. *Proceedings of ASME TURBOEXPO*, 4-7 June.

[92] Kettle P., Murray A. and Mynihan F. (1998) Control of a Brushless DC motor using an extended Kalman estimator. *PCIM'98 Intelligent Motion*, 385-392.

[93] Hagood N.W. and von Flotow A. (1991) Damping of Structural Vibrations with Piezoelectric Materials and Passive Electrical Networks. *Journal of Sound and Vibration* **146**(2), 243-268.

[94] Fein O.M. and Gaul L. (2004) An adaptive shunted piezo approach to reduce structural vibrations. *Proceedings of SPIE Vol. 5386. Smart Structures and Materials 2004: Damping and Isolation*, 393-404.

[95] Hagood N.W. and Crawley E.F. (1991) Experimental Investigation of Passive Enhancement of Damping for Space Structures. *Journal of Guidance, Control and Dynamics* **14**(6), 1100-1109.

[96] Fleming A.J., Behrens S. and Moheimani S.O.R. (2000) Synthetic impedance for implementation of piezoelectric shunt-damping circuits. *Electronics Letters* **36**(18), 1525-1526.

[97] Corr L.R. and Clark W.W. (2002) Comparison of low-frequency piezoelectric switching shunt techniques for structural damping. *Smart Materials and Structures* **11**, 370-376.

[98] Anderson E.H. and Hagood N.W. (1994) Simultaneous Piezoelectric Sensing/Actuation: Analysis And Application To Controlled Structures. *Journal of Sound and Vibration* **174**(5), 617-639.

[99] Wang K.W. (1995) Structural Vibration Suppression Via Parametric Control Actions – Piezoelectric Materials With Real-time Semi-Active Networks in: *Series on Stability, Vibration and Control of Structures Volume1: Wave Motion, Intelligent Structures and Nonlinear Mechanics*. Singapore, World Scientific, 112-134.

[100] Cole D.G. and Clark R.L. (1994) Adaptive Compensation of Piezoelectric Sensoriactuators. *Journal of Intelligent Material Systems and Structures* **5**, 665-672.

[101] Vippermann J.S. and Clark R.L. (1996) Implementation of an Adaptive Piezoelectric Sensoriactuator. *AIAA Journal* **34**(10), 2102-2109.

[102] Ma K. (2003) Vibration control of smart structures with bonded PZT patches: novel adaptive filtering algorithm and hybrid control scheme. *Smart Mater. Struct.* **12**, 473-482.

[103] Lee Y.-S. Elliott S.J. and Gardonio P. (2003) Matched piezoelectric double sensor/actuator pairs for beam motion control. *Smart Materials and Structures* **12**, 541-548.

[104] Oshima K., Takigami T. and Hayakawa Y. (1997) Robust Vibration Control of a Cantilever Beam Using Self-Sensing Actuator. *JSME International Journal. Series C* **40**(4), 681-687.

[105] Glad T. and Ljung L. (2000) *Control Theory. Multivariable and Nonlinear Methods*. London, Taylor & Francis.

[106] Forward R.L. (1979) Electromechanical transducer-coupled mechanical structure with negative capacitance compensation circuit. U.S. Patent 4,158,787. June 19.

[107] Wu S.-Y. (2000) Broadband piezoelectric shunts for structural vibration control. U.S. Patent 6,075,309. June 13.

[108] Behrens S., Fleming A.J. and Moheimani, S.O.R. (2003) A broadband controller for shunt piezoelectric damping of structural vibration. *Smart Mater. Struct.* **12**, 18-28.

[109] Arafa M. and Baz A. (2004) On the Nonlinear Behavior of Piezoelectric Actuators. *Journal of Vibration and Control* **10** (3), 387-398.

[110] Riordan R.H.S. (1967) Simulated inductors using differential amplifiers. *Electronics Letters* **3** (2), 50-51.

[111] Stanway R., Rongong J.A. and Sims N.D. (2003) Active constrained-layer damping: a state-of-the-art review. *Proc. Instn Mech. Engrs. Part I: J. Systems and Control Engineering* **217**, 437-456.

[112] Huang S.C., Inman D.J. and Austin E.M. (1996) Some design considerations for active and passive constrained layer damping treatments. *Smart Mater. Struct.* **5**, 301-313.

[113] Inman D.J. and Lam M.J. (1997) Active constrained layer damping treatments. Structural Dynamics: Recent Advances. *Proceedings of the 6th International Conference. Vol. 1*, 1-20.

[114] Crassidis J.L., Baz A. and Wereley N. (2000) H$_\infty$ Control of Active Constrained Layer Damping. *Journal of Vibration and Control* **6**(1), 113-136.

[115] Cabell, R.H. and Gibbs, G.P. (2000) Hybrid active/passive control of sound radiation from panels with constrained layer damping and model predictive feedback control. *Proceedings of Noise-CON2000. Newport Beach. 03-05 December 2000.*

[116] Richard C., Guyomar D., Audigier D. and Bassaler H. (2000) Enhanced semi passive damping using continuous switching of a piezoelectric device on an inductor. *Proceedings of SPIE Vol. 3989. Smart Structures and Materials 2000: Damping and Isolation*, 288-299.

[117] Abramovitch D. and Franklin G. (2002) A Brief History of Disk Drive Control. *IEEE Control Systems Magazine.*

[118] Behrens S., Fleming A.J. and Moheimani S.O.R. (2003) Electrodynamic Vibration Suppression. *Proceedings of SPIE Vol. 5052. Smart Structures and Materials: Damping and Isolation*, 344-355.

[119] Hanson B.M., Brown M.D. and Fisher J. (2001) Self-Sensing: Closed-Loop Estimation for a Linear Electromagnetic Actuator. *Proceedings of the American Control Conference, Arlington, Va, 25-27 June.*

[120] Voigt P.G.A.H. (1925) Improvements in or Relating to Thermionc Amplifying Circuits for Telephony. British Patent No. 231972 filed January 1924.

[121] Horrowitz P. and Hill W. (1980) *The Art of Electronics.* Cambridge University Press. 3rd Edition.

[122] de Boer E. (1961) Theory of Motional Feedback. *IRE Transaction on Audio* January-February, 15-21.

[123] Tanner R.L. (1951) Improving Loudspeaker Response with Motional Feedback. *Electronics* **142**, 228-240.

[124] Holle, W. (1952) Gegenkopplung an Lautsprechern. *Funk-Technik* **7**(18), 490-492.

[125] Holdaway, H.W. (1963) Design of Velocity-Feedback Transducer Systems for Stable Low-Frequency Behavior. *IEEE Transactions on Audio* September-October, 155-173.

[126] Holdaway, H.W. (1963) Controlling the Upper-Frequency Characteristics of Velocity-Feedback Loudspeaker Systems. *IEEE Transactions on Audio* September-October, 174-182.

[127] de Boer J. and Schenkel G. (1948) Electromechanical Feedback. *The Journal of the Acoustical Society of America* **20** (5), 641-647.

[128] Olson H.F. (1952) *Elements of Acoustical Engineering*. New York, D van Nostrand. 2nd edition. 4th reprint.

[129] Hall D.S. (1998) Speaker containing dual coil. U.S. Patent No. 5,832,096.

[130] Watkins W.H. (1974) Device to effectively eliminate the motion induced back-emf in a loudspeaker system in the region of fundamental acoustic resonance. U.S. Patent No. 3,838,216.

[131] Lace D.A. (1968) Moving coil electro-mechanical device. U.S. Patent 3,417,268.

[132] Burke A. (1959) Sound reproducer. U.S. Patent 2,897,291.

[133] Kagdis W.A. (1960) Loudspeaker construction. U.S. Patent 2,926,221.

[134] Guss R. (1962) Loudspeaker. U.S. Patent 3,055,991.

[135] Sotome H. (1972) Loudspeaker having annular diaphragm with double voice coil. U.S. Patent 3,665,124.

[136] Lee K.-T., Kim C.-J., Park N.-C. and Park Y.-P. (2003) Improvement of dynamic characteristics for optical pickup actuator by magnetic circuit. *Microsystem Technologies* **9**, 232-242.

[137] Woolvet G.A. (1977) *Transducers in digital systems*. London, IEE Control Engineering Series 3, IEE.

[138] Ackermann A., Steinbusch H., Vollmer T., Wang J., Jewell G.W. and Howe D. (2004) A spherical permanent magnet actuator for a high-fidelity force-feedback joystick. *Mechatronics* **14**, 327-339.

[139] Elieli, B. (1987) The application of an inductively coupled shorted turn and the dual-coil loudspeaker system. *AES Reprint No 2548. 83rd AES Convention,* G-2.

[140] Radcliffe C.J. and Gogate S.D. (1996) Velocity feedback compensation of electromechanical speakers for acoustic applications. *IFAC Triennial World Congress, San Francisco, Ca*, paper 3a-07-1.

[141] Miller J.M. (1950) Combining positive and negative feedback. *Electronics* March.

[142] Clements W. (1951) A new approach to loudspeaker damping. *Audio Engineering* August.

[143] Ginzton E.L. (1938) Balanced Feed-Back Amplifiers. *Proceedings of the Institute of Radio Engineers* **26** (11), 1367-1379.

[144] Mayer H.F. (1939) Control of the Effective Internal Impedance of Amplifiers by Means of Feedback. *Proceedings of the I.R.E* March, 213-217.

[145] Terman F.E. (1950) *Radio Engineers' Handbook*. London, McGraw Hill.

[146] Werner R.E. and Carrell R.M. (1958) Application of Negative Impedance Amplifier to Loudspeaker Systems. *Journal of the Audio Engineering Society* **6**(4), 240-243.

[147] Wentworth J.P. (1951) Loudspeaker Damping by the Use of Inverse Feedback. *Audio Engineering* December.

[148] Clements W. (1952) It's Positive Feedback. *Audio Engineering* May.

[149] Childs U.J. (1952) Loudspeaker Damping with Dynamic Negative Feedback. *Audio Engineering* February.

[150] Stahl K.E. (1981) Synthesis of Loudspeaker Mechanical Parameters by Electrical Means: A New Method for Controlling Low-Frequency Loudspeaker Behavior. *J. Audio Eng. Soc.* **29**(9), 587-596.

[151] Normandin R. (1984) Extended Low-Frequency Performance of Existing Loudspeaker Systems. *J. Audio Eng. Soc.* **32**(1/2), 18-22.

[152] Birt D. (1988) Loudspeaker Power Amplifiers with Load-Adaptive Source Impedance. *J. Audio Eng. Soc.* **36**(7/8), 552-561.

[153] Greiner R.A. and Travis M.S. Jr. (1984) Loudspeaker Distortion Reduction. *J. Audio Eng. Soc.* **32**(12), 956-963.

[154] Catrysse J.A.M. (1985) On the Design of Some Feedback Circuits for Loudspeakers. *J. Audio Eng. Soc.* **33**(6), 430-435.

[155] Lane S.A. and Clark R.L. (1998) Improving Loudspeaker Performance for Active Noise Control Applications. *J. Audio Eng. Soc.* **46**(6), 508-519.

[156] von Recklinghausen D.R. (1985) Low-Frequency Range Extension of Loudspeakers. *J. Audio Eng. Soc.* **33**(6), 440-446.

[157] Adams G.J. (1979) Optimisation and motional feedback techniques in loudspeaker system design. *Department of Electrical Engineering. The University of Southampton, Ph.D. thesis.*

[158] Thiele A.N. (1971) Loudspeakers in Vented Boxes: Part I. *J. Audio Eng. Soc.* **19**(5), 382-392.

[159] Thiele A.N. (1971) Loudspeakers in Vented Boxes: Part 2. *J. Audio Eng. Soc.* **19**(5), 471-483.

[160] Benjamin E. (1994) Audio Power Amplifiers for Loudspeaker Loads. *J. Audio Eng. Soc.* **42**(9), 670-683.

[161] Self D. (2000) *Audio Power Amplifier Design Handbook*. Oxford, Newnes. 2nd Edition.

[162] Borwick J. (1994) *Loudspeaker and Headphone Handbook*. Oxford, Focal Press. 2nd Edition.

[163] Bai M.R. and Wu H. (1999) Robust control of a sensorless bass-enhanced moving-coil loudspeaker system. *J.Acoust.Soc.Am.* **105**(6), 3283-3289.

[164] Fleming A.J. and Moheimani S.O.R (2005) Synthesis and Implementation of Sensor-Less Active Shunt Controllers for Electromagnetically Actuated Systems. *IEEE Transactions on Control Systems Technology* **13**(2), 246-261.

[165] Paulitsch C., Gardonio P. and Elliott S.J. (2004) Active Vibration Damping Using a Self-Sensing Electrodynamic Actuator. *Proceedings of SPIE Vol. 5386. Smart Structures and Materials: Damping and Isolation*, 282-293.

[166] Sodano H.A. and Bae J.-S. (2004) Eddy Current Damping in Structures. *The Shock and Vibration Digest* **36**(6), 469-478.

[167] Gardonio P. and Brennan M.J. (2004) Mobility and impedance methods in structural dynamics. Chapter 9 in: *Advanced Applications in Acoustics, Noise and Vibration*, edited by F.Fahy and J.Walker, London, Spon, 389-447.

[168] Meirovitch L. (1989) *Dynamis and Control of Structures*. New York, John Wiley.

[169] Snelling E.C. (1988) *Soft Ferrites Properties and Applications*. London, Butterworths.

[170] Inan U.S. and Inan A.S. (1998) *Engineering Electromagnetics*. Menlo Park, Addison-Wesley.

[171] Nasar S.A. and Boldea I. (1987) *Linear electric motors: Theory, Design, and Practical Applications*. Englewood Cliffs, Prenctice-Hall.

[172] Jufer M. (1994) Size limits and characteristic influence of electromagnetic actuators. *Actuator94, Bremen*, 15-17.06. 390-393.

[173] M. McCaig (1977) *Permanent magnets in theory and practice*. London, Pentech Press.

[174] Jurisch F. (2001) Entwicklungen auf dem Permanentmagnetsektor. *GMM-Fachbericht 33, VDE, Berlin*, 95-99.

[175] Hanselman D.C. (1994) *Brushless permanent-magnet motor design*. New York, McGraw-Hill.

[176] Ireland J.R. (1968) *Ceramic permanent-magnet motors*. New York, McGraw-Hill.

[177] Hendershot J.R. and Miller T.J.E. (1994) *Design of brushless permanent-magnet motors*. Oxford, Magna Physics Publishing and Clarendon Press.

[178] Product brochure GOUDSMIT MAGNETIC SUPPLIES B.V. P.O. Box 7, 5580 AA Waalre. The Netherlands. www.goudsmitmagnets.com.

[179] Nasar S.A., Boldea I. and Unnewehr L.E. (1993) *Permanent magnet, reluctance and self-synchronous motors*. Boca Raton, CRC Press.

[180] Czichos H. (1996) *Hütte Die Grundlagen der Ingenieurwissenschaften*. Berlin, Springer, 30th edition.

[181] Oberbeck C. and Ulbrich G. (2002) Design and optimisation of electromagnetic actuators for mechanical and automotive applications. *Actuator 2002. 8th International Conference on New Actuators. 10-12 June, Bremen.*

[182] Z.P. Bazant and L. Cedolin (1991) *Stability of structures elastic, inelastic, fracture and damage theories*. New York, Oxford University Press.

[183] Product brochure A.C.C.&S. 57, rue de la Grossau, BP 111, 67028 Strasbourg Cedex 1. France. www.servometer.fr.

[184] J.P. Den Hartog (1967) *Sterkteleer*. Utrecht/Antwerpen, Prisma-Technica, Het Spectrum.

[185] R.D. Blevins (1979) *Formulas for natural frequencies and mode shape*. New York, Van Nostrand.

[186] Slemon G.R. and Liu X. (1990) Core losses in permanent magnet motors. *IEEE Transactions on Magnetics* **26**(5), 1653-1655.

[187] Miyashita O., Ohniwa K., Fujimaki T. and Morikawa M. (1995) Analysis of the Flux-Lag Effect in an Iron Core. *Journal of the Japan Society of Applied Electromagnetics and Mechanics* **19**(5), 875-878.

[188] Paulitsch C., Gardonio P. and Elliott S.J. (2004) Active Vibration Suppression using an Electrodynamic, Inertial Actuator with Internal, Relative Velocity Sensor. *Procedings of ACTIVE 2004, Williamsburg, Va*, 20.-22.09.

[189] Paulitsch C., Gardonio P. and Elliott S.J. (2004) A lightweight, miniaturised, inertial actuator for active vibration control of mechanical structures. *Britain's younger engineers at the House of Commons, poster presentation*, London, 14.12.

[190] Paulitsch C., Gardonio P. and Elliott S.J. (2005) Active vibraton damping using an electrodynamic actuator with internal velocity sensor. *Proceedings of SPIE Vol. 5760. Smart Structures and Materials: Damping and Isolation*, 305-316.

[191] Paulitsch C., Gardonio P. and Elliott S.J. (2005) Internal Velocity Feedback for Stabilisation of Inertial Actuators for Active Vibration Control. *IUTAM Symposium on Vibration Control of Nonlinear Mechanisms and Structures, Munich*, 18.-22.07. (in print).

[192] Paulitsch C., Gardonio P. and Elliott S.J. (2005) Active Vibration Damping using a Lightweight Inertial Actuator. *Adaptronic Congress 2005, Göttingen*, 31.05./01.06. Paper No.12.

[193] Product brochure Geospace, LP, 7007 Pinemont, Houston, Texas 77040. USA. www.geospacelp.com

[194] Product brochure LMS, Researchpark Z1, Interleuvenlaan 68, 3001 Leuven. Belgium. www.lmsintl.com

[195] Bronstein I. N., Semendjajew K. A., Musiol G. and Mühlig H. (1997) *Taschenbuch der Mathematik*, chapter 2.2 and chapter 3.5.2.7, Frankfurt/Main, Harri Deutsch, 3rd Edition.

[196] Kohlmeier T., Seidemann V., Büttgenbach S. and Gatzen H.H. (2004) An investigation on technologies to fabricate microcoils for miniaturized actuator systems. *Microsystem Technologies* **10**, 175-181.

[197] Ahn C.A. and Allen M.G. (1993) A planar micromachined spiral inductor for integrated magnetic microactuator applications. *J. Micromech. Microeng.* **3**. 37-44.

[198] Martincic E., Figueras E., Cabruja E., Dufour-Gergam E. and Woytasik M. (2004) Magnetic micro-transformers realized with a flip-chip process. *J. Micromech. Microeng.* **14**. S55-S58.

[199] Budde T., Föhse M., Majjer B., Lüthje H., Bräuer G. and Gatzen H.H. (2004) An investigation on technologies to fabricate magnetic microcomponents for miniaturized actuator systems. *Microsystem Technologies* **10**, 237-240.

[200] Davis W.O., O'Reilly O.M. and Pisano A.P. (2004) On the Nonlinear Dynamics of Tether Suspensions for MEMS. *Transactions of the ASME Journal of Vibration and Acoustics* **126**, 326-331.

[201] Han J.S., Ko J.S., Kim Y.T. and Kwak B.M. (2002) Parametric study and optimisation of a micro-optical switch with a laterally driven electromagnetic microactuator. *J. Micromech. Microeng.* **12**, 939-947.

[202] Han J.S., Ko J.S. and Korvink J.G. (2004) Structural optimisation of a large-displacement electromagnetic Lorentz force microactuator for optical switching applications. *J. Micromech. Microeng.* **14**, 1585-1596.

[203] Feldmann M., Güttler J., Eickstätt J. and Büttgenbach S. (2004) A Novel Monolithic Micro Plunger Coil Actuator using Polymer Magnets and Double Layer Micro Coils. *Technical Digest of Eurosensors XVIII, Rome 12-15 Sept 2002*.

[204] Frank T. (1998) Two-axis electrodynamic mircopositioning devices. *J. Micromech. Microeng.* **8**, 114-118.

[205] Mizuno M. and Chetwynd D.G. (2003) Investigation of a resonance microgenerator. *J. Micromech. Microeng.* **13**, 209-216.

[206] Maluf N. and Williams K. (2004) *An Introduction to Microelectromechanical Systems Engineering*. Boston, Artech House.

[207] Wurmus H. and Kallenbach M. (1999) Chemomechanical Actuators chapter 6.8 in: *Adaptronics and Smart Structures* ed. H. Janocha, Berlin, Springer, 207-217.

[208] Gad-el-Hak M. (2002) *The MEMS Handbook*. Boca Raton, CRC Press.

[209] Boonen, R. Nabla Technisch Studiebureau, Riemst, Belgium.

[210] Okada, Y. and Ozawa, K. (2005) Energy regenerative and active control of electro-dynamic vibration damper. *IUTAM Symposium on Vibration Control of Nonlinear Mechanisms and Structures, Munich*, 18.-22.07. (in print).